Essentially Entropic Lattice Boltzmann Model

A Thesis
Submitted for the Degree of
DOCTOR OF PHILOSOPHY

by
MOHAMMAD ATIF

ENGINEERING MECHANICS UNIT
JAWAHARLAL NEHRU CENTRE FOR ADVANCED SCIENTIFIC RESEARCH
(A Deemed University)
Bangalore – 560 064

AUGUST 2019

Dedicated to my family

DECLARATION

I hereby declare that the matter embodied in the thesis entitled "**Essentially Entropic Lattice Boltzmann Model**" is the result of investigations carried out by me at the Engineering Mechanics Unit, Jawaharlal Nehru Centre for Advanced Scientific Research, Bangalore, India under the supervision of **Prof. Santosh Ansumali** and that it has not been submitted elsewhere for the award of any degree or diploma.

In keeping with the general practice in reporting scientific observations, due acknowledgment has been made whenever the work described is based on the findings of other investigators.

Mohammad Atif

CERTIFICATE

I hereby certify that the matter embodied in this thesis entitled “**Essentially Entropic Lattice Boltzmann Model**” has been carried out by **Mr. Mohammad Atif** at the Engineering Mechanics Unit, Jawaharlal Nehru Centre for Advanced Scientific Research, Bangalore, India under my supervision and that it has not been submitted elsewhere for the award of any degree or diploma.

Prof. Santosh Ansumali
(Research Supervisor)

Acknowledgements

The present thesis could not have been completed without the help from many people. First and foremost, I would like to express my sincere gratitude to my thesis advisor, Prof. Santosh Ansumali for his immense patience and constant support during the course of my PhD. He was available whenever I needed to discuss anything, be it personal or academic. I admire his approach towards tackling problems and I am grateful for the opportunity to learn from him. I would also like to thank Prof. K.R. Sreenivas, Prof. Ganesh Subramanian, and Prof. Meher Prakash for allowing me to attend their wonderful courses.

I am indebted to Prof. Bruce Boghosian, Prof. Ilya Karlin, and Prof. Alexander Wagner for their invaluable and constructive comments, without which the most important part of this thesis would not have attained its final form.

It is a pleasure to express my gratitude to Prof. Amol Marathe and Prof. Sai Jagan Mohan. They introduced me to the world of research during my undergraduate years at BITS Pilani. It is not an exaggeration to say that without their encouragement, I would not have joined JNCASR.

I would like to thank Chakradhar and Praveen for helping me with various computational issues from time to time. A portion of this thesis was accomplished while working with them. I would like to extend my thanks to DNS lab members – Samarth, Rhoheth, Akshay for keeping a lively atmosphere in the lab. Thanks are also due to my friends from JNC – Sambhavi, Aishwarya, Shveta, Shri, Anand, Krishnendu, Piyush, Prateek, Arun, and from Pilani – Akhilesh, Arnav, Aaditya Anand, Anurag, Sreekant, Gaurav, Palshikar, Chandak, with a special mention of my batchmates from Pilani — Pratik, Pulkit, Shaurya who joined JNC along with me and have spent countless hours together doing assignments and having discussions.

I am thankful for the support of my parents, brothers – Abdullah and Aquib, aunts – Tabassum and Shabeeh, uncles – Dr Md Amir Usmani and Prof. Furqan Ahmad, and cousins Qamar and Faisal, who have been around whenever there was a need.

I would also like to thank our administrative officer Mr Joydeep Deb, former administrative officer Mr A.N. Jayachandra, along with the academic coordinator Dr Princy, employees of the library, CompLab, hostel office, and other JNC staff for their cooperation.

Abstract

The success of the Moore's law in computing has led to many technological and scientific opportunities. The emerging exascale computing with its immense computational power can address several outstanding scientific problems. The primary challenge for utilizing the potential of these highly distributed computing architectures for large scientific application is to successfully handle the intensive floating point computation coupled with large data movements. It is thus imperative that successful algorithms exploit extreme parallelism and careful management of the data movement. In the past three decades, the lattice Boltzmann models have been established as viable alternatives for simulating fluid flows. They are highly amenable to parallelization due to their local nature, and can therefore efficiently utilize modern supercomputing clusters. Furthermore, they also tend to be more effective in terms of memory bandwidth utilization – an important bottleneck in high performance computing.

The lattice Boltzmann method constructs a simplified kinetic picture on a lattice designed to capture the physics of macroscopic flow through simple local micro-scale operations. A number of limitations of this method have been attributed to the loss of thermodynamic consistency while transitioning from the continuum to the discrete dynamics. This thesis attempts to review a few important features of continuum thermodynamics, such as the second law, in the framework of the lattice Boltzmann model. The entropic lattice Boltzmann models restore Boltzmann's H theorem (a generalization of the second law) to the discrete dynamics by numerically solving a nonlinear equation. The key innovation in this thesis is the construction of closed form analytical solutions to this nonlinear equation, thus, substantially reducing the computational requirement. This guarantees the numerical stability of the model in a computationally efficient manner. Furthermore, the discrete H theorem is also proved for the generalized quasi-equilibrium collision model equipped with two relaxation times.

For incorporating the temperature dynamics in a manner faithful to the kinetic theory, a numerically stable and thermodynamically consistent discrete velocity model is studied. The kinetic diffuse boundary conditions for the model is proposed. Simulations of various canonical test cases related to thermal and compressible hydrodynamics are performed, from which it is demonstrated that the proposed model remains numerically stable and is therefore capable of simulating compressible thermohydrodynamics.

List of Figures

2.1 The distribution of molecular speed as predicted by Maxwell for various parameters. 13

2.2 The trajectory for relaxation to equilibrium as per various collision models: the solid black curve represents the Boltzmann's collision kernel, the dashed blue line represents the BGK collision while the dash-dotted red lines represent the quasi-equilibrium model. Here, f is the pre-collisional state, f^* is the quasi-equilibrium and f^{eq} is the equilibirum state, whereas H_i are the isoentropy levels. 16

3.1 Finding the discrete equilibrium by evaluating the Maxwell-Boltzmann distribution at discrete points does not conserve the moments. In the figure, the area beneath the curve represents the density, which is different for the Maxwell-Boltzmann distribution and discrete equilibrium as Maxwell-Boltzmann distribution at discrete points. 20

4.1 Discretization of physical space in LBM. The discrete velocity $\boldsymbol{c}_i$ at any node $\boldsymbol{x}$ on the lattice connects to the neighboring nodes at $\boldsymbol{x} + \boldsymbol{c}_i\Delta t$, where Δt is the discrete time between successive collisions. 33

4.2 Sketch of of quasi-equilibrium collisional relaxation. 36

4.3 Building block of a crystallographic lattice in two dimensions, simple cubic links (left) and body-centered links (right) are depicted here. 38

4.4 Building block of a crystallographic grid in three dimensions, simple cubic links (left), face-centered cubic link (middle) and body-centered links (right). The dashed grid is offset by a distance $0.5\Delta x$ in each direction. 39

4.5 Communication between two processors on a crystallographic grid. 40

5.1 All the points on the chord joining any two points $(a, F(a)), (b, F(b))$ on convex function $F(z)$ lie above the function. 42

5.2 Known upper and lower bounds on $\log(1 + y)$. 43

5.3 Plots of $\log(1 + y)$ and its Taylor series expansion truncated at $N = 2, 5$. 44

5.4 Residue (hatched area) from Newton-Cotes quadratures is negative and progressively decreases in magnitude with increase in the order of quadrature. Here, we show the Trapezoid rule (top left), $\frac{1}{3}$Simpson's Rule (top right), Boole rule (bottom), and P_m are interpolating polynomials with m points. 47

5.5 $\log(1 + y)$ compared with its bounds from Newton-Cotes quadrature. 48

5.6 $\log(1 + y)$ compared with its bounds from Gauss-Legendre quadrature. 49

6.1 The entropic involution step: H_i are different entropy levels ($H_1 > H_2 > H_3$). Triangle denotes the polytope of positivity. Note that the pre-collisional state f and the mirror state f^{mirror} are at the same entropy level. The post collisional state f^* is at a lower entropy level. 57

6.2 (a) The triangular section of the plane inside which all the populations are positive, and outside of which one or more populations become negative. (b) Representation of a pre-collisional state f for which the mirror state is not defined. . . 60

(a) The polytope of positivity. 60

(b) Mirror state lies outside the polytope of positivity. 60
6.3 Behaviour of Eqs.(6.48),(6.58),(6.61),(6.63),(6.64) near the positive root. 65
6.4 Density (left column), velocity (middle column) and entropy (right column) plots from LBGK, $\alpha_{\text{Lower}}, \alpha_{\text{Higher}}, \alpha_{\text{ELBM}}$ at time $t = 500$ for viscosity $\nu = 1.0 \times 10^{-5}$. 69
6.5 Comparison between α_{Lower} and α_{ELBM} for the Sod shock tube. 69
(a) Snapshot of the path length for the shock tube simulation. 69
(b) Ratio of the turbulent viscosity correction to the kinematic viscosity. . . . 69
6.6 Comparison between α_{Higher} and α_{ELBM} for the Sod shock tube. 70
(a) Snapshot of the path length for the shock tube simulation. 70
(b) Ratio of the turbulent viscosity correction to the base viscosity. 70
6.7 Distribution of α_{Higher} and α_{ELBM} for lid driven cavity at Reynolds number 5000 and Mach number 0.05. Grid sizes are 64 × 64 (top), 96 × 96 (middle), 128 × 128 (bottom). The difference between the distribution of α_{Higher} and α_{ELBM} is seen to be insignificant. The solid black lines denote the region inside which 90% of the points lie. The locations of the solid lines are tabulated in Table 6.1. 71
6.8 Distribution of $\alpha_{\text{Higher}} - \alpha_{\text{ELBM}}$ for lid driven cavity at Reynolds number 5000 and Mach number 0.05. Grid sizes are 64 × 64 (left), 96 × 96 (center), 128 × 128 (right). The difference between the distribution reduces as the grid size increases. 72
6.9 Comparison of time evolution of global enstrophy $\bar{\Omega}$ between $\alpha_{\text{Lower}}, \alpha_{\text{Higher}}, \alpha_{\text{ELBM}}$ for the lid driven cavity at $\text{Re} = 5000$ and $\text{Ma} = 0.05$. The BGK solution is at a grid size of 256 × 256, however, $\alpha_{\text{Lower}}, \alpha_{\text{ELBM}}$ are at 96 × 96 (left) and 128 × 128 (right). Here, t^* is time non-dimensionalized via the convective time scale. The dissipative nature of α_{Lower} manifests in the form of reduced enstrophy. 72
6.10 Iso-vorticity contours for the lid driven cavity at Reynolds number of 5000 for various grid sizes. 73
(a) 64 × 64 73
(b) 96 × 96 73
(c) 128 × 128 73
6.11 Velocity profiles for the lid driven cavity at Reynolds number of 5000 and Mach number 0.05 for various grid sizes. 73
(a) x-velocity along the vertical centerline 73
(b) y-velocity along the horizontal centerline 73
6.12 Distribution of $\alpha_{\text{Iterate1}} - \alpha_{\text{ELBM}}$ for lid driven cavity at Reynolds number 5000 and Mach number 0.05. Grid sizes are 64 × 64 (left), 96 × 96 (center), 128 × 128 (right). The difference between the distribution reduces as the grid size increases. 74
6.13 Nondimensional iso-vorticity contours [(a)-(c)] for $\alpha_{\text{Lower}}, \alpha_{\text{Higher}}$ at grid size 256 × 256 and for BGK at 1024 × 1024 after one convection time. 75
(a) α_{Lower}, 256 × 256 75
(b) α_{Higher}, 256 × 256 75
(c) BGK, 1024 × 1024 75
6.14 Change in the global enstrophy $\Delta\Omega$ vs time for various square grids. Here, t^* is the nondimensional convection time. 75
6.15 Path length from the two schemes after one convection time on a grid of size 256 × 256. 76
(a) α_{Lower} 76
(b) α_{Higher} 76
6.16 Flow over NACA-0012 airfoil 77
(a) C_p at AoA=10° and $\text{Re} = 2.88 \times 10^6$. 77
(b) Visualization of the trailing edge at AoA=10° and $\text{Re} = 2.88 \times 10^6$. . . . 77
(c) Visualization of stall at AoA=12° and $\text{Re} = 5 \times 10^4$ 77

7.1 The energy shells in $RD3Q67$ model. 81

(a) SC1,SC2,SC3 81
(b) BCC$\frac{1}{2}$,BCC1,BCC$\frac{3}{2}$ 81
(c) FCC2,FCC3 81
7.2 Populations at each layer that see the top wall and need to be repopulated post streaming are listed in Table 7.2. 83
7.3 Non-dimensionalized mean planar velocity profiles obtained from $RD3Q67$ at various diffusion times compared against the analytical solution. 85
(a) Case (A) 85
(b) Case (B) 85
7.4 Temperature plots without including the thermal conductivity correction for different magnitudes of the top wall temperature. 86
7.5 L^2-norms of temperature 86
(a) L^2 norm at $\theta_{\text{top}} = 1.2\theta_0$ and different grid resolutions reveals second order convergence. 86
(b) Comparison for corrected and uncorrected thermal conductivity at various magnitudes of the top wall temperature. Here, resolution is kept fixed at $N = 32$. 86
7.6 Sketch representing the geometry of the two-dimensional box and the imposed wall temperatures. 87
7.7 Steady-state conduction in a two-dimensional plate. The solid lines are the analytical solution of the conduction equation while the symbols are from simulations. 87
(a) Temperature plots along constant x-lines 87
(b) Temperature plots along constant y-lines 87
7.8 Mean planar temperature profiles obtained from $RD3Q67$ at steady state compared against the analytical solution. 88
7.9 The figure shows the variation of density (ρ), velocity($\boldsymbol{u}$), and pressure (P) along the tube for the Sod's shock test. The figure contrasts $RD3Q67$ simulation results from run A (left) and B (right) with NSF equations at $t^* = 0.2$. 89
7.10 Temperature, density and pressure profiles for thermoacoustic convection at various times. Here $\bar{t} = t\nu/H^2$. The symbols are obtained from simulation while the lines are from the solution to the NSF equations. 90
(a) Normalized temperature $\bar{\theta} = (\theta - \theta_{\text{cold}})/(\theta_{\text{hot}} - \theta_{\text{cold}})$ 90
(b) Density $\bar{\rho} = \rho/\rho_0$ 90
(c) Pressure $\bar{P} = \rho\theta/(\rho_0\theta_{\text{cold}})$ 90
(d) $\langle\bar{P}\rangle$ is the volume averaged pressure 90
7.11 Temperature field for the Rayleigh-Bénard convection. The lines represent iso-temperature contours of temperature normalized from 0 to 1 in steps of 0.05. . . 92
(a) $\text{Ra} = 1.0 \times 10^4$ 92
(b) $\text{Ra} = 3.0 \times 10^4$ 92
(c) $\text{Ra} = 1.5 \times 10^5$ 92
(d) $\text{Ra} = 1.0 \times 10^7$ 92
7.12 Nu vs Ra, triangles are from current simulation, squares are from Ref.(Clever & Busse, 1974), line is empirical power law $\text{Nu} = 1.56(\text{Ra}/\text{Ra}_\text{c})^{0.296}$. 93
7.13 Mean planar profiles for $\text{Ra} = 2.5 \times 10^6$ averaged over ∼10 eddy turnover times. 94
(a) Planar average of nondimensional temperature 94
(b) Planar average of fluctuations in nondimensional temperature 94
(c) Planar average of fluctuations in nondimensional horizontal velocity . . . 94
(d) Planar average of fluctuations in nondimensional vertical velocity 94
7.14 Mean planar profiles for $\text{Ra} = 1.0 \times 10^8$ averaged over ∼10 eddy turnover times. 94
(a) Planar average of nondimensional temperature 94
(b) Planar average of fluctuations in nondimensional temperature 94

7.15 Visualizations of the temperature profile. 95
(a) Temperature at the vertical center planes for $\mathrm{Ra} = 2.5 \times 10^6$ 95
(b) Iso-temperature contours near the walls for $\mathrm{Ra} = 10^8$ 95
7.16 Grid convergence study for $\mathrm{Ra} = 10^4$ reveals second-order convergence. The converged $\mathrm{Nu_R}$ is 2.6311 with 360 points in the vertical direction. The line is the fitted curve. 95

8.1 Spurious currents around a two-dimensional droplet organize in a pattern of eight eddies. 98
8.2 Nondimensional error for the proposed discretization scheme for various η. It is seen that $\eta = 1/2$ is the best choice as it shows the least fluctuation. 105
8.3 Liquid vapour densities of the van der Waals fluid for various formulations at different reduced temperature $\theta^* = \theta/\theta_c$. The same plot is represented on the linear scale (left) and the logarithmic scale (right) to emphasize the error in density of the gas phase. 105
8.4 Spurious currents of the van der Waals fluid for various formulations at different reduced temperature $\theta^* = \theta/\theta_c$. 106
8.5 Equilibrium liquid and gas density $\rho/\rho_c = \rho^*$ obtained from $RD3Q41$ model for Carnahan Starling EoS (left) and Peng-Robinson type EoS compared against their respective Maxwell equal area construction at various $\theta/\theta_c = \theta^*$. 107
8.6 Deeply quenched liquid gas system forms a stable structure, typically a lamellar film, a cylindrical micelle, or a spherical droplet. Here, smaller droplets merge to form larger droplets. 108
8.7 Laplace law: setup (left) and relation between pressure, surface tension, and radius (right). 108
8.8 Taylors deformation test: A representation of the deformed droplet (left), and plot of D versus Ca (right). 109
8.9 Head-on collision between two droplets at $\rho_{\mathrm{liq}}/\rho_{\mathrm{gas}} \approx 13$, $\mathrm{Re} = 297.03$ and We= 19.47. 110
8.10 Offset collision between two droplets at $\rho_{\mathrm{liq}}/\rho_{\mathrm{gas}} \approx 13$, $\mathrm{Re} = 297.03$ and We= 19.47.111

List of Tables

4.1 Weights corresponding to discrete velocities for the basic models. 34
4.2 Representation of a sphere, an ellipsoid, and cut-section of a red blood cell (RBC) on a SC and BCC lattice at the same resolution. It is seen that the BCC lattice used by crystallographic LBM represents local curvatures in a more efficient manner as compared to the SC lattice used by the conventional LBM. 39

5.1 The functions $\log(1+y), t_5(y), t_2(y)$ and their associated errors. 44
5.2 $\log(1+y)$ and $\mathcal{I}^{(n)}_{\mathrm{NC}}$ and their associated errors. $\%\Delta\mathcal{I}^{(n)}_{\mathrm{NC}} = (\mathcal{I}^{(n)}_{\mathrm{NC}}/\log(1+y)-1)\times 100$ 49
5.3 $\log(1+y)$ and $\mathcal{I}^{(n)}_{\mathrm{GL}}$ and their associated errors. $\%\Delta\mathcal{I}^{(n)}_{\mathrm{GL}} = (\mathcal{I}^{(n)}_{\mathrm{GL}}/\log(1+y)-1)\times 100$ 49

6.1 Region around the LBGK value of $\alpha = 2$ where 90% of the points lie. It is seen that as the grid size increases the region becomes narrower. 70

7.1 Energy shells and their corresponding velocities with weights for $RD3Q67$ model, $\theta_0 = 0.7487399237215752$. 81
7.2 Incoming populations at each layer near the top wall. 83

8.1 Discretization scheme and the maximum magnitude of spurious current for various EoS on a grid of size $80 \times 80 \times 4$ for various EoS at $\theta/\theta_c = 0.9$ using the model $RD3Q41$. 106
8.2 Liquid and gas densities obtained from the proposed model compared with their corresponding Maxwell construction values for Carnahan-Starling EoS. 107
8.3 Liquid and gas densities obtained from the proposed model compared with their corresponding Maxwell construction values for Peng-Robinson type EoS. 107

Contents

Abstract **vii**

1 Introduction **1**
- 1.1 Motivation . . . 1
- 1.2 Entropic lattice Boltzmann model . . . 3
- 1.3 Outline of the thesis . . . 3

2 Kinetic theory of gases **7**
- 2.1 Distribution function and its moments . . . 7
- 2.2 The Boltzmann equation . . . 8
- 2.3 The Maxwell-Boltzmann distribution . . . 11
  - 2.3.1 Maxwell's derivation . . . 11
  - 2.3.2 Boltzmann's route . . . 13
  - 2.3.3 Properties of the Maxwell-Boltzmann distribution . . . 14
- 2.4 Collision Models . . . 14
  - 2.4.1 Bhatnagar-Gross-Krook model . . . 14
  - 2.4.2 Quasi-equilibrium model . . . 15
  - 2.4.3 Fokker-Planck model . . . 17
- 2.5 Conclusion . . . 17

3 Discrete kinetic modeling of thermohydrodynamics **19**
- 3.1 Discrete velocity models . . . 20
- 3.2 The Boltzmann BGK equation . . . 21
- 3.3 Hydrodynamic limit of the Boltzmann BGK equation . . . 22
- 3.4 Energy conserving discrete equilibrium distribution . . . 23
  - 3.4.1 Definition of temperature in the discrete kinetic theory . . . 25
- 3.5 Discrete entropic equilibrium . . . 26
  - 3.5.1 Special cases: $D1Q3, D2Q9, D3Q27$ . . . 27
  - 3.5.2 Perturbation series of the entropic equilibrium . . . 27
- 3.6 Conclusion . . . 30

4 The lattice Boltzmann model **31**
- 4.1 From continuous to discrete space-time . . . 32
  - 4.1.1 Time discretization . . . 32
  - 4.1.2 Space discretization . . . 33
- 4.2 Discrete isothermal equilibrium . . . 34
- 4.3 Other collision models in LBM . . . 35
  - 4.3.1 Quasi-equilibrium collision . . . 36
  - 4.3.2 Multiple relaxation time collision . . . 37
  - 4.3.3 Karlin-Bösch-Chikatamarla (KBC) collision . . . 37
- 4.4 Crystallographic lattice Boltzmann model . . . 38

5 Discrete Time $\mathcal{H}$ theorem: Some Sharp Inequalities 41
5.1 Bounds on the logarithm 42
5.2 The Hermite-Hadamard inequality 44
5.3 Extended Hermite-Hadamard inequality 46
5.3.1 Newton-Cotes quadratures 46
5.3.2 Gauss-Legendre quadrature 49
5.4 A few positive definite functions 51

6 Discrete Time $\mathcal{H}$ theorem: Single relaxation time entropic lattice Boltzmann model 53
6.1 Entropic lattice Boltzmann model 54
6.2 The entropic involution 56
6.2.1 Discussion on the over-relaxation 57
6.2.2 Near equilibrium limit of the entropic involution 57
6.2.3 Indeterminacy in the entropic involution 59
6.3 Exact solution to the path length: Essentially entropic lattice Boltzmann model . 60
6.3.1 Lower order solution 62
6.3.2 Higher order solution 63
6.3.3 Solving the higher degree polynomial 64
6.3.4 Implementing the exact solution 66
6.4 Comparison with ELBM and BGK 68
6.4.1 Sod shock tube 68
6.4.2 Lid driven cavity 69
6.4.3 Doubly periodic shear layer 74
6.5 Flow past NACA-0012 airfoil 74
6.6 Entropic route to modeling the subgrid viscosity 76
6.7 Conclusion 78

7 Lattice Boltzmann model for compressible thermohydrodynamics 79
7.1 The $RD3Q67$ Model 80
7.2 Kinetic boundary condition 82
7.3 Hydrodynamics: Start-up of simple shear flow 84
7.4 Heat conduction: Steady state 85
7.4.1 One-dimensional heat conduction 85
7.4.2 Two-dimensional cavity heated at the top 85
7.4.3 Viscous heat dissipation 87
7.5 Compressible thermohydrodynamics 88
7.5.1 Sod shock tube 88
7.5.2 Thermoacoustic convection 90
7.5.3 Rayleigh-Bénard convection 91
7.6 Outlook 93

8 Lattice Boltzmann model for nonideal fluids 97
8.1 Equations of state 98
8.2 Thermodynamics of a single component two-phase fluid 99
8.3 Incorporating nonideal effects in lattice Boltzmann 100
8.4 Evaluating derivatives on a lattice 102
8.5 Discrete derivative operator 103
8.6 Quenching of a liquid-gas system 106
8.7 Laplace law and Taylor's deformation test 106
8.8 Droplet Collision 109
8.9 Conclusions 110

9 Outlook **113**

Appendix A Evolution of the thermohydrodynamic moments **117**
A.1 Evolution of density 117
A.2 Evolution of velocity 118
A.3 Evolution of pressure, temperature, and the stress tensor 118
A.4 Evolution of the heat flux 119
A.5 Constraints on the weights of DVM 119

Appendix B Analytical solutions **121**
B.1 Analytical Solution for transient Couette/conduction 121
B.2 Analytical Solution for 2D Transient Conduction 122

Appendix C **125**
C.1 Discrete time $\mathcal{H}$ theorem for the generalized quasi-equilibrium model 125

References

Curriculum vitae

Chapter 1

Introduction

1.1 Motivation

Fluid flows are constitutive to a wide variety of scientific and engineering problems, owing to the fact that they encompass a vast range of spatial and temporal scales. An accurate prediction of the fluid flow has innumerable commercial applications in turbomachinery, petrochemical industries, hydraulic machines, inkjet printing, as well as is of great scientific interest for multiphase flows, non-Newtonian flows, hydrodynamic instability and transition to turbulence (Dixon & Hall, 2013; Oliemans, 2012; Batchelor, 2000; Leal, 2007). Fluid dynamics becomes crucial during scenarios that require knowledge of flows over an aortic stenosis, designing artificial heart valves, and predicting extreme weather patterns such as cyclones, floods, hurricanes. Additionally, a quick prediction of the atmospheric flows can lead to the prior knowledge of the expected rainfall, which will reduce losses in the regions that are dependent on the rain for the purpose of agricultural irrigation.

Although seemingly disparate, the various flows in the continuum regime, irrespective of the spatial and temporal scales, are similar and are governed by the Navier-Stokes-Fourier (NSF) equations (Batchelor, 2000). These equations can be simplified and solved to obtain a closed form solution for a large class of problems (Leal, 2007). However, they do not render a general solution for many realistic engineering and scientific problems, particularly in the case of turbulent flows where the nonlinearity of the NSF equations gives rise to chaotic beahviour. One has to, therefore, resort to numerical methods to solve them. The direct numerical simulations (DNS), where all the scales of the flow are resolved, are the most reliable numerical approaches for solving the NSF equations. However, the DNS of many realistic flows such as the turbulent flows requires grid sizes that are often too large (Pope, 2000). With the existing approaches, it is widely accepted that DNS of turbulent flows will be feasible only after a decade (Thantanapally *et al.*, 2013*a*; Slotnick *et al.*, 2014; Larsson & Wang, 2014). Thus, one looks for viable alternates to it such as the turbulence models. They reduce the computational load by modeling the subgrid phenomena and projecting it onto a coarse grid. However, the choice of these turbulence model is problem specific and hence these models lack universality.

Furthermore, the numerical modeling of many phenomena such as cloud dynamics turns out to be particularly challenging due to the mutual interaction of nonlinear physical processes occuring at widely different scales. At the micrometer scale the physics of cloud formation involves water vapour condensing to form liquid droplets or ice crystals, nucleation on aerosol particles, their growth and interaction, which is termed as “cloud microphysics”, while at the the kilometer scale there are large scale air motions, wind, pressure patterns, and thermodynamic interactions, which is called “cloud dynamics” (Houze Jr, 2014). The phenomena at the two scales are coupled, for example, the latent heat released during the condensation of water vapour drives the circulation in the atmosphere, sometimes causing instabilities that lead to severe weather conditions (Kuo, 1965). For a brief review of numerical cloud models the reader is referred to Guichard & Couvreux (2017). Many widely used numerical models explicitly simulate unsteady convective clouds via large eddy simulation of the Navier-Stokes equations coupled with parametrized bulk modeling of the microphysics (Thompson *et al.*, 2004; Guichard & Couvreux, 2017). Despite significant advances, the modeling of cloud microphysics is still an open problem with the most important gaps being our lack of understanding of the microphysics and the limitations of numerical models in representing the known microphysics (Khain *et al.*, 2000).

Further progress requires both better physical models of the various phenomena as well as enhanced capability to perform numerical simulations of turbulent flows. A uniform framework based on physics based models capable of simulating both the microphysics as well as the large scale dynamics is highly desired.

In the past three decades, the lattice Boltzmann method (LBM) has come up as a viable alternative for simulating fluid flows. In contrast to the conventional numerical methods that directly discretize and solve the NSF equation, the LBM solves a discrete kinetic equation which produces the NSF equations in the macroscopic limit. It is routinely used for fluid dynamic applications as wide-ranging as fluid turbulence, gaseous microflow, soft matter, polymer dynamics, relativistic flows, multiphase flows, etc. (Adhikari *et al.*, 2005; Mendoza *et al.*, 2010; Aidun & Clausen, 2010; Yudistiawan *et al.*, 2010; Singh *et al.*, 2013; Benzi *et al.*, 2013; Mazloomi *et al.*, 2015; Namburi *et al.*, 2016; Dorschner *et al.*, 2016*a*; Geier *et al.*, 2017). The method is based on the Boltzmann equation which tracks the evolution of single particle probability distribution function in the phase space. It constructs a simplified kinetic picture on a lattice designed to capture the physics of macroscopic flow through simple local micro-scale operations (Chen & Doolen, 1998; Succi, 2001). It has has met with significant success because of its ease of implementation due to the nonlinearities being localized. It is simple but highly parallelizable and can therefore efficiently utilize modern supercomputing clusters, which are often quite heterogeneous. Furthermore, it also tends to be more efficient in terms of memory bandwidth utilization, an important bottleneck in high performance computing (Aidun & Clausen, 2010; Shet *et al.*, 2013). Due to these attractive features, the lattice Boltzmann method gained tremendous success and is now a well established tool for simulating isothermal incompressible hydrodynamics.

It should be noted that within a few years of its introduction, the application of LBM had been successfully extended to flows with particle suspensions, two-phase flows and phase transitions, binary mixtures, and gaseous microflows at moderate Knudsen numbers (Shan & Chen, 1993; Ladd, 1994; Yudistiawan *et al.*, 2010; Ansumali *et al.*, 2006; Arcidiacono *et al.*, 2006). The current LBMs can integrate any equation of state to simulate phase transitions in a thermodynamically consistent manner (Swift *et al.*, 1996; Yuan & Schaefer, 2006; Mazloomi *et al.*, 2015). This is due to the fact that the LBMs, being a mesoscopic tool, are especially useful for complex systems where the macroscopic governing equations are not available whereas the microscopic physics is known (He & Doolen, 2002).

Despite their simplicity and versatility, the inceptive lattice Boltzmann models faced two issues:

- They lacked a consistent methodology for modeling the temperature dynamics, which restricted their applicability to isothermal flows. Some progress was made starting with the work of Alexander *et al.* (1993), but the thermal lattice Boltzmann models remained less robust than their isothermal counterparts (McNamara *et al.*, 1997). Efforts to circumvent this problem led to the introduction of the double distribution function models, where one set of distribution function solved the isothermal hydrodynamics and the other set solved the macroscopic energy equation for the temperature dynamics (Shan, 1997; He *et al.*, 1998*b*). The drawback of such models was that a faithful representation of the particle picture of the kinetic theory was compromised.

- They were difficult to use for problems such as turbulence where very sharp gradients can exist if the simulations are under-resolved. The rise of numerical instability was attributed to the violation of the $\mathcal{H}$ theorem (which states that in any irreversible process the entropy is a non-decreasing function of time) (Karlin *et al.*, 1999; Succi *et al.*, 2002*b*), and was mitigated by reinstating the $\mathcal{H}$ theorem to the discrete time dynamics (Ansumali & Karlin, 2000; Boghosian *et al.*, 2001; Ansumali & Karlin, 2002*c*; Boghosian *et al.*, 2003). The resulting models, called the entropic lattice Boltzmann models (ELBM), were found to be capable of simulating high Reynolds number flows (Chikatamarla & Karlin, 2013*a*; Namburi *et al.*, 2016; Atif *et al.*, 2017, 2018).

1.2 Entropic lattice Boltzmann model

The entropic lattice Boltzmann model (ELBM) is an alternate methodology, which restores the $\mathcal{H}$ theorem for discrete space-time evolution (Karlin *et al.*, 1998; Wagner, 1998; Karlin *et al.*, 1999; Chen & Teixeira, 2000; Boghosian *et al.*, 2001; Succi *et al.*, 2002*b*; Ansumali *et al.*, 2003; Boghosian *et al.*, 2003). It was a paradigm shift for computational fluid dynamics where the numerical stability of a hydrodynamic solver was enforced by insisting on adherence to the thermodynamics at the discrete time level (Succi *et al.*, 2002*b*). The ELBM is accepted as a viable tool for simulation of turbulence, multiphase flows, as well as microflows due to its unconditional numerical stability (Ansumali *et al.*, 2006; Aidun & Clausen, 2010; Chikatamarla & Karlin, 2013*b*; Mazloomi *et al.*, 2015; Atif *et al.*, 2017).

The ELBM requires an additional step known as the entropic involution step. It involves a numerical search for the solution to a highly nonlinear equation. Considerable efforts have been made to ensure the correctness and efficient implementation of this step (Ansumali & Karlin, 2000, 2002*a*; Tosi *et al.*, 2006; Chikatamarla *et al.*, 2006; Brownlee *et al.*, 2007; Gorban & Packwood, 2012). However, there is scope for a better theoretical understanding of the ELBM if one is able to obtain a analytical solution to the nonlinear equation. For example:

- The analytical solution could be understood as an implicit model of the unresolved scales of the flow via the thermodynamic entropy, and may provide a new insight into the sub-grid modeling of turbulence.
- It will help enhance the efficiency of the ELBM by avoiding a numerical search for the path length.

Therefore, an analytical solution to the nonlinear equation is highly desirable.

To summarize, before the applicability of the LBM can be extended to realistic multiscale scenarios, the following concerns need to be addressed:

- How to model the complete macroscopic thermohydrodynamics using only a single distribution function in a manner faithful to the kinetic theory?
- How to construct the the discrete equilibrium for these models? What are the requirements on the parameters of such models?
- How to obtain an analytical solution to the nonlinear equation in the ELBM?
- Could the analytical solution be interpreted as an implicit model of the unresolved scales of the flow? This will provide a new insight into the subgrid modeling of turbulence via the thermodynamic route.

1.3 Outline of the thesis

The lattice Boltzmann models, which are based on the discrete velocity models of the kinetic theory, are described in this thesis. The thermodynamic consistency is crucial for constructing such models so that they display nonlinear numerical stability along with the correct thermohydrodynamic behaviour (Atif *et al.*, 2017, 2018). This thesis broadly answers two questions:

- Can the discrete time $\mathcal{H}$ theorem be established in an analytically tractable manner? We show that not only it is possible but once can write a closed form solution to a highly nonlinear equation.

- What are the constraints on the discrete velocity set so that the accurate thermohydrodynamic behaviour is recovered as the macroscopic limit of the model kinetic equation?
- How to write the equilibrium distribution for any discrete velocity model such that the positivity of the equilibrium distribution is preserved?

The overall organization of the thesis is as follows:

In Chapter 2, a brief introduction to the kinetic theory of gases is presented and the important properties of the Boltzmann equation are discussed. Following Maxwell's and Boltzmann's routes, the Maxwell-Boltzmann distribution is derived and some of its important properties are discussed. A few simplifications of the Boltzmann's collision kernel that retain its essential properties, yet are simple enough to implement are also described along with the $\mathcal{H}$ theorem associated with each of them.

In Chapter 3, the constraints on the parameters of any discrete velocity model of the kinetic theory necessary to obtain the correct thermohydrodynamics are derived. Firstly, the constraints due to the isotropy and independence from preference to any direction are discussed. Next, the moment chain and the macroscopic limit of the discrete kinetic equation (Boltzmann Bhatnagar-Gross-Krook) is discussed, followed by the derivation of the constraints on the discrete equilibrium distribution. A systematic approach for deriving the discrete equilibrium distribution and its series expansion is discussed. These series expansions tend to become negative at large Mach number or temperature deviations, however, they are useful for analyzing the macroscopic limit of the model.

In Chapter 4, the lattice Boltzmann model, which falls under the category of the discrete velocity models but is discrete in space and time too, is presented. A few collision models used in the lattice Boltzmann model are then discussed, followed by a brief discussion on the recently developed crystallographic lattice Boltzmann model, its computational cost and the parallelization strategy.

In Chapter 5, a systematic approach to obtain the bounds on any convex functions upto the desired accuracy is formulated. This approach is based on quadrature rules and the bounds obtained can be interpreted as rational or Padé approximations to the convex function. The lower order quadrature rules provide loose bounds on the function, while the higher order ones provide sharper bounds. The Hermite-Hadamard inequality, which also provides upper and lower bounds on convex functions, is proved using only convexity arguments (Niculescu & Persson, 2007). Using the proposed approach of constructing the bounds, the Hermite-Hadamard inequality is extended. These bounds become useful while proving the discrete time $\mathcal{H}$ theorem for the lattice Boltzmann models.

In Chapter 6, the entropic lattice Boltzmann model (ELBM), a nonlinearly stable discrete space-time methodology, that guarantees adherence to the $\mathcal{H}$ theorem is presented. The geometric interpretation of the entropic involution step, which is the backbone of the ELBM is given. The entropic involution step involves solving a highly nonlinear equation, that is conventionally done by using iterative methods. A novel methodology which replaces the entropic involution step with an exact solution to the nonlinear equation is proposed. This exact solution is found by exploiting the various bounds on the convex functions given in Chapter 5. Simulations of the one-dimensional shock tube show that there is no appreciable difference between the results obtained from exact solution and the iterative solution. However, the exact solution avoids expensive iterations and is thus computationally less expensive than the iterative solution. Further, via the simulations of the classical lid driven cavity and flow past NACA0012 airfoil it is demonstrated that the proposed methodology is well suited for simulating interior as well as exterior flows. The simulations exhibit good match with the results available in the literature.

In Chapter 7, an energy conserving lattice Boltzmann model based on sixty-seven discrete velocities is introduced. The kinetic diffuse boundary conditions for the model is proposed. Simulations of various canonical test cases related to thermal and compressible hydrodynamics are performed, from which it is demonstrated that the proposed model remains numerically stable and is thus capable of simulating thermohydrodynamics.

In Chapter 8, the lattice Boltzmann model for nonideal fluids and multiphase flows is revisited. The coexistence curve from the nonideal interactions given by the van der Waals, Carnahan-Starling, and Peng-Robinson equation of state are obtained. A discretization scheme that reduces the magnitude of the spurious currents and remains stable for larger liquid-vapour density ratios is proposed. Simulations of canonical test cases like deeply-quenched liquid vapour system, Laplace's law and Taylor's droplet deformation are performed to benchmark the model. Finally, the simulations of binary droplet collision are performed.

In Chapter 9, an outlook for the present work is discussed.

Chapter 2

Kinetic theory of gases

Classical thermodynamics provides a phenomenological description of the macroscopic state of any system at equilibrium in terms of measurable quantities such as the temperature, heat, work, entropy, etc. (Callen, 1998). Considering the fact that all systems are composed of microscopic particles such as the atoms and molecules, it should be possible to obtain the macroscopic behaviour from the motion of the microscopic particles. The kinetic theory provides the statistical description of the macroscopic dynamics at the molecular level (Cercignani, 1988; Liboff, 2003).

At the heart of the kinetic theory lies the famous Boltzmann equation (Grad, 1949). It describes the statistical behaviour of a thermodynamic system even away from equilibrium. The Boltzmann equation and its various simplications have long been employed as a model for fluid dynamics. These simplications are two fold:

- The complexity of the collision kernel given by Boltzmann becomes a hindrance in the numerical simulations as well as in the theoretical analysis of initial and boundary value problems. Several simplications for the collision kernel such as the Bhatnagar-Gross-Krook (BGK) (Bhatnagar *et al.*, 1954), Fokker-Planck (Lebowitz *et al.*, 1960; Singh & Ansumali, 2015), quasi-equilibrium model (Ansumali *et al.*, 2007*a*) have been proposed. These models retain the basic features of the Boltzmann collision kernel, while they end up sacrificing some other features. For example, the Prandtl number given by Boltzmann's kernel is 2/3, while that of BGK is 1 and Fokker-Planck is 3/2 (Singh & Ansumali, 2015). However, in both BGK and Fokker-Planck it is known how to tune the Prandtl number to arbitrary values (Thantanapally *et al.*, 2013*b*; Singh *et al.*, 2016).

- The original description given by Boltzmann dealt with continuous velocity space, i.e., the particles could attain any velocity in the range of $-\infty$ to ∞. It has been shown that discrete velocity models (DVMs), where one assumes that the particles can move only in a predecided set of directions, with as few as six directions can capture the structure of the shock wave (Broadwell, 1964). The lattice Boltzmann model which falls into the broad category of DVMs, is a well accepted model for hydrodynamics. In 2-dimensions, it requires as few as nine discrete velocities to capture macroscopic hydrodynamics.

The objective of both the simplications is to get rid of unnecessary microscopic details, and keep only the information pertinent to the macroscopic dynamics.

In this chapter, we will review the basic concepts of the continuous kinetic theory as well as the simplified collision models. Furthermore, we also discuss discrete velocity models and simplified collision models. The chapter is arranged as follows: In Section 2.1, we introduce the single particle probability distribution function and its moments in the context of macroscopic thermohydrodynamics. In Section 2.2, we discuss the Boltzmann equation and its important properties. In Section 2.3, we follow Maxwell and Boltzmann's derivation of the equilibrium distribution and discuss its important properties. Finally, in Section 2.4, we discuss some of the widely used alternatives to the Boltzmann's collision kernel.

2.1 Distribution function and its moments

In the kinetic theory, one considers a collection of N identical point particles where each individual particle is undergoing a constant and random motion. In the hard-sphere model, these particles undergo collision if they try to occupy the same location at the same instant. The smallest length scale at the molecular level is known as the mean-free path l_{mfp}. This is defined as the the average distance traveled by the particles between successive collisions. Similarly, the smallest time scale present in the system is the mean-free time, which is defined as the average time spent by particles between successive collisions. The Knudsen number ($\mathrm{Kn} = l_{\mathrm{mfp}}/L_{\mathrm{ref}}$) is defined as the ratio of the mean free path and the characteristic macroscopic length scale L_{ref} of the system. In the limit of $\mathrm{Kn} \to 0$, the fluid behaves as a continuum. As the Knudsen number increases the flow becomes rarefied and gradually transitions to a free-molecular regime. Our domain of interest is $\mathrm{Kn} \ll 1$, where the fluid can be modeled as a continuum and the macroscopic hydrodynamic equations predict the accurate behaviour of the system.

Instead of attempting a detailed description of the trajectory of each individual particle in the phase space, the kinetic theory provides the statistical description of their motion. The central quantity of interest is the single particle probability distribution function $f(\boldsymbol{x}, \boldsymbol{c}, t)$ with $f d\boldsymbol{c}$ being probability of finding a particle moving with velocity in the range $\boldsymbol{c}$ to $\boldsymbol{c} + d\boldsymbol{c}$ at time t and location $\boldsymbol{x}$. It is convenient to define bilinear action between two functions of molecular velocity $\phi(\boldsymbol{c})$ and $\psi(\boldsymbol{c})$ as

$$\langle \phi, \psi \rangle = \int d\boldsymbol{c}\, \phi(\boldsymbol{c})\, \psi(\boldsymbol{c}). \tag{2.1}$$

In D-dimensions, the hydrodynamic fields such as mass density ρ, the velocity $\boldsymbol{u}$, and the energy density E are related to the moments of the distribution function

$$\left\langle f, \left\{ 1, \boldsymbol{c}, \frac{\boldsymbol{c}^2}{2} \right\} \right\rangle = \{\rho, \rho \boldsymbol{u}, E\}, \tag{2.2}$$

with $E = \mathcal{E} + \rho u^2/2$, where the internal energy $\mathcal{E} = Dp/2$, and p is the thermodynamic pressure. The ideal gas equation of state $p = \rho\, \theta$ relates the thermodynamic pressure with the temperature. Here, $\theta = k_B T/m$ is the scaled temperature T, with k_B as the Boltzmann constant and m as the mass of the particle, hereafter assumed to be unity. Here onwards the fluctuating velocity is defined as $\boldsymbol{\xi} = \boldsymbol{c} - \boldsymbol{u}$ and we restrict our discussion to three dimensions ($D = 3$) unless otherwise stated. Other relevant quantities in thermal hydrodynamics are the stress tensor $\sigma_{\alpha\beta} = \overline{\langle f, \xi_\alpha \xi_\beta \rangle}$ and the heat flux $q_\alpha = \left\langle f, \xi_\alpha \xi^2/2 \right\rangle$, where the symmetrized traceless part $\overline{A_{\alpha\beta}}$ for any second order tensor $A_{\alpha\beta}$ is

$$\overline{A_{\alpha\beta}} = \frac{1}{2}\left(A_{\alpha\beta} + A_{\beta\alpha} - \frac{2}{3} A_{\gamma\gamma} \delta_{\alpha\beta} \right). \tag{2.3}$$

It is often convenient to rewrite the stress tensor as $\sigma_{\alpha\beta} = \langle f, c_\alpha c_\beta \rangle - \rho u_\alpha u_\beta - p \delta_{\alpha\beta}$ and the heat flux as $q_\alpha = \left\langle f, c_\alpha c^2/2 \right\rangle - u_\alpha (E + p) - u_\beta \sigma_{\alpha\beta}$. For subsequent uses, we also define third moment $Q_{\alpha\beta\gamma} = \langle f, \xi_\alpha \xi_\beta \xi_\gamma \rangle$ with its traceless part as

$$\overline{Q_{\alpha\beta\gamma}} = Q_{\alpha\beta\gamma} - \frac{2}{5}\left(q_\alpha \delta_{\beta\gamma} + q_\beta \delta_{\alpha\gamma} + q_\gamma \delta_{\beta\alpha} \right). \tag{2.4}$$

Similarly, we define the contracted fourth moment $R_{\alpha\beta\gamma\zeta} = \left\langle f, \xi^2 \xi_\alpha \xi_\beta \right\rangle$, its traceless part $\overline{R_{\alpha\beta}} = \overline{\langle f, \xi^2 \xi_\alpha \xi_\beta \rangle}$ and its trace $R = \left\langle f, \xi^4 \right\rangle$.

2.2 The Boltzmann equation

The Boltzmann equation describes the time evolution of the distribution function $f(\mathbf{x}, \boldsymbol{c}, t)$ under the action of external forces and internal collisions. One of the first assumptions in deriving the Boltzmann equation is that the collisions occupy only a very small time and that the gas is sufficiently dilute that only binary collisions are important (Chapman & Cowling, 1970). In explicit form, the Boltzmann equation is (Cercignani, 1988)

$$\frac{\partial f}{\partial t}+c_\alpha\frac{\partial f}{\partial x_\alpha}+g_\alpha\frac{\partial f}{\partial c_\alpha}=\mathcal{J}\left(f,f\right), \tag{2.5}$$

where g_α is the acceleration due to external force and $\mathcal{J}$ is the collision kernel. The left hand side of the equation describes the time rate of change of the distribution function in an elemental volume due to the flux of particles across the bounding surfaces, and the right hand side represents the binary collisions among particles which leads to particles jumping from one elemental volume to another in the velocity space.

It is evident that just after the collision, the particles are correlated because of the conservation of the mass, momentum, and the energy. However, these correlations decay exponentially and therefore the probability of the two correlated molecules undergoing another collision is effectively zero. The Boltzmann equation relies on the famous molecular chaos (*"Stosszahlansatz"*) assumption which asserts that the velocities of the colliding particles before collision are uncorrelated, i.e.,

$$f_{12}\left(\boldsymbol{x}_1,\boldsymbol{c}_1,\boldsymbol{x}_2,\boldsymbol{c}_2,t\right)=f\left(\boldsymbol{x}_1,\boldsymbol{c}_1,t\right)f\left(\boldsymbol{x}_2,\boldsymbol{c}_2,t\right). \tag{2.6}$$

The collision operator with molecular chaos approximation is

$$\mathcal{J}=\int d\boldsymbol{c}_2\int d\boldsymbol{k}\,k_1\left[f(\boldsymbol{c}_1)f(\boldsymbol{c}_2)-f(\boldsymbol{c})f(\boldsymbol{c}')\right], \tag{2.7}$$

where $\boldsymbol{c}_1$ and $\boldsymbol{c}_2$ are pre-collisional velocities, $\boldsymbol{c}'$ and $\boldsymbol{c}$ are post-collisional velocities, $d\boldsymbol{k}$ represents an element of the solid angle, and the function k_1 captures the collision cross section and magnitude of relative velocity of the colliding particles.

A few important properties of the Boltzmann equation are listed below:

1. **Collisional invariants:** The binary collisions are assumed to be elastic in nature and do not alter the mass, momentum, and energy of the system, therefore,

   $$\left\langle\mathcal{J},\left\{1,\boldsymbol{c},\boldsymbol{c}^2\right\}\right\rangle=\left\{0,\boldsymbol{0},0\right\}. \tag{2.8}$$

   Thus, the local (in position space) hydrodynamic fields can change only due to redistribution of particles in position space.

2. **Conservation laws:** Taking the moments of the Boltzmann equation (Eq.(2.5)) and using Eq.(2.8) one obtains the macroscopic conservation laws as

   $$\begin{aligned}\partial_t\rho+\partial_\alpha(\rho u_\alpha)&=0,\\ \partial_t(\rho u_\alpha)+\partial_\beta\left(\rho u_\alpha u_\beta+p\delta_{\alpha\beta}+\sigma_{\alpha\beta}\right)&=\rho g_\alpha,\\ \partial_t E+\partial_\beta\left[\left(E+p\right)u_\beta+\sigma_{\beta\gamma}u_\gamma+q_\beta\right]&=\rho u_\alpha g_\alpha.\end{aligned} \tag{2.9}$$

   It should be noted here that the conservation laws emerge from the set of collisional invariants only and should hold irrespective of the form of the collision term. This feature of the Boltzmann equation allows to obtain the same set of macroscopic equations from various other forms of the collision terms. It is also evident that the conservation laws are consistent with the equations of continuum mechanics.

3. **Zero point of the collision:** The Maxwell-Boltzmann distribution f^{MB},

   $$f^{\mathrm{MB}}=\rho\left(\frac{3\rho}{4\pi\mathcal{E}}\right)^{\frac{3}{2}}\exp\left[\frac{-3\rho\xi^2}{4\mathcal{E}}\right]. \tag{2.10}$$

   is the solution to the equation

   $$\mathcal{J}(f,f)=0. \tag{2.11}$$

This implies that when $f = f^{\mathrm{MB}}$

$$f(\boldsymbol{c})f(\boldsymbol{c}') = f(\boldsymbol{c}_1)f(\boldsymbol{c}_2), \tag{2.12}$$

which is known as the condition of detailed balance, i.e., for every pair of particles with velocities $\boldsymbol{c}, \boldsymbol{c}'$, that collide and attain the velocities $\boldsymbol{c}_1, \boldsymbol{c}_2$ there is an opposite pair of particles with the velocities $\boldsymbol{c}_1, \boldsymbol{c}_2$ that collide and attain the velocities $\boldsymbol{c}, \boldsymbol{c}'$.

4. $\mathcal{H}$ **theorem:** Boltzmann extended the second law of thermodynamics to non-equilibrium situations by defining the H-function as

$$\mathcal{H}(t) = \int d\boldsymbol{c}_1 f(\boldsymbol{c}_1) \log f(\boldsymbol{c}_1). \tag{2.13}$$

The derivative of $\mathcal{H}$ with respect to t is

$$\frac{\partial \mathcal{H}}{\partial t} = \int d\boldsymbol{c}_1 \frac{\partial}{\partial t}\left(f(\boldsymbol{c}_1)\log f(\boldsymbol{c}_1)\right) = \int d\boldsymbol{c}_1 \frac{\partial f(\boldsymbol{c}_1)}{\partial t}(1 + \log f(\boldsymbol{c}_1)). \tag{2.14}$$

Assuming the absence of external forces ($g_\alpha = 0$), and substituting the Boltzmann equation in the above equation yields

$$\frac{\partial \mathcal{H}}{\partial t} = -\frac{\partial J^H_\alpha}{\partial x_\alpha} + \Gamma^{(B)}, \tag{2.15}$$

where the entropy flux $J^H_\alpha \left\langle f \log f, c_\alpha \right\rangle$ and the entropy production is

$$\Gamma^{(B)} = \int d\boldsymbol{c}_1 \int d\boldsymbol{c}_2 \int d\boldsymbol{k}\, k_1 \left[f(\boldsymbol{c}_1)f(\boldsymbol{c}_2) - f(\boldsymbol{c})f(\boldsymbol{c}')\right](1 + \log f(\boldsymbol{c}_1)). \tag{2.16}$$

The entropy flux does not contribute to the total entropy production of the system with appropriate boundary conditions (say, a specular wall or periodic boundaries). In the entropy production term, we interchange the coordinates of $\boldsymbol{c}_1$ and $\boldsymbol{c}_2$ to obtain

$$\Gamma^{(B)} = \int d\boldsymbol{c}_1 \int d\boldsymbol{c}_2 \int d\boldsymbol{k}\, k_1 \left[f(\boldsymbol{c}_1)f(\boldsymbol{c}_2) - f(\boldsymbol{c})f(\boldsymbol{c}')\right]\left(1 + \log f(\boldsymbol{c}_2)\right), \tag{2.17}$$

Adding the Eqns. (2.16) and (2.17), and dividing by 2 one obtains

$$\Gamma^{(B)} = \frac{1}{2}\int d\boldsymbol{c}_1 \int d\boldsymbol{c}_2 \int d\boldsymbol{k}\, k_1 \left[f(\boldsymbol{c}_1)f(\boldsymbol{c}_2) - f(\boldsymbol{c})f(\boldsymbol{c}')\right]\left(2 + \log f(\boldsymbol{c}_1) + \log f(\boldsymbol{c}_2)\right). \tag{2.18}$$

Similarly, we interchange the dummy variables $\boldsymbol{c}_1 \leftrightarrow \boldsymbol{c}$ and $\boldsymbol{c}_2 \leftrightarrow \boldsymbol{c}'$, add the resulting entropy production to the above equation and divide by 2 to obtain final form of entropy production as

$$\Gamma^{(B)} = \frac{1}{4}\int d\boldsymbol{c}_1 \int d\boldsymbol{c}_2 \int d\boldsymbol{k}\, k_1 \left[f(\boldsymbol{c}_1)f(\boldsymbol{c}_2) - f(\boldsymbol{c})f(\boldsymbol{c}')\right] \log \frac{f(\boldsymbol{c})f(\boldsymbol{c}')}{f(\boldsymbol{c}_1)f(\boldsymbol{c}_2)}. \tag{2.19}$$

It is seen that the production of entropy is always negative, because the logarithm is positive or negative depending on whether $f(\boldsymbol{c})f(\boldsymbol{c}')$ is larger or smaller than $f(\boldsymbol{c}_1)f(\boldsymbol{c}_2)$, and is always opposite in sign to the term in square brackets. Hence, the entropy is a non-increasing quantity in time (Chapman & Cowling, 1970; Reichl, 1999). Therefore, the $\mathcal{H}$ function keeps decreasing until the Maxwell-Boltzmann distribution is achieved at which point it attains a minima. The $\mathcal{H}$ theorem states that for any solution of the Boltzmann equation, $\mathcal{H}$ function is a non-increasing function of time, i.e., $\Gamma^{(B)} \leq 0$. The equality holds when the distribution attains the Maxwell-Boltzmann form, where $\Gamma^{(B)} = 0$ due to Eq.(2.12).

5. **Entropy at equilibrium:** The thermodynamic entropy is well defined for both equilibrium and non-equilibrium states (Cercignani, 1997)

$$S_B = -k_B \mathcal{H}[f]. \tag{2.20}$$

which is proportional to negative of the $\mathcal{H}$ at equilibrium. Therefore, Boltzmann regarded the $\mathcal{H}$ theorem as a non-equilibrium generalization of the second law of thermodynamics (which states that the thermodynamic entropy is a non-decreasing function of time). The entropy of a monoatomic ideal gas at equilibrium can be obtained by substituting $f = f^{\mathrm{MB}}$ in the above relation and evaluating the integral $\int d\boldsymbol{c} f^{\mathrm{MB}} \log f^{\mathrm{MB}}$ as

$$S_B^{\mathrm{eq}} = \rho k_B \left[\log \frac{1}{\rho}\left(\frac{4\pi\mathcal{E}}{3\rho}\right)^{3/2} + \frac{3}{2}\right]. \tag{2.21}$$

However, the second law is a property of an N-particle density function for any possible dynamics, whereas, the H theorem is derived as a Lyapunov functional of the kinetic equation. In classical thermodynamics, the temperature T is defined as

$$\frac{1}{T} = \frac{\partial S_B^{\mathrm{eq}}}{\partial \mathcal{E}}, \tag{2.22}$$

provided the number of particles and the volume is constant. Similarly, it can be seen that the scaled temperature θ follows

$$\frac{1}{\theta} = -\frac{\partial \mathcal{H}[f^{\mathrm{MB}}]}{\partial \mathcal{E}}. \tag{2.23}$$

It will be shown in Chapter 3 that the thermodynamically consistent discrete velocity models satisfy this relation between the internal energy, entropy, and temperature.

2.3 The Maxwell-Boltzmann distribution

In the previous section, it was highlighted that the Maxwell-Boltzmann distribution is the zero point of the collision where the condition of detailed balance is achieved, and that at this state the entropy production term vanishes. In this section, we will follow Maxwell's and Boltzmann's derivation of this distribution and will list some of its important properties.

2.3.1 Maxwell's derivation

Maxwell's derivation of the equilibrium distribution was based only on the principles of isotropy and independence of orthogonal directions. He considered a system of N identical hard-sphere particles left for a long enough period of time so as to attain equilibrium, and sought to find the average number of particles with velocity in a given interval (Maxwell, 1860).

In a co-moving reference frame, let the number of particles with peculiar velocity in the interval $(\xi_\alpha, \xi_\alpha + d\xi_\alpha)$ be $N\bar{f}(\xi_\alpha)$, where $\bar{f}(\xi_\alpha)$ is a function yet to be determined. Maxwell assumed that the velocity ξ_x in x-direction of a particle will not affect its ξ_y, ξ_z, the velocities in y, z-directions, and vice versa, as they are independent to each other. Then, the number of particles with velocity in the interval (ξ_x, ξ_y, ξ_z) to $(\xi_x + d\xi_x, \xi_y + d\xi_y, \xi_z + d\xi_z)$ is

$$N\bar{f}(\xi_x)\bar{f}(\xi_y)\bar{f}(\xi_z) d\xi_x\, d\xi_y\, d\xi_z, \tag{2.24}$$

i.e., the number of particles in an element of volume $d\xi_x d\xi_y d\xi_z$, therefore the number of particles in unit volume is

$$N\bar{f}(\xi_x)\bar{f}(\xi_y)\bar{f}(\xi_z). \tag{2.25}$$

Since the system is independent from preference to a direction,

$$\bar{f}(\xi_x)\bar{f}(\xi_y)\bar{f}(\xi_z) = \phi(\xi_x^2)\,\phi(\xi_y^2)\,\phi(\xi_z^2). \tag{2.26}$$

Further, realizing that the choice of the coordinate is perfectly arbitrary, Maxwell postulated that the number of particles should be a function of the magnitude of the vector only, i.e.,

$$\bar{f}(\xi_x)\bar{f}(\xi_y)\bar{f}(\xi_z) = \phi\left(\xi_x^2 + \xi_y^2 + \xi_z^2\right). \tag{2.27}$$

Solving the above equation, one finds

$$\bar{f}(\xi_\alpha) = C\exp(A\xi_\alpha^2). \tag{2.28}$$

If $A > 0$, the number of particles becomes a diverging quantity and hence become infinite, therefore $A < 0$ which implies $A = -1/a^2$, where a is some constant, thereby making the number of particles with velocity in $(\xi_\alpha, \xi_\alpha + d\xi_\alpha)$

$$NC\exp\left(-\frac{1}{a^2}\xi_\alpha^2\right)d\xi_\alpha. \tag{2.29}$$

Integrating the above expression from $\xi_\alpha = -\infty$ to $\xi_\alpha = \infty$ and equating it to the total number of particles, we find that $C = 1/(a\sqrt{\pi})$. Therefore,

$$\bar{f}(\xi_\alpha) = \frac{1}{a\sqrt{\pi}}\exp\left(-\frac{\xi_\alpha^2}{a^2}\right). \tag{2.30}$$

From the above expression, the following properties of $\tilde{f}$ are deduced:

1. The number of particles with velocities in the interval (ξ_x, ξ_y, ξ_z) to $(\xi_x + d\xi_x, \xi_y + d\xi_y, \xi_z + d\xi_z)$ is

$$\frac{N}{(a\sqrt{\pi})^3}\exp\left(-\frac{\boldsymbol{\xi}^2}{a^2}\right)d\boldsymbol{\xi}. \tag{2.31}$$

2. The number of particles with speed in $(\xi, \xi + d\xi)$ is

$$\frac{4N}{a^3\sqrt{\pi}}\xi^2\exp\left(-\frac{\xi^2}{a^2}\right)d\xi. \tag{2.32}$$

   This is depicted in Figure 2.1 for $N = 1000$, from where it is seen that for a system with the same number of particles at equilibrium, as a increases the distribution becomes broader.

3. The average value of peculiar speed of all the particles in the system is $2a/\sqrt{\pi}$.

4. The average value of $\xi^2/2$ is $3a^2/4$. Since we know that the average of $\xi^2/2$ is $3\theta/2$ we obtain $a = \sqrt{2\theta}$, substituting which we obtain the familiar form of the Maxwell-Boltzmann distribution (Eq.(2.10)).

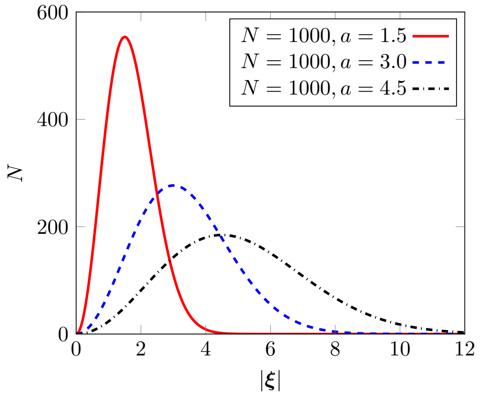

Figure 2.1: The distribution of molecular speed as predicted by Maxwell for various parameters.

2.3.2 Boltzmann's route

Boltzmann defined the local $\mathcal{H}$ function as

$$\mathcal{H}[f] = \int f(\boldsymbol{x}, \boldsymbol{c}, t) \log f(\boldsymbol{x}, \boldsymbol{c}, t) d\boldsymbol{c}. \tag{2.33}$$

The equilibrium distribution is the minimizer of the $\mathcal{H}$ function under the constraints of mass, momentum, and energy conservation,i.e.,

$$\int d\boldsymbol{c}\, f^{\mathrm{MB}} = \rho, \int d\boldsymbol{c}\, c_\kappa f^{\mathrm{MB}} = \rho u_\kappa, \int d\boldsymbol{c}\, c^2 f^{\mathrm{MB}} = 3\rho\theta + \rho u^2. \tag{2.34}$$

The constrained minimization is performed by getting the absolute minimum of the function

$$\Xi = \int d\boldsymbol{c} \left(f \log f + \mu f + \zeta_\kappa \xi_\kappa f + \gamma \xi^2 f \right), \tag{2.35}$$

where $\mu, \zeta_\kappa, \gamma$ are the Lagrange multipliers associated with the mass, momentum, and energy conservation respectively. Evaluating $d\Xi/df$ and equating it to zero, one obtains the equilibrium distribution

$$f^{\mathrm{MB}} = \exp\left(-\mu - \zeta_\kappa c_\kappa - \gamma c^2\right) = \mathcal{K} \exp\left[-\gamma \left(c_\kappa + \frac{\zeta_\kappa}{2\gamma} \right)^2 \right], \tag{2.36}$$

where $\mathcal{K} = \exp[-\mu + \zeta_\kappa^2/(4\gamma)]$. Imposing the mass, momentum and energy conservation on the above expression, one obtains

$$\zeta_\kappa = -2\gamma u_\kappa, \quad \mathcal{K} = \frac{\rho}{(\pi/\gamma)^{3/2}}, \quad \gamma = \frac{1}{2\theta}, \tag{2.37}$$

substituting which we obtain the familiar form of the Maxwell-Boltzmann distribution

$$f^{\mathrm{MB}} = \rho \left(\frac{m}{2\pi k_B T} \right)^{3/2} \exp\left[-\frac{m(c_\kappa - u_\kappa)^2}{2k_B T} \right]. \tag{2.38}$$

The procedure to evaluate discrete equilibrium for DVMs is similar, where the discrete $\mathcal{H}$ function is minimized under the constraints of mass, momentum, and energy conservation.

2.3.3 Properties of the Maxwell-Boltzmann distribution

For subsequent uses, following properties of the Maxwell Boltzmann distribution f^{MB} are listed here:

1. It is the minimizer of the local $\mathcal{H}$ function under the constraints of mass, momentum, and energy conservation.

2. The first few moments of the f^{MB} are the collisional invariants, i.e.,

$$\int d\boldsymbol{c}\, f^{\mathrm{MB}} = \rho, \qquad \int d\boldsymbol{c}\, c_\alpha f^{\mathrm{MB}} = \rho u_\alpha, \qquad \int d\boldsymbol{c}\, c^2 f^{\mathrm{MB}} = 3\rho\theta + \rho u^2, \tag{2.39}$$

   and the higher moments are

$$\sigma^{\mathrm{MB}}_{\alpha\beta} = 0, \quad q^{\mathrm{MB}}_{\alpha} = 0, \quad Q^{\mathrm{MB}}_{\alpha\beta\gamma} = 0, \quad \overline{R^{\mathrm{MB}}_{\alpha\beta}} = 0, \quad R^{\mathrm{MB}} = 15\rho\,\theta^2. \tag{2.40}$$

3. $\log f^{\mathrm{MB}}$ is a collisional invariant since

$$\log f^{\mathrm{MB}} = -\mu - \zeta_\kappa c_\kappa - \gamma c^2, \tag{2.41}$$

   is a linear combination of the conserved moments.

4. f^{MB}, a zero of the collision kernel $\mathcal{J}$, satisfies the condition of detailed balance, i.e.,

$$f(\boldsymbol{c}_1) f(\boldsymbol{c}_2) = f(\boldsymbol{c}) f(\boldsymbol{c}'). \tag{2.42}$$

5. The entropy production vanishes when $f = f^{\mathrm{MB}}$.

6. f^{MB} is symmetric about $c_\alpha = u_\alpha$, which implies

$$f^{\mathrm{MB}}(\boldsymbol{c}, \boldsymbol{u}) = f^{\mathrm{MB}}(-\boldsymbol{c}, -\boldsymbol{u}). \tag{2.43}$$

7. f^{MB} is always positive.

These properties of the Maxwell-Boltzmann distribution need to be respected while simplifying the collision kernel or while constructing DVMs in order to have a faithful representation of the kinetic theory.

2.4 Collision Models

In the hydrodynamic limit, the continuum Navier-Stokes-Fourier (NSF) description emerges not only from the detailed kinetic description, but also from its simplified models. These simplified models make the numerical simulations of hydrodynamics efficient by discarding irrelevant information of the collisions. Here, we list some of the widely used collision models.

2.4.1 Bhatnagar-Gross-Krook model

A collision model used widely due to its simplicity is the Bhatnagar-Gross-Krook (BGK) model (Bhatnagar *et al.*, 1954). This model exploits the fact that the role of collisions is to relax the distribution function to its equilibrium f^{MB}. This model assumes that all moments relax at the same rate τ which physically corresponds to the mean free time. The collision term for this model reads

$$\mathcal{J}_{\mathrm{BGK}} = \frac{1}{\tau} \left(f^{\mathrm{MB}}(\rho, \mathbf{u}, \theta) - f \right), \tag{2.44}$$

where the time parameter τ is the relaxation time over which the distribution functions relax to the equilibrium state. This model provides a qualitatively correct dynamics of the Boltzmann equation. It has the same collisional invariants, conservation laws, and the zero point of the collision as the Boltzmann kernel.

The $\mathcal{H}$ theorem: This model satisfies the $\mathcal{H}$ theorem, with the entropy production as

$$\begin{aligned}\Gamma^{(\mathrm{BGK})} &= \langle \mathcal{J}_{\mathrm{BGK}}, \log f\rangle = \frac{1}{\tau}\int d\boldsymbol{c}\,\left(f^{\mathrm{MB}}(\rho,\mathbf{u},\theta) - f\right)\log f \\ &= \frac{1}{\tau}\int d\boldsymbol{c}\left(f^{\mathrm{MB}}(\rho,\mathbf{u},\theta) - f\right)\log\frac{f}{f^{\mathrm{MB}}} + \frac{1}{\tau}\int d\boldsymbol{c}\left(f^{\mathrm{MB}}(\rho,\mathbf{u},\theta) - f\right)\log f^{\mathrm{MB}},\end{aligned} \tag{2.45}$$

where the second term is zero because of conservation of collisional invariants, hence

$$\Gamma^{(\mathrm{BGK})} = \frac{1}{\tau}\int d\boldsymbol{c}\left(f^{\mathrm{MB}}(\rho,\mathbf{u},\theta) - f\right)\log\frac{f}{f^{\mathrm{MB}}} \leq 0, \tag{2.46}$$

where, we have used the inequality

$$(X - Y)\log\frac{Y}{X} \leq 0. \tag{2.47}$$

However, because of presence of only one time scale τ, the thermal diffusivity ($\alpha_T = \tau\theta$) and the momentum diffusivity ($\nu = \tau\theta$) cannot be fixed independently. Therefore, an important limitation of the model is the constraint on Prandtl number, which is restricted to unity. Many modifications of BGK model, with the aim to model non-unitary Prandtl numbers are available in the literature. The quasi-equilibrium models (Gorban & Karlin, 1994; Levermore, 1996), the ellipsoidal BGK model, which satisfy the $\mathcal{H}$ theorem (Holway Jr, 1966; Andries *et al.*, 2000), and the Shakhov model (Shakhov, 1968) are three such examples.

2.4.2 Quasi-equilibrium model

The Prandtl number predicted by the BGK model is unity as opposed to 2/3, the value predicted by the Boltzmann equation. This limitation emerges due to the fact that unlike Boltzmann dynamics, BGK dynamics assumes that all higher order moments relax with the same rate. This can be fixed if different moments are made to relax at different rates via a time-scale hierarchy (Gorban & Karlin, 1994). The main idea is to divide the set of independent moments of the distribution function f into three parts

$$\mathcal{M}(f) = \{\mathcal{M}^{\mathrm{Slow}}(f), \mathcal{M}^{\mathrm{Quasi-slow}}(f), \mathcal{M}^{\mathrm{Fast}}(f)\}, \tag{2.48}$$

where $\mathcal{M}^{\mathrm{Slow}}(f)$ are the set of conserved moments. The higher order moments $\mathcal{M}^{\mathrm{Quasi-slow}}(f)$ and $\mathcal{M}^{\mathrm{Fast}}(f)$ are not conserved. In order to introduce the time-scale hierarchy in a thermodynamically consistent manner, the quasi-equilibrium distribution f^* is defined as the minimizer of the H function under the constraint of $\mathcal{M}^{\mathrm{Slow}}(f)$ and $\mathcal{M}^{\mathrm{Quasi-slow}}(f)$ being conserved, therefore,

$$\mathcal{M}^{\mathrm{Slow}}(f) = \mathcal{M}^{\mathrm{Slow}}(f^*), \qquad \mathcal{M}^{\mathrm{Quasi-slow}}(f) = \mathcal{M}^{\mathrm{Quasi-slow}}(f^*). \tag{2.49}$$

The precise choice of the quasi-slow moment depends on the physical context (Ansumali *et al.*, 2007*a*). The collision term is modeled by two-step relaxation as:

$$\mathcal{J}_{\mathrm{QE}} = \frac{1}{\tau}\left[f^*\left(\mathcal{M}^{\mathrm{Slow}}, \mathcal{M}^{\mathrm{Quasi-slow}}\right) - f\right] + \frac{1}{\tau_1}\left[f^{\mathrm{MB}}(\rho,\mathbf{u},\theta) - f^*\left(\mathcal{M}^{\mathrm{Slow}}, \mathcal{M}^{\mathrm{Quasi-slow}}\right)\right], \tag{2.50}$$

where τ and τ_1 are the two relaxation times. Thus, in the quasi-equilibrium model the relaxation to equilibrium is split in two steps: in the first step the distribution function relaxes to

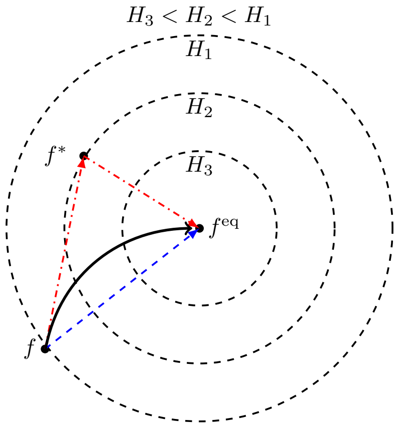

Figure 2.2: The trajectory for relaxation to equilibrium as per various collision models: the solid black curve represents the Boltzmann's collision kernel, the dashed blue line represents the BGK collision while the dash-dotted red lines represent the quasi-equilibrium model. Here, f is the pre-collisional state, f^* is the quasi-equilibrium and f^{eq} is the equilibirum state, whereas H_i are the isoentropy levels.

the quasi-equilibrium state with a faster relaxation time τ, and in the second step the quasi-equilibrium relaxes to the equilibrium state with slower relaxation time τ_1. In case $\tau = \tau_1$, the quasi-equilibrium model reduces to the BGK model. It has the same collisional invariants and conservation laws as the Boltzmann kernel. The availability of two relaxation time scales allows fixing the thermal diffusivity independent of the kinematic viscosity (Ansumali *et al.*, 2007*a*).

The $\mathcal{H}$ theorem: This model also satisfies the $\mathcal{H}$ theorem, with the entropy production as

$$\begin{aligned}\Gamma^{(\mathrm{QE})} = \langle \mathcal{J}_{\mathrm{QE}}, \log f\rangle &= \int d\boldsymbol{c} \left[\frac{1}{\tau}\left(f^* - f\right) + \frac{1}{\tau_1}\left(f^{\mathrm{MB}}\left(\rho, \mathbf{u}, \theta\right) - f^*\right)\right] \log f \\ &= \frac{\tau_1 - \tau}{\tau_1 \tau} \int d\boldsymbol{c}\left(f^* - f\right) \log f + \frac{1}{\tau} \int d\boldsymbol{c}\left(f^{\mathrm{MB}}\left(\rho, \mathbf{u}, \theta\right) - f^*\right) \log f \\ &= \frac{\tau_1 - \tau}{\tau_1 \tau} \int d\boldsymbol{c}\left(f^* - f\right) \log \frac{f}{f^*} + \frac{1}{\tau} \int d\boldsymbol{c}\left(f^{\mathrm{MB}}\left(\rho, \mathbf{u}, \theta\right) - f^*\right) \log \frac{f}{f^{\mathrm{MB}}} \\ &+ \frac{\tau_1 - \tau}{\tau_1 \tau} \int d\boldsymbol{c}\left(f^* - f\right) \log f^* + \frac{1}{\tau} \int d\boldsymbol{c}\left(f^{\mathrm{MB}}\left(\rho, \mathbf{u}, \theta\right) - f^*\right) \log f^{\mathrm{MB}},\end{aligned} \tag{2.51}$$

where the last two terms are zero because of the conservation of moments, hence

$$\Gamma^{(\mathrm{QE})} = \frac{\tau_1 - \tau}{\tau_1 \tau} \int d\boldsymbol{c}\left(f^* - f\right) \log \frac{f}{f^*} + \frac{1}{\tau} \int d\boldsymbol{c}\left(f^{\mathrm{MB}}\left(\rho, \mathbf{u}, \theta\right) - f^*\right) \log \frac{f}{f^{\mathrm{MB}}} \leq 0, \tag{2.52}$$

is non-positive as long as $\tau \leq \tau_1$. Here, it should be noted that in continuous velocity space, the quasi-equilibrium collision kernel is not applicable for $\mathrm{Pr} > 1$, since

$$\int d\boldsymbol{c}\, f^* = \int d\boldsymbol{c}\, \rho \exp\left[-\mu - \zeta_\kappa c_\kappa - \gamma c^2 - \lambda_\kappa c^2 c_\kappa\right], \tag{2.53}$$

is a diverging quantity. However, the discrete velocity models are free from such issues.

Figure 2.2 compares the trajectory for relaxation to equilibrium for the Boltzmann, BGK and quasi-equilibrium collision kernels.

2.4.3 Fokker-Planck model

Fokker-Planck model by Lebowitz *et al.* (1960) models the relaxation to equilibrium as diffusive dynamics in velocity space. The collision term for the Fokker-Planck model is

$$\mathcal{J}_{\mathrm{FP}} = \frac{1}{\tau_{\mathrm{FP}}} \frac{\partial}{\partial c_\alpha} \left(\xi_\alpha f + \theta \frac{\partial f}{\partial c_\alpha} \right). \tag{2.54}$$

This model is thermodynamically consistent and leads so the same set of collisional invariants, macroscopic conservation laws, and zero of the collision as the Boltzmann equation (Singh *et al.*, 2016).

The $\mathcal{H}$ theorem: The Fokker-Planck model satisfies the $\mathcal{H}$ theorem, with the entropy production as

$$\Gamma^{(\mathrm{FP})} = \langle \mathcal{J}_{\mathrm{FP}}, \log f \rangle = -\frac{1}{\tau_{\mathrm{FP}}} \int d\boldsymbol{\xi} \left(\xi_\alpha + \frac{\theta}{f} \frac{\partial f}{\partial c_\alpha} \right) \frac{\partial f}{\partial c_\alpha} = \frac{3\rho}{\tau_{\mathrm{FP}}} - \frac{\theta}{\tau_{\mathrm{FP}}} \int d\boldsymbol{\xi} \frac{1}{f} \frac{\partial f}{\partial c_\alpha} \frac{\partial f}{\partial c_\alpha} \leq 0, \tag{2.55}$$

owing to the identity

$$\begin{aligned} \int d\boldsymbol{\xi} f \left(\frac{\partial \log \frac{f}{f^{\mathrm{MB}}}}{\partial \xi_\alpha} \right)^2 &= \int d\boldsymbol{\xi} \left[\frac{1}{f} \frac{\partial f}{\partial c_\alpha} \frac{\partial f}{\partial c_\alpha} + f \frac{\partial \log f^{\mathrm{MB}}}{\partial c_\alpha} \frac{\partial \log f^{\mathrm{MB}}}{\partial c_\alpha} - 2 \frac{\partial f}{\partial c_\alpha} \frac{\partial \log f^{\mathrm{MB}}}{\partial c_\alpha} \right] \\ &= \int d\boldsymbol{\xi} \left[\frac{1}{f} \frac{\partial f}{\partial c_\alpha} \frac{\partial f}{\partial c_\alpha} + \frac{f}{\theta^2} + 2 \frac{\xi_\alpha}{\theta} \frac{\partial f}{\partial c_\alpha} \right] = -\frac{3\rho}{\theta} + \int d\boldsymbol{\xi} \frac{1}{f} \frac{\partial f}{\partial c_\alpha} \frac{\partial f}{\partial c_\alpha} \geq 0. \end{aligned} \tag{2.56}$$

A limitation of this model is that it restricts the Prandtl number to 3/2. A variation of the Fokker-Plank model for independently tuning the transport coefficients and the equation of state was proposed in Singh & Ansumali (2015). The Fokker-Planck model is useful for gaseous microflows at intermediate Knudsen numbers (Singh *et al.*, 2016)

2.5 Conclusion

In this chapter, we have reviewed the basics of the kinetic theory of gases. We have discussed the basic properties of the Maxwell-Boltzmann distribution that will play a central role while constructing the discrete equilibrium for discrete in velocity space kinetic theory. We have discussed a few collision models along with their $\mathcal{H}$ theorems. In the next chapter, we will discuss the Boltzmann BGK model in more detail and derive its macroscopic limit.

Chapter 3

Discrete kinetic modeling of thermohydrodynamics

The molecular velocity $\boldsymbol{c}$ is continuous in the kinetic theory of gases, whereas in the discrete velocity models (DVM) it is restricted to a set $\boldsymbol{c} = \{\boldsymbol{c}_1, \cdots \boldsymbol{c}_{N_d}\}$ consisting of N_{d} vectors (Broadwell, 1964; Monaco & Preziosi, 1991). Once the discrete velocity set is defined, one can create a discrete analogue of the collision term. In order to study the binary collision dynamics, Broadwell (1964) chose the discrete form of Boltzmann type binary collision term. In LBM, one typically chooses BGK type relaxation dynamics. For any DVM, there are two questions that need to be addressed: What is the equilibrium distribution for the DVM, and, how to ensure recovery of the hydrodynamic moments for small N_d?

The Maxwell-Boltzmann distribution f^{MB} has a great significance in the continuous kinetic theory (Chapman & Cowling, 1970; Liboff, 2003). In the previous chapter, we derived the Maxwell-Boltzmann distribution as the minimizer of the Boltzmann's $\mathcal{H}$ functional under the constraint of collisional invariants being conserved. However, if one aims to construct a discrete velocity model (DVM) of the kinetic theory that retains the most important properties of continuous kinetic theory, the discrete equilibrium distribution f_i^{eq} is necessarily different from f_i^{MB} (the Maxwell-Boltzmann distribution evaluated at discrete points). This is because the moments of f^{MB} show departure from the moments of f_i^{MB} (Shan & He, 1998*a*; Ansumali *et al.*, 2003), i.e.,

$$\int d\boldsymbol{c}\, f^{\text{MB}} \neq \sum_{i=1}^{N_d} f_i^{\text{MB}}, \quad \int d\boldsymbol{c}\, c_\alpha f^{\text{MB}} \neq \sum_{i=1}^{N_d} f_i^{\text{MB}} c_{i\alpha}. \tag{3.1}$$

The error in evaluating the moments are introduced because one is approximating an integral (see Figure 3.1) and a pointwise approximation is not expected to preserve the integral quantities. Of course, the errors can be minimized by keeping the number of discrete velocities very large. However, for computational efficiency and tractability one would like to recover the properties of the continuous kinetic theory with as few discrete velocities as possible. In LBM, one looks at discrete velocity models such that

$$\int d\boldsymbol{c}\, \psi(\boldsymbol{c}) f = \sum_{i=1}^{N_d} \psi_i f_i, \tag{3.2}$$

at least for lower order polynomials $\psi(\boldsymbol{c})$. The above equation can be understood as calculating the moments via generalized Gaussian quadrature. It was demonstrated by Boghosian & Coveney (1998) that by demanding the first three moments and the trace of the fourth moment of the discrete equilibrium distribution match the corresponding moments of the Maxwell-Boltzmann distribution, the macroscopic equations thermohydrodynamics could be recovered.

The discrete equilibrium distribution is constructed as the minimizer of the discrete $\mathcal{H}$ functional under the constraint of collisional invariants being conserved (Ansumali *et al.*, 2003). The aim of this chapter is to emphasize the conditions on f_i^{eq} that are necessary to obtain the Navier-Stokes-Fourier (NSF) equations as the hydrodynamic limit of the discrete kinetic equation. These conditions manifest in the form of restrictions on the moments of f_i^{eq}. This restriction on the moments further dictates whether the choice of the discrete velocity set is acceptable. In this chapter, we first demonstrate that the moments of f_i^{eq} should be the same as

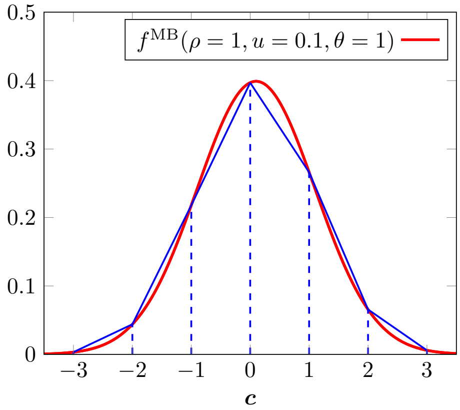

Figure 3.1: Finding the discrete equilibrium by evaluating the Maxwell-Boltzmann distribution at discrete points does not conserve the moments. In the figure, the area beneath the curve represents the density, which is different for the Maxwell-Boltzmann distribution and discrete equilibrium as Maxwell-Boltzmann distribution at discrete points.

the moments of f_i^{MB} in order to have correct thermohydrodynamic limit of the discrete kinetic equation. We then derive the conditions on the discrete velocity set that lead to the correct form of the moments of f_i^{eq}.

This chapter is organized as follows: In Section 3.1, we discuss the restrictions on the discrete velocity set due to the arguments of isotropy and independence from preference to any direction. In Section 3.2, we derive the moment chain associated with the discrete kinetic equation, i.e., the Boltzmann BGK equation, and, in Section 3.3 we derive the conditions on the equilibrium moments that are required in order to obtain the NSF equations as the hydrodynamic limit of the Boltzmann BGK equation. In Section 3.4, we derive the series expansion of energy conserving discrete equilibrium distribution and obtain the restrictions on the discrete velocity set. Finally, in Section 3.5, we derive the discrete equilibrium by minimizing the discrete $\mathcal{H}$ functional.

3.1 Discrete velocity models

In any DVM, one restricts the molecular velocity to a few chosen directions that constitute a discrete velocity set $\boldsymbol{c} = \{\boldsymbol{c}_1, \cdots \boldsymbol{c}_{N_d}\}$. The central quantity in any DVM is the discrete population set $f = \{f_1(\boldsymbol{x}, t), \cdots f_{N_d}(\boldsymbol{x}, t)\}$, understood here as a vector in the N_d dimensional vector space. We define the bilinear action between two vectors $\phi(\boldsymbol{c}_i)$ and $\psi(\boldsymbol{c}_j)$ as

$$\langle \phi, \psi \rangle = \sum_{i=1}^{N_{\mathrm{d}}} \phi_i \, \psi_i. \tag{3.3}$$

To avoid preference to any specific direction, one imposes a few restrictions on the discrete velocity set $\boldsymbol{c}$ (Yudistiawan *et al.*, 2010; Shet *et al.*, 2013):

1. The discrete velocity set is chosen such that for each vector $\boldsymbol{c}_i \in \boldsymbol{c}$, the vector $-\boldsymbol{c}_i$ is also present in the set.

2. For each vector with components (c_{i1}, c_{i2}, c_{i3}), all the permutations

$$\{(c_{i2}, c_{i1}, c_{i3}), (c_{i1}, c_{i3}, c_{i2}), (c_{i3}, c_{i1}, c_{i2}), (c_{i2}, c_{i3}, c_{i1}), (c_{i3}, c_{i2}, c_{i1})\}$$

are also member of the velocity set. This also allows us to assort the discrete velocity energy shells, each shell containing the velocities with equal magnitude (Karlin *et al.*, 1999).

Here, it is interesting to note that Maxwell's original derivation of f^{MB} was based on the arguments of spatial isotropy and independence of the equilibrium distribution from preference to a specific direction (Maxwell, 1860). The above two conditions imply that for any velocity vector with components $(c_{i1}, c_{i2}, c_{i3}) \in \boldsymbol{c}$, we must have all the vectors with components $(\pm c_{i1}, \pm c_{i2}, \pm c_{i3}) \in \boldsymbol{c}$. These conditions ensure that in the discrete case with any vector $\phi(\boldsymbol{c}^2)$ we have

$$\begin{aligned}
&\left\langle \phi, c_x^{2n} \right\rangle = \left\langle \phi, c_y^{2n} \right\rangle = \left\langle \phi, c_z^{2n} \right\rangle, \\
&\left\langle \phi, c_x^{2n} c_y^{2m} \right\rangle = \left\langle \phi, c_y^{2n} c_z^{2m} \right\rangle = \left\langle \phi, c_z^{2n} c_x^{2m} \right\rangle, \\
&\left\langle \phi, c_x^{2n} c_y^{2m} c_z^{2p} \right\rangle = \left\langle \phi, c_y^{2n} c_z^{2p} c_x^{2m} \right\rangle = \left\langle \phi, c_x^{2p} c_y^{2m} c_z^{2n} \right\rangle, \\
&\left\langle \phi, c_x^{2n+1} \right\rangle = \left\langle \phi, c_y^{2n+1} \right\rangle = \left\langle \phi, c_z^{2n+1} \right\rangle = 0,
\end{aligned} \tag{3.4}$$

where n and m are the natural numbers. These conditions render the velocity set spatially isotropic and independence from preference to any particular direction. In this thesis, we only consider the discrete velocity sets which satisfy the above constraints.

3.2 The Boltzmann BGK equation

The time evolution of the distribution function in the dilute gas limit is given by the Boltzmann equation (Chapman & Cowling, 1970; Cercignani, 1988). However, a simplified model called the Boltzmann Bhatnagar-Gross-Krook (BGK) model is widely known to be sufficient to describe Navier-Stokes-Fourier dynamics (Bhatnagar *et al.*, 1954)

$$\partial_t f\left(\mathbf{x}, \mathbf{c}, t\right) + (\boldsymbol{c} \cdot \nabla) f\left(\mathbf{x}, \mathbf{c}, t\right) = -\frac{1}{\tau}\left[f\left(\mathbf{x}, \mathbf{c}, t\right) - f^{\mathrm{eq}}(\rho\left(\mathbf{x}, t\right), \boldsymbol{u}\left(\mathbf{x}, t\right), \theta\left(\mathbf{x}, t\right))\right], \tag{3.5}$$

with τ as the collisional relaxation time and the equilibrium distribution f^{eq}. In the continuous case f^{eq} is taken as f^{MB}, however, in the discrete case f^{eq} should be the minimizer of the discrete H function. In this section, we distinguish between f^{eq} and f^{MB} to highlight properties of f^{eq} of any discrete velocity model which are needed to derive Navier-Stokes-Fourier equations. The conservation laws obtained upon integrating the Boltzmann BGK equation are

$$\begin{aligned}
\partial_t \rho + \partial_\alpha(\rho u_\alpha) &= 0, \\
\partial_t(\rho u_\alpha) + \partial_\beta\left(\rho u_\alpha u_\beta + p\delta_{\alpha\beta} + \sigma_{\alpha\beta}\right) &= 0, \\
\partial_t e + \partial_\beta\left(\left(e + p\right) u_\beta + \sigma_{\beta\gamma} u_\gamma + q_\beta\right) &= 0.
\end{aligned} \tag{3.6}$$

These equations contain higher order moment such as the stress tensor and the heat flux. The evolution of the stress tensor obtained by taking the second moment of the kinetic equation (Eq.(3.5)) is (see Appendix A for detailed derivation)

$$\partial_t \sigma_{\alpha\beta} + u_\gamma \partial_\gamma \sigma_{\alpha\beta} + \partial_\gamma \overline{Q_{\alpha\beta\gamma}} + \sigma_{\alpha\beta}\partial_\gamma u_\gamma + 2\overline{\sigma_{\gamma\beta}\partial_\gamma u_\alpha} + 2p\overline{\partial_\beta u_\alpha} + \frac{4}{5}\overline{\partial_\beta q_\alpha} = \frac{1}{\tau}\left(\sigma^{\mathrm{eq}}_{\alpha\beta} - \sigma_{\alpha\beta}\right). \tag{3.7}$$

Similarly, the evolution of heat flux obtained by taking the third moment of the kinetic equation [Eq.(3.5)] is (see Appendix A for detailed derivation)

$$\begin{split}\partial_t q_\alpha + \frac{1}{2}\partial_\beta\left(\overline{R_{\alpha\beta}} + \frac{1}{3}R\,\delta_{\alpha\beta}\right) + \overline{Q_{\alpha\beta\gamma}}\partial_\gamma u_\beta + \partial_\beta\left(q_\alpha u_\beta\right) + \frac{7}{5}q_\beta\partial_\beta u_\alpha + \frac{2}{5}q_\alpha\partial_\beta u_\beta + \frac{2}{5}q_\beta\partial_\alpha u_\beta \\ -\frac{5}{2}\frac{p}{\rho}\partial_\alpha p - \frac{\sigma_{\alpha\beta}}{\rho}\partial_\beta p - \frac{5}{2}\frac{p}{\rho}\partial_\theta\sigma_{\alpha\theta} - \frac{\sigma_{\alpha\beta}}{\rho}\partial_\theta\sigma_{\beta\theta} = \frac{1}{\tau}\left(q_\alpha^{\rm eq} - q_\alpha\right).\end{split} \tag{3.8}$$

These evolution equations form the moment chain and can be seen to contain one higher moment than the moment whose evolution they represent, i.e., the evolution of density contains momentum, the evolution of momentum contains the viscous stress, and so on. In the continuous case this chain goes on to infinity, while in the discrete case the moment chain closes at a finite level and forms a set of N_d coupled partial differential equations (Cercignani, 1988; Ansumali *et al.*, 2007*b*; Broadwell, 1964).

3.3 Hydrodynamic limit of the Boltzmann BGK equation

In this section, we derive the hydrodynamic limit associated with the Boltzmann BGK equation. The description is kept generic so that it is valid for the continuous (in velocity) Boltzmann BGK equation as well as its discrete velocity analogues. As the aim of the section is to construct an energy conserving discrete velocity model, we intend to highlight the conditions on the discrete equilibrium distribution required to recover the Navier-Stokes-Fourier equations as the hydrodynamic limit of the kinetic equation. In order to obtain the hydrodynamic limit from the equations in the moment chain, following the Chapman-Enskog procedure, we expand the distribution function and the time derivative as

$$f = f^{(0)} + \tau f^{(1)} + \mathcal{O}(\tau^2), \tag{3.9}$$

$$\partial_t = \partial_t^{(0)} + \tau\partial_t^{(1)} + \mathcal{O}(\tau^2). \tag{3.10}$$

The non-conserved moments $M^{\rm fast}$ are also expanded about their respective equilibriums in order of τ as

$$M^{\rm fast} = M^{\rm eq}(\rho, \boldsymbol{u}, \theta) + \tau M^{(1)} + \mathcal{O}(\tau^2), \tag{3.11}$$

where $M^{\rm fast} = \left\{\sigma_{\alpha\beta}, q_\alpha, Q_{\alpha\beta\gamma}, \overline{R_{\alpha\beta}}, R\right\}$. Keeping in mind the objective of obtaining the Navier-Stokes-Fourier equations at the zeroth and first order of τ, a number of comments can be made:

- The velocity evolution obtained upon performing algebraic manipulations on the Eqns.(3.6) is

  $$\partial_t u_\alpha + u_\beta\partial_\beta u_\alpha + \frac{1}{\rho}\partial_\alpha p + \frac{1}{\rho}\partial_\gamma\sigma_{\alpha\gamma} = 0, \tag{3.12}$$

  in which at $\mathcal{O}(1)$ we obtain

  $$\partial_t^{(0)} u_\alpha + u_\beta\partial_\beta u_\alpha + \frac{1}{\rho}\partial_\alpha p + \frac{1}{\rho}\partial_\beta\left(\sigma_{\alpha\beta}^{\rm eq} - \sigma_{\alpha\beta}^{\rm MB}\right) = 0, \tag{3.13}$$

  from where we see that Euler dynamics upto $\mathcal{O}(u^{n-1})$ is obtained provided $\sigma_{\alpha\beta}^{\rm eq} - \sigma_{\alpha\beta}^{\rm MB} = \mathcal{O}(u^n)$. It is typical to demand that $\sigma_{\alpha\beta}^{\rm eq} - \sigma_{\alpha\beta}^{\rm MB} = \mathcal{O}(u^4)$.

- The temperature evolution can also be obtained upon performing algebraic manipulations on the Eqns.(3.6)

$$\partial_t \theta + u_\alpha \partial_\alpha \theta + \frac{2}{3}\theta \partial_\beta u_\beta + \frac{2}{3\rho}\sigma_{\alpha\beta}\partial_\alpha u_\beta + \frac{2}{3\rho}\partial_\alpha q_\alpha = 0, \tag{3.14}$$

in which at $\mathcal{O}(1)$ we obtain

$$\partial_t^{(0)}\theta + u_\alpha \partial_\alpha \theta + \frac{2}{3}\theta \partial_\beta u_\beta + \frac{2}{3\rho}\left(\sigma_{\alpha\beta}^{\rm eq} - \sigma_{\alpha\beta}^{\rm MB}\right)\partial_\alpha u_\beta + \frac{2}{3\rho}\partial_\alpha\left(q_\alpha^{\rm eq} - q_\alpha^{\rm MB}\right) = 0, \tag{3.15}$$

from where we see that the Euler dynamics upto $\mathcal{O}(u^{n-1})$ is obtained provided $\sigma_{\alpha\beta}^{\rm eq} - \sigma_{\alpha\beta}^{\rm MB} = \mathcal{O}(u^n)$ and $q_\alpha^{\rm eq} - q_\alpha^{\rm MB} = \mathcal{O}(u^n)$.

- From the evolution of stress given by Eq.(3.7), after ignoring $\sigma_{\alpha\beta}^{\rm eq} - \sigma_{\alpha\beta}^{\rm MB}$ terms, we have at $\mathcal{O}(1)$

$$\partial_\gamma\left(\overline{Q_{\alpha\beta\gamma}^{\rm eq} - Q_{\alpha\beta\gamma}^{\rm MB}}\right) + 2p\overline{\partial_\beta u_\alpha} + \frac{4}{5}\overline{\partial_\beta\left(q_\alpha^{\rm eq} - q_\alpha^{\rm MB}\right)} = -\sigma_{\alpha\beta}^{(1)}, \tag{3.16}$$

from where it can be seen that the accurate form of the viscous stress is recovered upto $\mathcal{O}(u^{n-1})$ if $q_\alpha^{\rm eq} - q_\alpha^{\rm MB} = \mathcal{O}(u^n)$ and $Q_{\alpha\beta\gamma}^{\rm eq} - Q_{\alpha\beta\gamma}^{\rm MB} = \mathcal{O}(u^n)$.

- Similarly, after substituting $R^{\rm MB} = 15\rho\,\theta^2$ in the evolution of heat flux given by Eq. (3.8), we have at $\mathcal{O}(1)$

$$\begin{aligned}\partial_t^{(0)}\left(q_\alpha^{\rm eq} - q_\alpha^{\rm MB}\right) + \frac{1}{2}\partial_\beta\left(\overline{R_{\alpha\beta}^{\rm eq} - R_{\alpha\beta}^{\rm MB}}\right) + \frac{1}{6}\partial_\alpha\left(R^{\rm eq} - R^{\rm MB}\right) + \left(\overline{Q_{\alpha\beta\gamma}^{\rm eq} - Q_{\alpha\beta\gamma}^{\rm MB}}\right)\partial_\gamma u_\beta \\ +\partial_\beta\left[\left(q_\alpha^{\rm eq} - q_\alpha^{\rm MB}\right)u_\beta\right] + \frac{7}{5}\left(q_\beta^{\rm eq} - q_\beta^{\rm MB}\right)\partial_\beta u_\alpha + \frac{2}{5}\left(q_\alpha^{\rm eq} - q_\alpha^{\rm MB}\right)\partial_\beta u_\beta \\ +\frac{2}{5}\left(q_\beta^{\rm eq} - q_\beta^{\rm MB}\right)\partial_\alpha u_\beta + \frac{5}{2}p\,\partial_\alpha\theta = -q_\alpha^{(1)},\end{aligned} \tag{3.17}$$

from where it can be seen that the Fourier's law is recovered till $\mathcal{O}(\eta^{n-1})$ if $R^{\rm eq} - R^{\rm MB} = \mathcal{O}(\eta^n)$, $Q_{\alpha\beta\gamma}^{\rm eq} - Q_{\alpha\beta\gamma}^{\rm MB} = \mathcal{O}(\eta^n)$ and $q_\alpha^{\rm eq} - q_\alpha^{\rm MB} = \mathcal{O}(\eta^n)$ where $\eta = \theta/\theta_0 - 1$. Also, the above equation at $u_\alpha = 0$ becomes

$$\frac{1}{6}\partial_\alpha\left(R^{\rm eq} - R^{\rm MB}\right) + \frac{5}{2}p\,\partial_\alpha\theta = -q_\alpha^{(1)}, \tag{3.18}$$

from where it can be seen that the main source of error in the Fourier's law is the term $R^{\rm eq} - R^{\rm MB}$.

Therefore, in order to recover the Navier-Stokes-Fourier equations accurately we require the Knudsen number $\mathrm{Kn} = \tau \mathrm{c_s}/\mathrm{L_{ref}}$ to be small, and the equilibrium moments of any DVM to mimic as closely as possible the moments of the Maxwell-Boltzmann distribution. The $RD3Q67$ model discussed later in this thesis will have

$$\sigma_{\alpha\beta}^{\rm eq} - \sigma_{\alpha\beta}^{\rm MB} = \mathcal{O}(u_\alpha u_\beta \eta^3), \quad q_\alpha^{\rm eq} - q_\alpha^{\rm MB} = \mathcal{O}(u^3\eta^3), \quad R^{\rm eq} - R^{\rm MB} = \mathcal{O}(\eta^4). \tag{3.19}$$

3.4 Energy conserving discrete equilibrium distribution

The link between the series expression for the discrete isothermal equilibrium and the Maxwell-Boltzmann distribution is well understood (Shan & He, 1998*a*). In this section, we first derive the series expansion for the isothermal equilibrium at arbitrary velocities from the Maxwell-Boltzmann distribution. We then invert the argument and construct the series expansion for the energy conserving equilibrium at arbitrary temperatures and zero velocity from the Maxwell-Boltzmann distribution.

The discrete isothermal distribution $f^{\mathrm{eq}}(\rho, \boldsymbol{u}, \theta_0)$ from the Maxwell-Boltzmann distribution is obtained in two-steps (Shan & He, 1998*a*). First, the local Maxwell-Boltzmann distribution at $\theta = \theta_0$ is projected to a finite basis expansion around a global Maxwell-Boltzmann distribution with zero velocity and reference temperature θ_0 to obtain

$$\hat{f}^{\mathrm{eq}}\left(\rho, \boldsymbol{u}, \theta_0, \boldsymbol{c}\right) = \omega(\boldsymbol{c}) \sum_{n=0}^{N} \frac{1}{n!} a^{(n)} H^{(n)}(\boldsymbol{c}), \tag{3.20}$$

where $\omega(\boldsymbol{c}) = f^{\mathrm{MB}}\left(\rho = 1, \boldsymbol{u} = 0, \theta_0, \boldsymbol{c}\right)$, $H^{(n)}(\boldsymbol{c})$ are the orthogonal Hermite polynomials, and $a^{(n)}$ are the coefficients of expansion. Notice that even the expanded version is consistent with the requirement that conserved moments of the equilibrium distribution are preserved (Shan & He, 1998*a*). The series expansion of the isothermal ($\theta = \theta_0$) equilibrium is then obtained as

$$\hat{f}^{\mathrm{eq}}\left(\rho, \boldsymbol{u}, \theta_0, \boldsymbol{c}\right) = \rho\, \omega(\boldsymbol{c}) \left(1 + \frac{\boldsymbol{c} \cdot \boldsymbol{u}}{\theta_0} + \frac{(\boldsymbol{c} \cdot \boldsymbol{u})^2 - u^2 \theta_0}{2\theta_0^2} + \frac{(\boldsymbol{c} \cdot \boldsymbol{u})^3 - 3\theta_0 u^2 (\boldsymbol{c} \cdot \boldsymbol{u})}{6\theta_0^3}\right). \tag{3.21}$$

The above expression is the series expansion around $\boldsymbol{u} = 0$, but is still continuous in velocity space. To obtain the series expression corresponding to discrete velocities, a quadrature evaluation is performed following the Gaussian quadrature

$$\int d\boldsymbol{c}\, \phi(\boldsymbol{c}) \omega(\boldsymbol{c}) = \sum_i w_i \phi(\boldsymbol{c}_i), \tag{3.22}$$

with w_i as weights and $\boldsymbol{c}_i$ as nodes. The Hermite coefficients for the discrete velocity model then become

$$a^{(n)} = \int d\boldsymbol{c}\, \omega(\boldsymbol{c}) \frac{\hat{f}^{\mathrm{eq}}\left(\rho, \boldsymbol{u}, \theta_0, \boldsymbol{c}\right)}{\omega(\boldsymbol{c})} H^{(n)}(\boldsymbol{c}) = \sum_i w_i \frac{\hat{f}^{\mathrm{eq}}\left(\rho, \boldsymbol{u}, \theta_0, \boldsymbol{c}_i\right)}{\omega(\boldsymbol{c}_i)} H^{(n)}(\boldsymbol{c}_i). \tag{3.23}$$

For efficient computation, we define a transformation $f_i^{\mathrm{eq}}\left(\rho, \boldsymbol{u}, \theta_0\right) = w_i \hat{f}^{\mathrm{eq}}\left(\rho, \boldsymbol{u}, \theta_0, \boldsymbol{c}_i\right) / \omega(\boldsymbol{c}_i)$, and hence the discrete equilibrium is written as

$$f_i^{\mathrm{eq}}\left(\rho, \boldsymbol{u}, \theta_0\right) = \rho\, w_i \left(1 + \frac{\boldsymbol{c}_i \cdot \boldsymbol{u}}{\theta_0} + \frac{(\boldsymbol{c}_i \cdot \boldsymbol{u})^2 - u^2 \theta_0}{2\theta_0^2} + \frac{(\boldsymbol{c} \cdot \boldsymbol{u})^3 - 3\theta_0 u^2 (\boldsymbol{c} \cdot \boldsymbol{u})}{6\theta_0^3}\right). \tag{3.24}$$

The above expression for discrete isothermal equilibrium conserves the mass and momentum. Here, one needs to use the following properties of the weights:

$$\sum_i w_i = 1, \quad \sum_i w_i c_{i\alpha} c_{i\beta} = \theta_0 \delta_{\alpha\beta}, \quad \sum_i w_i c_{i\alpha} c_{i\beta} c_{i\eta} c_{i\zeta} = \theta_0 \Delta_{\alpha\beta\eta\zeta}, \tag{3.25}$$

and that the odd moments of weight are zero. Here $\Delta_{\alpha\beta\eta\zeta} = \delta_{\alpha\beta}\delta_{\eta\zeta} + \delta_{\alpha\zeta}\delta_{\beta\eta} + \delta_{\alpha\eta\zeta}\delta_{\beta\zeta}$ is the fourth-order isotropic tensor.

Following the same idea as the isothermal case, we now find $\tilde{f}_i^{\mathrm{eq}}\left(\rho, \boldsymbol{u} = 0, \theta\right)$, the discrete equilibrium distribution at zero velocity and arbitrary temperature. We first write the local Maxwell-Boltzmann distribution as a product of the global Maxwell-Boltzmann distribution $\tilde{f}^{\mathrm{eq}}\left(\rho, \boldsymbol{u} = 0, \theta, \boldsymbol{c}\right)$ and a function of molecular velocity $\boldsymbol{c}$ as

$$\tilde{f}^{\mathrm{eq}}\left(\rho, \boldsymbol{u} = 0, \theta, \boldsymbol{c}\right) = \rho \frac{\omega(\boldsymbol{c})}{(1+\eta)^{\frac{3}{2}}} \exp\left(\frac{\boldsymbol{c}^2 \eta}{2\theta_0 (1+\eta)}\right), \tag{3.26}$$

where $\eta = \theta/\theta_0 - 1$. The equilibrium at non-zero velocity can be written as an expansion around this zero velocity state. Now, performing a quadrature evaluation followed by expanding and collecting the terms with like powers of η one obtains

$$\begin{aligned} \tilde{f}_i^{\mathrm{eq}}(\rho, \boldsymbol{u}=0, \theta) = w_i \rho \Bigg[1 &+ \frac{\eta}{2\theta_0}(\boldsymbol{c}_i^2 - 3\theta_0) + \frac{\eta^2}{8\theta_0^2}\left(\boldsymbol{c}_i^4 - 10\boldsymbol{c}_i^2\theta_0 + 15\theta_0^2\right) \\ &+ \frac{\eta^3}{48\theta_0^3}\left(\boldsymbol{c}_i^6 - 21\boldsymbol{c}_i^4\theta_0 + 105\boldsymbol{c}_i^2\theta_0^2 - 105\theta_0^3\right) + \frac{\eta^4}{384\theta_0^4}\left(\boldsymbol{c}_i^8 - 36\boldsymbol{c}_i^6\theta_0 + 378\boldsymbol{c}_i^4\theta_0^2 - 1260\boldsymbol{c}_i^2\theta_0^3 + 945\theta_0^4\right) \\ &+ \mathcal{O}(\eta^5) \Bigg]. \end{aligned} \tag{3.27}$$

Notice that the momentum associated with $\tilde{f}_i^{\mathrm{eq}}$ is zero by construction as odd-order moments of any DVM are zero. The requirement that $\tilde{f}_i^{\mathrm{eq}}$ conserve mass and energy, i.e.,

$$\left\langle \tilde{f}^{\mathrm{eq}}, \{1, \boldsymbol{c}^2\} \right\rangle = \{\rho, 3\rho\theta\}, \tag{3.28}$$

is satisfied upto $\mathcal{O}(\eta^4)$ if we impose following conditions on the weights (see Appendix A.5 for derivation)

$$\left\langle w, \{1, \boldsymbol{c}^2, \boldsymbol{c}^2\boldsymbol{c}^2, \boldsymbol{c}^2\boldsymbol{c}^2\boldsymbol{c}^2, \boldsymbol{c}^2\boldsymbol{c}^2\boldsymbol{c}^2\boldsymbol{c}^2, \boldsymbol{c}^2\boldsymbol{c}^2\boldsymbol{c}^2\boldsymbol{c}^2\boldsymbol{c}^2\} \right\rangle = \left\{1, 3\theta_0, 15\theta_0^2, 105\theta_0^3, 945\theta_0^4, 10395\theta_0^5\right\}. \tag{3.29}$$

The above conditions on w_i, c_i, θ_0 constitute indispensable constraints on the parameters of any DVM in order to have energy conservation and dynamics accurate upto $\mathcal{O}(\eta^5)$.

There is, however, one issue with these series expansions. The positivity, an essential feature of the Maxwell-Boltzmann distribution, is not guaranteed for the series expansions and is violated at large velocities and temperature deviations (Ansumali *et al.*, 2003). The positivity is guaranteed if one evaluates the Lagrange multipliers and then finds the discrete equilibrium, which is explained in the forthcoming section. However, the appropriate series expansion of such equilibrium distributions must be the same as the series expansions given by Eqs.(3.24),(3.27). We also note that the methodology presented in this section differs from McNamara *et al.* (1997); Vahala *et al.* (1998); Chikatamarla & Karlin (2006) in not using single expansion in two variables (velocity and deviation from reference temperature).

3.4.1 Definition of temperature in the discrete kinetic theory

In this section, we show that the thermodynamic relation between entropy, internal energy, and temperature is obeyed by the discrete velocity model too. We start with the Maxwell-Boltzmann distribution Eq.(2.10) at zero velocity

$$f^{\mathrm{MB}}(\rho, u=0, \mathcal{E}, \boldsymbol{c}) = \rho\left(\frac{3\rho}{4\pi\mathcal{E}}\right)^{\frac{3}{2}} \exp\left[\frac{-3\rho\boldsymbol{c}^2}{4\mathcal{E}}\right], \tag{3.30}$$

with the internal energy $\mathcal{E} = (3/2)\rho\theta$. The local Maxwell-Boltzmann distribution is written as a product of the reference state $\omega(\boldsymbol{c}) = f^{\mathrm{MB}}(\rho = 1, u = 0, \mathcal{E}_0, \boldsymbol{c})$ and a function of molecular velocity $\boldsymbol{c}$ as

$$\hat{f}^{\mathrm{eq}}(\rho, u=0, \mathcal{E}, \boldsymbol{c}) = \rho\, \omega(\boldsymbol{c}) \left(\frac{\mathcal{E}_0}{\mathcal{E}}\right)^{3/2} \exp\left[-\frac{3\rho\boldsymbol{c}^2}{4\mathcal{E}} + \frac{3\boldsymbol{c}^2}{4\mathcal{E}_0}\right]. \tag{3.31}$$

Following the same procedure as above, $\mathcal{H}[\hat{f}^{\mathrm{eq}}(\rho, u=0, \mathcal{E}, \boldsymbol{c})]$ becomes

$$\mathcal{H}[\hat{f}^{\mathrm{eq}}(\rho, u=0, \mathcal{E}, \boldsymbol{c})] = \int d\boldsymbol{c}\,\omega(\boldsymbol{c}) \frac{\hat{f}^{\mathrm{eq}}}{\omega(\boldsymbol{c})} \log \hat{f}^{\mathrm{eq}} = \sum w_i \frac{\hat{f}_i^{\mathrm{eq}}}{\omega(c_i)} \log \hat{f}_i^{\mathrm{eq}} \tag{3.32}$$

We employ the transformation $\tilde{f}_i^{\mathrm{eq}}(\rho, u=0, \mathcal{E}_0) = w_i \hat{f}^{\mathrm{eq}}(\rho, u=0, \mathcal{E}_0, \boldsymbol{c}_i)/\omega(\boldsymbol{c}_i)$, which using Eq.(3.31) gives

$$\tilde{f}_i^{\mathrm{eq}} = \rho w_i \left(\frac{\mathcal{E}_0}{\mathcal{E}}\right)^{3/2} \exp\left[-\frac{3\rho c^2}{4\mathcal{E}} + \frac{3c^2}{4\mathcal{E}_0}\right]. \tag{3.33}$$

Under this transformation, Eq.(3.32) becomes

$$\begin{aligned} \mathcal{H}[\hat{f}^{\mathrm{eq}}(\rho, u=0, \mathcal{E}, \boldsymbol{c})] = \sum \tilde{f}_i^{\mathrm{eq}} \log \frac{\tilde{f}_i^{\mathrm{eq}} \omega(\boldsymbol{c}_i)}{w_i} &= \sum \tilde{f}_i^{\mathrm{eq}} \log \frac{\tilde{f}_i^{\mathrm{eq}}}{w_i} + \sum \tilde{f}_i^{\mathrm{eq}} \left[\frac{3}{2} \log \frac{3\rho}{4\pi\mathcal{E}_0} - \frac{3c^2}{4\mathcal{E}_0}\right] \\ &= \sum \tilde{f}_i^{\mathrm{eq}} \log \frac{\tilde{f}_i^{\mathrm{eq}}}{w_i} + \left[\frac{3}{2}\rho \log \frac{3\rho}{4\pi\mathcal{E}_0} - \frac{3\mathcal{E}}{2\mathcal{E}_0}\right], \end{aligned} \tag{3.34}$$

where substituting $\tilde{f}_i^{\mathrm{eq}}$ from Eq.(3.33) one obtains

$$\mathcal{H} = \sum \tilde{f}_i^{\mathrm{eq}} \left[\log \rho + \frac{3}{2} \log \frac{\mathcal{E}_0}{\mathcal{E}} - \frac{3\rho c^2}{4\mathcal{E}} + \frac{3c^2}{4\mathcal{E}_0}\right] + \left[\frac{3}{2}\rho \log \frac{3\rho}{4\pi\mathcal{E}_0} - \frac{3\mathcal{E}}{2\mathcal{E}_0}\right] \tag{3.35}$$

$$= \rho \log \rho + \frac{3}{2}\rho \log \frac{\mathcal{E}_0}{\mathcal{E}} - \frac{3\rho}{2} + \left[\frac{3}{2}\rho \log \frac{3}{4\pi\mathcal{E}_0}\right]. \tag{3.36}$$

Taking a derivative of the above expression with respect to $\mathcal{E}$, one obtains

$$\frac{\partial \mathcal{H}}{\partial \mathcal{E}} = -\frac{3\rho}{2\mathcal{E}} = -\frac{1}{\theta}. \tag{3.37}$$

Typically, Eq.(3.33) involves some errors depending on the discrete velocity models that have been ignored here.

3.5 Discrete entropic equilibrium

In this section, the discrete equilibrium distribution is derived such that the positivity is guaranteed. It is demonstrated that its series form is the same as the series expansions derived in the previous section. We begin with the discrete convex entropy function of the Boltzmann form

$$H = \sum_{i=1}^{N_d} f_i \left(\log \frac{f_i}{w_i} - 1\right),$$

and construct the discrete equilibrium as its minimizer under the constraints of local conservation laws (Karlin *et al.*, 1998; Boghosian *et al.*, 2003; Wagner, 1998; Chen & Teixeira, 2000; Karlin *et al.*, 1999; Succi *et al.*, 2002*b*; Ansumali *et al.*, 2003; Ansumali & Karlin, 2005). This constrained minimization can be performed by getting absolute minimum of the functional

$$\Xi = \sum_{i=1}^{N_d} \left[f_i \left(\log \frac{f_i}{w_i} - 1\right) + \hat{\mu} f_i + \zeta_\kappa c_{i\kappa} f_i + \gamma c_i^2 f_i\right], \tag{3.38}$$

where $\hat{\mu}, \zeta_\kappa, \gamma$ are the Lagrange multipliers associated with mass, momentum and energy respectively (Ansumali & Karlin, 2005; Ansumali *et al.*, 2003). Solving the minimization problem

$\partial\Xi/\partial f = 0$, one obtains the equilibrium distribution as

$$f_i^{\mathrm{eq}} = w_i \rho \exp(-\mu - \zeta_\kappa c_{i\kappa} - \gamma c_i^2), \tag{3.39}$$

where for convenience we have transformed the Lagrange multiplier $\hat{\mu} = \mu - \log\rho$. Note that this form of the discrete equilibrium distribution guarantees the positivity. For every discrete velocity model, one finds the Lagrange multipliers with high accuracy to preserve the positive form of equilibrium (Chikatamarla *et al.*, 2006).

The five Lagrange multipliers and thus the equilibrium populations f_i^{eq} are found in the explicit form if the system of five equations representing mass, momentum, and energy conservation

$$\sum_{i=1}^{N_d} f_i^{\mathrm{eq}}\{1, c_{i\alpha}, c_i^2\} = \{\rho, \rho u_\alpha, \rho u^2 + 3\rho\theta\}, \tag{3.40}$$

were explicitly invertible.

3.5.1 Special cases: $D1Q3, D2Q9, D3Q27$

For a few special cases such as the $D1Q3$ model (and its higher dimension extensions $D2Q9$ and $D3Q27$) the Lagrange multipliers can be evaluated in explicit form (Ansumali *et al.*, 2003). For the isothermal $D1Q3$ model, the discrete velocity set is $\{-1, 0, 1\}$ with reference temperature θ_0 and weights $\{1/6, 4/6, 1/6\}$. Therefore,

$$f_i^{\mathrm{eq}} = w_i \rho \exp(-\mu - \zeta_\kappa c_{i\kappa}), \tag{3.41}$$

which gives

$$f_{-1}^{\mathrm{eq}} = \frac{1}{6}AB, \quad f_0^{\mathrm{eq}} = \frac{4}{6}A, \quad f_1^{\mathrm{eq}} = \frac{1}{6}\frac{A}{B}, \tag{3.42}$$

where $A = \rho\exp(-\mu), B = \exp(-\zeta_\kappa)$. The mass and momentum conservation constraints

$$\rho = \frac{1}{6}A\left(\frac{1}{B} + 4 + B\right), \quad \rho u = \frac{1}{6}A\left(B - \frac{1}{B}\right), \tag{3.43}$$

can be solved to obtain

$$A = \rho\left(2 - \sqrt{1+3u^2}\right), \quad B = \frac{2u + \sqrt{1+3u^2}}{1-u}. \tag{3.44}$$

Therefore, the general formula for discrete entropic equilibrium in D dimensions is written as

$$f_i^{\mathrm{eq}} = w_i \rho \prod_{\alpha=1}^{D} \left(2 - \sqrt{1+3u_\alpha^2}\right)\left[\frac{2u_\alpha + \sqrt{1+3u_\alpha^2}}{1-u_\alpha}\right]^{c_{i\alpha}}. \tag{3.45}$$

It can be seen that the equilibrium is positive for all $u_\alpha < 1$.

However, other than these special cases the explicit solutions are not known. Therefore, one often uses a numerical route to compute the Lagrange multipliers and thus find the entropic equilibrium (Frapolli *et al.*, 2015; Dorschner *et al.*, 2016*a*,*b*). For numerical methodologies to solve for the Lagrange multipliers the reader is referred to Namburi (2017).

3.5.2 Perturbation series of the entropic equilibrium

We now derive the expansion of the entropic equilibrium as a perturbation series around a reference state. The series serves two purposes:

1. In any numerical methodology of finding the equilibrium distribution, the series provides a good guess for the Lagrange multipliers (and thus allows faster convergence to the true entropic equilibrium).
2. The series form can be employed to analyze the hydrodynamic limit.

We use this approximate polynomial form of the equilibrium to derive the moments of the equilibrium and comment on its accuracy.

As pointed out earlier, the system given by Eqns.(3.40) does not render an explicit solution. Therefore, we try to evaluate the explicit solution at a reference state of mean velocity $\boldsymbol{u} = 0$. We define the Lagrange multipliers at this reference state as $\mu^{(0)}, \zeta_\kappa^{(0)}, \gamma^{(0)}$, the equilibrium distribution is $\tilde{f}_i^{\mathrm{eq}} \equiv f_i^{\mathrm{eq}}(\rho, \boldsymbol{u}=0, \theta) = w_i \rho \exp(-\mu^{(0)} - \zeta_\kappa^{(0)} c_{i\kappa} - \gamma^{(0)} c_i^2)$, and the five conservation equations reduce to

$$\sum_{i=1}^{N_d} \tilde{f}_i^{\mathrm{eq}} \{1, c_{i\alpha}, c_i^2\} = \{\rho, 0, 3\rho\theta\} \equiv \{\rho, 0, 3\rho\theta_0(1+\eta)\}, \tag{3.46}$$

where $\eta = \theta/\theta_0 - 1$. In the above system of equations, one can group together the terms of discrete velocities $\boldsymbol{c}_i$ with the opposite discrete velocities $-\boldsymbol{c}_i$ terms in the momentum conservation equations and find the solution $\boldsymbol{\zeta}^{(0)} = 0$. Hence we obtain

$$\tilde{f}_i^{\mathrm{eq}} \equiv f_i^{\mathrm{eq}}(\rho, \boldsymbol{u}=0, \theta) = w_i \rho \exp(-\mu^{(0)} - \gamma^{(0)} c_i^2). \tag{3.47}$$

However, the other two Lagrange multipliers $\mu^{(0)}$ and $\gamma^{(0)}$ can still not be evaluated in the explicit form. Therefore, we choose another reference state with $\theta = \theta_0$ within this reference state. At the new reference state we define the Lagrange multipliers as $\mu^{(0,0)}, \gamma^{(0,0)}$, and it is trivial to check that $\mu^{(0,0)} = \gamma^{(0,0)} = 0$ satisfies the mass and the energy conservation condition. We first construct the perturbation series for $\tilde{f}_i^{\mathrm{eq}}$ around this reference state. To this effect, we expand the Lagrange multipliers around $\mu^{(0,0)}$ and $\gamma^{(0,0)}$ in powers of η

$$\begin{aligned} \mu^{(0)} &= \mu^{(0,0)} + \eta\mu^{(0,1)} + \eta^2\mu^{(0,2)} + \eta^3\mu^{(0,3)} + \cdots, \\ \gamma^{(0)} &= \gamma^{(0,0)} + \eta\gamma^{(0,1)} + \eta^2\gamma^{(0,2)} + \eta^3\gamma^{(0,3)} + \cdots. \end{aligned} \tag{3.48}$$

Substituting Eq.(3.48) in Eq.(3.47) one obtains

$$\tilde{f}_i^{\mathrm{eq}} = w_i\rho\left(1 - \eta\left[\mu^{(0,1)} + \gamma^{(0,1)}c_i^2\right] - \eta^2\left[\mu^{(0,2)} + \gamma^{(0,2)}c_i^2 - \frac{1}{2}\left(\mu^{(0,1)} + \gamma^{(0,1)}c_i^2\right)^2\right] + \cdots\right), \tag{3.49}$$

with the requirement that

$$\left\langle \tilde{f}^{\mathrm{eq}}, \{1, c^2\}\right\rangle = \{\rho, 3\rho\theta_0(1+\eta)\}. \tag{3.50}$$

The Lagrange multipliers evaluated by comparing the terms at every orders of η on the both sides of Eq.(3.50) are

$$\begin{aligned} \mu^{(0)} &= \frac{3}{2}\eta - \frac{3}{4}\eta^2 + \frac{3}{6}\eta^3 - \frac{3}{8}\eta^4 + \mathcal{O}(\eta^5), \\ \gamma^{(0)} &= -\frac{1}{2\theta_0}\eta + \frac{1}{2\theta_0}\eta^2 - \frac{1}{2\theta_0}\eta^3 + \frac{1}{2\theta_0}\eta^4 + \mathcal{O}(\eta^5), \end{aligned} \tag{3.51}$$

provided w_i satisfy the constraints in Eq.(3.29). The procedure is general enough and can be used to find the series expansion for $\tilde{f}_i^{\mathrm{eq}}$ upto any arbitrary order in η. The expression accurate upto $\mathcal{O}(\eta^4)$ is

$$\tilde{f}_i^{\rm eq} = w_i\rho\bigg[1+\frac{\eta}{2\theta_0}(c_i^2-3\theta_0)+\frac{\eta^2}{8\theta_0^2}\left(c_i^4-10c_i^2\theta_0+15\theta_0^2\right)+\frac{\eta^3}{48\theta_0^3}\left(c_i^6-21c_i^4\theta_0+105c_i^2\theta_0^2-105\theta_0^3\right) \\ +\frac{\eta^4}{384\theta_0^4}\left(c_i^8-36c_i^6\theta_0+378c_i^4\theta_0^2-1260c_i^2\theta_0^3+945\theta_0^4\right)\bigg], \tag{3.52}$$

provided the lattice parameters satisfy conditions given in Eq.(3.29). Notice that the above expression is same as the Eq.(3.27) evaluated in Section 3.4.

The next step is to derive the equilibrium distribution at non-zero velocity by expanding the Lagrange multipliers in ϵ (representing smallness of the Mach number) as

$$\begin{aligned}\mu &= \mu^{(0)}+\epsilon\mu^{(1)}+\epsilon^2\mu^{(2)}+\epsilon^3\mu^{(3)}+\mathcal{O}(\epsilon^4),\\ \zeta_\kappa &= \zeta_\kappa^{(0)}+\epsilon\zeta_\kappa^{(1)}+\epsilon^2\zeta_\kappa^{(2)}+\epsilon^3\zeta_\kappa^{(3)}+\mathcal{O}(\epsilon^4),\\ \gamma &= \gamma^{(0)}+\epsilon\gamma^{(1)}+\epsilon^2\gamma^{(2)}+\epsilon^3\gamma^{(3)}+\mathcal{O}(\epsilon^4).\end{aligned} \tag{3.53}$$

Substituting the above expressions in Eq.(3.39) and collecting terms with like powers of ϵ one obtains

$$f_i^{\rm eq} = \tilde{f}_i^{\rm eq}\Bigg(1-\epsilon\left[\mu^{(1)}+\zeta_\kappa^{(1)}c_{i\kappa}+\gamma^{(1)}c_i^2\right]-\epsilon^2\bigg[\mu^{(2)}+\zeta_\kappa^{(2)}c_{i\kappa}+\gamma^{(2)}c_i^2 \\ -\frac{1}{2}\left(\mu^{(1)}+\zeta_\kappa{}^{(1)}c_{i\kappa}+\gamma^{(1)}c_i^2\right)^2\bigg]+\cdots\Bigg). \tag{3.54}$$

The mass, momentum, and energy conservation requirements

$$\left\langle f^{\rm eq},\{1,c_\alpha,c^2\}\right\rangle = \{\rho,\rho u_\alpha\epsilon,3\rho\theta+\rho u^2\epsilon^2\}, \tag{3.55}$$

are compared at various orders of ϵ to find the Lagrange multipliers

$$\begin{aligned}\mu &= \mu^{(0)}+\epsilon^2\mu^{(2)}+\mathcal{O}(\epsilon^4),\\ \zeta_\kappa &= \zeta_\kappa^{(0)}-\epsilon\frac{u_\alpha}{\theta}+\epsilon^3\frac{u^2u_\alpha}{\theta^2}\mathcal{A}+\mathcal{O}(\epsilon^4),\\ \gamma &= \gamma^{(0)}+\mathcal{O}(\epsilon^4).\end{aligned} \tag{3.56}$$

where $\mathcal{A}=\left\langle \tilde{f}_i^{\rm eq},c_{ix}^2c_{iy}^2\right\rangle/(3\rho\theta^2)-1/3$, provided an additional isotropy condition at the eighth order

$$\left\langle w,c^4c_\alpha c_\beta c_\gamma c_\kappa\right\rangle = 63\theta_0^4\Delta_{\alpha\beta\gamma\kappa}, \tag{3.57}$$

is imposed. Substituting the Lagrange multipliers in Eq.(3.54), we obtain the expression for discrete equilibrium accurate upto $\mathcal{O}(\epsilon^3)$

$$f_i^{\rm eq} = \tilde{f}_i^{\rm eq}\left\{1+\frac{u_\alpha c_{i\alpha}}{\theta}-\frac{u^2}{2\theta}+\frac{1}{2}\left(\frac{u_\alpha c_{i\alpha}}{\theta}\right)^2+\frac{1}{6}\left(\frac{u_\alpha c_{i\alpha}}{\theta}\right)^3-\frac{u^2u_\alpha c_{i\alpha}}{2\theta^2}(1-\mathcal{A})\right\}. \tag{3.58}$$

The moments of the equilibrium distribution are

$$\left\langle f^{\rm eq},\{1,c_\alpha,c^2,c_\alpha c_\beta,c^2c_\alpha\}\right\rangle \\ = \left\{\rho,\rho u_\alpha,3\rho\theta+\rho u^2,\rho\theta\delta_{\alpha\beta}+\rho u_\alpha u_\beta+\mathcal{O}(u_\alpha u_\beta\eta^3),5\rho\theta u_\alpha+\rho u^2u_\alpha+\mathcal{O}(u^3\eta^3)\right\}, \tag{3.59}$$

and they match the moments of the Maxwell-Boltzmann distribution upto a high accuracy. Any discrete velocity model whose equilibrium distribution satisfies the above condition will have correct thermohydrodynamic limit. The 41 velocity model of Chikatamarla & Karlin (2009) and the off-lattice 27 velocity model of Yudistiawan *et al.* (2010) have sixth order isotropy imposed on the moments of their weights.

3.6 Conclusion

In this chapter, we have derived the constraints on the parameters w_i, c_i, θ_0 of any DVM in order to have a faithful representation of the continuous kinetic theory. These constraints are

$$\left\langle w, \left\{1, \boldsymbol{c}^2, \boldsymbol{c}^2\boldsymbol{c}^2, \boldsymbol{c}^2\boldsymbol{c}^2\boldsymbol{c}^2, \boldsymbol{c}^2\boldsymbol{c}^2\boldsymbol{c}^2\boldsymbol{c}^2, \boldsymbol{c}^2\boldsymbol{c}^2\boldsymbol{c}^2\boldsymbol{c}^2\boldsymbol{c}^2\right\}\right\rangle = \left\{1, 3\theta_0, 15\theta_0^2, 105\theta_0^3, 945\theta_0^4, 10395\theta_0^5\right\}. \tag{3.60}$$

We have also demonstrated that the moments of the Maxwell-Boltzmann distribution need to be imitated by the discrete equilibrium distribution to obtain the correct thermohydrodynamic limit of the kinetic equation. The above constraints along with $\left\langle w, c^4 c_\alpha c_\beta c_\gamma c_\kappa \right\rangle = 63\theta_0^4 \Delta_{\alpha\beta\gamma\kappa}$ allows the discrete entropic equilibrium to imitate the moments of the Maxwell-Boltzmann distribution upto high accuracy as

$$\langle f^{\mathrm{eq}}, 1\rangle = \left\langle f^{\mathrm{MB}}, 1\right\rangle, \quad \langle f^{\mathrm{eq}}, c_\alpha\rangle = \left\langle f^{\mathrm{MB}}, c_\alpha\right\rangle, \quad \left\langle f^{\mathrm{eq}}, c^2\right\rangle = \left\langle f^{\mathrm{MB}}, c^2\right\rangle, \tag{3.61}$$

$$\langle f^{\mathrm{eq}}, c_\alpha c_\beta\rangle = \left\langle f^{\mathrm{MB}}, c_\alpha c_\beta\right\rangle + \mathcal{O}(u^2\eta^3), \quad \left\langle f^{\mathrm{eq}}, c^2 c_\alpha\right\rangle = \left\langle f^{\mathrm{MB}}, c^2 c_\alpha\right\rangle + \mathcal{O}(u^3\eta^3). \tag{3.62}$$

In Chapter 7, we will show that the above constraints can be satisfied on a crystallographic lattice with sixty-seven discrete velocities, which will be employed to simulate various canonical test cases related to thermohydrodynamics.

Chapter 4

The lattice Boltzmann model

The lattice Boltzmann model (LBM) aims to construct a simplified kinetic picture on a lattice designed to capture the physics of macroscopic flow through simple local micro-scale operations (Succi, 2001; Chen & Doolen, 1998; Aidun & Clausen, 2010). This highly efficient and easily parallelizable method is routinely used as an alternative numerical method for applications as wide-ranging as fluid turbulence, gaseous microflow, soft matter, polymer dynamics, relativistic flows, etc. (Chen & Doolen, 1998; Thantanapally *et al.*, 2013*a*; Singh *et al.*, 2013; Thampi *et al.*, 2013*b*; Mendoza *et al.*, 2010; Benzi *et al.*, 2013; Chen *et al.*, 2004; Ansumali *et al.*, 2007*b*; Chen *et al.*, 1992; Qian *et al.*, 1992; Lallemand & Luo, 2000; Aidun & Clausen, 2010; Chen & Doolen, 1998; Benzi *et al.*, 1992; Higuera *et al.*, 1989; Succi, 2001; Succi *et al.*, 2002*b*; Namburi *et al.*, 2016; Yudistiawan *et al.*, 2010; Ladd, 1993; Adhikari *et al.*, 2005).

However, the lower order LBMs have so far been a successful methodology only for incompressible isothermal hydrodynamics and gaseous microflow in slip flow regime. Extensions of LBM for thermohydrodynamics and compressible flows are relatively less successful so far (McNamara *et al.*, 1997). While the higher order extension of the LBM for weakly compressible but isothermal situations show promising results for turbulence (Chikatamarla *et al.*, 2010) and the thermal models in incompressible regime are well established, a uniform framework for thermohydrodynamics valid for compressible flows are not fully developed yet. Typically, higher-order LBMs also perform much better for resolving complex phenomena such as Knudsen boundary layer (Sofonea, 2006; Ansumali *et al.*, 2007*b*; Ambruş & Sofonea, 2012). Recent works have indicated that even in the case of turbulence, better performance is obtained due to the fact that the hydrodynamic limit of the higher-order LBM is cubically correct and thus Galilean invariant to the leading order (Frapolli *et al.*, 2016*b*; Namburi *et al.*, 2016). This topic of higher order lattice Boltzmann models will be the subject of Chapter 7.

An important realization in the subject was that the nonlinear stability in the method could be restored by enforcing the thermodynamics inherent in the original Boltzmann description (Karlin *et al.*, 1998; Wagner, 1998; Karlin *et al.*, 1999; Succi *et al.*, 2002*b*; Ansumali *et al.*, 2003; Ansumali & Karlin, 2005). These class of models known as the entropic lattice Boltzmann model (ELBM) constitute a discrete space-time kinetic theory that ensures nonlinear stability via the discrete time version of the second law of thermodynamics (the $\mathcal{H}$ theorem). The entropic formulation leads to nonlinear stabilization of standard LBM in context of flows with sharp gradients and highly non-equilibrium situations (Succi *et al.*, 2002*b*; Aidun & Clausen, 2010; Karlin *et al.*, 1998; Boghosian *et al.*, 2003; Wagner, 1998; Chen & Teixeira, 2000; Karlin *et al.*, 1999; Succi *et al.*, 2002*b*; Ansumali *et al.*, 2003; Ansumali & Karlin, 2005).

In this chapter, we first derive the discrete in space and time evolution of the populations. We then review the methodology to construct lower order lattice Boltzmann models which are effective in the context of isothermal incompressible flows. It is followed by a brief discussion on the collision operators used regularly in LBM and the recently developed LBM based on a crystallographic grid (Namburi *et al.*, 2016). This chapter is organized as follows: In Section 4.1 we review the derivation of discrete evolution of populations from the discrete in velocity Boltzmann BGK equation. In Section 4.2 we discuss the constraints on lattice parameters required to obtain the correct hydrodynamic limit. In Section 4.3 we briefly review some of the collision models other than the BGK model used in LBM. Finally, in Section 4.4 we discuss the crystallographic grid and its advantages in the context of hydrodynamic simulations.

4.1 From continuous to discrete space-time

Similar to other DVM, in LBM the velocity space is discretized into a discrete velocity set $\boldsymbol{c} = \{\boldsymbol{c}_i, i = 1 \cdots N_d\}$ with the populations f_i as the basic working element. The discrete velocity set has to satisfy certain isotropy conditions discussed previously in Chapter 3. The discrete in velocity Boltzmann BGK equation reads

$$\partial_t f_i(\boldsymbol{x}, t) + c_{i\alpha}\partial_\alpha f_i(\boldsymbol{x}, t) = \Omega_i(f_i(\boldsymbol{x}, t)), \tag{4.1}$$

where Ω_i is the collision operator given by

$$\Omega_i(f_i(\boldsymbol{x}, t)) = \frac{1}{\tau}\left[f_i^{\text{eq}}(\rho(\boldsymbol{x}, t), \boldsymbol{u}(\boldsymbol{x}, t), \theta(\boldsymbol{x}, t)) - f_i(\boldsymbol{x}, t)\right],$$

and f_i are populations corresponding to discrete velocity $\boldsymbol{c}_i$, f_i^{eq} is the discrete equilibrium distribution, and τ is the collisional relaxation time. However, unlike other DVMs, the LBM builds the kinetic theory in discrete space and time too. In the forthcoming subsections, we will obtain the fully discrete in space and time evolution of populations from the Eq.(4.1).

4.1.1 Time discretization

The Eq.(4.1) constitutes a set of N_d coupled partial differential equations. It has two natural time scales: τ associated with collisional relaxation, and the one associated with sound propagation. The time scale of sound propagation is much larger than that of collision. In order to have a numerically efficient scheme it is desirable to have large time steps, i.e., $\Delta t \gg \tau$.

The left hand side of Eq.(4.1) is $(\partial_t + c_\alpha\partial_\alpha)f_i$, which corresponds to the derivative along a characteristic, hence a solution is obtained from the integration along the characteristics (He & Luo, 1997*a*,*b*; He *et al.*, 1998*a*). The formal solution can hence be written as

$$f_i(\boldsymbol{x} + \boldsymbol{c}\Delta t, t + \Delta t) = f(\boldsymbol{x}, t) + \int_{s=0}^{s=\Delta t} \Omega_i(f_i(\boldsymbol{x} + \boldsymbol{c}\Delta t, t + \Delta t))ds. \tag{4.2}$$

The integral is approximated via the trapezoid rule to obtain the implicit relation

$$f_i(\boldsymbol{x} + \boldsymbol{c}\Delta t, t + \Delta t) = f(\boldsymbol{x}, t) + \frac{\Delta t}{2}\left[\Omega_i(f_i(\boldsymbol{x} + \boldsymbol{c}\Delta t, t + \Delta t)) + \Omega_i(f_i(\boldsymbol{x}, t))\right] + \mathcal{O}(\Delta t^3). \tag{4.3}$$

In order to make it explicit, we define a transformed variable g_i as

$$\begin{aligned} g_i(\boldsymbol{x}, t) &= f_i(x, t) - \frac{\Delta t}{2}\Omega_i(f_i(\boldsymbol{x}, t)) \\ &= \left(1 + \frac{\Delta t}{2\tau}\right) f_i(x, t) - \frac{\Delta t}{2\tau} f_i^{\text{eq}}[\rho(\boldsymbol{x}, t), \boldsymbol{u}(\boldsymbol{x}, t), \theta(\boldsymbol{x}, t)]. \end{aligned} \tag{4.4}$$

Notice that the conserved moments of f_i and g_i are the same, i.e.,

$$\langle g, 1\rangle = \langle f, 1\rangle = \rho, \quad \langle g, c_\alpha\rangle = \langle f, c_\alpha\rangle = \rho u_\alpha, \quad \left\langle g, c^2\right\rangle = \left\langle f, c^2\right\rangle = 3\rho\theta + \rho u^2, \tag{4.5}$$

hence $g_i^{\text{eq}} = f_i^{\text{eq}}$. By substituting g_i in Eq.(4.3) we obtain

$$g_i(\boldsymbol{x} + \boldsymbol{c}\Delta t, t + \Delta t) = g_i(\boldsymbol{x}, t) + \frac{2\Delta t}{2\tau + \Delta t}\left[g_i^{\text{eq}}(\rho(\boldsymbol{x}, t), \boldsymbol{u}(\boldsymbol{x}, t), \theta(\boldsymbol{x}, t)) - g_i(\boldsymbol{x}, t)\right]. \tag{4.6}$$

The conserved moments are the moments of the transformed variable g_i, but the non-conserved moments like stress tensor or the heat flux need to be evaluated as moments of f_i as per their defintion. For example, the stress tensor $\sigma_{\alpha\beta}$ and the heat flux q_α are available as

$$\sigma_{\alpha\beta} = \langle f, \xi_\alpha \xi_\beta \rangle = \frac{2\tau}{2\tau + \Delta t} \langle g, \xi_\alpha \xi_\beta \rangle, \quad q_\alpha = \left\langle f, \frac{1}{2}\xi^2 \xi_\alpha \right\rangle = \frac{2\tau}{2\tau + \Delta t} \left\langle g, \frac{1}{2}\xi^2 \xi_\alpha \right\rangle. \tag{4.7}$$

Here onwards, the transformed variable g_i will be called f_i, and the thermohydrodynamic moments will be evaluated as explained above.

4.1.2 Space discretization

The physical space is discretized into a series of grid nodes that together comprise a lattice. At any node on the lattice, the neighboring nodes are located at distance of $\Delta x = m\mathbf{c}_i \Delta t$, where m is a natural number (Succi, 2001; Chikatamarla & Karlin, 2009). Figure 4.1 depicts the lattice connections in a D2Q9 model, where each neighbouring point is at a distance of $\boldsymbol{x} + \boldsymbol{c}_i \Delta t$.

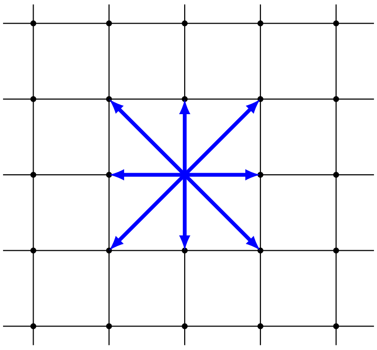

Figure 4.1: Discretization of physical space in LBM. The discrete velocity $\boldsymbol{c}_i$ at any node $\boldsymbol{x}$ on the lattice connects to the neighboring nodes at $\boldsymbol{x} + \boldsymbol{c}_i \Delta t$, where Δt is the discrete time between successive collisions.

The particularly attractive feature of LBM is that the neighbouring points are located at a distance of $\boldsymbol{x} + \boldsymbol{c}_i \Delta t$. This allows for construction of a numerically efficient and easily parallelizable algorithm, where Eq.(4.6) is implemented as a two step procedure:

1. **Streaming/Advection**: Here, f_i streams along the direction of respective discrete velocities. This is written as

$$f_i(\mathbf{x} + \mathbf{c}_i \Delta t, t + \Delta t) = f_i^*(\mathbf{x}, t). \tag{4.8}$$

2. **Collision**: The populations collide at each node and relax towards local equilibrium

$$f_i^*(\mathbf{x}, t) = f_i(\mathbf{x}, t) + \alpha\beta \left(f_i^{\mathrm{eq}}(\rho, \mathbf{u}, \theta) - f_i(\mathbf{x}, t) \right), \tag{4.9}$$

   where $\alpha = 2$, and $\beta = \Delta t / (2\tau + \Delta t)$ is related to the kinematic viscosity ν via relaxation time $\tau = \nu / \theta_0$, with θ_0 as the reference temperature.

The entropic formulation of LBM has an extra step where α is calculated as the root of the entropy estimate

$$\mathcal{H}[f(\mathbf{x}, t) + \alpha \left(f^{\mathrm{eq}}(\rho, \boldsymbol{u}, \theta) - f(\mathbf{x}, t) \right)] - \mathcal{H}[f(\mathbf{x}, t)] = 0, \tag{4.10}$$

where $\mathcal{H}$ is a convex entropy function. It restores the thermodynamic consistency embedded in the Boltzmann description (Ansumali & Karlin, 2005) and ensures the $\mathcal{H}$ theorem for discrete space-time formulation, and thus leads to a nonlinearly stable solver that is effective in the

Discrete velocity	$D3Q15$	$D3Q19$	$D3Q27$
$(\pm1,0,0),(0,\pm1,0),(0,0,\pm1)$	1/9	1/18	2/27
$(\pm1,\pm1,0),(\pm1,0,\pm1),(0,\pm1,\pm1)$	-	1/36	1/54
$(\pm1,\pm1,\pm1)$	1/72	-	1/216

Table 4.1: Weights corresponding to discrete velocities for the basic models.

context of flows with sharp gradients. Thus, entropic LBM is quite suitable for the case of thermal and compressible flows where gradients can be sharp (McNamara *et al.*, 1997).

4.2 Discrete isothermal equilibrium

The choice of the discrete equilibrium distribution is considered crucial in LBM. It has to ensure that the macroscopic hydrodynamics equations recovered upon Chapman-Enskog expansion of the Boltzmann BGK equation agree with the Navier-Stokes equations. The discrete isothermal equilibrium is required to conserve the mass and momentum (energy conservation is ignored here), i.e.,

$$\langle f^{\rm eq}, \{1, \boldsymbol{c}\}\rangle = \{\rho, \rho\boldsymbol{u}\}, \tag{4.11}$$

and was historically evaluated by projecting the Maxwell-Boltzmann distribution on the Hermite basis to obtain a computationally appealing polynomial expression Chen *et al.* (1992); Benzi *et al.* (1992); Shan & He (1998*b*)

$$f_i^{\rm eq}(\rho, \mathbf{u}) = w_i\rho\left[1 + \frac{u_\alpha c_{i\alpha}}{\theta_0} + \frac{u_\alpha u_\beta}{2\,\theta_0^2}\left(c_{i\alpha}c_{i\beta} - \theta_0\delta_{\alpha\beta}\right)\right], \tag{4.12}$$

where the reference temperature θ_0, the velocities $\boldsymbol{c}_i$ and the weights w_i are lattice dependent parameters with

$$w_i > 0,\ \langle w, 1\rangle = 1. \tag{4.13}$$

Substituting Eq.(4.12) into Eq.(4.11) the parameters $w_i, \boldsymbol{c}_i, \theta_0$ are constrained as

$$\langle w, c_\alpha c_\beta\rangle = \theta_0\delta_{\alpha\beta} \Rightarrow \left\langle w, c^2\right\rangle = 3\theta_0, \tag{4.14}$$

where we have used the conditions on moments of weights as specified by Eq.(3.4).

In addition to Eq.(4.11), $f_i^{\rm eq}$ should satisfy a few other constraints in order to recover correct hydrodynamics for low Mach isothermal flows. For example, it is important to ensure that the second moment of $f_i^{\rm eq}$ is the same as that obtained from the Maxwell-Boltzmann distribution, i.e.,

$$\langle f^{\rm eq}, c_\alpha c_\beta\rangle = \rho u_\alpha u_\beta + \rho\theta_0\delta_{\alpha\beta}, \tag{4.15}$$

which adds another constraint

$$\langle w, c_\alpha c_\beta c_\gamma c_\kappa\rangle = \theta_0^2\Delta_{\alpha\beta\gamma\kappa} \Rightarrow \left\langle w, \{c^2c_x^2, c^4\}\right\rangle = \{5\theta_0^2, 15\theta_0^2\}, \tag{4.16}$$

where $\Delta_{\alpha\beta\gamma\kappa} = \delta_{\alpha\beta}\delta_{\gamma\kappa} + \delta_{\alpha\gamma}\delta_{\beta\kappa} + \delta_{\alpha\kappa}\delta_{\beta\gamma}$ is the fourth order isotropic tensor. The well-known models like the $D3Q15$, $D3Q19$, and $D3Q27$ satisfy these conditions. They have $\theta_0 = 1/3$ and the weights corresponding to their discrete velocities are tabulated in Table 4.1.

As pointed out in Chapter 3, it is evident that in the limit of $\tau \to 0$, the zeroth order hydrodynamic equation is the Euler equation. The Navier-Stokes dynamics is correctly recovered provided

$$\langle f^{\rm eq}, c_\alpha c_\beta c_\gamma\rangle = \rho u_\alpha u_\beta u_\gamma + \rho\theta_0\left(u_\alpha\delta_{\beta\gamma} + u_\beta\delta_{\alpha\gamma} + u_\gamma\delta_{\alpha\beta}\right). \tag{4.17}$$

Due to the absence of the cubic term in Eq.(4.12), the above condition is satisfied only up to linear order by widely used lower order lattice Boltzmann models (Qian & Zhou, 1998). This condition on third moment can be fulfilled if the discrete equilibrium distribution is of the form (Shan & He, 1998*b*; Ansumali & Karlin, 2005; Chikatamarla & Karlin, 2009; Vahala *et al.*, 1998)

$$f_i^{\mathrm{eq}}(\rho, \boldsymbol{u}) = w_i\rho\left[1 + \frac{u_\alpha c_{i\alpha}}{\theta_0} + \frac{u_\alpha u_\beta}{2\,\theta_0^2}\left(c_{i\alpha}c_{i\beta} - \theta_0\delta_{\alpha\beta}\right) + \frac{u_\alpha u_\beta u_\gamma c_{i\gamma}}{6\,\theta_0^3}\left(c_{i\alpha}c_{i\beta} - 3\theta_0\delta_{\alpha\beta}\right)\right]. \tag{4.18}$$

The above expression and Eq.(4.17) impose further restriction on the weights as

$$\langle w, c_\alpha c_\beta c_\gamma c_\kappa c_\zeta c_\eta\rangle = \theta_0^3\Delta_{\alpha\beta\gamma\kappa\zeta\eta} \Rightarrow \langle w, \{c^2 c_x^2 c_y^2, c^4 c_x^2, c^6\}\rangle = \{7\theta_0^3, 35\theta_0^3, 105\theta_0^3\}, \tag{4.19}$$

where $\Delta_{\alpha\beta\gamma\kappa\zeta\eta}$ is the sixth-order isotropic tensor. However, only very high order models are known to satisfy such constraint in 3-dimensions (Chikatamarla & Karlin, 2009).

As discussed previously in Section 3.5, the polynomial expression given by Eq.(4.18) can attain negative values for large velocities. The entropic equilibrium ensures positivity of the equilibrium populations and is now accepted to be more robust and stable way of constructing the discrete equilibrium distribution (Ansumali *et al.*, 2003; Ansumali & Karlin, 2005). However, the constraints on the lattice parameters remain the same regardless of which form of equilibrium is used. Here, we remind that a closed form expression [see Sec. 3.5.1] for the discrete entropic equilibrium can be obtained for the $D1Q3, D2Q9, D3Q27$ lattices. However, a numerical route is employed to find the discrete equilibrium for other lattices.

To summarize, the procedure for constructing models for low Mach isothermal hydrodynamics is to find discrete velocities $\boldsymbol{c}_i$ on the lattice whose corresponding equilibrium f_i^{eq} mimics the moments of the Maxwell-Boltzmann distribution. The conditions that are considered indispensable for the velocity space discretization, which lead to cubically correct hydrodynamics are

$$\begin{aligned} \langle w, \{1, c_\alpha c_\beta\}\rangle &= \{1, \theta_0\delta_{\alpha\beta}\}, \\ \langle w, \{c_\alpha c_\beta c_\gamma c_\kappa, c_\alpha c_\beta c_\gamma c_\kappa c_\zeta c_\eta\}\rangle &= \{\theta_0^2\Delta_{\alpha\beta\gamma\kappa}, \theta_0^3\Delta_{\alpha\beta\gamma\kappa\zeta\eta}\}. \end{aligned} \tag{4.20}$$

The zero-one-three model proposed by Chikatamarla & Karlin (2006) satisfies $R^{\mathrm{eq}} = R^{\mathrm{MB}} + \mathcal{O}(u^4)$, and was is suitable for isothermal and weakly compressible flows. Another excellent methodology to construct lattices takes the quadrature route and is employed to propose various models in two and three dimensions in Sbragaglia *et al.* (2009); Shan (2010).

4.3 Other collision models in LBM

The BGK approximation is used widely in the continuous kinetic theory as well as in the LBM due to its simplicity. However, due to the single relaxation time approximation in the BGK model, the Prandtl number is fixed at unity. A similar limitation exists for the gaseous mixture where Schmidt number has a fixed value. Various approximations for the collision operator have been proposed in order to have arbitrary values of the transport coefficient (Chen *et al.*, 2010; Soe *et al.*, 1998; Luo & Girimaji, 2002; Asinari & Karlin, 2010; Luo & Girimaji, 2003; Ansumali *et al.*, 2007*a*; Thantanapally *et al.*, 2013*b*). However, an important progress in the field was the realization that although the hydrodynamic limit of different collision models are the same, they exhibit different numerical stability behavior. Thus, a great deal of effort was made to identify collision models with better numerical stability (d'Humières, 2002; Lallemand & Luo, 2000; Thantanapally *et al.*, 2013*b*; Karlin *et al.*, 2014). In this section, we briefly review some of the collision models often used for LBM simulations.

4.3.1 Quasi-equilibrium collision

The quasi-equilibrium collision kernel (Gorban & Karlin, 1994; Levermore, 1996), a two relaxation time model where different moments relax at different rates, was discussed for the continuous kinetic theory in Section 2.4.2. For completeness, we briefly discuss the quasi-equilibrium model in the context of LBM in this section. This model allows one to achieve arbitrary values of the transport coefficients and thereby tune the Prandtl number (Pr). The central idea is to divide the set of independent moments into three parts

$$\mathcal{M} = \{\mathcal{M}^{\text{Slow}}, \mathcal{M}^{\text{Quasi-slow}}, \mathcal{M}^{\text{Fast}}\}, \tag{4.21}$$

where $\mathcal{M}^{\text{Slow}} = \{\rho, \mathbf{u}, \theta\}$ are the set of conserved moments, and $\mathcal{M}^{\text{Quasi-Slow}}$ and $\mathcal{M}^{\text{Fast}}$ are the set of non-conserved moments. The relaxation rate of $\mathcal{M}^{\text{Quasi-Slow}}$ is slower than that of $\mathcal{M}^{\text{Fast}}$ (Gorban & Karlin, 1994). The choice of the quasi-slow and the fast moments depends on the physical context (Ansumali *et al.*, 2007*a*). For example,

$$\mathcal{M}^{\text{Quasi-Slow}} = \begin{cases} q_\alpha, & \text{Pr} < \text{Pr}_{\text{BGK}} \\ \sigma_{\alpha\beta}, & \text{Pr} > \text{Pr}_{\text{BGK}}, \end{cases} \tag{4.22}$$

where $q_\alpha, \sigma_{\alpha\beta}$ are the heat flux and the stress tensor respectively.

The collision kernel for the quasi-equilibrium model is

$$\Omega_i = \frac{1}{\tau}\left[f_i^*\left(\mathcal{M}^{\text{Quasi-slow}}\right) - f_i\right] + \frac{1}{\tau_1}\left[f_i^{\text{eq}}(\rho, \mathbf{u}, \theta) - f_i^*\left(\mathcal{M}^{\text{Quasi-Slow}}\right)\right], \tag{4.23}$$

where τ and τ_1 are two relaxation times which allows fixing two independent transport coefficients. For this model, the thermodynamic consistency in terms of H-theorem dictates $\tau \leq \tau_1$. The quasi-equilibrium state $f_i^*\left(\mathcal{M}^{\text{Quasi-slow}}\right)$ is the minimum of the H-function with slow and quasi-slow moments being conserved. Figure 4.2 depicts the quasi-equilibrium collision kernel, where f is the pre-collisional state, f^{eq} is the equilibrium state, and f^* is the quasi-equilibrium state. The relaxation from f to f^* takes time τ, followed by the relaxation from f^* to f^{eq} which takes time τ_1.

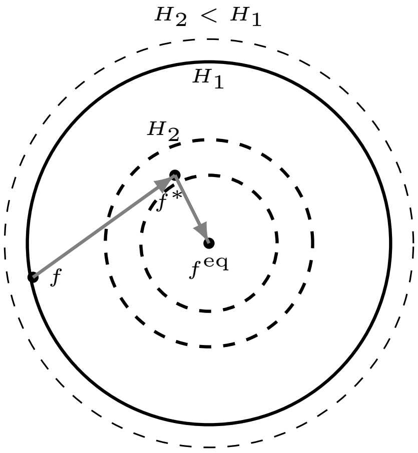

Figure 4.2: Sketch of of quasi-equilibrium collisional relaxation.

It should be noted that in the continuous kinetic theory, this model is limited to $\text{Pr} > \text{Pr}_{\text{BGK}}$

due to the presence of the quasi-equilibrium state $f^*\left(\mathcal{M}^{\text{Quasi-slow}}\right)$ in the collision term,

$$f^*\left(\mathcal{M}^{\text{Quasi-Slow}}\right) = \begin{cases} \exp\left(-\mu - \zeta_\kappa c_\kappa - \gamma c^2 - \chi_\alpha c^2 c_\alpha\right), & \mathrm{Pr} < \mathrm{Pr}_{\mathrm{BGK}} \\ \exp\left(-\mu - \zeta_\kappa c_\kappa - \psi_{\alpha\beta} c_\alpha c_\beta\right), & \mathrm{Pr} > \mathrm{Pr}_{\mathrm{BGK}}, \end{cases} \tag{4.24}$$

where $\mu, \zeta, \gamma, \psi, \chi$ are the Lagrange multipliers associated with mass, momentum, energy, stress tensor, and heat flux respectively. For $\mathrm{Pr} < \mathrm{Pr}_{\mathrm{BGK}}$, the moments of f^* written as

$$\int d\boldsymbol{c}\, c^m f_i^*\left(\mathcal{M}^{\text{Quasi-Slow}}\right), \text{ where } m \geq 0, \tag{4.25}$$

cannot be evaluated because the integral diverges (tends to infinity) as $c \to -\infty$. However, the discrete kinetic theory does not encounter such a limitation because the integrals are replaced by summation over a finite velocity set, hence, are always finite.

4.3.2 Multiple relaxation time collision

As stated earlier, the BGK collision model restricts the relaxation of all the moments to the same rate thereby limiting the Prandtl number to unity. Unlike the lattice Boltzmann BGK formulation, in a multi-relaxation model each higher order moment has its own relaxation time. The relaxation time parameters are carefully chosen so as to separate the time scales at which different moments relax. As most of these relaxation times have no physical significance in the context of incompressible hydrodynamics, many of these rates are set arbitrarily to achieve optimal stability (Higuera *et al.*, 1989; Lallemand & Luo, 2000). The evolution of population reads as (d'Humières, 2002)

$$\tilde{f}\left(\mathbf{x} + \mathbf{c}\Delta t, t + \Delta t\right) - \tilde{f}\left(\mathbf{x}, t\right) = -M^{-1}\hat{S}\left[\tilde{m}(\mathbf{x}, t) - \tilde{m}^{\mathrm{eq}}(\mathbf{x}, t)\right], \tag{4.26}$$

where M is a transformation matrix mapping vector $\tilde{f}$ in velocity space to a vector $\tilde{m}$ in moment space. Here, $\hat{S} = M \cdot S \cdot M^{-1}$ is a collision matrix diagonal in moment space whose eigenvalues are the inverse of the relaxation times which lie between 0 to 2. Hence, $\tilde{m} = M\tilde{f}$ and $\tilde{f} = M^{-1}\tilde{m}$. The size of the vector $\tilde{m}$ is dictated by the number of moments corresponding to the discrete velocity model in consideration.

The streaming takes place in the velocity space, and the collision is executed in moment space by mapping the populations onto it. The eigenvalues of $\hat{S}$ are such that non-conserved moments relax faster than the conserved ones. For a comprehensive review of the MRT based collision models the reader is directed to Coreixas *et al.* (2019). Due to the improved numerical stability of these models, they are heavily used in numerical simulations (Aidun & Clausen, 2010). The improved numerical stability is due to the choice of the relaxation time of each non-conserved moment. One of the drawbacks of these models is that for 3 dimensions or higher-order lattices the number of relaxation parameters that need to be fine-tuned becomes large and thus the computational efficiency is affected (Coreixas *et al.*, 2019).

4.3.3 Karlin-Bösch-Chikatamarla (KBC) collision

This model, popularly known as the KBC model, exploits the Gibb's principle which states that optimal (equilibrium) states are points of entropy maximum under relevant constraints. Here, the equilibrium state is constructed by maximizing the entropy under the constraints of over-relaxation of hydrodynamic stresses. Therefore, constructing the equilibrium state does not require any tunable parameter setting (Karlin *et al.*, 2014). The kinetic equation is remodeled as

$$f_i\left(\mathbf{x} + \mathbf{c_i}, t + 1\right) = (1 - \beta)\, f_i\left(\mathbf{x}, t\right) + \beta f_i^{\mathrm{mirror}}\left(\mathbf{x}, t\right), \tag{4.27}$$

where the mirror state is written as a linear combination of kinematic part (k_i), shear part (s_i) and the remaining higher order moments (h_i). The mirror state is

$$f_i^{\mathrm{mirror}} = k_i + \left(2s_i^{\mathrm{eq}} - s_i\right) + \left[(1-\gamma)\, h_i + \gamma h_i^{\mathrm{eq}}\right], \tag{4.28}$$

where the relaxation parameter γ is computed by maximizing the entropy in the post collision state as the root of

$$\sum_i \Delta h_i \ln\left[1 + \frac{(1-\beta\gamma)\,\Delta h_i - (2\beta-1)\,\Delta s_i}{f_i^{\mathrm{eq}}}\right] = 0, \tag{4.29}$$

with $\Delta h_i = h_i - h_i^{\mathrm{eq}}$ and $\Delta s_i = s_i - s_i^{\mathrm{eq}}$. This model shows remarkable improvement in the stability behavior and thus in recent years is increasingly being used for turbulence simulations (Frapolli *et al.*, 2018)

4.4 Crystallographic lattice Boltzmann model

Historically, the lattice chosen for the LBM has been the simple cubic (SC) lattice which demands that the grid is refined near the solid body or in zones of extreme flow variations (Filippova & Hänel, 1998; Succi *et al.*, 2002*a*). It was recently shown that the optimal discretization of position space for the LBM is a body centered cubic (BCC) arrangement of grid points, which led to a new class of models called crystallographic LBM (Namburi *et al.*, 2016). Figures 4.3 and 4.4 depict the building blocks and the links of a BCC lattice in two and three dimensions respectively. It comprises of two simple cubic (SC) lattices displaced by a distance of $0.5\Delta x$ in each direction. The two grids are connected via discrete velocities as shown in the figures.

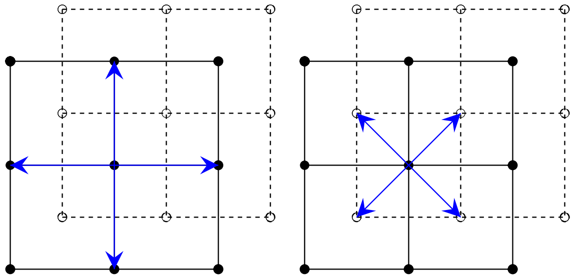

Figure 4.3: Building block of a crystallographic lattice in two dimensions, simple cubic links (left) and body-centered links (right) are depicted here.

Another well known fact in the computer graphics literature is that the volume representation (or rendering) is better on the BCC lattice (Entezari *et al.*, 2009). As the BCC grid is more points at the boundaries, it was also found to represent the boundaries well. To illustrate the difference between SC and BCC lattices, Table 4.2 depicts various rendered images on them. Like the traditional SC grids, the BCC grid also preserves the ease of streaming along the links while increasing the local accuracy. A comment about parallelization of BCC grid is in order: while parallelizing a BCC grid, we need to communicate outgoing populations of two layers (in the SC grid outgoing populations from only one layer are communicated). This is illustrated in the Figure 4.5, where the black lines (solid and dashed) represent the computational grid and the red lines represent the dummy grid. Before implementing the advection routine, the outgoing populations from the computational grid of the Processor A are copied to the dummy grid of Processor B and vice versa. We then implement the advection routine as usual.

The number of grid points for which data needs to be communicated (at every face) for parallelization on a BCC grid of size $2N^3$ is at least $2N^2$. On the other hand, for a standard

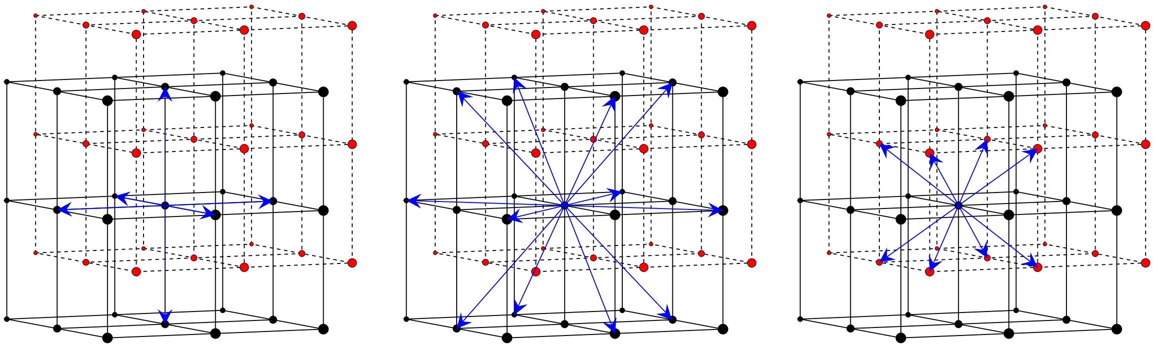

Figure 4.4: Building block of a crystallographic grid in three dimensions, simple cubic links (left), face-centered cubic link (middle) and body-centered links (right). The dashed grid is offset by a distance $0.5\Delta x$ in each direction.

Lattice	Sphere	Ellipsoid	RBC
SC	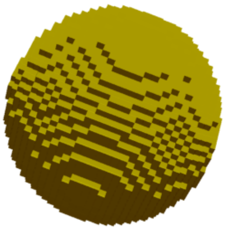	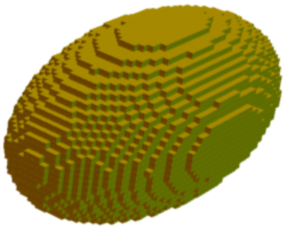	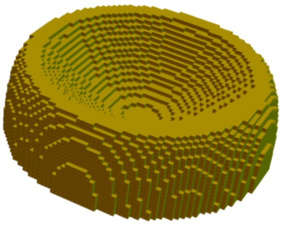
BCC	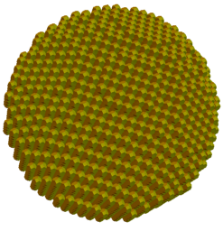	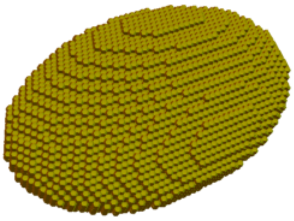	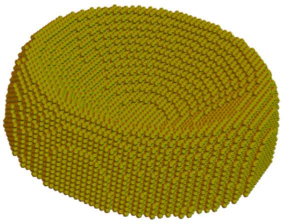

Table 4.2: Representation of a sphere, an ellipsoid, and cut-section of a red blood cell (RBC) on a SC and BCC lattice at the same resolution. It is seen that the BCC lattice used by crystallographic LBM represents local curvatures in a more efficient manner as compared to the SC lattice used by the conventional LBM.

simple cubic grid of size $(2^{1/3}N)^3$ the number of grid points for which data needs to be communicated is $(2^{1/3}N)^2$. Thus, there is $\sim 26\%$ increase in data traffic for the BCC method as compared to the SC based method. This cannot lead to any noticable performance change in communication speed as typical data size for communication in LBM is in the range of ~ 20 MB even for problem size as large as 256^3 per node while a modern communication network (InfiniBand) is capable of transfering more than a GB per cycle. Thus, similar to the standard LBM cost of communication is negligible even for BCC based LBM.

Additionally, the the artificial closure on the third order moment of single speed models $(D3Q19, D3Q27)$, i.e.,

$$\left\langle f, c_\alpha^3 \right\rangle = c^2 \left\langle f, c_\alpha \right\rangle , \tag{4.30}$$

is avoided due to the crystallographic nature of the lattice. This effect plays an important role for nonvanishing Knudsen numbers where capturing the Knudsen boundary layer is necessary (Ansumali *et al.*, 2007*b*). Here, due to rarefaction effects a slip velocity develops in the regions near the wall and hence a deviation from the Navier-Stokes solution is witnessed.

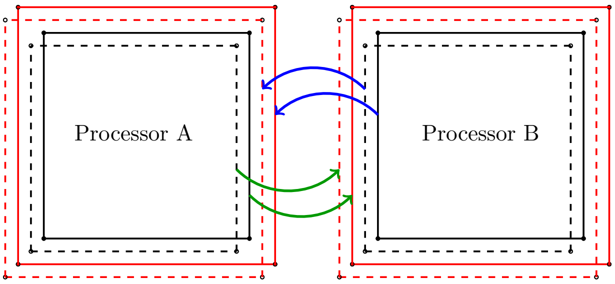
Processor A
Processor B

Figure 4.5: Communication between two processors on a crystallographic grid.

Chapter 5

Discrete Time $\mathcal{H}$ theorem: Some Sharp Inequalities

The discrete time $\mathcal{H}$ theorem for the lattice Boltzmann model requires bounds on the $\mathcal{H}$ function. This requires approximation of $\log(1+y)$ for $y \in (-1, \infty)$ via sharp inequalities. Indeed, in statistical physics and information theory, logarithm is one of the recurring elementary functions to represent entropy. Boltzmann and Gibbs entropy are perhaps the two most widely used example. Other representative examples are the Fermi-Dirac, the Bose-Einstien, the Tsallis, and the Burg form of the entropy (Burg, 1967; Tsallis, 1988; Wehrl, 1978). Another example of such a function is the so called offset logarithmic integral $\text{Li}(y)$ defined as

$$\text{Li}(y) = \int_2^y \frac{1}{\log z} dz. \tag{5.1}$$

This function often appears in number theory (Abramowitz & Stegun, 1965). Similar integrals are found in applications of exponential integrals related to quantum field theory, Gibbs phenomena, and solutions of Laplace equations in semiconductor physics [see (Hörmander, 1971; Zee, 2010; Sofo, 2016) and references therein]. Another interesting example from financial mathematics is 'The Rule of 72'. It is an approximation to the time required for an investment to grow by a factor of n, compounded at an interest rate of $r\%$ per period (Meadows, 2008). The exact time required is

$$T = \frac{\ln n}{\ln(1 + r/100)}, \tag{5.2}$$

which for $n = 2$ is $T \approx 72/r$. These approximations can be made more accurate if the the bounds on such functions are known in polynomial and rational form.

In this chapter, we investigate the various polynomial and rational function based inequalities for a class of such functions. The methodology used for obtaining such bound is to rely on the fact that for the integrals where integrand has certain geometric feature such as convexity, one can find bounded approximation in a systematic fashion. The key idea is to contrast the area under a special class of functions such as convex functions with its approximations in terms of polynomials or rational functions. The motivation for the same is due to a less discussed aspect of the Hermite-Hadamard inequality for convex functions $F(z)$ i.e.,

$$\int_a^b F(z) dz \leq \frac{b-a}{2} \left[F(a) + F(b) \right]. \tag{5.3}$$

The above inequality has a simple geometric interpretation that the trapezoid approximation for the integral is always an over-estimation due to the fact that for convex function [see Figure 5.1]. Here, we remind that the trapezoid rule is a basic technique for evaluating a definite integral by approximating the area under the curve as a trapezium and calculating its area. The inequality follows from the basic definition of a convex function that each point on the chord joining any two points $(a, F(a)), (b, F(b))$ on convex function $F(z)$ lies above the function, i.e.,

$$\lambda F(a) + (1 - \lambda) F(b) \geq F(\lambda a + (1 - \lambda) b). \tag{5.4}$$

This is also known as Jensen's inequality and is depicted in Figure 5.1 (area of the trapezoid is $(b-a)[F(a) + F(b)]/2$). It is evident from the figure that inequality follows from the convexity of integrand.

Here, we review the generalization of this law and their applications in mathematical physics. While many of these generalization are increasingly better understood in mathematical literature (Bessenyei, 2008; Franjić & Pečarić, 2011; Franjic & Pecaric, 2012), applications of these generalizations are mostly not there. In subsequent sections, we illustrate how several important functions such as $\log(1+y)$ or offset logarithmic integral $\mathrm{Li}(y)$ can be approximated in a systematic fashion using their integral representation. To do so, we often resort to convexity of the integrand. We illustrate that approximating the integral via quadrature provides a systematic procedure to obtain upper and lower bound for a class of function. Final result shows that at least for the logarithm, Padé approximation has an alternate interpretation.

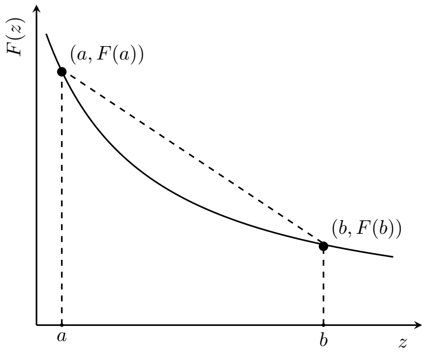

Figure 5.1: All the points on the chord joining any two points $(a, F(a)), (b, F(b))$ on convex function $F(z)$ lie above the function.

In what follows, we begin with the integral definition of $\log(1+y)$, i.e.,

$$\log(1+y) = \int_0^y \frac{1}{1+z} dz, \tag{5.5}$$

where the integrand is an $2n$-convex function, i.e., its even $(2n)$ derivatives are positive. An additional feature of the above integrand is that its odd $(2n+1)$ derivatives are negative. Indeed, we deal with generic integral of the form

$$f(y) = \int_a^y F(z) dz, \tag{5.6}$$

where the integrand is an $2n$-convex function. As stated earlier, such functions often appear in scientific applications.

This chapter is organized as follows: in Section 5.1, we review some of the commonly discussed bounds for logarithm. In Section 5.2, we give the proof of the classical Hermite-Hadamard inequality using convexity arguments. In Section 5.3, using the bounds on $\log(1+y)$ we propose an extension of the Hermite-Hadamard inequality. Along with each bound we also remark on the error associated with it and the domain of its validity. Finally, in Section 5.4 we list some positive definite functions that are used in the context of the discrete time $\mathcal{H}$ theorem.

5.1 Bounds on the logarithm

In this section, we briefly review commonly discussed bounds for logarithm, and get a first idea about them by evaluating their errors at $y = -0.5, -0.25, 0.25, 0.5$. These values of y are a reasonable representation of the nondimensional departure of the populations from the equilibirum. To begin with we remind that one of the elementary bounds on the log is (Love,

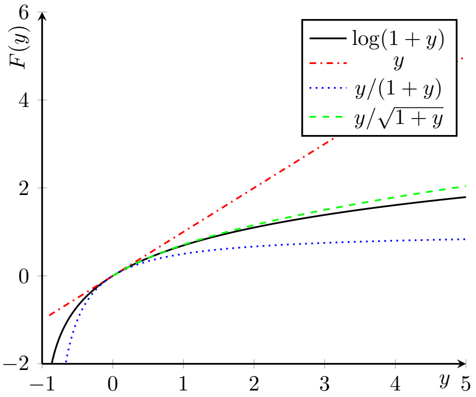

Figure 5.2: Known upper and lower bounds on $\log(1+y)$.

1980)

$$\frac{y}{1+y} \leq \log(1+y) \leq y, \quad y > -1, \tag{5.7}$$

which implies that the upper bound on $\log(1+y)$ is provided by $F(y) = y$ line (Figure 5.2). However, this bound is too weak to be useful as an approximation as the errors at $y = -0.5, -0.25, 0.25, 0.5$ are $45\%, 15\%, -10\%, -18\%$ for the left inequality and for $-28\%, -13\%, 12\%, 23\%$ the right inequality respectively. Indeed, we do know a better bound (Topse, 2007)

$$\frac{2y}{2+y} \leq \log(1+y) \leq \frac{y(2+y)}{2(1+y)}, \quad y > 0\,\{\text{reverse for} -1 < y < 0\}. \tag{5.8}$$

This is a better approximation as at $y = -0.5, -0.25, 0.25, 0.5$ the errors are approximately $-3.9\%, -0.68\%, -0.4\%, -1.3\%$ for the left inequality and $8.2\%, 1.3\%, 0.8\%, 2.7\%$ for the right inequality respectively. Finally, we also have much stricter upper bound in terms of the sqrt function as

$$\log(1+y) \leq \frac{y}{\sqrt{1+y}}, \quad y > 0, \tag{5.9}$$

which gives only $2\%, 0.3\%, 0.20\%, 0.68\%$ error at $y = -0.5, -0.25, 0.25, 0.5$ respectively. Finally, it should be mentioned that if we restrict our attention to a subset of real line, we do know better approximation. For example in range of $y \in (0, 0.45)$, we have (Kozma, 2018)

$$\log(1+y) \geq y - \frac{y^2}{2} + \frac{y^3}{4}, \quad 0 \leq y \leq\sim 0.45, \text{reverse elsewhere}, \tag{5.10}$$

which gives an error of $-5.3\%, -0.87\%, -0.2\%, 0.2\%$ at $y = -0.5, -0.25, 0.25, 0.5$ respectively.

One can also write the Taylor series of $\log(1+y)$ as

$$\log(1+y) = \sum_{k=1}^{\infty} (-1)^{k+1} \frac{y^k}{k} \equiv y - \frac{y^2}{2} + \frac{y^3}{3} - \frac{y^4}{4} + \cdots. \tag{5.11}$$

We highlight that in the domain $y \in (-1, 0)$ each term of the above series is negative definite. In this domain, $\log(1+y)$ is itself negative and is summation of an infinite number of negative terms. Therefore, any finite truncation of the series is always larger than $\log(1+y)$, i.e.,

$$\log(1+y) < \sum_{k=1}^{N} (-1)^{k+1} \frac{y^k}{k}. \tag{5.12}$$

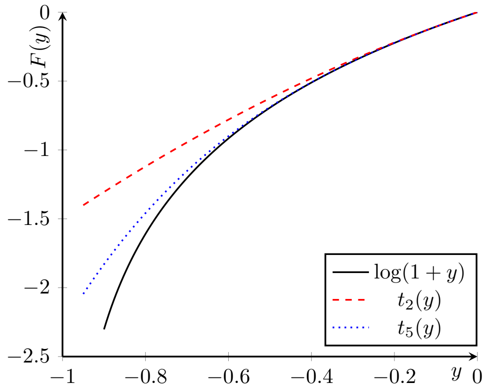

Figure 5.3: Plots of $\log(1+y)$ and its Taylor series expansion truncated at $N = 2, 5$.

y	$\log(1+y)$	$t_2(y)$	% Error in $t_2(y)$	$t_5(y)$	% Error in $t_5(y)$
-0.9	-2.30259	-1.3050	-43.32	-1.8301	-20.51
-0.5	-0.69315	-0.6250	-9.831	-0.6885	-0.6644
-0.1	-0.10536	-0.1050	-0.3421	-0.1054	-0.0002
-0.01	-0.01005	-0.0100	-0.0033	-0.01005	0.0000

Table 5.1: The functions $\log(1+y), t_5(y), t_2(y)$ and their associated errors.

The above inequality provides an upper bound on $\log(1+y)$ for $y \in (-1, 0)$. For illustration, we consider two truncations of the above series $t_2(y)$ and $t_5(y)$ truncated at $N = 2$ and $N = 5$ respectively, where

$$t_2(y) = y - \frac{y^2}{2}, \tag{5.13}$$

$$t_5(y) = y - \frac{y^2}{2} + \frac{y^3}{3} - \frac{y^4}{4} + \frac{y^5}{5}. \tag{5.14}$$

Figure 5.3 shows the graph of $\log(1+y), t_2(y), t_5(y)$ in the domain $y \in (-1, 0)$. The values of functions $\log(1+y), t_5(y), t_2(y)$ and their associated errors for a few representative y are tabulated in Table 5.1. It is seen that $t_5(y)$ has smaller error as compared to $t_2(y)$ and is hence a tighter bound on $\log(1+y)$. This methodology can be extended to construct even tighter bounds on $\log(1+y)$ by considering more terms in Eq.(5.12).

5.2 The Hermite-Hadamard inequality

The Hermite-Hadamard inequality plays an important role in the theory of convex functions and its applications to other fields. This inequality states that for any convex function $F(z)$

$$F\left(\frac{a+b}{2}\right) \leq \frac{1}{b-a}\int_a^b F(z)dz \leq \frac{1}{2}\left[F(a) + F(b)\right]. \tag{5.15}$$

As discussed in the introduction, the right hand side of the inequality follows from convexity of the integrand and trapezoid approximation of the integral. To prove the left inequality we rewrite the integral as

$$\frac{1}{b-a}\int_a^b F(z)dz = \frac{1}{b-a}\int_a^{(a+b)/2} F(z)dz + \frac{1}{b-a}\int_{(a+b)/2}^b F(z)dz, \tag{5.16}$$

and introduce a parametric representation via the transformation (Niculescu & Persson, 2007)

$$z(s) = \begin{cases} \frac{a+b}{2} - s\frac{b-a}{2} & a \leq z \leq \frac{a+b}{2} \\ \frac{a+b}{2} + s\frac{b-a}{2} & \frac{a+b}{2} \leq z \leq b \end{cases} \tag{5.17}$$

With these transformations, the integral in Eq.(5.16) is re-written as

$$\frac{1}{b-a}\int_a^b F(z)dz = \int_0^1 \frac{1}{2}\left[F\left(A\right) + F\left(B\right)\right]ds, \tag{5.18}$$

where

$$A = \frac{(a+b) - s(b-a)}{2}, \; B = \frac{(a+b) + s(b-a)}{2}.$$

Also, from the Jensens inequality [Eq.(5.4)] for $\lambda = 1/2$ one obtains

$$F\left(\frac{A+B}{2}\right) \leq \frac{1}{2}[F(A) + F(B)]. \tag{5.19}$$

Integrating the above equation for $s = 0$ to $s = 1$, we have

$$\int_0^1 F\left(\frac{A+B}{2}\right) ds \leq \int_0^1 \frac{1}{2}\left[F\left(A\right) + F\left(B\right)\right]ds. \tag{5.20}$$

Recognizing that the right hand side of Eq.(5.18) is the same as right hand side of Eq.(5.20), one obtains

$$\int_0^1 F\left(\frac{A+B}{2}\right) ds \leq \frac{1}{b-a}\int_a^b F(z)dz, \tag{5.21}$$

where substituting A and B gives

$$F\left(\frac{a+b}{2}\right) \leq \frac{1}{b-a}\int_a^b F(z)dz. \tag{5.22}$$

Therefore, using only the convexity arguments we have shown that the Hermite-Hadamard inequality provides both upper and lower bounds on any convex function. The upper bound is just the integral approximated via the trapezoid rule and the lower bound is the integral approximated as the value of the function at the midpoint.

Finally, when we apply Eq.(5.15) on Eq.(5.5), we get

$$\frac{2y}{2+y} \leq \log\left(1+y\right) \leq \frac{y(2+y)}{2(1+y)}. \tag{5.23}$$

Similarly, from Eq.(5.15), for $F(z) = \log z, a = 1, b = y$, we have

$$\log\frac{1+y}{2} \leq \frac{y}{y-1}\log y - 1 \leq \log\sqrt{y}, \tag{5.24}$$

and for $F(z) = 1/\log z, a = 2, b = y$, we have

$$\log\frac{2}{y+2} \leq \frac{\mathrm{Li}(y)}{y-2} \leq \frac{\log\sqrt{2y}}{(\log 2)(\log y)}. \tag{5.25}$$

This provides the motivation that quadrature rules can be exploited to construct bounds on integral of convex functions.

5.3 Extended Hermite-Hadamard inequality

In the previous section, we demonstrated that the Hermite-Hadamard inequality provides useful upper and bounds for convex functions. We also highlighted that the upper bounds given by the Hermite-Hadamard inequality is the approximation from the trapezoid rule, which is the lowest order member of the Newton-Cotes quadrature family. Similarly, the lower bound provided by the Hermite-Hadamard inequality is the approximation of the function as the value at the midpoint, which is the lowest order member of the Gauss-Lengendre quadrature family. In this section, we show that the Hermite-Hadamard inequality can be extended for positive $2n$-convex functions by exploiting the sharper bounds from higher order quadratures.

5.3.1 Newton-Cotes quadratures

The general expression for the Newton-Cotes quadrature is written as

$$\int_{y_0}^{y_1} F(z)dz = \mathcal{I}_{\text{NC}}^{(n)} + R_{\text{NC}}^{(n)}, \tag{5.26}$$

where $\mathcal{I}_{\text{NC}}^{(n)}$ is the approximation and $R_{\text{NC}}^{(n)}$ is the residue for n^{th} order quadrature. Here, in order to integrate a function over an interval $[a, b]$, the interval is divided into n equal parts of length $(b-a)/n$. We then find the fitting polynomial and integrate it over the interval to approximate the area under the curve. The trapezoid rule ($n = 1$), 1/3 Simpson's rule ($n = 2$), and Boole's rule ($n = 4$) fall under this category (Abramowitz & Stegun, 1965).

In what follows, we show that the residues associated with all these quadratures are negative, therefore the approximations obtained provide upper bounds on the integral of the $2n$-convex function. We also observe that among these three quadrature rules, the higher order quadrature provides sharper bounds on the integral. We begin by briefly reviewing the algebraic formulae of the trapezoid, 1/3 Simpson's, and Boole's rule.

- **Trapezoid rule**: The trapezoid rule for evaluating the integral is depicted in Figure 5.4(a) and is given by (Abramowitz & Stegun, 1965)

  $$\int_{y_0}^{y_0+H} F(z)dz = I_{\text{NC}}^{(1)} - \frac{H^3}{12}F^{(2)}(\xi), \quad (y_0 < \xi < y_0 + H), \tag{5.27}$$

  where

  $$I_{\text{NC}}^{(1)} = \frac{H}{2}\left[F(y_0) + F(y_0 + H)\right].$$

- **1/3 Simpson's rule**: Here, the interval is divided into two equal parts and the area is approximated as the integral of a quadratic polynomial. It is given by

  $$\int_{y_0}^{y_0+H} F(z)dz = I_{\text{NC}}^{(2)} - \frac{H^5}{90\cdot 2^5}F^{(4)}(\xi), \quad (y_0 < \xi < y_0 + H), \tag{5.28}$$

  where

  $$I_{\text{NC}}^{(2)} = \frac{H}{6}\left[F(y_0) + 4F\left(y_0 + \frac{H}{2}\right) + F(y_0 + H)\right].$$

  Figure 5.4(b) depicts the 1/3 Simpson's rule.

- **Boole's rule**: Here, the interval is divided into four equal parts and the area is approxi-

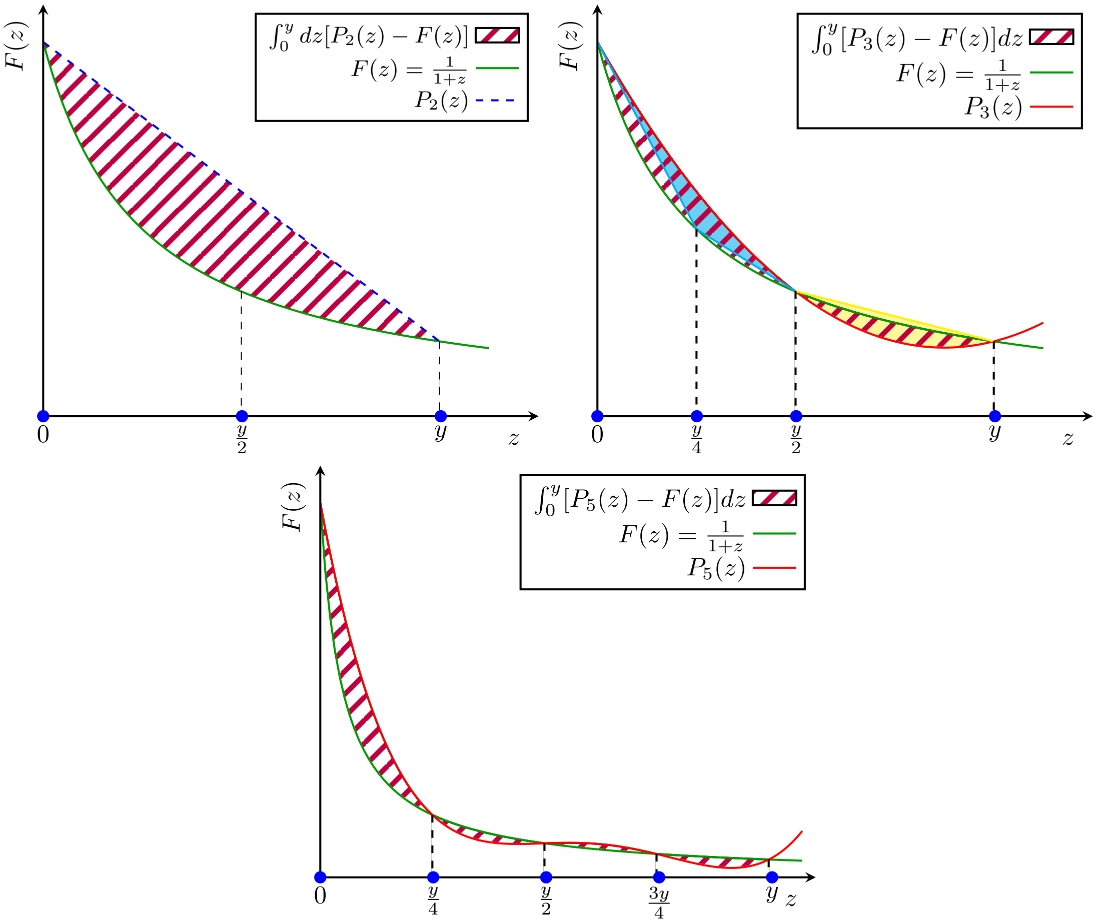

Figure 5.4: Residue (hatched area) from Newton-Cotes quadratures is negative and progressively decreases in magnitude with increase in the order of quadrature. Here, we show the Trapezoid rule (top left), $\frac{1}{3}$Simpson's Rule (top right), Boole rule (bottom), and P_m are interpolating polynomials with m points.

mated by integral of a quintic polynomial. It is given by

$$\int_{y_0}^{y_0+H} F(z)dz = I_{\text{NC}}^{(4)} - \frac{8H^7}{945 \cdot 4^7} F^{(6)}(\xi), \quad (y_0 < \xi < y_0 + H), \tag{5.29}$$

where

$$I_{\text{NC}}^{(4)} = \frac{H}{90}\left[7F(y_0) + 32F\left(y_0 + \frac{H}{4}\right) + 12F\left(y_0 + \frac{H}{2}\right) + 32F\left(y_0 + \frac{3H}{4}\right) + 7F(y_0 + H)\right].$$

Figure 5.4(c) depicts the Boole's rule.

As $F(z)$ is a $2n$-convex function, its even derivatives $F^{(2n)}(\xi)$ are positive, hence, the residues associated with all above quadratures are negative. Therefore, all the three approximations over-estimate the integral and provide upper bounds to it, i.e.,

$$\int_{y_0}^{y_0+H} F(z)dz \leq I_{\text{NC}}^{(1)}, \quad \int_{y_0}^{y_0+H} F(z)dz \leq I_{\text{NC}}^{(2)}, \quad \int_{y_0}^{y_0+H} F(z)dz \leq I_{\text{NC}}^{(4)}. \tag{5.30}$$

Evaluating the integral in Eq.(5.6) for $F(z) = 1/(1+z)$ via the above three quadratures, one obtains (Khattri, 2009)

$$\begin{aligned} \mathcal{I}_{\text{NC}}^{(1)}(y) &= \frac{y}{2}\left[1 + \frac{1}{1+y}\right], \\ \mathcal{I}_{\text{NC}}^{(2)}(y) &= \frac{y}{6}\left[1 + \frac{8}{2+y} + \frac{1}{1+y}\right], \\ \mathcal{I}_{\text{NC}}^{(4)}(y) &= \frac{y}{90}\left[7 + \frac{128}{4+y} + \frac{48}{4+2y} + \frac{128}{4+3y} + \frac{7}{1+y}\right]. \end{aligned} \tag{5.31}$$

The percentage error associated with each expression is tabulated in Table 5.2. Figure 5.5 shows the plot of $\log(1+y)$ and the expressions in Eq.(5.31). It is observed that the residues are negative and their magnitude progressively decreases with increase in order of quadrature, i.e., in other words higher order quadratures provide sharper bounds. Therefore,

$$\log(1+y) \leq \mathcal{I}_{\text{NC}}^{(4)}(y) \leq \mathcal{I}_{\text{NC}}^{(2)}(y) \leq \mathcal{I}_{\text{NC}}^{(1)}(y). \tag{5.32}$$

If required even tighter bounds can be constructed by considering even higher order quadratures.

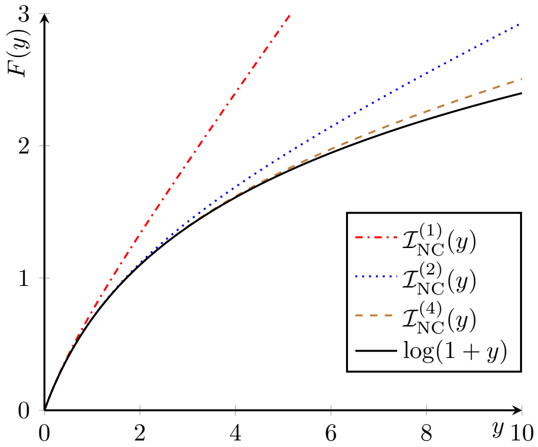

Figure 5.5: $\log(1+y)$ compared with its bounds from Newton-Cotes quadrature.

y	$\log(1+y)$	$\mathcal{I}_{\rm NC}^{(4)}$	$\mathcal{I}_{\rm NC}^{(2)}$	$\mathcal{I}_{\rm NC}^{(1)}$	$\%\Delta\mathcal{I}_{\rm NC}^{(4)}$	$\%\Delta\mathcal{I}_{\rm NC}^{(2)}$	$\%\Delta\mathcal{I}_{\rm NC}^{(1)}$
0.01	0.009950	0.009950	0.0099503	0.0099505	0.00	0.00	0.00165
0.1	0.095310	0.095310	0.0953102	0.0954545	0.00	0.00	0.15146
1.0	0.693147	0.693147	0.6944444	0.75	0.0039	0.1871	8.2021
10.0	2.397895	2.504881	2.9292929	5.454545	4.4616	22.1610	127.47

Table 5.2: $\log(1+y)$ and $\mathcal{I}_{\rm NC}^{(n)}$ and their associated errors. $\%\Delta\mathcal{I}_{\rm NC}^{(n)} = (\mathcal{I}_{\rm NC}^{(n)}/\log(1+y)-1)\times 100$

y	$\log(1+y)$	$\mathcal{I}_{\rm GL}^{(3)}$	$\mathcal{I}_{\rm GL}^{(2)}$	$\mathcal{I}_{\rm GL}^{(1)}$	$\%\Delta\mathcal{I}_{\rm GL}^{(3)}$	$\%\Delta\mathcal{I}_{\rm GL}^{(2)}$	$\%\Delta\mathcal{I}_{\rm GL}^{(1)}$
0.01	0.0099503	0.0099503	0.0099503	0.0099502	0.00	0.00	-0.00083
0.1	0.0953102	0.0953102	0.0953101	0.0952381	0.00	-0.00004	-0.07563
1.0	0.6931471	0.6931471	0.6923077	0.6666667	-0.0036	-0.12111	-3.8203
10.0	2.3978953	2.3978952	2.1686747	1.6666667	-2.9131	-9.55924	-30.4946

Table 5.3: $\log(1+y)$ and $\mathcal{I}_{\rm GL}^{(n)}$ and their associated errors. $\%\Delta\mathcal{I}_{\rm GL}^{(n)} = (\mathcal{I}_{\rm GL}^{(n)}/\log(1+y)-1)\times 100$

5.3.2 Gauss-Legendre quadrature

In this section, we evaluate the integral in Eq.(5.6) via Gauss-Legendre quadrature and show that the residue associated with each approximation in positive and hence the approximations provide lower bounds on $\log(1+y)$ in $y \in [0,\infty)$.

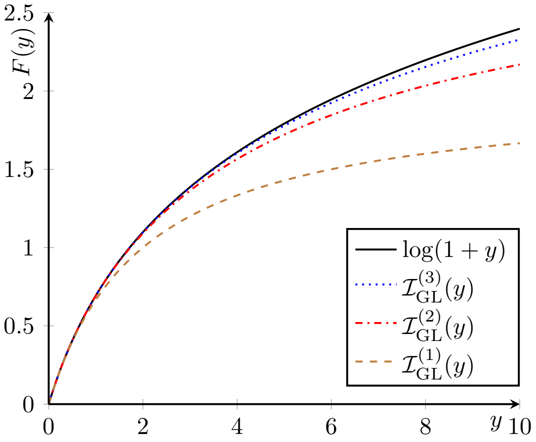

Figure 5.6: $\log(1+y)$ compared with its bounds from Gauss-Legendre quadrature.

Approximating the integral in Eq.(5.6) via n point Gauss-Legendre quadrature one obtains (Abramowitz & Stegun, 1965),

$$\int_{y_0}^{y_0+H} F(z)dz = \mathcal{I}_{\rm GL}^{(n)}(y) + \frac{H^{2n+1}(n!)^4}{(2n+1)[(2n)!]^3}F^{(2n)}(\xi), \tag{5.33}$$

where

$$\mathcal{I}_{\rm GL}^{(n)}(y) = \frac{H}{2}\sum_{i=1}^{n} w_i F(y_i).$$

Here w_i, y_i are weights and abscissas, ξ is a point inside the domain and $F^{(2n)}$ is even derivative of an $2n$-convex function. We begin by reviewing the algebraic forms of the first few members of the Gauss-Legendre quadratures:

- **One point** ($n = 1$): The one point Gauss-Legendre quadrature for evaluating an intergral from y_0 to y_0+H is

$$\int_{y_0}^{y_0+H} F(z)dz = \mathcal{I}_{\rm GL}^{(n)}(y) + \frac{H^3}{24}F^{(2)}(\xi), \tag{5.34}$$

where

$$\mathcal{I}_{\rm GL}^{(1)}(y) = \frac{H}{2}w_0 F\left(y_0+\frac{H}{2}\right), \quad w_0 = 2.$$

- **Two point** $(n=2)$: The two point Gauss-Legendre quadrature is

$$\int_{y_0}^{y_0+H} F(z)dz = \mathcal{I}_{\rm GL}^{(2)}(y) + \frac{H^5}{6912}F^{(4)}(\xi), \tag{5.35}$$

where

$$\mathcal{I}_{\rm GL}^{(2)}(y) = \frac{H}{2}\left[w_1 F\left(y_0+\frac{H}{2}+\frac{H}{2\sqrt{3}}\right) + w_2 F\left(y_0+\frac{H}{2}-\frac{H}{2\sqrt{3}}\right)\right], \quad w_1 = w_2 = 1.$$

- **Three point** $(n=3)$: The three point Gauss-Legendre quadrature is

$$\int_{y_0}^{y_0+H} F(z)dz = \mathcal{I}_{\rm GL}^{(3)}(y) + \frac{H^7}{2016000}F^{(6)}(\xi), \tag{5.36}$$

where

$$\mathcal{I}_{\rm GL}^{(3)}(y) = \frac{H}{2}\left[w_0 F\left(y_0+\frac{H}{2}\right) + w_1 F\left(y_0+\frac{H}{2}+\frac{H}{2}\sqrt{\frac{3}{5}}\right) + w_2 F\left(y_0+\frac{H}{2}-\frac{H}{2}\sqrt{\frac{3}{5}}\right)\right],$$
$$w_0 = \frac{8}{9}, w_1 = w_2 = \frac{5}{9}. \tag{5.37}$$

As $F(z)$ is a $2n$-convex function, its even derivatives $F^{(2n)}(\xi)$ are positive, hence, the residues associated with all above quadratures are also positive. Therefore, all the three approximations under-estimate the integral and provide lower bounds to it, i.e.,

$$\int_{y_0}^{y_0+H} F(z)dz \geq I_{\rm GL}^{(1)}, \quad \int_{y_0}^{y_0+H} F(z)dz \geq I_{\rm GL}^{(2)}, \quad \int_{y_0}^{y_0+H} F(z)dz \geq I_{\rm GL}^{(4)}. \tag{5.38}$$

Evaluating the integral in Eq.(5.6) for $F(z) = 1/(1+z)$ via the above three quadratures, one obtains

$$\mathcal{I}_{\rm GL}^{(1)}(y) = \frac{2y}{(2+y)},$$
$$\mathcal{I}_{\rm GL}^{(2)}(y) = \frac{6y+3y^2}{6+6y+y^2},$$
$$\mathcal{I}_{\rm GL}^{(3)}(y) = \frac{60y+60y^2+11y^3}{60+90y+36y^2+3y^3}.$$

Figure 5.6 depicts the various approximations $\mathcal{I}_{\rm NC}^{(n)}$ from n point Gauss-Legendre quadrature compared with $\log(1+y)$, and the percentage error associated with each expression is tabulated in Table 5.3. It is seen that the higher order quadratures provide sharper lower bounds, i.e.,

$$\mathcal{I}_{\rm GL}^{(1)}(y) \leq \mathcal{I}_{\rm GL}^{(2)}(y) \leq \mathcal{I}_{\rm GL}^{(3)}(y) \leq \log(1+y), \quad y > 0. \tag{5.39}$$

However, in the interval $y \in (-1, 0)$ the bounds from Gauss-Legendre quadrature show opposite behaviour, i.e.,

$$\log(1+y) \leq \mathcal{I}_{\mathrm{GL}}^{(3)}(y) \leq \mathcal{I}_{\mathrm{GL}}^{(2)}(y) \leq \mathcal{I}_{\mathrm{GL}}^{(1)}(y), \quad -1 < y < 0. \tag{5.40}$$

5.4 A few positive definite functions

In this section, we list a few positive definite functions and their domain of validity that are obtained by using the bounds on $\log(1+y)$ proposed in the previous sections. In the interval $y \in (-1, 0)$, using Eq.(5.12) we define

$$G_1(y) = (1+y)\left[-\log(1+y) + y - \frac{y^2}{2}\right] > 0, \tag{5.41}$$

$$G_6(y) = (1+y)\left[-\log(1+y) + y - \frac{y^2}{2} + \frac{y^3}{3} - \frac{y^4}{4} + \frac{y^5}{5}\right] > 0. \tag{5.42}$$

In the interval $y \in [0, \infty)$, using Eq.(5.32) we define

$$G_2(y) = (1+y)\left[-\log(1+y) + \mathcal{I}_{\mathrm{NC}}^{(1)}\right] \geq 0, \tag{5.43}$$

$$G_7(y) = (1+y)\left[-\log(1+y) + \mathcal{I}_{\mathrm{NC}}^{(3)}\right] \geq 0, \tag{5.44}$$

and in the interval $y \in (-1, \infty)$, using Eq.(5.39) and Eq.(5.40) we define

$$G_3(y) = y\left[\log(1+y) - \mathcal{I}_{\mathrm{GL}}^{(1)}\right] \geq 0, \tag{5.45}$$

$$G_8(y) = y\left[\log(1+y) - \mathcal{I}_{\mathrm{GL}}^{(3)}\right] \geq 0. \tag{5.46}$$

In the subsequent chapters, we will show that these functions play a crucial role in proving the discrete time $\mathcal{H}$ theorem.

Chapter 6

Discrete Time $\mathcal{H}$ theorem: Single relaxation time entropic lattice Boltzmann model

The lattice Boltzmann model (LBM) is an efficient kinetic formulation of nonlinear hydrodynamic phenomena in terms of a discrete set of populations restricted on lattices with appropriate symmetries (Frisch *et al.*, 1986; Chen *et al.*, 1992; Ansumali *et al.*, 2003). The Navier-Stokes dynamics emerges from this kinetic model by an appropriate choice of discrete equilibrium that respects macroscopic constraints (McNamara & Zanetti, 1988; Qian *et al.*, 1992; Benzi *et al.*, 1992). Historically, the approach of choosing the equilibrium from macroscopic dynamics in LBM emerged as a computationally attractive alternative to the Boolean particle dynamics of the lattice gas model (Frisch *et al.*, 1986; McNamara & Zanetti, 1988; Higuera *et al.*, 1989). However, this top-down approach of LBM lost many desirable features of the lattice gas such as the unconditional numerical stability, the $\mathcal{H}$ theorem and consequently the faithful representation of microscopic Boltzmann dynamics (Karlin *et al.*, 1999; Succi *et al.*, 2002*b*). The absence of discrete time $\mathcal{H}$ theorem results in the growth of numerical instabilities in standard LBM. This often makes simulations with low viscosity and/or large spatial gradients for hydrodynamics and large density ratios for multiphase flows unstable (Karlin *et al.*, 1999; Succi *et al.*, 2002*b*; Mazloomi *et al.*, 2015).

The entropic lattice Boltzmann model (ELBM) is an alternate methodology, which restores the $\mathcal{H}$ theorem for discrete space-time evolution (Karlin *et al.*, 1998; Wagner, 1998; Karlin *et al.*, 1999; Chen & Teixeira, 2000; Boghosian *et al.*, 2001; Succi *et al.*, 2002*b*; Ansumali *et al.*, 2003; Boghosian *et al.*, 2003). It was a paradigm shift for computational fluid dynamics where the numerical stability of a hydrodynamic solver was enforced by insisting on adherence to the thermodynamics at the discrete time level (Succi *et al.*, 2002*b*). The ELBM is accepted as a viable tool for simulation of turbulence, multiphase flows, as well as microflows due to its unconditional numerical stability and has shown remarkable improvement over the traditional LBM (Ansumali *et al.*, 2006; Aidun & Clausen, 2010; Chikatamarla & Karlin, 2013*b*; Mazloomi *et al.*, 2015; Atif *et al.*, 2017).

The ELBM requires an additional step known as the entropic involution step. It involves a numerical search for the discrete path length corresponding to jump to a mirror state on the iso-entropic surface. Considerable efforts have been made to ensure the correctness and efficient implementation of this step (Ansumali & Karlin, 2000, 2002*a*; Tosi *et al.*, 2006; Chikatamarla *et al.*, 2006; Brownlee *et al.*, 2007; Gorban & Packwood, 2012). However, there is scope for a better theoretical understanding of the ELBM if one is able to obtain a closed form expression for the discrete path length. For example:

- The variable discrete path length could be understood as an implicit modeling of the unresolved scales of the flow via the thermodynamic route, and may provide a new insight into the sub-grid modeling of turbulence.
- It will enhance the efficiency of the ELBM by avoiding a numerical search for the path length.
- It will resolve the ambiguities in the implementation of ELBM. It should be noted that for some rare events, the details of which will be given later, the entropic involution step

has no solution, and hence there is no unique definition of the path length (Gorban & Packwood, 2012).

In this chapter, we reformulate the ELBM and obtain a closed form analytic solution for the discrete path length. The essential idea is to relax the entropy equality condition used in ELBM and replace it with the constraint that entropy must increase within a discrete time step. The simplicity of the exact solution removes the computational overhead and algorithmic complexity associated with ELBM. The proposed methodology is devoid of indeterminacy due to its exact nature. This chapter is organized as follows: In Sec.6.1 we briefly review the entropic lattice Boltzmann model. In Section 6.2 we describe the entropic involution step in its traditional form and derive its near-equilibrium limit. In Section 6.3, we propose a methodology to construct exact solutions for the path length. In Section 6.4, we perform a detailed comparison of the behaviour of the exact solutions, the ELBM and the BGK. In Section 6.5 we present the simulation of a NACA0012 airfoil at Reynolds number 2.88×10^6, and in Section 6.6 we derive the expression for turbulent viscosity corresponding to the analytic solution.

6.1 Entropic lattice Boltzmann model

In this section, we introduce the LBM and its entropic formulation in D dimensions. For completeness, we reiterate some of the definitions made in Chapter 2. As stated earlier, in LBM, one defines a set of discrete velocities $\mathbf{c}_i$, $i = 1, \cdots, N$ such that they form links of a space-filling lattice (Succi, 2001), and at every lattice node $\boldsymbol{x}$ and time t a set of discrete populations $f(\boldsymbol{c}_i, \boldsymbol{x}, t) \equiv f_i$. Here, the set of populations f_i is understood as a vector $\boldsymbol{f} = \{f_1, f_2, \cdots, f_N\}$ in the N dimensional phase space, where N is the number of discrete populations. We define the bilinear action between two functions of discrete velocities ϕ and ψ as

$$\langle \phi, \psi \rangle = \sum_{i=1}^{N} \phi_i \psi_i. \tag{6.1}$$

Analogous to continuous kinetic theory, the hydrodynamic variables such as the mass density ρ, velocity $\mathbf{u}$, and the scaled temperature θ are defined as

$$\rho = \langle f, 1 \rangle, \quad \rho \boldsymbol{u} = \langle f, \boldsymbol{c} \rangle, \quad \rho u^2 + D\rho\theta = \left\langle f, \boldsymbol{c}^2 \right\rangle. \tag{6.2}$$

The evolution of populations for a time step Δt is written as two step process:

1. The discrete free-flight as

$$\boldsymbol{f}(\boldsymbol{x} + \boldsymbol{c}_i \Delta t, t + \Delta t) = \boldsymbol{f}^*(\boldsymbol{x}, t), \tag{6.3}$$

which shifts the populations in position space. Similar to free flight of molecules, this step preserves entropy.

2. The collisional relaxation towards the discrete equilibrium given by

$$\boldsymbol{f}^*(\boldsymbol{x}, t) = \boldsymbol{f}(\boldsymbol{x}, t) + \alpha\beta \left[\boldsymbol{f}^{\mathrm{eq}}(\mathcal{M}^{\mathrm{slow}}(\boldsymbol{x}, t)) - \boldsymbol{f}(\boldsymbol{x}, t)\right], \tag{6.4}$$

often modeled by a single relaxation model of Bhatnagar-Gross-Krook (BGK) (Bhatnagar *et al.*, 1954) with mean free time τ. Here $\mathcal{M}^{\mathrm{slow}}(\boldsymbol{x}, t) = \{\rho(\boldsymbol{x}, t), \boldsymbol{u}(\boldsymbol{x}, t), \theta(\boldsymbol{x}, t)\}$ are the collisional invariants. Often for isothermal LBMs, $\theta(\boldsymbol{x}, t)$ is disregarded from $\mathcal{M}^{\mathrm{slow}}(\boldsymbol{x}, t)$. For the standard LBM, $\alpha = 2$, whereas in the entropic LBM α is treated as a variable and evaluated at each point and time step such that the $\mathcal{H}$ theorem is satisfied. This is discussed in detail in Sections 6.2-6.3. The dimensionless discrete relaxation parameter β,

$$\beta = \frac{\Delta t}{2\tau + \Delta t}, \tag{6.5}$$

is bounded in the interval $0 < \beta < 1$. Notice that $\beta = 1$ implies $\tau = 0$. Since the kinematic viscosity $\nu = \tau\theta$, $\beta = 1$ implies that there is zero dissipation in the system.

It should be noted that the discrete free-flight that denotes the convection process leads to no dissipation (thus no entropy production) (Wagner, 1998). The collisional relaxation, however, has non-zero entropy production due to relaxation of the populations towards the equilibrium values but is entirely a local event.

Historically, the discrete isothermal equilibrium at a reference temperature θ_0 was chosen as (Qian *et al.*, 1992)

$$f_i^{\mathrm{eq}} = w_i\rho\left[1 + \frac{u_\alpha c_\alpha}{\theta_0} + \frac{u_\alpha u_\beta}{2\theta_0^2}\left(c_\alpha c_\beta - \theta_0\delta_{\alpha\beta}\right)\right], \tag{6.6}$$

which was sufficient to recover the Navier-Stokes dynamics upto $\mathcal{O}(u^2)$. However, this polynomial form of discrete equilibrium permits the populations to attain negative values thus making the simulations numerically unstable (Karlin *et al.*, 1999; Succi *et al.*, 2002*b*). A method that resolves the issue of non-positive form of equilibrium distribution is to construct the discrete equilibrium $\boldsymbol{f}^{\mathrm{eq}}$ as the minimizer of the convex function, known as the $\mathcal{H}$ function, under the constraint that the mass density, the momentum density, and the energy density (ignored for isothermal scenarios) are conserved (Karlin *et al.*, 1999; Boghosian *et al.*, 2001). The $\mathcal{H}$ function was taken in Boltzmann form as (Karlin *et al.*, 1999; Ansumali *et al.*, 2003; Ansumali & Karlin, 2005)

$$\mathcal{H}[f] = \sum_{i=1}^{N} f_i \log\frac{f_i}{w_i} = \left\langle f, \log\frac{f}{w}\right\rangle, \tag{6.7}$$

with weights $w_i > 0$. The discrete entropic equilibrium thus obtained is of the form

$$f_i^{\mathrm{eq}} = w_i\rho\exp\left(-\mu - \zeta_\alpha c_{i\alpha} - \gamma c_i^2\right), \tag{6.8}$$

where $\mu, \zeta_\alpha, \gamma$ are the Lagrange multipliers. For the $D1Q3$ model, and its higher dimension extensions $D2Q9, D3Q27$ the discrete isothermal equilibrium in the explicit form is

$$f_i^{\mathrm{eq}}(\rho, u_\alpha, \theta_0) = w_i\rho\prod_{i=1}^{D}(2 - \sqrt{1+\tilde{u}_\alpha^2})\left[\frac{2\tilde{u}_\alpha/\sqrt{3} + \sqrt{1+\tilde{u}_\alpha^2}}{1 - \tilde{u}_\alpha/\sqrt{3}}\right]^{c_{i\alpha}/\sqrt{3\theta_0}} \tag{6.9}$$

where $\tilde{u}_\alpha = u_\alpha/\sqrt{\theta_0}$. However, for most models the Lagrange multipliers cannot be evaluated in explicit form and need to calculated numerically. The series expansion of the entropic equilibrium provided the lattice is sufficiently isotropic was obtained in Chapter 3 as

$$f_i^{\mathrm{eq}} = \tilde{f}_i^{\mathrm{eq}}\left[1 + \frac{u_\alpha c_{i\alpha}}{\theta} - \frac{u^2}{2\theta} + \frac{1}{2}\left(\frac{u_\alpha c_{i\alpha}}{\theta}\right)^2 + \frac{1}{6}\left(\frac{u_\alpha c_{i\alpha}}{\theta}\right)^3 - \frac{u^2 u_\alpha c_{i\alpha}}{2\theta^2}\left(1 - \mathcal{A}\right)\right], \tag{6.10}$$

where $\mathcal{A} = \left\langle \tilde{f}_i^{\mathrm{eq}}, c_{ix}^2 c_{iy}^2 \right\rangle /(3\rho\theta^2) - 1/3$, and

$$\tilde{f}_i^{\mathrm{eq}} = w_i\rho\Bigg[1 + \frac{\eta}{2\theta_0}(\boldsymbol{c}_i^2 - 3\theta_0) + \frac{\eta^2}{8\theta_0^2}\left(\boldsymbol{c}_i^4 - 10\boldsymbol{c}_i^2\theta_0 + 15\theta_0^2\right) + \frac{\eta^3}{48\theta_0^3}\big(\boldsymbol{c}_i^6 - 21\boldsymbol{c}_i^4\theta_0 + 105\boldsymbol{c}_i^2\theta_0^2 \\ - 105\theta_0^3\big) + \frac{\eta^4}{384\theta_0^4}\left(\boldsymbol{c}_i^8 - 36\boldsymbol{c}_i^6\theta_0 + 378\boldsymbol{c}_i^4\theta_0^2 - 1260\boldsymbol{c}_i^2\theta_0^3 + 945\theta_0^4\right) + \mathcal{O}(\eta^5)\Bigg], \tag{6.11}$$

for models that satisfy Eqs.(3.29). Here $\eta = \theta/\theta_0 - 1$, and it can be seen that $\tilde{f}_i^{\mathrm{eq}}(\rho, u_\alpha, \theta = \theta_0) = w_i\rho$ and that Eq.(6.10) is the same as Eq.(6.6) upto $\mathcal{O}(u^2)$.

6.2 The entropic involution

The existence of the entropy function $\mathcal{H}$, accompanied with the entropic equilibrium derived in a variational fashion, provides an opportunity for creating a nonlinearly stable numerical method (Karlin *et al.*, 1999; Succi *et al.*, 2002*b*). As the convection process [Eq.(6.3)] does not lead to entropy production, a nonlinearly stable LBM can be achieved by making the collisional relaxation to equilibrium [Eq.(6.4)] adhere to the $\mathcal{H}$ theorem, or in other words, by ensuring that the entropy production during the collision is non-positive.

The collision step given by Eq.(6.4) is understood in geometric terms as follows: in an N dimensional phase space, starting from the pre-collisional state $\boldsymbol{f}$ one covers a path length of $\alpha\beta$ in the direction of $\boldsymbol{f}^{\mathrm{eq}} - \boldsymbol{f}$ to arrive at the post-collisional state $\boldsymbol{f}^*$, i.e.,

$$\boldsymbol{f}^* = \boldsymbol{f} + \alpha\beta[\boldsymbol{f}^{\mathrm{eq}} - \boldsymbol{f}], \tag{6.12}$$

Here, we have dropped the position and time coordinates $\boldsymbol{x}, t$ as the collision step is local in position space and instantaneous. In the standard LBM, $\alpha = 2$, however, in ELBM α deviates from its standard value of 2 and is found such that the $\mathcal{H}$ theorem is satisfied.

We now define a mirror state

$$\boldsymbol{f}^{\mathrm{mirror}} = \boldsymbol{f} + \alpha(\boldsymbol{f}^{\mathrm{eq}} - \boldsymbol{f}), \tag{6.13}$$

which is essentially $\boldsymbol{f}^*$ from Eq. (6.12) with $\beta = 1$. Recall that $\beta = 1$ is a zero dissipation state, therefore,

$$\mathcal{H}[\boldsymbol{f}^{\mathrm{mirror}}] = \mathcal{H}[\boldsymbol{f}]. \tag{6.14}$$

Hence, starting from $\boldsymbol{f}$ and moving in the direction of $\boldsymbol{f}^{\mathrm{eq}} - \boldsymbol{f}$ the maximum allowable path length that could be covered is α, beyond which $\mathcal{H}$ will begin to increase, and the $\mathcal{H}$ theorem will be violated. This is depicted in Figure 6.1 where the circles are iso-entropic contours and $H_1 > H_2 > H_3 > H[f^{\mathrm{eq}}]$. The path length α is evaluated numerically by solving the nonlinear equation Eq. (6.14) for α (Ansumali & Karlin, 2002*a*; Tosi *et al.*, 2006; Chikatamarla *et al.*, 2006). Once the path length α and therefore the mirror state are known, the post-collisional state is found by the linear contraction

$$\boldsymbol{f}^* = \boldsymbol{f}^{\mathrm{mirror}} - \alpha(1-\beta)[\boldsymbol{f}^{\mathrm{eq}} - \boldsymbol{f}] = \boldsymbol{f} + \alpha\beta[\boldsymbol{f}^{\mathrm{eq}} - \boldsymbol{f}]. \tag{6.15}$$

Since $0 < \beta < 1$, it is guaranteed that

$$\mathcal{H}[\boldsymbol{f}^*] < \mathcal{H}[\boldsymbol{f}^{\mathrm{mirror}}]. \tag{6.16}$$

To summarize, the ELBM ensures adherence to the $\mathcal{H}$ theorem in the collision by first "over-relaxing" the populations to an isentropic (zero dissipation) mirror state followed by adding dissipation which ensures a non-positive entropy production (Karlin *et al.*, 1999).

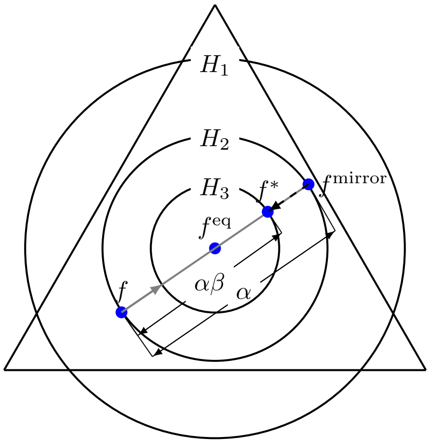

Figure 6.1: The entropic involution step: H_i are different entropy levels ($H_1 > H_2 > H_3$). Triangle denotes the polytope of positivity. Note that the pre-collisional state f and the mirror state f^{mirror} are at the same entropy level. The post collisional state f^* is at a lower entropy level.

6.2.1 Discussion on the over-relaxation

The over-relaxation of the populations is an important feature of the discrete dynamics as it allows one to achieve any desirable time steps independent of the relaxation time. In Figure 6.1, all the states on the line segment $\boldsymbol{f}^{\mathrm{mirror}} - \boldsymbol{f}^{\mathrm{eq}}$ are over-relaxed states, while those on the line segment $\boldsymbol{f}^{\mathrm{eq}} - \boldsymbol{f}$ are under-relaxed. A numerical scheme via the first order Euler discretization of the Boltzmann BGK equation is possible. It reads as

$$\begin{aligned} f(\boldsymbol{x}+\boldsymbol{c}\Delta t, t+\Delta t) &= f(\boldsymbol{x},t) + \frac{\Delta t}{\tau}\left[f^{\mathrm{eq}} - f(\boldsymbol{x},t)\right] + \mathcal{O}(\Delta t^2) \\ &= \left(1 - \frac{\Delta t}{\tau}\right) f(\boldsymbol{x},t) + \frac{\Delta t}{\tau} f^{\mathrm{eq}}. \end{aligned} \tag{6.17}$$

It displays unconditional numerical stability if $\Delta t \ll \tau$. This is an under-relaxing scheme and corresponds to $\alpha < 1$ as the discrete dynamics never crosses the equilibrium state. The $\mathcal{H}$ theorem for this scheme is trivially satisfied as the post-collisional state is a convex combination of the pre-collisional state and the equilibrium state.

For flows with a large Reynolds number, the viscosity is small and hence $\tau \to 0$. As the under-relaxation requires $\Delta t \ll \tau$, it also sets a severe restriction on the time step, i.e., $\tau \to 0 \Rightarrow \Delta t \to 0$. However, for faster convergence it is desirable to have large time steps, thus a numerical scheme which permits $\Delta t \gg \tau$ is desirable. The over-relaxation schemes allow $\Delta t \gg \tau$ and correspond to $\alpha > 1$.

6.2.2 Near equilibrium limit of the entropic involution

In a well resolved simulation, the entropic involution step gives the solution $\alpha = 2$. This is seen in what follows. The dimensionless departure from the equilibrium is defined as

$$x_i = \frac{f_i^{\mathrm{eq}}}{f_i} - 1. \tag{6.18}$$

As all f_i, f_i^{eq} are positive, $x_i \in (-1, \infty)$. Here, the lower limit is due to the extreme case of one of the $f_i^{\mathrm{eq}} \to 0$, whereas the upper limit is due to one of the $f_i \to 0$. The equilibrium distribution of the populations f_i^{eq} is

$$f_i^{\text{eq}} = w_i \exp(-\lambda - \zeta_\kappa c_{i\kappa} - \gamma c_i^2) \Rightarrow w_i = f_i^{\text{eq}} \exp(\lambda + \zeta_\kappa c_{i\kappa} + \gamma c_i^2), \tag{6.19}$$

where w_i is weight specific to discrete velocity $\boldsymbol{c}_i$ $(i = 1...N)$. The Lagrange multipliers $\lambda, \zeta_\kappa, \gamma$ are calculated by imposing the conservation of mass, momentum and energy respectively (in an isothermal setting $\gamma = 0$). Therefore, from the form of $\mathcal{H}$ from Eq.(6.7) we have

$$\mathcal{H}[\boldsymbol{f}^{\text{mirror}}] - \mathcal{H}[\boldsymbol{f}] = \left\langle f^{\text{mirror}}, \log \frac{f^{\text{mirror}}}{w} \right\rangle - \left\langle f, \log \frac{f}{w} \right\rangle. \tag{6.20}$$

Substituting $\boldsymbol{f}^{\text{mirror}}$ from Eq.(6.13) in the above equation we obtain

$$\mathcal{H}[\boldsymbol{f}^{\text{mirror}}] - \mathcal{H}[\boldsymbol{f}] = \left\langle f + \alpha(f^{\text{eq}} - f), \log \frac{f + \alpha(f^{\text{eq}} - f)}{w} \right\rangle - \left\langle f, \log \frac{f}{w} \right\rangle, \tag{6.21}$$

which upon using the definition of x_i from Eq.(6.18) gives

$$\begin{aligned}\mathcal{H}[\boldsymbol{f}^{\text{mirror}}] - \mathcal{H}[\boldsymbol{f}] &= \left\langle f(1+\alpha x), \log \frac{f(1+\alpha x)}{w} \right\rangle - \left\langle f, \log \frac{f}{w} \right\rangle \\ &= \langle f(1+\alpha x), \log(1+\alpha x) \rangle + \left\langle f(1+\alpha x), \log \frac{f}{w} \right\rangle - \left\langle f, \log \frac{f}{w} \right\rangle \\ &= \langle f\,(1+\alpha x)\,, \log(1+\alpha x) \rangle - \alpha \left\langle f, x \log \frac{w}{f} \right\rangle.\end{aligned} \tag{6.22}$$

Substituting w_i from Eq.(6.19) one obtains

$$\begin{aligned}\mathcal{H}[\boldsymbol{f}^{\text{mirror}}] - \mathcal{H}[\boldsymbol{f}] &= \langle f, (1+\alpha x)\log(1+\alpha x) \rangle - \alpha \left\langle f, x \log \frac{f^{\text{eq}} \exp(\lambda + \zeta_\kappa c_{i\kappa} + \gamma c_i^2)}{f} \right\rangle \\ &= \langle f, (1+\alpha x)\log(1+\alpha x) \rangle - \alpha \langle f, x \log(1+x) \rangle - \underline{\alpha\lambda \langle f, x \rangle} \\ &\quad - \underline{\alpha\zeta_\kappa \langle f, x c_\kappa \rangle} - \underline{\alpha\gamma \langle f, x c^2 \rangle}\end{aligned} \tag{6.23}$$

where we have substituted $f_i^{\text{eq}}/f_i = 1 + x_i$ and the underlined terms are zero because

$$\begin{aligned}\langle f, x \rangle &= \sum_i (f^{\text{eq}} - f_i) = \rho - \rho = 0, \\ \langle f, x c_\kappa \rangle &= \sum_i (f^{\text{eq}} c_{i\kappa} - f_i c_{i\kappa}) = \rho u_\kappa - \rho u_\kappa = 0, \\ \langle f, x c^2 \rangle &= \sum_i (f^{\text{eq}} c_i^2 - f_i c_i^2) = \rho e - \rho e = 0.\end{aligned} \tag{6.24}$$

Therefore, the path length α is the root of the equation

$$\mathcal{H}[\boldsymbol{f}^{\text{mirror}}] - \mathcal{H}[\boldsymbol{f}] = \langle f, (1+\alpha x)\log(1+\alpha x) \rangle - \alpha \langle f, x \log(1+x) \rangle. \tag{6.25}$$

In a well resolved simulation, the dimensionless departure of populations from the equilibrium is small, i.e.,

$$|x_i| \ll 1. \tag{6.26}$$

Hence, expanding the logarithms about $x_i = 0$ via Taylor series one obtains

$$\mathcal{H}[\boldsymbol{f}^{\text{mirror}}] - \mathcal{H}[\boldsymbol{f}] = \alpha \left(\frac{\alpha}{2} - 1 \right) \langle f, x^2 \rangle + O(x^3).$$

Thus, for small departure from the equilibrium, the non-trivial root of $\mathcal{H}[\boldsymbol{f}^{\text{mirror}}] - \mathcal{H}[\boldsymbol{f}] = 0$ is $\alpha = 2$. Therefore, the ELBM reduces to the standard LBM.

Illustration via $D1Q2$ lattice
We derive the expanded form of Eq.(6.25) for the $D1Q2$ lattice (Mohamad & Kuzmin, 2012). This is a one dimensional lattice that has only 2 discrete velocities $c_1 = \{1\}$ and $c_{-1} = \{-1\}$. It lacks degree of freedom to model hydrodynamics, however, is simple enough to show the analytical form of $\mathcal{H}[\boldsymbol{f}^{\text{mirror}}] - \mathcal{H}[\boldsymbol{f}]$,

$$\begin{aligned}\Delta\mathcal{H} \equiv \mathcal{H}[\boldsymbol{f}^{\text{mirror}}] - \mathcal{H}[\boldsymbol{f}] = {} & f_1(1+\alpha x_1)\log(1+\alpha x_1) - \alpha f_1 x_1 \log(1+\alpha x_1) \\ & + f_{-1}(1+\alpha x_{-1})\log(1+\alpha x_{-1}) - \alpha f_{-1} x_{-1}\log(1+\alpha x_{-1}).\end{aligned} \tag{6.27}$$

For this lattice, $f_1^{\text{eq}} = f_{-1}^{\text{eq}} = \rho/2$, therefore, $x_1 = \rho/(2f_1) - 1, x_{-1} = \rho/(2f_{-1}) - 1$, substituting which in the above equation one obtains

$$\begin{aligned}\Delta\mathcal{H} = {} & \left[f_1 + \alpha\left(\frac{\rho}{2} - f_1\right)\right]\log\left[1 + \alpha\left(\frac{\rho}{2f_1} - 1\right)\right] - \alpha\left(\frac{\rho}{2} - f_1\right)\log\left(\frac{\rho}{2f_1}\right) \\ & + \left[\rho - f_1 + \alpha\left(-\frac{\rho}{2} + f_1\right)\right]\log\left[1 + \alpha\left(\frac{\rho}{2(\rho - f_1)} - 1\right)\right] - \alpha\left(-\frac{\rho}{2} + f_1\right)\log\left(\frac{\rho}{2(\rho - f_1)}\right),\end{aligned} \tag{6.28}$$

where we have substituted $f_{-1} = \rho - f_1$ from the mass conservation constraint. The above equation is further simplified by introducing the scaled population $\tilde{f}_1 = f_i/\rho$ as

$$\begin{aligned}\frac{\Delta\mathcal{H}}{\rho} = \left[\tilde{f}_1 + \alpha\left(\frac{1}{2} - \tilde{f}_1\right)\right]\log\frac{2\tilde{f}_1 + \alpha(1 - 2\tilde{f}_1)}{2(1-\tilde{f}_1) + \alpha(2\tilde{f}_1 - 1)} + \log\left[1 + \alpha\left(\frac{1}{2(1-\tilde{f}_1)} - 1\right)\right] \\ + \tilde{f}_1\log\left[\frac{1-\tilde{f}_1}{\tilde{f}_1}\right].\end{aligned} \tag{6.29}$$

From the above equation, we see that the complexity associated with the Eq.(6.25) makes it difficult to obtain a solution even for the simplistic $D1Q2$ lattice. This problem aggravates for more complicated lattices.

6.2.3 Indeterminacy in the entropic involution

There exists another important structure in the phase space: the polytope of positivity (Gorban & Packwood, 2012). It is the region inside which all the populations are positive but outside of which one or more populations become negative. The involution step exhibits no solution when the iso-entropic surfaces are partially outside the polytope of positivity (entropy level H_1 in Figure 6.1). This is due to the presence of the logarithm in the entropy function which cannot be defined when one of the populations is negative. It should be noted that these events are rare and even if one encounters such cases it is known how to construct the path length (Ansumali & Karlin, 2002*a*; Mazloomi M. *et al.*, 2015).

Illustration via $D1Q3$ lattice
We illustrate via $D1Q3$ lattice the rare scenario where the mirror state is not defined. The $D1Q3$ lattice has three populations f_1, f_2, f_3. The mass conservation constraint requires that $f_1 + f_2 + f_3 = \rho$, a plane in the phase space on which the entire discrete dynamics is constrained. Figure 6.2(a) shows the triangular section of the plane inside which all the populations are positive, and outside of which one or more populations become negative. Figure 6.2(b) represents a scenario where the mirror state is not defined as one of the populations is negative, hence the

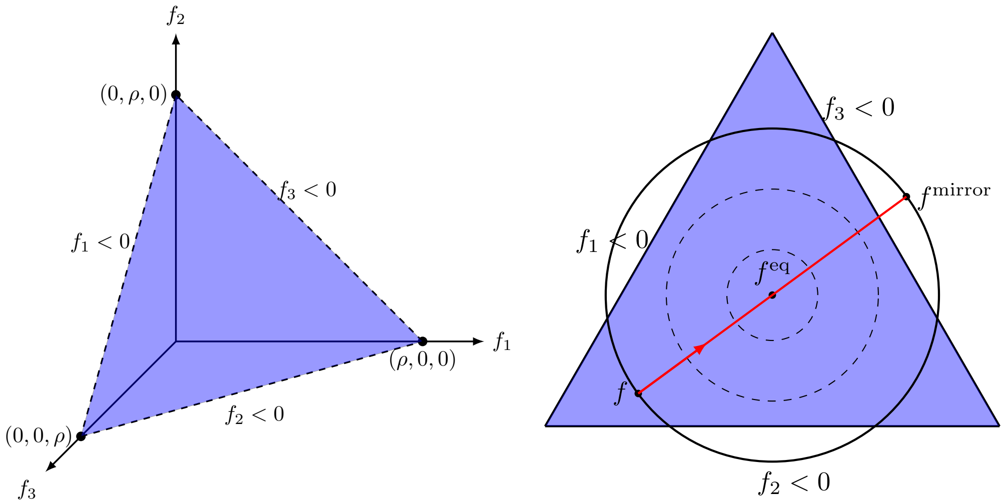

(a) The polytope of positivity.

(b) Mirror state lies outside the polytope of positivity.

Figure 6.2: (a) The triangular section of the plane inside which all the populations are positive, and outside of which one or more populations become negative. (b) Representation of a pre-collisional state f for which the mirror state is not defined.

mirror state cannot be defined.

6.3 Exact solution to the path length: Essentially entropic lattice Boltzmann model

As discussed in the previous section, the discrete path length α is available as the non-trivial root of the equation

$$\mathcal{H}[\boldsymbol{f}^{\mathrm{mirror}}] - \mathcal{H}[\boldsymbol{f}] = \langle f, (1+\alpha x)\log(1+\alpha x)\rangle - \alpha \langle f, x\log(1+x)\rangle = 0. \tag{6.30}$$

The above equation is highly nonlinear and is typically solved by a combination of bisection and Newton-Raphson method (Ansumali & Karlin, 2000, 2002*c*). Considerable efforts have been put in to ensure that the correct solution is obtained in an efficient manner (Ansumali & Karlin, 2002*a*; Tosi *et al.*, 2006; Chikatamarla *et al.*, 2006; Brownlee *et al.*, 2007).

In this section, we present an alternate construction of ELBM where the discrete path length α is known in explicit form and has no indeterminacy. The key idea is to obtain α by directly considering the natural criterion of monotonic decrease of $\mathcal{H}$ with time (Atif *et al.*, 2017). This implies solving an inequality

$$\Delta\mathcal{H} \equiv \mathcal{H}[\boldsymbol{f}^*] - \mathcal{H}[\boldsymbol{f}] < 0. \tag{6.31}$$

The inequality, by construction, accepts multiple solutions. For example, when $\alpha \leq 1$ the inequality is trivially satisfied as the new state is a convex combination of the old state and the equilibrium (Wagner, 1998). However, one is interested in over-relaxed collision, where the new state is no longer a convex combination of the old state and equilibrium. This corresponds to the real solutions of Eq.(6.31) in the range $1 < \alpha < \infty$ (Karlin *et al.*, 1999). Among the multiple solutions of the inequality, we are looking for the maximal path length α such that

$$\Delta\mathcal{H} \to 0. \tag{6.32}$$

As in ELBM, the solution should reduce to standard LBM close to equilibrium ($\alpha = 2$). Indeed, the present methodology is valid for both discrete velocity models of LBM as well as the continuous in velocity Boltzmann-BGK equations, where the summation in the bilinear action needs to be replaced by appropriate integrals.

The general idea behind obtaining an analytical expression for the path length α is as follows: we intend to split $\Delta\mathcal{H}$ into two parts,

$$\Delta\mathcal{H} = H(\alpha) + H^{(B)}, \tag{6.33}$$

where $H^{(B)}$ is chosen such that it is non-positive, and $H(\alpha)$ is a polynomial. The polynomial

$$H(\alpha) = 0, \tag{6.34}$$

is solved for the path length α. The discrete time $\mathcal{H}$ theorem is satisfied as $H^{(B)}$ is non-positive and contributes to the entropy production, i.e.,

$$\Delta\mathcal{H} = H^{(B)} \leq 0. \tag{6.35}$$

A word of caution is in order here. As stated earlier, the inequality $\Delta\mathcal{H} \leq 0$ by construction accepts multiple solutions. These solutions are not identical but differ in two ways:

1. Not all the solutions reduce to the standard LBM ($\alpha = 2$) in the limit of $x_i \to 0$. Our interest is only in the solutions that reduce to the standard LBM for $x_i \to 0$.
2. The entropy production corresponding to each solution dictates its dissipative nature, i.e., as the magnitude of $H^{(B)}$ increases the dynamics becomes more and more dissipative. This is the reason why we are interested in the solution such that $\Delta\mathcal{H} \to 0$. This point will be elucidated in the forthcoming section, where we will derive two expressions for α, one of which will be more dissipative than the other.

Applying the same procedure as given in Eqs.(6.22)–(6.23), we have from Eq.(6.31),

$$\Delta\mathcal{H} = \mathcal{H}[\boldsymbol{f}^*] - \mathcal{H}[\boldsymbol{f}] = \left\langle f^*, \log\frac{f^*}{w}\right\rangle - \left\langle f, \log\frac{f}{w}\right\rangle \tag{6.36}$$

where by substituting $f_i^* = f_i(1+\alpha\beta x_i)$ [Eq.(6.4) and Eq.(6.18)] one obtains

$$\Delta\mathcal{H} = \left\langle f, (1+\alpha\beta x)\log\frac{f\,(1+\alpha\beta x)}{w}\right\rangle - \left\langle f, \log\frac{f}{w}\right\rangle. \tag{6.37}$$

Upon substituting w_i from Eq.(6.19), the above equation is rewritten as

$$\begin{aligned}\Delta\mathcal{H} &= \langle f, (1+\alpha\beta x)\log(1+\alpha\beta x)\rangle - \alpha\beta\left\langle f, x\log\frac{w}{f}\right\rangle \\ &= \langle f, (1+\alpha\beta x)\log(1+\alpha\beta x)\rangle - \alpha\beta\,\langle f, x\log(1+x)\rangle\,.\end{aligned} \tag{6.38}$$

Further, we introduce a decomposition of distributions f in terms of the departure from equilibrium as (Gorban *et al.*, 1996)

$$\Omega^+ = \{f_i : x_i \geq 0\} \quad \text{and} \quad \Omega^- = \{f_i : -1 < x_i < 0\}.$$

This asymmetry of the range of x is crucial in the subsequent derivation of the exact solution. With this decomposition, we also partition the bilinear action into two partial contributions

$$\langle f, \psi\rangle_{\Omega^\pm} = \sum_{f_i\in\Omega^\pm} f_i\psi_i.$$

Under this decomposition, the Eq.(6.38) becomes

$$\begin{aligned}\Delta\mathcal{H} = \left\langle f, (1+\alpha\beta x)\log(1+\alpha\beta x)\right\rangle_{\Omega^-} &+ \left\langle f, (1+\alpha\beta x)\log(1+\alpha\beta x)\right\rangle_{\Omega^+} \\ &- \alpha\beta\left\langle f, x\log(1+x)\right\rangle_{\Omega^-} - \alpha\beta\left\langle f, x\log(1+x)\right\rangle_{\Omega^+}.\end{aligned} \tag{6.39}$$

We now derive the solutions to $\Delta\mathcal{H} \leq 0$ by splitting the Eq.(6.39) into a polynomial and an entropy production term as explained above.

6.3.1 Lower order solution

Before deriving the analytical expression for the path length, we list some non-negative functions from Chapter 5:

$$G_1(y) = -(1+y)\log(1+y) + y + \frac{y^2}{2} - \frac{y^3}{2} > 0 \qquad y \in (-1,0), \tag{6.40}$$

$$G_2(y) = -(1+y)\log(1+y) + y + \frac{y^2}{2} \geq 0 \qquad y \in [0,\infty), \tag{6.41}$$

$$G_3(y) = y\log(1+y) - \frac{2y^2}{2+y} \geq 0 \qquad y \in (-1,\infty). \tag{6.42}$$

Upon adding and subtracting the same terms, Eq. (6.39) is written as

$$\begin{aligned}\Delta\mathcal{H} = &\left\langle f, (1+\alpha\beta x)\log(1+\alpha\beta x) - \mathcal{A}_1\right\rangle_{\Omega^-} + \left\langle f, \mathcal{A}_1\right\rangle_{\Omega^-} \\ &+ \left\langle f, (1+\alpha\beta x)\log(1+\alpha\beta x) - \mathcal{A}_2\right\rangle_{\Omega^+} + \left\langle f, \mathcal{A}_2\right\rangle_{\Omega^+} \\ &-\alpha\beta\left\langle f, x\log(1+x) - \mathcal{A}_3\right\rangle - \alpha\beta\left\langle f, \mathcal{A}_3\right\rangle,\end{aligned} \tag{6.43}$$

where

$$\mathcal{A}_1 = \alpha\beta x + \frac{\alpha^2\beta^2x^2}{2} - \frac{\alpha^3\beta^3x^3}{2}, \mathcal{A}_2 = \alpha\beta x + \frac{\alpha^2\beta^2x^2}{2}, \mathcal{A}_3 = \frac{2x^2}{2+x}.$$

Now, identifying that $\langle f, x\rangle_{\Omega^+} + \langle f, x\rangle_{\Omega^-} = \langle f, x\rangle = 0$ due to conservation laws, the above equation is re-organized as

$$\begin{aligned}\Delta\mathcal{H} = &\left\langle f, \underbrace{(1+\alpha\beta x)\log(1+\alpha\beta x) - \mathcal{A}_1}_{-G_1(\alpha\beta x)}\right\rangle_{\Omega^-} + \left\langle f, \underbrace{(1+\alpha\beta x)\log(1+\alpha\beta x) - \mathcal{A}_2}_{-G_2(\alpha\beta x)}\right\rangle_{\Omega^+} \\ &- \alpha\beta\left\langle f, \underbrace{x\log(1+x) - \mathcal{A}_3}_{G_3(x)}\right\rangle - \alpha\beta\left\langle f, \frac{2x^2}{2+x}\right\rangle + \underbrace{\alpha^2\beta^2\left\langle f, \frac{x^2}{2}\right\rangle}_{\mathcal{M}} - \underbrace{\alpha^3\beta^3\left\langle f, \frac{x^3}{2}\right\rangle_{\Omega^-}}_{\mathcal{N}}.\end{aligned} \tag{6.44}$$

We now consider the terms $\mathcal{M}, \mathcal{N}$ which are split as

$$\begin{aligned}\mathcal{M} &\equiv \alpha^2\beta^2\left\langle f, \frac{x^2}{2}\right\rangle \equiv \alpha^2\beta\left\langle f, \frac{x^2}{2}\right\rangle + \alpha^2\beta(\beta-1)\left\langle f, \frac{x^2}{2}\right\rangle, \\ \mathcal{N} &\equiv \alpha^3\beta^3\left\langle f, \frac{x^3}{2}\right\rangle_{\Omega^-} \equiv \alpha^3\beta\left\langle f, \frac{x^3}{2}\right\rangle_{\Omega^-} + \alpha^3\beta(\beta^2-1)\left\langle f, \frac{x^3}{2}\right\rangle_{\Omega^-}.\end{aligned} \tag{6.45}$$

Hence, Eq.(6.44) is written in a compact form as

$$\Delta\mathcal{H} = \alpha\beta H_1(\alpha) + H^{(B)}, \tag{6.46}$$

where

$$H^{(B)} = -\langle f, G_1(\alpha\beta x)\rangle_{\Omega_-} - \langle f, G_2(\alpha\beta x)\rangle_{\Omega_+} - \alpha\beta\,\langle f, G_3(x)\rangle + \alpha^2\beta(\beta-1)\left\langle f, \frac{x^2}{2}\right\rangle - \alpha^3\beta(\beta^2-1)\left\langle f, \frac{x^3}{2}\right\rangle_{\Omega^-}, \quad (6.47)$$

and

$$H_1(\alpha) = -\alpha^2\left\langle f, \frac{x^3}{2}\right\rangle_{\Omega^-} + \alpha\left\langle f, \frac{x^2}{2}\right\rangle - \left\langle f, \frac{2x^2}{2+x}\right\rangle. \quad (6.48)$$

Due to non-negative nature of the functions G_1, G_2, G_3 in their respective domains [Eqs.(6.40)-(6.42)] and $\beta < 1$, all the terms in Eq.(6.47) are non-positive, hence,

$$H^{(B)} \leq 0. \quad (6.49)$$

The positive root of the quadratic equation

$$H_1(\alpha) = 0, \quad (6.50)$$

is easily found. Therefore, from Eq.(6.46)

$$\Delta\mathcal{H} = H^{(B)} \leq 0. \quad (6.51)$$

As $H_1(0) < 0 < H_1(2)$, a root of Eq.(6.48) bounded in $(0,2)$ exists. It is given by

$$\alpha = \frac{1 - \left[1 - 8\Theta_-\left(1 - \frac{\Theta_+ + \Theta_-}{2} + \Gamma\right)\right]^{\frac{1}{2}}}{2\Theta_-}, \quad (6.52)$$

where

$$\Theta_\pm = \frac{\langle f, x^3\rangle_{\Omega\pm}}{\langle f, x^2\rangle}, \qquad \Gamma = \frac{\left\langle \frac{x^4}{4+2x}\right\rangle}{\langle f, x^2\rangle}.$$

Upon expanding the α_{Lower} and ignoring $O(\Theta_\pm^2)$ terms one obtains its limit

$$\lim_{x_i\to 0} \alpha_{\text{Lower}} = 2 - \Theta_+ + 3\Theta_- = 2 - \Theta + 4\Theta_-, \quad (6.53)$$

which has the limiting value of 2, the path length for standard LBM. It is evident that $\alpha_{\text{Lower}} < 2$. Henceforth, the path length given by Eq.(6.52) will be called α_{Lower} because it is constructed by employing lower order bounds on the logarithm.

6.3.2 Higher order solution

In this section, we derive the path length α by exploiting the sharper bounds on the logarithms. We first list some non-negative functions:

$$G_6(y) = -(1+y)\log(1+y) + G_9(y) > 0 \qquad y \in (-1, 0), \quad (6.54)$$

$$G_7(y) = -(1+y)\log(1+y) + (1+y)\mathcal{I}^{(3)}_{\text{NC}} \geq 0 \qquad y \in [0, \infty), \quad (6.55)$$

$$G_8(y) = y\log(1+y) - y\mathcal{I}^{(3)}_{\text{GL}} \geq 0 \qquad y \in (-1, \infty). \quad (6.56)$$

where $G_9(y) = y + y^2/2 - y^3/6 + y^4/12 - y^5/20 + y^6/5$. Following the same methodology as the previous section we add and subtract the same terms from Eq. (6.22) to obtain

$$\begin{aligned}\Delta\mathcal{H} = {} & \Big\langle f, \underbrace{(1+\alpha\beta x)\log(1+\alpha\beta x) - G_9(\alpha\beta x)}_{-G_6(\alpha\beta x)}\Big\rangle_{\Omega^-} + \Big\langle f, \underbrace{(1+\alpha\beta x)\Big(\log(1+\alpha\beta x) - \mathcal{I}^{(3)}_{\text{NC}}(\alpha\beta x)\Big)}_{-G_7(\alpha\beta x)}\Big\rangle_{\Omega^+} \\ & \underbrace{-\alpha\beta\Big\langle f, x\Big(\log(1+x) - \mathcal{I}^{(3)}_{\text{GL}}(x)\Big)\Big\rangle}_{-\alpha\beta G_8(x)} + \Big\langle f, (1+\alpha\beta x)\mathcal{I}^{(3)}_{\text{NC}}(\alpha\beta x)\Big\rangle_{\Omega^+} + \Big\langle f, G_9(\alpha\beta x)\Big\rangle_{\Omega^-} \\ & - \alpha\beta\Big\langle f, x\mathcal{I}^{(3)}_{\text{GL}}(x)\Big\rangle.\end{aligned} \tag{6.57}$$

The underbraced terms in the above equation are negative definite and contribute to the entropy production $H^{(B)}$. The last three terms, after factoring out $\alpha\beta$, form a quintic polynomial like equation $\hat{H}(\alpha)$,

$$\begin{aligned}\hat{H}(\alpha) = {} & -\Big\langle f, \frac{\alpha^2\beta^2x^3}{6} - \frac{\alpha^3\beta^3x^4}{12} + \frac{\alpha^4\beta^4x^5}{20} - \frac{\alpha^5\beta^5x^6}{5}\Big\rangle_{\Omega^-} + \Big\langle f, \frac{\alpha\beta x^2}{2}\Big\rangle - \Big\langle f, \frac{2\alpha^2\beta^2x^3}{15}\Big(\frac{2}{4+\alpha\beta x} \\ & + \frac{1}{4+2\alpha\beta x} + \frac{2}{4+3\alpha\beta x}\Big)\Big\rangle_{\Omega^+} - \Big\langle f, \frac{60x^2+60x^3+11x^4}{60+90x+36x^2+3x^3}\Big\rangle,\end{aligned} \tag{6.58}$$

the solution to which is the desired path length. The above equation has at least one positive root as $\hat{H}(0) < 0 < \hat{H}(\infty)$ which can be found using any numerical method. In order to preserve the computational efficiency of the model, in the next section, we solve the above equation by converting it into a quadratic.

6.3.3 Solving the higher degree polynomial

In this section, we solve Eq.(6.58) by converting it to a quadratic. The conversion to a quadratic is performed by extracting a few negative terms from the Eq.(6.58). These extracted terms then contribute to the entropy production $H^{(B)}$.

As stated earlier, the Eq.(6.58) has a positive root since $\hat{H}(0) < 0 < \hat{H}(\infty)$. We assume that upper and lower bounds on the root α exist. A suitable choice for the lower bound is α_{Lower} while the upper bound h will be later evaluated. Therefore,

$$\alpha_{\text{Lower}} < \alpha < h, \tag{6.59}$$

where Converting $\hat{H}(\alpha)$ to a quadratic is a two step procedure and is explained in the following subsections.

Exploiting the lower bound

Using the lower bound α_{Lower}, in Eq.(6.58) we split the term

$$\begin{aligned} & -\Big\langle f, \frac{2\alpha^2\beta^2x^3}{15}\Big(\frac{2}{4+\alpha\beta x} + \frac{1}{4+2\alpha\beta x} + \frac{2}{4+3\alpha\beta x}\Big)\Big\rangle_{\Omega^+} \equiv -\Big\langle f, \frac{2\alpha\beta^2x^3}{15}\Big(\frac{2}{\frac{4}{\alpha_{\text{Lower}}}+\beta x} \\ & + \frac{1}{\frac{4}{\alpha_{\text{Lower}}}+2\beta x} + \frac{2}{\frac{4}{\alpha_{\text{Lower}}}+3\beta x}\Big)\Big\rangle_{\Omega^+} - \Big\langle f, \frac{2\alpha\beta^2x^3}{15}\Big(\Big\{\frac{2}{\frac{4}{\alpha}+\beta x} - \frac{2}{\frac{4}{\alpha_{\text{Lower}}}+\beta x}\Big\} \\ & + \Big\{\frac{1}{\frac{4}{\alpha}+2\beta x} - \frac{1}{\frac{4}{\alpha_{\text{Lower}}}+2\beta x}\Big\} + \Big\{\frac{2}{\frac{4}{\alpha}+3\beta x} - \frac{2}{\frac{4}{\alpha_{\text{Lower}}}+3\beta x}\Big\}\Big)\Big\rangle_{\Omega^+},\end{aligned} \tag{6.60}$$

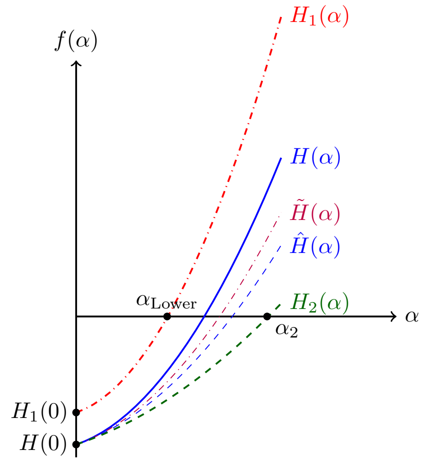

Figure 6.3: Behaviour of Eqs.(6.48),(6.58),(6.61),(6.63),(6.64) near the positive root.

where each term in curly braces is positive (as $\alpha_{\text{Lower}} < \alpha$) thereby making the second term negative. Here, recognizing that the negative term contributes to the entropy production $H^{(B)}$, we obtain the quintic polynomial $\tilde{H}(\alpha)$,

$$\tilde{H}(\alpha) = -\alpha^2\beta^2 \left\langle f, \frac{x^3}{6} - \frac{\alpha\beta x^4}{12} + \frac{\alpha^2\beta^2 x^5}{20} - \frac{\alpha^3\beta^3 x^6}{5} \right\rangle_{\Omega-} + \alpha\left[\left\langle f, \frac{x^2}{2}\right\rangle - \left\langle f, \frac{2\alpha_{\text{Lower}}\beta^2 x^3}{15}\left(\frac{2}{4+\alpha_{\text{Lower}}x} + \frac{1}{4+2\alpha_{\text{Lower}}x} + \frac{2}{4+3\alpha_{\text{Lower}}x}\right)\right\rangle_{\Omega+}\right] - \left\langle f, \frac{60x^2+60x^3+11x^4}{60+90x+36x^2+3x^3}\right\rangle. \tag{6.61}$$

Essentially, while converting $\hat{H}(\alpha)$ to $\tilde{H}(\alpha)$, we have shifted the negative definite terms in Eq.(6.60) to the entropy production, hence, the curve for $\tilde{H}(\alpha)$ lies above $\hat{H}(\alpha)$ (see Figure 6.3). It follows that an upper bound on the root of $\hat{H}(\alpha)$ will also serve as the upper bound for the root of $\tilde{H}(\alpha)$.

Exploiting the upper bound

Using the upper bound h, in Eq.(6.61) we split the term

$$-\left\langle f, \frac{\alpha^2\beta^2x^3}{6} - \frac{\alpha^3\beta^3x^4}{12} + \frac{\alpha^4\beta^4x^5}{20} - \frac{\alpha^5\beta^5x^6}{5}\right\rangle_{\Omega-} \equiv -\alpha^2\beta^2\left\langle f, \frac{x^3}{6} - \frac{h\beta x^4}{12} + \frac{h^2\beta^2x^5}{20} - \frac{h^3\beta^3x^6}{5}\right\rangle_{\Omega-} - \alpha^2\beta^2\left\langle f, -\frac{(\alpha-h)\beta x^4}{12} + \frac{(\alpha^2-h^2)\beta^2x^5}{20} - \frac{(\alpha^3-h^3)\beta^3x^6}{5}\right\rangle_{\Omega-}, \tag{6.62}$$

where the second term is negative, due to $x_i < 0, x_i \in \Omega^-$ and $\alpha < h$. Now, substituting Eq.(6.62) into Eq.(6.61) and again recognizing that the negative terms contribute to the entropy production $H^{(B)}$, we obtain the quadratic in α,

$$H(\alpha) = -\alpha^2\beta^2 \left\langle f, \frac{x^3}{6} - \frac{h\beta x^4}{12} + \frac{h^2\beta^2 x^5}{20} - \frac{h^3\beta^3 x^6}{5} \right\rangle_{\Omega-} + \alpha\left[\left\langle f, \frac{x^2}{2}\right\rangle - \left\langle f, \frac{2\alpha_{\text{Lower}}\beta^2 x^3}{15}\left(\frac{2}{4+\alpha_{\text{Lower}}x} + \frac{1}{4+2\alpha_{\text{Lower}}x} + \frac{2}{4+3\alpha_{\text{Lower}}x}\right)\right\rangle_{\Omega+}\right] - \left\langle f, \frac{60x^2+60x^3+11x^4}{60+90x+36x^2+3x^3}\right\rangle. \tag{6.63}$$

The above quadratic has a positive root α_{Higher} as $H(0) < 0 < H(\infty)$ which is the desired path length.

It remains to specify the upper bound h. For this we consider the quadratic equation $H_2(\alpha) = H(\alpha)|_{h=0}$,

$$H_2(\alpha) = -\alpha^2\beta^2\left\langle f, \frac{x^3}{6}\right\rangle_{\Omega^-} + \alpha\left[\left\langle f, \frac{x^2}{2}\right\rangle - \left\langle f, \frac{2k\beta^2x^3}{15}\left(\frac{2}{4+kx} + \frac{1}{4+2kx} + \frac{2}{4+3kx}\right)\right\rangle_{\Omega^+}\right] - \left\langle f, \frac{60x^2+60x^3+11x^4}{60+90x+36x^2+3x^3}\right\rangle, \tag{6.64}$$

whose positive root is α_2. Therefore, $H_2(\alpha_2) = 0$ and

$$H(\alpha_2) = \alpha_2^2\beta^2\left\langle f, \frac{h\beta x^4}{12} - \frac{h^2\beta^2x^5}{20} + \frac{h^3\beta^3x^6}{5}\right\rangle_{\Omega^-} + H_2(\alpha_2). \tag{6.65}$$

As $H(0) < 0 < H(\alpha_2)$, a root of $H(\alpha)$ lies in the interval $(0, \alpha_2)$ (see Figure 6.3). Hence, a suitable choice for the upper bound is $h = \alpha_2$. The positive root of Eq.(6.63) will henceforth be called α_{Higher} and has the limit

$$\lim_{x_i \to 0} \alpha_{\text{Higher}} = 2 + \left(\frac{4\beta^2}{3} - 1\right)\frac{\langle f, x^3\rangle}{\langle f, x^2\rangle}. \tag{6.66}$$

Unlike α_{Lower}, which was always less than 2, no such comment can be made about α_{Higher}. Thus α_{Higher} mimics an important feature of the ELBM where the path length fluctuates about the BGK value of 2.

6.3.4 Implementing the exact solution

The post-collisional populations are updated via the routine

$$f_i^* = f_i + \alpha\beta[f_i^{\text{eq}} - f_i], \tag{6.67}$$

where the path length α needs to be evaluated at each grid point. We begin by calculating

$$x_i = \frac{f_i^{\text{eq}}}{f_i} - 1, \tag{6.68}$$

where $i = 1 \to N$ for a lattice with N discrete velocities. To evaluate a summation on one of the sub-divisions Ω^- or Ω^+ we sum over the populations in the concerned sub-division. For instance, to calculate

$$a_1 = \left\langle f, \frac{x^3}{2}\right\rangle_{\Omega^-}$$

the pseudo-code is:

```
$a_1 = 0$
for each integer $i$ in 1 to $N$ do
    if $x_i < 0$ then
        $a_1 = a_1 + f_i * x_i^3$
    end if
end for
$a_1 = a_1 * 0.5$
Return $a_1$
```

To find the path length α we execute the following steps:

- **Step 1**: Find the $|x_i|^{\max}$ with maximum magnitude and minimum $x_i^{\min}$ amongst all x_i.

```
if $|x_i|^{\max} < 1e-3$ then
    $\alpha = 2$
else
    Proceed with Steps 2 to 5
end if
```

- **Step 2**: Find α_{Lower} available as the positive root of the Eq.(6.48)

$$\alpha_{\text{Lower}} = \frac{-b_1 + \left[b_1^2 - 4a_1c_1\right]^{\frac{1}{2}}}{-2a_1} = \frac{2c_1}{b_1 + \left[b_1^2 - 4a_1c_1\right]^{\frac{1}{2}}}, \tag{6.69}$$

[to avoid numerical issues while dealing with small numbers we have multiplied the root with its conjugate (Press *et al.*, 1992)], where,

$$a_1 = \left\langle f, \frac{x^3}{2} \right\rangle_{\Omega^-}, b_1 = \left\langle f, \frac{x^2}{2} \right\rangle, c_1 = \left\langle f, \frac{2x^2}{2+x} \right\rangle. \tag{6.70}$$

```
Find $a_1, b_1, c_1$
if $a_1 < 0 \,\&\, b_1 > 0 \,\&\, c_1 > 0$ then
    $\alpha_{\text{Lower}}$ from Eq.(6.69)
else
    $\alpha_{\text{Lower}} = 2$
end if
```

- **Step 3**: Find the upper bound h available as the positive root of the Eq.(6.64)

$$h = \frac{2c}{b + [b^2 - 4a_2c]^{\frac{1}{2}}}, \tag{6.71}$$

where

$$a_2 = \beta^2 \left\langle f, \frac{x^3}{6} \right\rangle_{\Omega^-}, c = \left\langle f, \frac{60x^2 + 60x^3 + 11x^4}{60 + 90x + 36x^2 + 3x^3} \right\rangle,$$
$$b = \left[\left\langle f, \frac{x^2}{2} \right\rangle - \left\langle f, \frac{2\alpha_{\text{Lower}}\beta^2 x^3}{15} \left(\frac{2}{4 + \alpha_{\text{Lower}}x} + \frac{1}{4 + 2\alpha_{\text{Lower}}x} + \frac{2}{4 + 3\alpha_{\text{Lower}}x} \right) \right\rangle_{\Omega^+} \right], \tag{6.72}$$

```
Find $a_2, b_2, c_2$
if $a_2 < 0 \,\&\, b > 0 \,\&\, c > 0$ then
    $h$ from Eq.(6.71)
else
    $h = 2$
end if
```

- **Step 4**: The path length α_{Higher} is found as the positive root of the Eq.(6.63)

$$\alpha_{\text{Higher}} = \frac{2c}{b + [b^2 - 4ac]^{\frac{1}{2}}}, \tag{6.73}$$

where

$$a = \beta^2 \left\langle f, \frac{x^3}{6} - \frac{h\beta x^4}{12} + \frac{h^2\beta^2 x^5}{20} - \frac{h^3\beta^3 x^6}{5} \right\rangle_{\Omega^-} \tag{6.74}$$

```
Find $a$
if $a < 0 \,\&\, b > 0 \,\&\, c > 0$ then
    $\alpha = \alpha_{\text{Higher}}$ from Eq.(6.73)
else
    $\alpha = 2$
end if
```

- **Step 5**: (Rare events) Although, the exact solution to the path length is always found, we need to ensure that the post collisional populations do not become negative due to the boundary conditions or in the case of of extremely under-resolved situations. To this effect, an extra step might be required. We again stress that these situations are extremely rare. The maximum permitted value of the path length such that all the post collisional populations remain positive is $\alpha^{\max} = -1/(\beta x_i^{\min})$. Therefore,

```
if $\alpha > \alpha^{\max}$ then
    $\alpha = 0.9\alpha^{\max}$
else if $\alpha < 1$ then
    $\alpha = 1.$
end if
```

6.4 Comparison with ELBM and BGK

Having obtained the exact solutions for the path length ($\alpha_{\text{Lower}}, \alpha_{\text{Higher}}$) we compare their behaviour with BGK ($\alpha = 2$) and iterative ELBM (α_{ELBM}). To this effect, we consider three well known setups: the one dimensional Sod shock tube, the lid driven cavity, and the doubly periodic shear layer. It is illustrated here that α_{Lower} is more dissipative than α_{Higher} and hence is not the ideal choice for hydrodynamics. Nevertheless, it is useful for the construction of α_{Higher} as demonstrated in the previous section.

6.4.1 Sod shock tube

In order to compare the behaviour of $\alpha_{\text{Lower}}, \alpha_{\text{Higher}}$ with α_{ELBM}, we consider the one dimensional shock tube using the $D1Q3$ lattice. In this setup, the domain is initialized with step density as $f^{\text{eq}}(\rho = 1.5, u = 0)$ in the left half of domain and $f^{\text{eq}}(\rho = 0.75, u = 0)$ in the right half. The presence of a sharp discontinuity in the density initial condition at the center of the domain generates a moving compressive shock front in the low density region and rarefaction front in the high density region. These two fronts leave behind in the tube a central contact region of uniform pressure and velocity (Laney, 1998).

The density, velocity, and entropy profiles shown in Figure 6.4 illustrate that the numerical oscillations are sharply reduced in the case of α_{Lower} (which is indicative of its dissipative nature), whereas for BGK, α_{Higher}, and α_{ELBM} the oscillations are prominent.

Figure 6.5(a) compares α_{Lower} and α_{ELBM}. It is evident that the path lengths show departure from $\alpha = 2$ (BGK value) only in a narrow region compressive shock front and the rarefaction front. It can also be seen that the value of α_{Lower} is always smaller than 2, while that of α_{ELBM} fluctuates about 2. In Sec.6.6, we demonstrate that departure of α from 2 can be interpreted

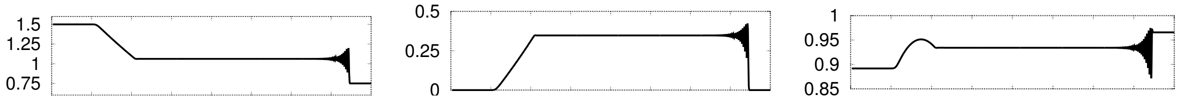

(a) LBGK, Density (b) LBGK, Velocity (c) LBGK, Entropy

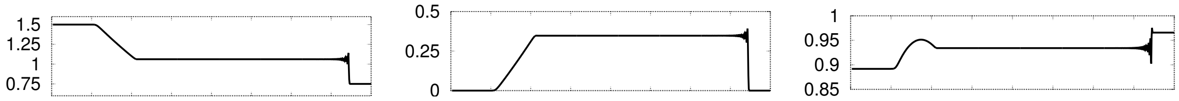

(d) α_{Lower}, Density (e) α_{Lower}, Velocity (f) α_{Lower}, Entropy

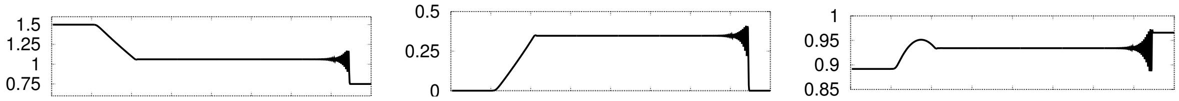

(g) α_{ELBM}, Density (h) α_{ELBM}, Velocity (i) α_{ELBM}, Entropy

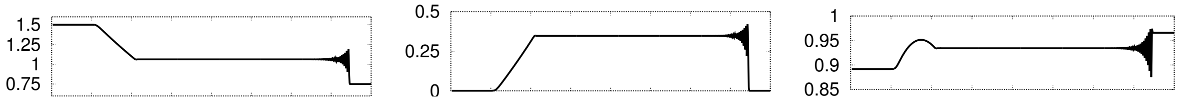

(j) α_{Higher}, Density (k) α_{Higher}, Velocity (l) α_{Higher}, Entropy

Figure 6.4: Density (left column), velocity (middle column) and entropy (right column) plots from LBGK, $\alpha_{\text{Lower}}, \alpha_{\text{Higher}}, \alpha_{\text{ELBM}}$ at time $t = 500$ for viscosity $\nu = 1.0 \times 10^{-5}$.

as a turbulent viscosity correction ν_T. Figure 6.5(b) plots ν_T/ν_0, from where it is seen that at the location of the shock front the turbulent viscosity correction for $\alpha_{\text{Lower}}$is more than 250% of the kinematic viscosity ν_0, while that of α_{ELBM} is only $\sim 47\%$. Figure 6.6(a) compares the path length from α_{Higher} and it is seen that for this setup α_{Higher} exhibits smaller fluctuations than the α_{ELBM}. Figure 6.6(b) shows that the turbulent viscosity correction for α_{ELBM} is $\sim 47\%$, whereas for α_{Higher} it is $\sim 42\%$.

6.4.2 Lid driven cavity

In this section, we consider the time evolution of enstrophy, defined as square of the vorticity, for a lid driven cavity at a Reynolds number (Re) of 5000 using the $D2Q9$ lattice. For this setup, the LBGK ($\alpha = 2$) is numerically unstable at smaller grid sizes of $64 \times 64, 96 \times 96$, and

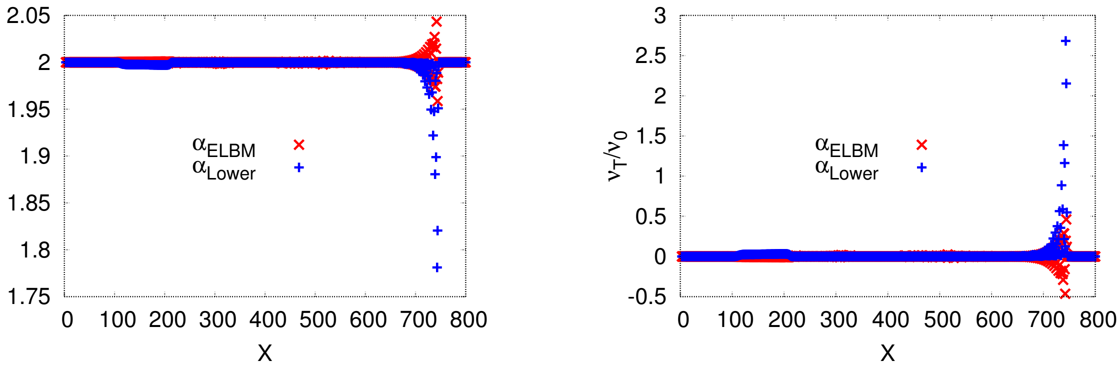

(a) Snapshot of the path length for the shock tube simulation.

(b) Ratio of the turbulent viscosity correction to the kinematic viscosity.

Figure 6.5: Comparison between α_{Lower} and α_{ELBM} for the Sod shock tube.

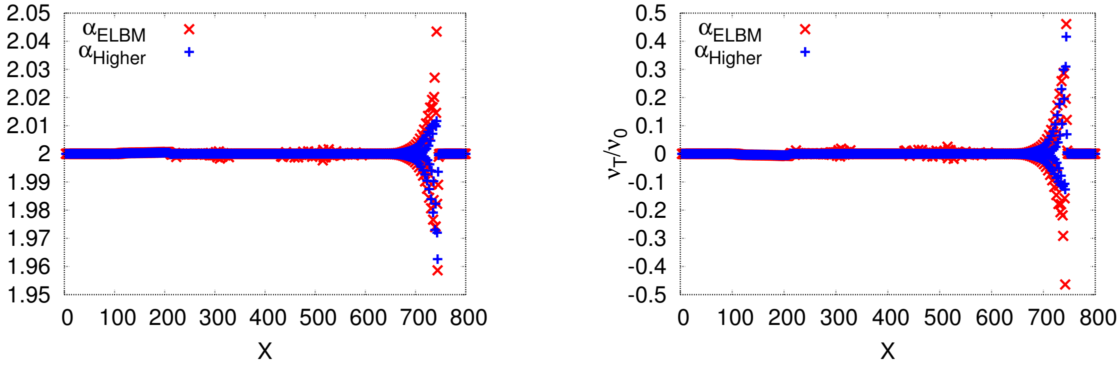

(a) Snapshot of the path length for the shock tube simulation.

(b) Ratio of the turbulent viscosity correction to the base viscosity.

Figure 6.6: Comparison between α_{Higher} and α_{ELBM} for the Sod shock tube.

	64×64	96×96	128×128
α_{Higher}	2 ± 0.00179	2 ± 0.00080	2 ± 0.00039
α_{ELBM}	2 ± 0.00177	2 ± 0.00073	2 ± 0.00029

Table 6.1: Region around the LBGK value of $\alpha = 2$ where 90% of the points lie. It is seen that as the grid size increases the region becomes narrower.

128×128, however, it becomes stable at a larger grid of size 256×256. The entropic formulations $\alpha_{\text{Lower}}, \alpha_{\text{Higher}}, \alpha_{\text{ELBM}}$ are stable at all grid sizes. We compare the enstrophy obtained from BGK at grid size 256×256 with that of $\alpha_{\text{Lower}}\alpha_{\text{Higher}}, \alpha_{\text{ELBM}}$ at 96×96 and 128×128 in Figure 6.9. It is evident that the enstrophy predicted by $\alpha_{\text{ELBM}}, \alpha_{\text{Higher}}$ and BGK are comparable, while that of α_{Lower} lies much below. Therefore, we conclude that the solution provided by α_{Lower} is dissipative. This is attributed to the high magnitude of $H^{(B)}$ in Eq. (6.51) due to loose bounds on the logarithms.

Here, we would like to establish that there is no significant difference between the path lengths α_{Higher} and α_{ELBM}. To this effect, we analyze the lid driven cavity for three different grid resolutions and show that the instantaneous values of α_{Higher} and α_{ELBM} show insignificant difference. We simulate the lid driven cavity at Re $= 5000$ and Mach number (Ma) $= 0.05$ using α_{Higher} for 1000 convection times. From the populations thus obtained, we evaluate α_{Higher} and α_{ELBM} on the entire grid, and plot their distribution in Figure 6.7. It is evident that α_{Higher} and α_{ELBM} show insignificant deviation at all grid sizes. From Figure 6.7 and Table 6.1 it can also be seen that as the grid size increases the distribution of the path lengths becomes narrower and more points lie closer to the LBGK value of $\alpha = 2$.

Further, Figure 6.10 depicts the iso-vorticity contours for the lid driven cavity at Reynolds number of 5000 for various grid sizes using α_{Higher}. It is seen that even extremely under-resolved grids remain numerically stable and give correct large scale structures. However, at coarse resolutions like 64×64 and 96×96 the finer structures are distorted. The finer structures become correct at a slightly higher resolution of 128×128. It should be repeated here that at grid size of 128×128 the LBGK ($\alpha = 2$) is numerically unstable. In Figure 6.11, we plot the velocities along vertical and horizontal centerlines and show a good match with Ghia *et al.* (1982).

We also briefly investigate the idea that the path length α_{Lower} could be exploited as a guess value for the iterative root finder. To this effect, we calculate the first iterate α_{Iterate1} and compare it with α_{ELBM}. Figure 6.12 depicts $\alpha_{\text{Iterate1}} - \alpha_{\text{ELBM}}$ for the three grid sizes. It is seen that the difference is insignificant in the bulk of the domain and becomes $\sim \mathcal{O}(10^{-3})$ only near the top and right walls.

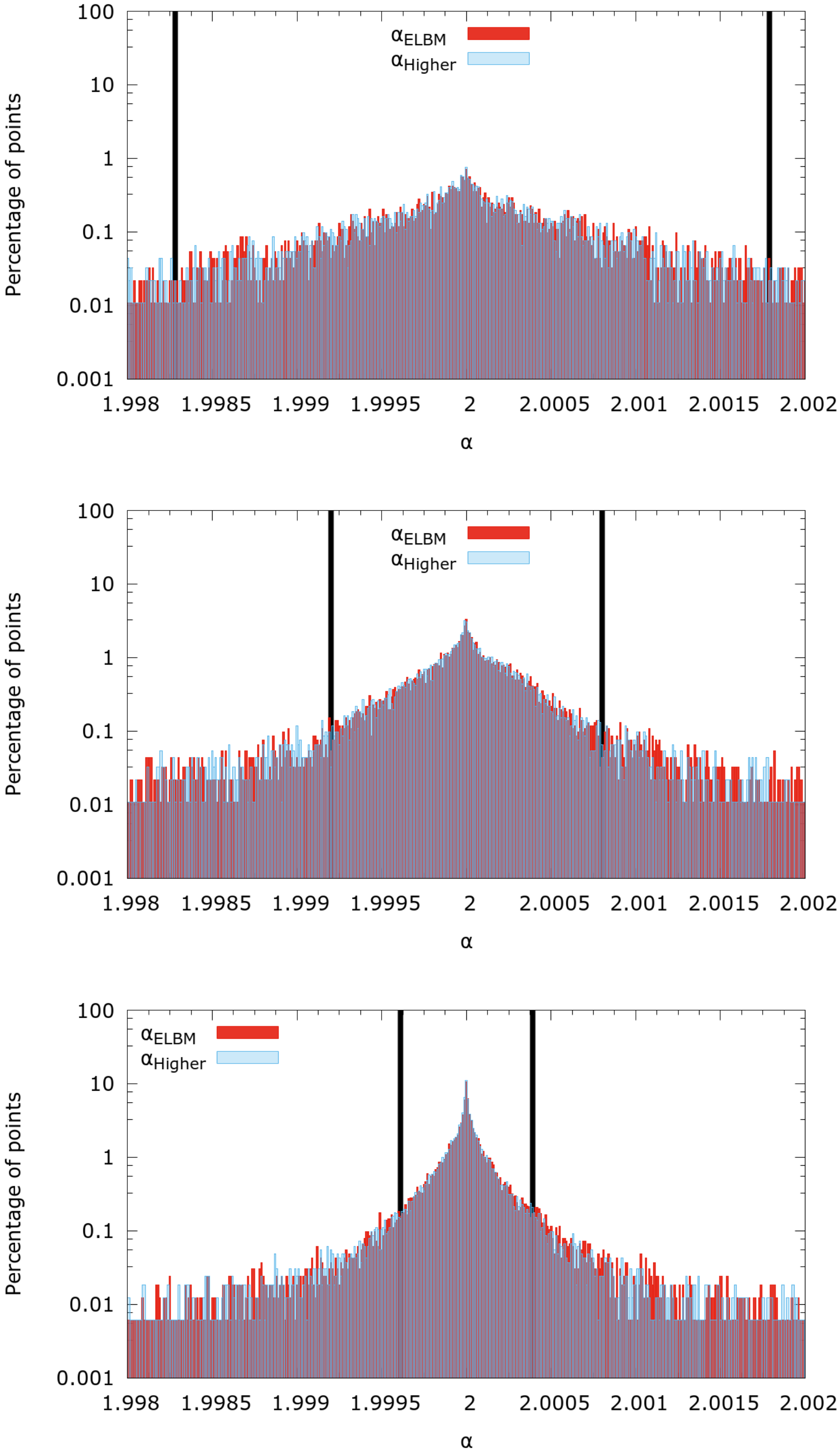

Figure 6.7: Distribution of α_{Higher} and α_{ELBM} for lid driven cavity at Reynolds number 5000 and Mach number 0.05. Grid sizes are 64×64 (top), 96×96 (middle), 128×128 (bottom). The difference between the distribution of α_{Higher} and α_{ELBM} is seen to be insignificant. The solid black lines denote the region inside which 90% of the points lie. The locations of the solid lines are tabulated in Table 6.1.

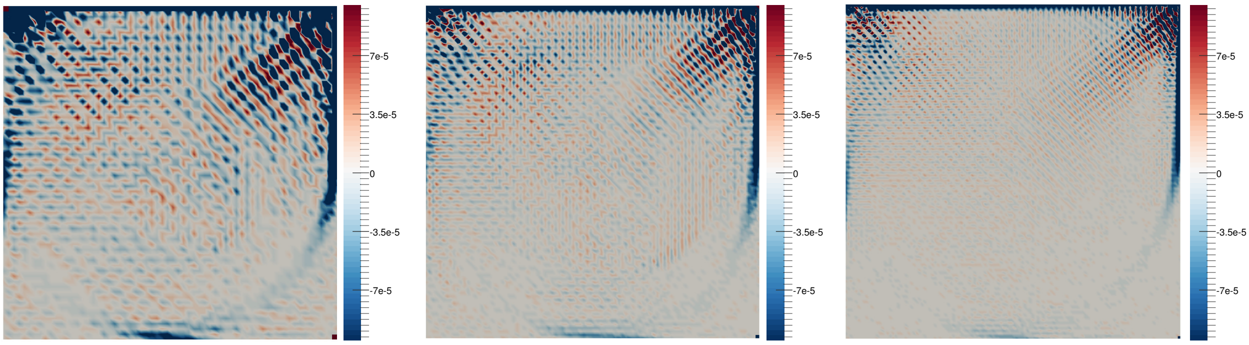

Figure 6.8: Distribution of $\alpha_{\text{Higher}} - \alpha_{\text{ELBM}}$ for lid driven cavity at Reynolds number 5000 and Mach number 0.05. Grid sizes are 64×64 (left), 96×96 (center), 128×128 (right). The difference between the distribution reduces as the grid size increases.

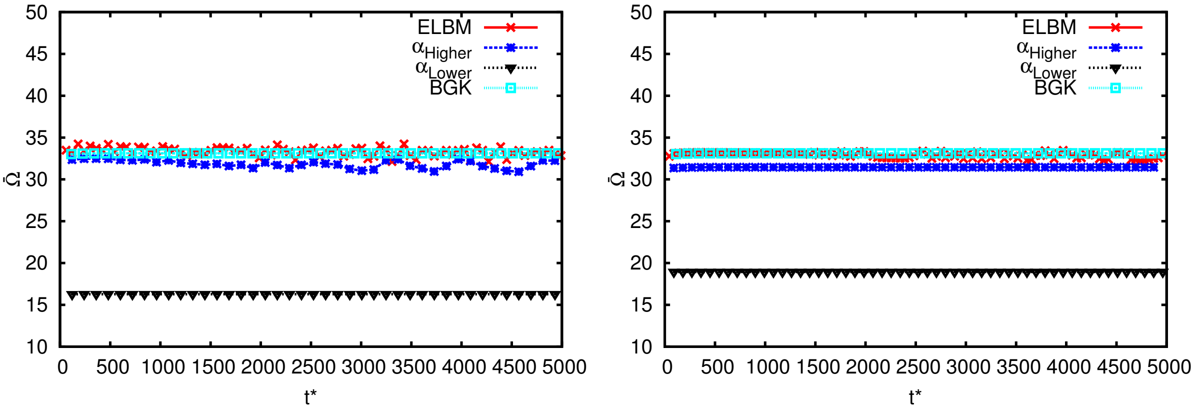

Figure 6.9: Comparison of time evolution of global enstrophy $\bar{\Omega}$ between $\alpha_{\text{Lower}}, \alpha_{\text{Higher}}, \alpha_{\text{ELBM}}$ for the lid driven cavity at Re = 5000 and Ma = 0.05. The BGK solution is at a grid size of 256×256, however, $\alpha_{\text{Lower}}, \alpha_{\text{ELBM}}$ are at 96×96 (left) and 128×128 (right). Here, t^* is time non-dimensionalized via the convective time scale. The dissipative nature of α_{Lower} manifests in the form of reduced enstrophy.

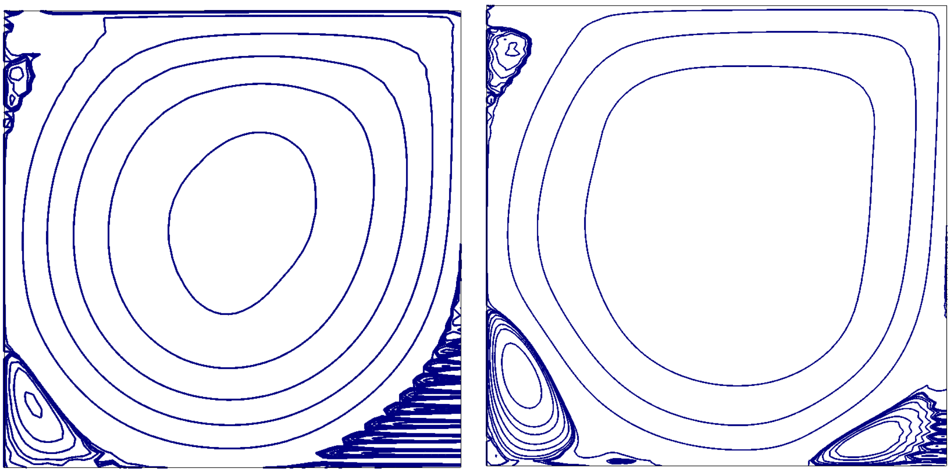

(a) 64 × 64 (b) 96 × 96

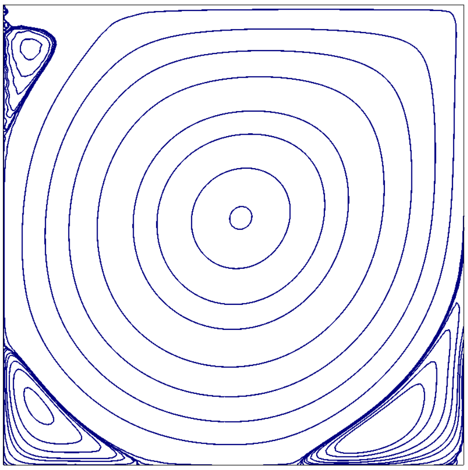

(c) 128 × 128

Figure 6.10: Iso-vorticity contours for the lid driven cavity at Reynolds number of 5000 for various grid sizes.

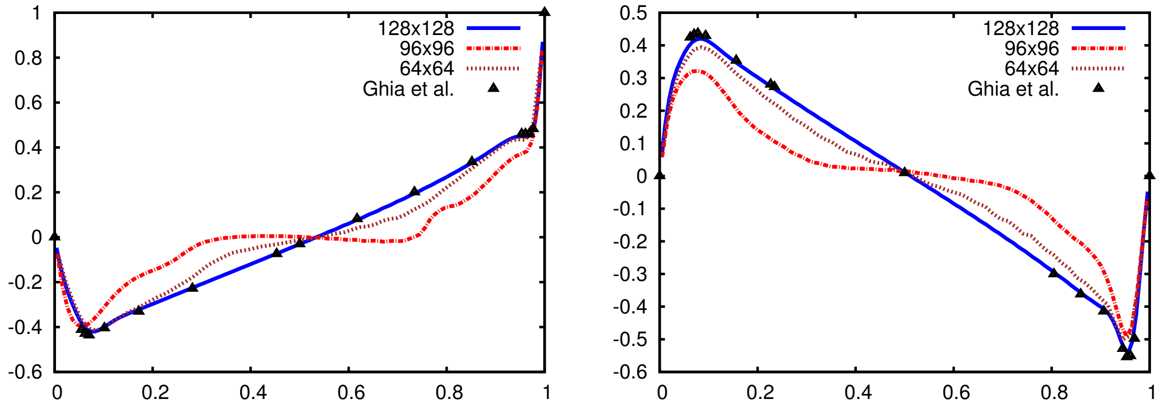

(a) x-velocity along the vertical centerline (b) y-velocity along the horizontal centerline

Figure 6.11: Velocity profiles for the lid driven cavity at Reynolds number of 5000 and Mach number 0.05 for various grid sizes.

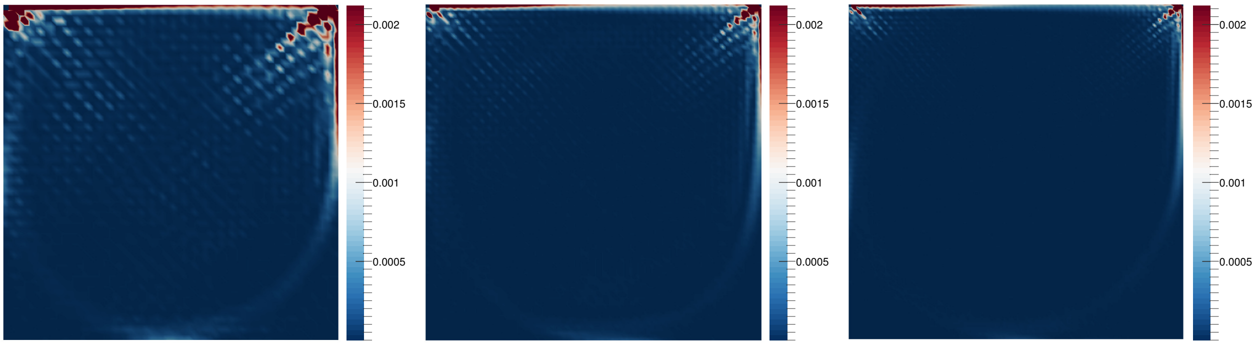

Figure 6.12: Distribution of $\alpha_{\text{Iterate1}} - \alpha_{\text{ELBM}}$ for lid driven cavity at Reynolds number 5000 and Mach number 0.05. Grid sizes are 64×64 (left), 96×96 (center), 128×128 (right). The difference between the distribution reduces as the grid size increases.

6.4.3 Doubly periodic shear layer

In this section, we compare the behaviour of $\alpha_{\text{Lower}}, \alpha_{\text{Higher}}$ with the BGK by considering the setup of doubly periodic shear layer (Minion & Brown, 1997). The initial velocity field comprises of two shear layers given by

$$u_x(y) = \begin{cases} U_0 \tanh[(4y-1)/w], & y \le 1/2 \\ U_0 \tanh[(3-4y)/w], & y > 1/2 \end{cases} \tag{6.75}$$

$$u_y(x) = U_0 \delta \sin[2\pi(x+1/4)], \tag{6.76}$$

where $w = \delta = 0.05, U_0 = 0.04$ and x, y are nondimensionalized coordinates. The viscosity is calculated from the Reynolds number which for the present case is fixed at 3×10^4. It is known that for this setup, the numerical disturbances may lead to formation of spurious vortices in the braids at poor grid resolutions (Minion & Brown, 1997; Coreixas *et al.*, 2017).

Figure 6.13 depicts the iso-vorticity contours for $\alpha_{\text{Lower}}, \alpha_{\text{Higher}}$ at grid size of 256×256 and for BGK at 1024×1024 obtained after one convection time. A qualitative comparison of the three plots reveals that the vortex structure is smudged for α_{Lower}, while the vortex structure of α_{Higher} on a grid of 256×256 is the same as that of BGK at 1024×1024. A quantitative analysis of the flow is performed by measuring the change in global enstrophy over time and is plotted in Figure 6.14. It is evident that α_{Higher} on a smaller lattice behaves the same as the BGK on a much larger lattice, while α_{Lower} exhibits dissipation that manifests in the form of reduced enstrophy. Finally, in Figure 6.15 we show the magnitude of the path lengths $\alpha_{\text{Lower}}, \alpha_{\text{Higher}}$, from where it evident that while α_{Lower} always remains smaller than 2, α_{Higher} fluctuates about 2. This again corroborates the dissipative nature of α_{Lower}.

6.5 Flow past NACA-0012 airfoil

As the exact solution for the path length inherits nonlinear stability of ELBM and provides significant speedup for entropic solvers, model free simulations of turbulence or multiphase flows for complex scientific and engineering applications with existing computational resources becomes a distinct possibility. Flow over aerodynamic geometries at realistic Reynolds number is considered a challenging problem due to the complex turbulence phenomena involved and high resolution required to capture the flow properties (Hosseini *et al.*, 2016). To this effect simulation of viscous flow over a NACA-0012 airfoil at 10° angle of attack(AoA) and Reynolds number 2.88×10^6 and Mach 0.05 is performed using the $RD3Q67$ model with 6000 points along the chord (Ch) on a grid of size $28Ch \times 14Ch \times 13$. Figure 6.16(a) shows the coefficient of

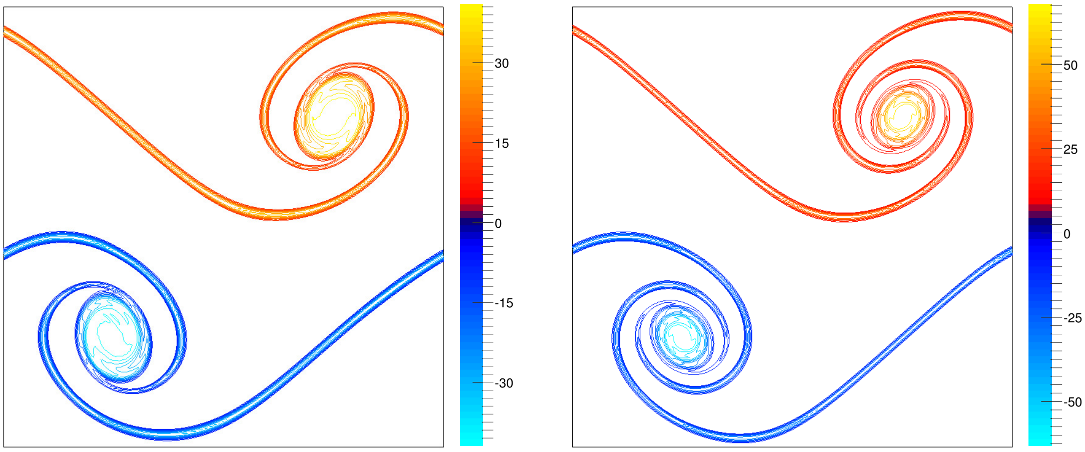

(a) $\alpha_{\text{Lower}}, 256 \times 256$ (b) $\alpha_{\text{Higher}}, 256 \times 256$

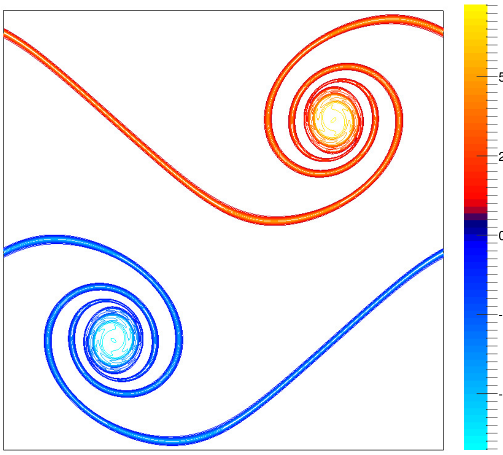

(c) BGK, 1024 × 1024

Figure 6.13: Nondimensional iso-vorticity contours [(a)-(c)] for $\alpha_{\text{Lower}}, \alpha_{\text{Higher}}$ at grid size 256×256 and for BGK at 1024×1024 after one convection time.

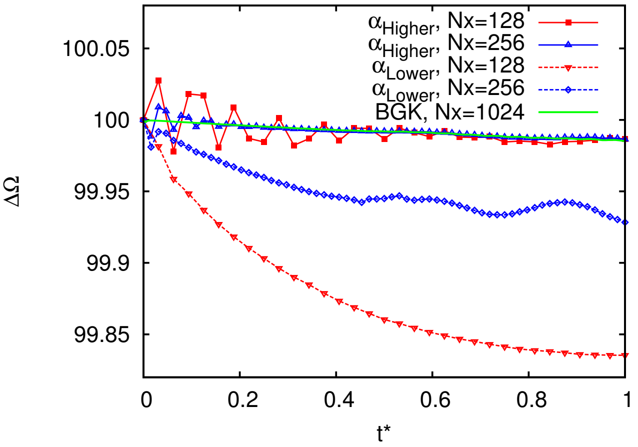

Figure 6.14: Change in the global enstrophy $\Delta\Omega$ vs time for various square grids. Here, t^* is the nondimensional convection time.

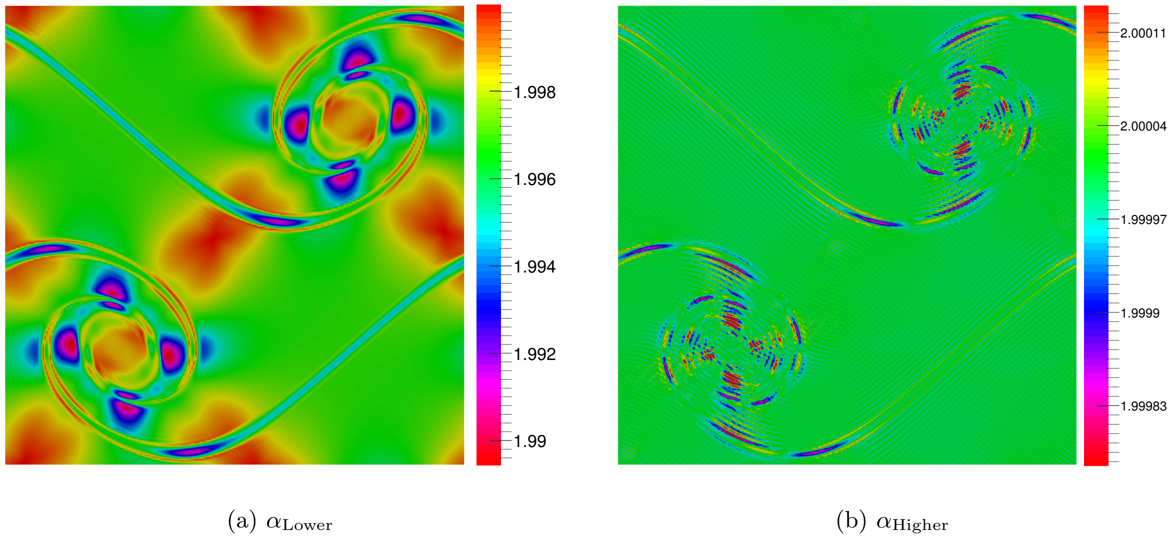

(a) α_{Lower} (b) α_{Higher}

Figure 6.15: Path length from the two schemes after one convection time on a grid of size 256 × 256.

pressure(C_p) compared with experiment (Gregory & O'reilly, 1973) and Figure 6.16(b) shows a snapshot of instantaneous vorticity field. A NACA-0012 airfoil in stall (Figure 6.16(c)) is also simulated at Reynolds number 5×10^4 and Ma 0.1 using 1600 points along the chord on a grid of size $28Ch \times 14Ch \times 321$. [1]

6.6 Entropic route to modeling the subgrid viscosity

In this section, we demonstrate in the limit $x_i \to 0$ the exact path length can be interpreted as a form of sub-grid model (Malaspinas *et al.*, 2008; Karlin *et al.*, 2015). For this purpose we consider from Eq.(6.53) the simplified departure of α from 2, i.e., $\alpha = \alpha_{\text{Lower}} = 2 - \Theta$. From the Chapman-Enskog expansion we know the relation of the kinematic viscosity ν,

$$\nu = \theta\tau = \theta\Delta t\left(\frac{1}{\alpha\beta} - \frac{1}{2}\right).$$

The path length α dictates whether the kinematic viscosity is larger or smaller than the base viscosity ν_0, where

$$\nu_0 = \theta\Delta t\left(\frac{1}{2\beta} - \frac{1}{2}\right). \tag{6.77}$$

A path length smaller than 2 implies an addition of viscosity that in turn smooths the gradients, whereas, a path length larger than 2 corresponds to removal of viscosity which sharpens the gradients (Karlin *et al.*, 2015). The turbulent viscosity correction ν_T is then found as

$$\nu_T = \nu - \nu_0 = \theta\left(\tau + \frac{\Delta t}{2}\right)\frac{\Theta}{2-\Theta}. \tag{6.78}$$

From Grad's 13 moment approximation $f = f^{\text{MB}}\left(1 + \Omega_{ijk}\right)$, where

$$\Omega_{ijk} = \frac{\sigma_{ij}\xi_i\xi_j}{2p\theta} - \frac{q_k\xi_k}{p\theta}\left(1 - \frac{\xi^2}{5\theta}\right),$$

---

[1] The airfoil simulations were performed by Chakradhar Thantanapally in SankhyaSutra Labs, Bangalore

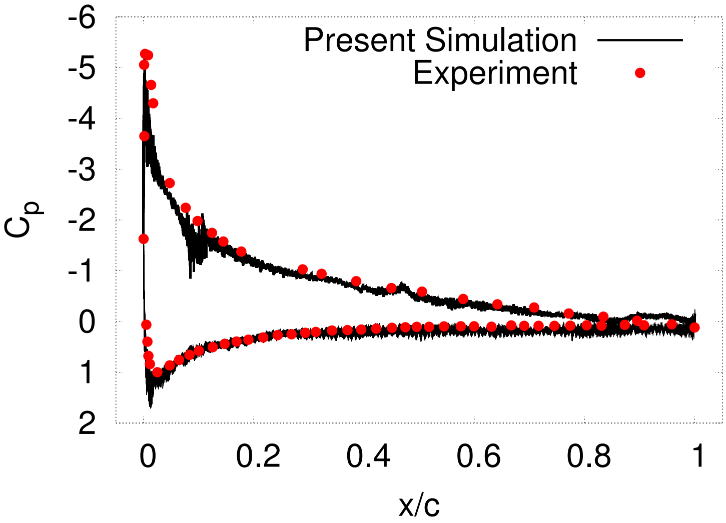

(a) C_p at AoA=10° and Re $= 2.88 \times 10^6$.

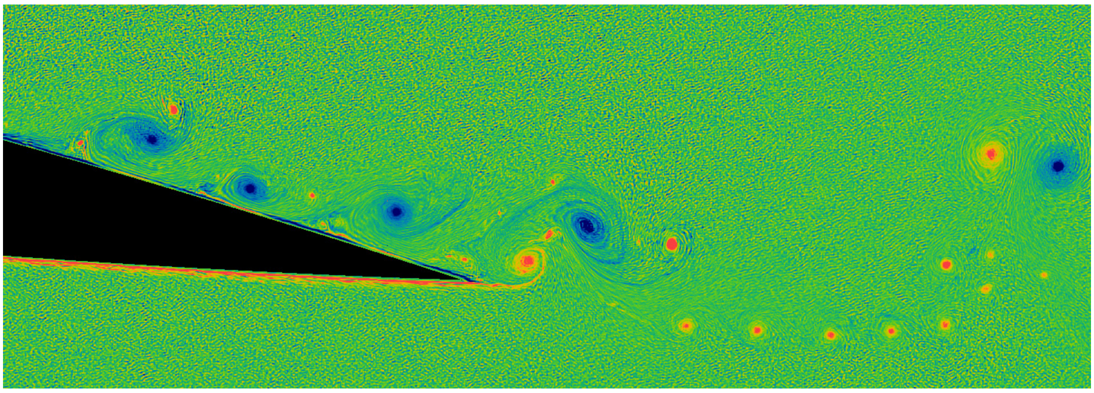

(b) Visualization of the trailing edge at AoA=10° and Re $= 2.88 \times 10^6$.

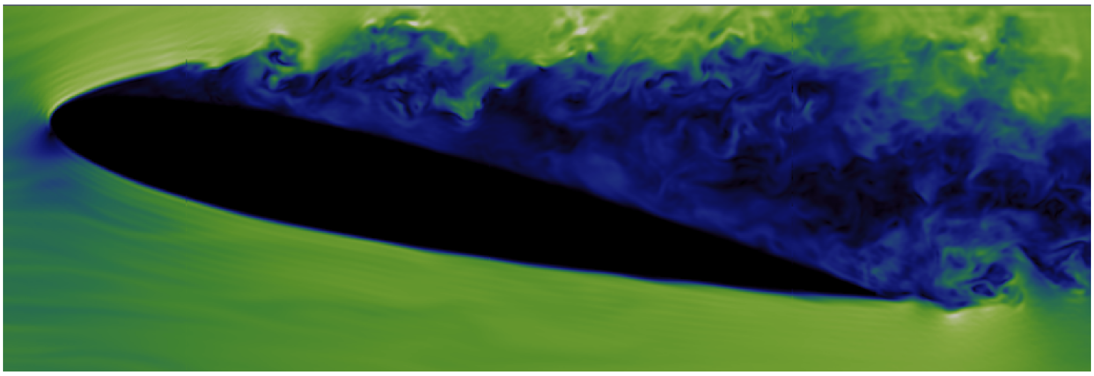

(c) Visualization of stall at AoA=12° and Re $= 5 \times 10^4$

Figure 6.16: Flow over NACA-0012 airfoil

f^{MB} is the Maxwell-Boltzmann distribution, ξ_i is the peculiar velocity, p is the pressure, θ is the temperature, σ_{ij} is the traceless part of symmetric stress tensor and q_k is the heat flux. We evaluate the two integrals,

$$\int_{-\infty}^{\infty} f x^2 d\boldsymbol{\xi} = \int_{-\infty}^{\infty} f^{\mathrm{MB}} \left(1 - \Omega_{ijk}\right) \Omega_{abc}\Omega_{def} d\boldsymbol{\xi} = \frac{1}{2p\theta}\sigma_{kl}\sigma_{lk} - \frac{1}{p^2\theta}\sigma_{jk}\sigma_{km}\sigma_{mj}, \tag{6.79}$$

$$\int_{-\infty}^{\infty} f x^3 d\boldsymbol{\xi} = \int_{-\infty}^{\infty} f^{\mathrm{MB}} \left(1 - 2\Omega_{ijk}\right) \Omega_{abc}\Omega_{def}\Omega_{xyz} d\boldsymbol{\xi} = -\frac{1}{p^2\theta}\sigma_{kl}\sigma_{lm}\sigma_{mk} + O(\sigma^4), \tag{6.80}$$

where assuming minute change in temperature, $O(q^2)$ terms have been ignored. Substituting $\boldsymbol{\sigma} = \rho\tau\theta\boldsymbol{S}$, $\boldsymbol{S}$ being the strain rate tensor and recognizing that $\boldsymbol{S}$ scales as $\boldsymbol{\nabla u}$, which is negligible for well resolved lattices we find the viscosity correction as

$$\nu_T = -\tau\theta\left(\tau + \frac{\Delta t}{2}\right)\frac{S_{ij}S_{jk}S_{ki}}{S_{mn}S_{nm} + \tau S_{ab}S_{bc}S_{ca}} \approx -\tau\theta\,\frac{\Delta t}{2}\frac{S_{ij}S_{jk}S_{ki}}{S_{mn}S_{nm}}, \tag{6.81}$$

as for hydrodynamic applications $\Delta t \gg \tau$. Notice that for very fine grid resolutions ($\Delta t \to 0$) the viscosity correction vanishes. The above expression for turbulent viscosity resembles the one previously seen in Malaspinas *et al.* (2008). It is also similar to Smagorinsky's model where the turbulent viscosity ν_T is

$$\nu_T = (c\Delta x)^2\sqrt{S_{ij}S_{ji}}, \tag{6.82}$$

in that, both scale like the strain rate tensor and also distinct from it because of emergence of the third invariant of the symmetrized strain rate tensor. (Smagorinsky *et al.*, 1965; Deardorff, 1970)

6.7 Conclusion

To conclude, this new exact solution is a step forward in the theoretical development of ELBM. The methodology to construct the exact solutions α_{Lower} and α_{Higher} can be extended to derive other expressions for the path length. However, we find that α_{Higher} is sufficient for hydrodynamic applications. The more dissipative solution α_{Lower} could also be employed to model very viscous flows in the vicinity of walls. In Appendix C, the discrete time $\mathcal{H}$ theorem is proved for the quasi-equilibrium model, which extends the second law to discrete dynamics for non-unitary Prandtl number flows.

Furthermore, this essentially entropic LBM provides an important first step in providing statistical mechanics route to sub-grid scale modeling. For example, using discrete entropic space-time dynamics for Boltzmann BGK equation, we have shown that the correction to viscosity ν_T is

$$\nu_T = -\tau\theta\,\frac{\Delta t}{2}\frac{S_{ij}S_{jk}S_{ki}}{S_{mn}S_{nm}}, \tag{6.83}$$

where S_{ij} is the strain rate tensor (Malaspinas *et al.*, 2008; Chikatamarla *et al.*, 2006). This emergence of the third invariant of symmetrized strain rate tensor is distinct from Smagorinsky's model for turbulent viscosity. Though physically appealing (Meneveau, 2011), further detailed numerical and theoretical analysis of current framework are needed to establish usefulness of this approach for theoretical sub-grid modeling. Finally, we highlight the fact that entropic formulation of continuous (in velocity space) BGK model provides a new discrete dynamical system analogue of Boltzmann dynamics. Thus, a Boltzmann like framework extends the second law to discrete dynamical systems too.

Chapter 7

Lattice Boltzmann model for compressible thermohydrodynamics

The initial lattice Boltzmann models were developed for simulating isothermal incompressible hydrodynamics. However, their domain of applicability was extended to thermal flows soon afterwards (Alexander *et al.*, 1993; Shan, 1997). In general, the thermal LBMs fall into three categories:

1. The passive-scalar approach (Bartoloni *et al.*, 1993; Shan, 1997) relies on the fact that the temperature behaves like a passive scalar provided viscous heat dissipation and compression work done by the pressure are negligible. Here, an extra distribution function is employed to solve the passive-scalar equation for temperature. These models were only capable of simulating compressible flows in the incompressible limit, and gave rise to unphysical phenomena for turbulent flows (Guo *et al.*, 2002).

2. The most popular methodology for simulating thermal flows in the LBM are the double population models where one models hydrodynamic on one set of population and solves the energy dynamics on the other (He *et al.*, 1998*a*). However, these models have been largely restricted to incompressible flows. As extension for compressible hydrodynamics requires multispeed models where one of the established model has 41 velocities (Chikatamarla & Karlin, 2009), a double distribution function approach would require at least 56 velocities (15 for energy dynamics). Furthermore, these models contain gradient operator term (that are non-trivial to evaluate numerically) in the evolution equation for the temperature and imposing the boundary conditions are non-trivial, and thus the simplicity of the isothermal LBM had been compromised (Peng *et al.*, 2003).

3. The multispeed approach is a generalization of the isothermal LBM (Alexander *et al.*, 1993), where one adds additional velocities to the basic LBM to acquire higher order isotropy and obtain the correct temperature dynamics. This requires a higher order model with equilibrium distribution which includes higher-order velocity terms. Even though this is a theoretically feasible approach, previous multispeed models suffered severe numerical instability and the working range for temperature variation was narrow (McNamara *et al.*, 1997).

In the recent years, multispeed models have witnessed a revival even for isothermal hydrodynamics. The motivation behind these models is their better accuracy in the velocity space that is relevant for microflows and enhanced numerical stability in turbulent flows due to better Galilean invariance (Chikatamarla *et al.*, 2006; Chikatamarla & Karlin, 2009). Most of these higher order models starts from the fact that the LBM is a low Mach number discretization (using Guasss-Hermite quadrature) of the Boltzmann equation with BGK approximation for the collision (Abe, 1997; He & Luo, 1997*a*,*b*; Shan & He, 1998*b*; Ansumali *et al.*, 2003; Yudistiawan *et al.*, 2010). A number of multispeed Cartesian lattices have been constructed using the quadrature approach by Shan (2010) which ensure an accurate evaluation of moments of the distribution (Shan *et al.*, 2006).

It is intriguing that conventional multispeed thermal models are unstable while multispeed isothermal models developed in recent years have shown better stability for turbulent flows (Chikatamarla *et al.*, 2010). The recent multispeed entropic models are also stable for both thermal and turbulent flows (Frapolli *et al.*, 2014, 2015). In these models, an expansion of local equilibrium distribution around the rest state is performed. For the thermal multispeed models, an additional expansion around reference temperature is also performed. These models explicitly impose sixth and/or eighth order isotropy of the zero velocity and reference temperature equilibrium (Yudistiawan *et al.*, 2010; Chikatamarla & Karlin, 2009). The enhanced stability of these entropic thermal models suggests that the instability is related to the way the discrete equilibrium is constructed. Starting from the formal entropic equilibrium, it was shown by Ansumali & Karlin (2005) that one should first construct equilibrium at zero velocity but non-zero variation in temperature followed by expansion in Mach number around this state. One would expect such an expansion to be more stable than a direct two variable expansion in Mach and temperature deviation. Finally, it is conjectured that the working temperature range does not change substantially for entropic models unless eighth order isotropy is imposed and the narrow temperature range is related to the way the discrete velocity models are constructed. In this chapter, we validate the stability of a higher order multispeed model with sixty-seven discrete velocities for various canonical cases of compressible thermohydrodynamics.

This chapter is organized as follows: In Section 7.1 we will derive a higher-order $RD3Q67$ model which satisfies the eighth order isotropy conditions. In Section 7.2 we propose implementation for kinetic diffuse boundary condition for higher order crystallographic models. We then employ the $RD3Q67$ model to simulate compressible and thermal flows and demonstrate its accuracy and stability. We consider a number of setups, beginning with simple transient hydrodynamics in Section 7.3 and steady state heat conduction in Section 7.4. In Section 7.5 we simulate a few test cases like Sod shock tube, thermoacoustic convection and the classical Rayleigh-Bénard convection.

7.1 The $RD3Q67$ Model

In Chapter 4, it was shown that in order to get the correct thermohydrodynamic limit, the moments of equilibrium distribution must match the moments of the Maxwell-Boltzmann distribution. The conditions on the moments of the equilibrium are translated to constraints on the weights, discrete velocities, and the reference temperature θ_0 of the lattice. To summarize, the constraints are

$$\begin{aligned}\langle w, \{1, c_\alpha c_\beta\}\rangle &= \{1, \theta_0 \delta_{\alpha\beta}\},\\ \langle w, \{c_\alpha c_\beta c_\gamma c_\kappa, c_\alpha c_\beta c_\gamma c_\kappa c_\zeta c_\eta\}\rangle &= \{\theta_0^2 \Delta_{\alpha\beta\gamma\kappa}, \theta_0^3 \Delta_{\alpha\beta\gamma\kappa\zeta\eta}\},\\ \left\langle w, \{c^4 c_\alpha c_\beta c_\gamma c_\kappa, c^{10}\}\right\rangle &= \{63\theta_0^4 \Delta_{\alpha\beta\gamma\kappa}, 10395\theta_0^5\},\end{aligned} \tag{7.1}$$

which using Eq.(3.4) are written in the explicit form as a system of ten equations

$$\begin{aligned}\langle w, 1\rangle = 1, \left\langle w, c^2\right\rangle = 3\theta_0, \left\langle w, c^4\right\rangle = 15\theta_0^2, \left\langle w, c^2 c_x^2\right\rangle = 5\theta_0^2,\\ \left\langle w, c^6\right\rangle = 105\theta_0^3, \left\langle w, c^2 c_x^2 c_y^2\right\rangle = 7\theta_0^3, \left\langle w, c^4 c_x^2\right\rangle = 35\theta_0^3,\\ \left\langle w, c^8\right\rangle = 945\theta_0^4, \left\langle w, c^4 c_x^4\right\rangle = 189\theta_0^4, \left\langle w, c^{10}\right\rangle = 10395\theta_0^5.\end{aligned} \tag{7.2}$$

As the total number of constraints is ten, we will require eight energy shells that when combined with w_0 and θ_0 will make a total of ten unknowns. The eight energy shells chosen are 3 SC, 2 FCC and 3 BCC. The set of Eqs.(7.1) has many solutions and we accept the one that satisfies the condition that all w_i are real and positive. The discrete velocities and the weights corresponding to each shell are listed the Table 7.1, and the relevant energy shells are depicted in Figure 7.1. The eighth order moments of the weights that are not imposed in the model with their respective

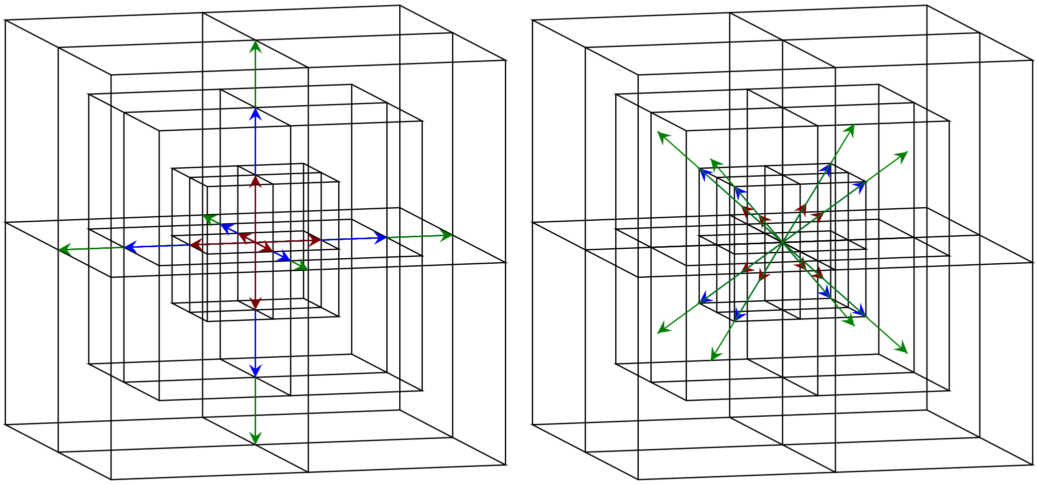

(a) SC1,SC2,SC3 (b) BCC$\frac{1}{2}$,BCC1,BCC$\frac{3}{2}$

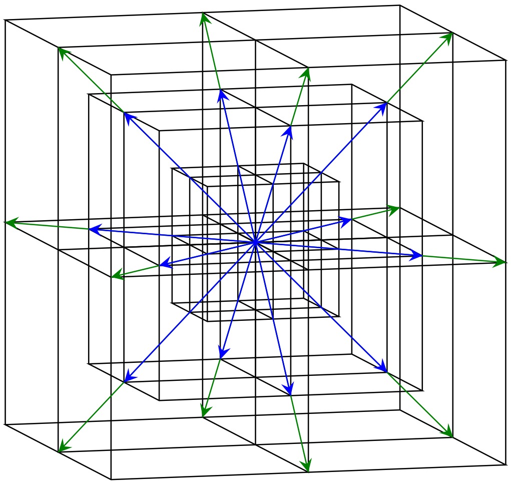

(c) FCC2,FCC3

Figure 7.1: The energy shells in $RD3Q67$ model.

Shells	Discrete Velocities ($\boldsymbol{c}_i$)	Weight(w_i)
0	$(0,0,0)$	0.062612244873699
SC1	$(\pm1,0,0)\,,(0,\pm1,0)\,,(0,0,\pm1)$	0.07078157740182597
SC2	$(\pm2,0,0)\,,(0,\pm2,0)\,,(0,0,\pm2)$	0.018477181295835005
SC3	$(\pm3,0,0)\,,(0,\pm3,0)\,,(0,0,\pm3)$	0.001159725348044425
FCC2	$(\pm2,\pm2,0)\,,(0,\pm2,\pm2)\,,(\pm2,\pm2,0)$	0.003016018666364516
FCC3	$(\pm3,\pm3,0)\,,(0,\pm3,\pm3)\,,(\pm3,\pm3,0)$	0.000023115090889762186
BCC$\frac{1}{2}$	$(\pm0.5,\pm0.5,\pm0.5)$	0.005042859365786889
BCC1	$(\pm1,\pm1,\pm1)$	0.03854231746999835
BCC$\frac{3}{2}$	$(\pm1.5,\pm1.5,\pm1.5)$	0.0012157288848419236

Table 7.1: Energy shells and their corresponding velocities with weights for $RD3Q67$ model, $\theta_0 = 0.7487399237215752$.

percentage error are

$$
\begin{aligned}
\left\langle w, c_x^8 \right\rangle &= 104.260789709991\, \theta_0^4, \quad \%\text{error} = 0.70\%,\\
\left\langle w, c_x^6 c_y^2 \right\rangle &= 13.5316387022748\, \theta_0^4, \quad \%\text{error} = 9.79\%,\\
\left\langle w, c_x^4 c_y^4 \right\rangle &= 13.5316387022748\, \theta_0^4, \quad \%\text{error} = 9.79\%,\\
\left\langle w, c_x^4 c_y^2 c_z^2 \right\rangle &= 1.77468903818019\, \theta_0^4, \quad \%\text{error} = 40.84\%.
\end{aligned}
$$

The series approximation of the equilibrium distribution for the set of discrete velocities is

$$
f_i^{\text{eq}} = \tilde{f}_i^{\text{eq}} \left(1 + \frac{u_\alpha c_{i\alpha}}{\theta} - \frac{u^2}{2\theta} + \frac{1}{2} \left(\frac{u_\alpha c_{i\alpha}}{\theta} \right)^2 + \frac{1}{6} \left(\frac{u_\alpha c_{i\alpha}}{\theta} \right)^3 - \frac{u^2 u_\alpha c_{i\alpha}}{2\theta^2} \left(1 - \mathcal{A}\right) \right), \tag{7.3}
$$

where $\mathcal{A} = 0.085582531\, \eta^3\, \theta_0^2/\theta^2$, $\eta = \theta/\theta_0 - 1$ and $\tilde{f}_i^{\text{eq}}$ accurate upto $\mathcal{O}(\eta^4)$ is given by Eq.(3.27). The equilibrium moments for this model are

$$
\langle f_i^{\text{eq}}, c_{i\alpha} c_{i\beta} \rangle = \rho\theta\delta_{\alpha\beta} + \rho u_\alpha u_\beta \left(1 - \frac{9}{2}\mathcal{A} \right) + \frac{3}{2}\mathcal{A}\, \rho u^2\, \delta_{\alpha\beta}, \tag{7.4}
$$

$$
\left\langle f_i^{\text{eq}}, c_i^2 c_{i\alpha} \right\rangle = 5\rho\theta u_\alpha + \rho u^2 u_\alpha \left(1 - \frac{3}{2}\mathcal{A} - \mathcal{B} \right), \tag{7.5}
$$

where $\mathcal{B} = 0.018853638\, \eta^4\, \theta_0^3/\theta^3$. From the relation $\sigma_{\alpha\beta}^{\text{eq}} = \langle f_i^{\text{eq}}, c_{i\alpha} c_{i\beta} \rangle - \rho u_\alpha u_\beta - p\delta_{\alpha\beta}$ one obtains

$$
\sigma_{\alpha\beta}^{\text{eq}} = \frac{3}{2}\mathcal{A}\rho(u^2 \delta_{\alpha\beta} - 3u_\alpha u_\beta), \tag{7.6}
$$

and from the relation $q_\alpha^{\text{eq}} = \left\langle f_i^{\text{eq}}, c^2 c_{i\alpha}/2 \right\rangle - u_\alpha(E + p) - u_\beta \sigma_{\alpha\beta}^{\text{eq}}$ we have

$$
q_\alpha^{\text{eq}} = \rho u^2 u_\alpha \left(-\frac{3}{2}\mathcal{A} + \frac{1}{2}\mathcal{B} \right), \tag{7.7}
$$

and

$$
R^{\text{eq}}(u = 0) = \sum \tilde{f}_i^{\text{eq}} c_i^4 = 15\rho\theta^2 + 6.051158073\rho\theta_0^2\eta^4. \tag{7.8}
$$

From Eq.(7.6) and $\mathcal{A}$ we see that the error in $\sigma_{\alpha\beta}^{\text{eq}}$ is of $\mathcal{O}(u^2\eta^3)$, Similarly, from Eq.(7.7) and $\mathcal{B}$ the error in q_α^{eq} is of $\mathcal{O}(u^3\eta^3)$, while the error in $R^{\text{eq}}(u = 0)$ from Eq.(7.8) is of $\mathcal{O}(\eta^4)$. The viscosity for this model is $\mu = \tau p$ and the thermal conductivity is $\kappa = (5/2)\mu$. Further, as pointed out earlier in Eq.(3.18) the main source of error in the Fourier's law is the term containing $(R^{\text{eq}} - R^{\text{MB}})$, which for the current model is $6.051158073\rho\eta^4\theta_0^2$. The error could be reduced by taking into account this deviation via correction of thermal conductivity. This is shown in Section 7.4.1. The form of corrected thermal conductivity is

$$
\kappa = \frac{5}{2}\mu \left(1 + 1.613642153\eta^3 \frac{\theta_0}{\theta} \right). \tag{7.9}
$$

It is evident that as $\theta \to \theta_0 \Rightarrow \eta \to 0$, and hence the correction in thermal conductivity vanishes.

7.2 Kinetic boundary condition

In this section, we will present the kinetic diffuse boundary condition (Gatignol, 1977; Ansumali & Karlin, 2002*b*; Sbragaglia & Sugiyama, 2010; Meng & Zhang, 2014) and its implementation for the proposed model. This boundary condition assumes that upon encountering the wall the populations completely forget their history. It also assumes that the time spent by the population inside the wall is negligible as compared to any characteristic time. Here, for illustration we will

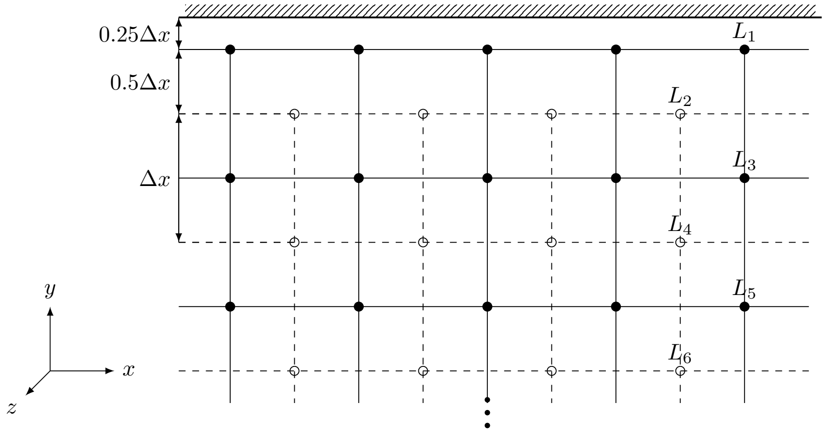

Figure 7.2: Populations at each layer that see the top wall and need to be repopulated post streaming are listed in Table 7.2.

Layer	Incoming populations f^I_{i,L_k}	Total number
L_1	$(0,-1,0),(\pm1,-1,\pm1)$ $(0,-2,0),(\pm2,-2,0),(0,-2,\pm2)$ $(0,-3,0),(\pm3,-3,0),(0,-3,\pm3)$ $(\pm1.5,-1.5,\pm1.5),(\pm0.5,-0.5,\pm0.5)$	23
L_2	$(0,-1,0),(\pm1,-1,\pm1)$ $(0,-2,0),(\pm2,-2,0),(0,-2,\pm2)$ $(0,-3,0),(\pm3,-3,0),(0,-3,\pm3)$ $(\pm1.5,-1.5,\pm1.5)$	19
L_3	$(0,-2,0),(\pm2,-2,0),(0,-2,\pm2)$ $(0,-3,0),(\pm3,-3,0),(0,-3,\pm3)$ $(\pm1.5,-1.5,\pm1.5)$	14
L_4	$(0,-2,0),(\pm2,-2,0),(0,-2,\pm2)$ $(0,-3,0),(\pm3,-3,0),(0,-3,\pm3)$	10
L_5	$(0,-3,0),(\pm3,-3,0),(0,-3,\pm3)$	5
L_6	$(0,-3,0),(\pm3,-3,0),(0,-3,\pm3)$	5

Table 7.2: Incoming populations at each layer near the top wall.

consider the top wall with the normal in y-direction. The boundary condition for other walls is formulated in the same manner. For higher-order and crystallographic models, such as the one proposed in the previous sections, populations from multiple layers constitute the outgoing set of populations and need to be properly identified. Note that the incoming and outgoing populations are reflection of each other about the wall.

For the $RD3Q67$ model, at each wall we encounter six layers $L_k, k = 1...6$ (see Figure 7.2) that have populations missing post streaming and need to be refilled. These layers L_k are at a distance of $0.25\Delta x + 0.5(k-1)\Delta x$. The total number of incoming/outgoing populations at the layers L_1 to L_6 are $23, 19, 14, 10, 5, 5$ respectively. The incoming populations are listed in Table 7.2. The outgoing populations $f^{\mathrm{O}}_{i,L_k}, k = 1...6$ are diffused into the wall and are reflected back in form of a new distribution $f^{\mathrm{I}}_{i,L_k}, k = 1...6$. The magnitude of incoming populations f^{I}_{i,L_k} is updated via the relation

$$\begin{aligned} f^I_{i,L_h}(\boldsymbol{x},t) &= \frac{\sum_{k=1,3,5}\sum f^{\mathrm{O}}_{i,L_k}(\boldsymbol{x},t)|c_{iy}|}{\sum_{k=1,3,5}\sum f^{\mathrm{eq}}_{i,L_k}(\rho_{\mathrm{w}},\boldsymbol{u}_w,\theta_{\mathrm{w}})|c_{iy}|} f^{\mathrm{eq}}_{i,L_h}(\rho_{\mathrm{w}},\boldsymbol{u}_w,\theta_{\mathrm{w}}), \qquad h=1,3,5, \\ f^I_{i,L_h}(\boldsymbol{x},t) &= \frac{\sum_{k=2,4,6}\sum f^{\mathrm{O}}_{i,L_k}(\boldsymbol{x},t)|c_{iy}|}{\sum_{k=2,4,6}\sum f^{\mathrm{eq}}_{i,L_k}(\rho_{\mathrm{w}},\boldsymbol{u}_w,\theta_{\mathrm{w}})|c_{iy}|} f^{\mathrm{eq}}_{i,L_h}(\rho_{\mathrm{w}},\boldsymbol{u}_w,\theta_{\mathrm{w}}), \qquad h=2,4,6, \end{aligned} \tag{7.10}$$

where i are the populations at each L_k corresponding to Table 7.2, $\rho_w = 1$ and the u_w, θ_w are wall velocity and temperature respectively. The above prescription conserves the mass flux at the boundary. The minor fluctuations introduced in mass due to difference $\sum(f^{\mathrm{O}}_{i,L_k} - f^{\mathrm{I}}_{i,L_k})$ are eliminated by manipulating the stationary population f_0 at each node. However, the implementation of the complex boundary conditions (any thing other than bounce-back) is a non-trivial open question. Extensions of the bounce-back boundary condition for imposing temperature and velocity are the diffuse bounce-back boundary condition (Krithivasan *et al.*, 2014) or the boundary condition proposed by Frapolli *et al.* (2016*a*). We leave the extension of kinetic diffuse boundary condition as subject of subsequent studies with the following suggestion as possible remedy

$$f^I_{i,L_h}(\boldsymbol{x},t) = \sum_j \frac{f^{\mathrm{O}}_{j,L_h}(\boldsymbol{x},t)|\boldsymbol{c}_j\cdot\boldsymbol{n}|}{\sum f^{\mathrm{eq}}_{j,L_h}(\rho_{\mathrm{w}},\boldsymbol{u}_w,\theta_{\mathrm{w}})|\boldsymbol{c}_j\cdot\boldsymbol{n}|} f^{\mathrm{eq}}_{i,L_h}(\rho_{\mathrm{w}},\boldsymbol{u}_w,\theta_{\mathrm{w}}), \qquad h=1..6. \tag{7.11}$$

In the above equation, each outgoing population contributes individually to each incoming population.

7.3 Hydrodynamics: Start-up of simple shear flow

In this section, we consider the start-up flow of fluid situated between two parallel plates due to sudden movement of the plates. These tests are used to assess the accuracy of transient dynamics. We consider two cases:

- Case (A): at $t = 0$ the plate at $y = 0$ begins to move with a constant velocity U_{wall} in x-direction. The other plate at $y = H$ is kept stationary. The analytical expression for velocity profile is (Leal, 2007)

$$\bar{u}(\bar{y},\bar{t}) = (1-\bar{y}) - \sum_{n=1}^{\infty} \frac{2}{n\pi}\exp(-n^2\pi^2\bar{t})\sin n\pi\bar{y}, \tag{7.12}$$

  where the non-dimensionalized variables $\bar{u} = u/U_{\mathrm{wall}}, \bar{y} = y/H$ and $\bar{t} = t\nu/H^2$ with ν as the kinematic viscosity. The solution for velocity profile at sufficiently long time is $\bar{u}(y, t=\infty) = 1-\bar{y}$.

- Case (B): at $t = 0$ the plate at $y = 0$ begins to move with a constant velocity $-U_{\mathrm{wall}}$ and other plate at $y = H$ begins to move with a constant velocity U_{wall}. The analytical expression for velocity profile is (Appendix B.1)

$$\bar{u}(\bar{y},\bar{t}) = \bar{y} + \sum_{n=1}^{\infty} \frac{1+\cos n\pi}{n\pi}\exp(-n^2\pi^2\bar{t})\sin n\pi\bar{y}.$$

These setups were simulated on a grid of size 8 × 128 × 8 points with wall imposed in y-directions and periodic boundary condition in the other two directions. The velocity of the moving wall was taken to be $U_{\mathrm{wall}} = 0.02$. The kinematic viscosity was chosen such that the

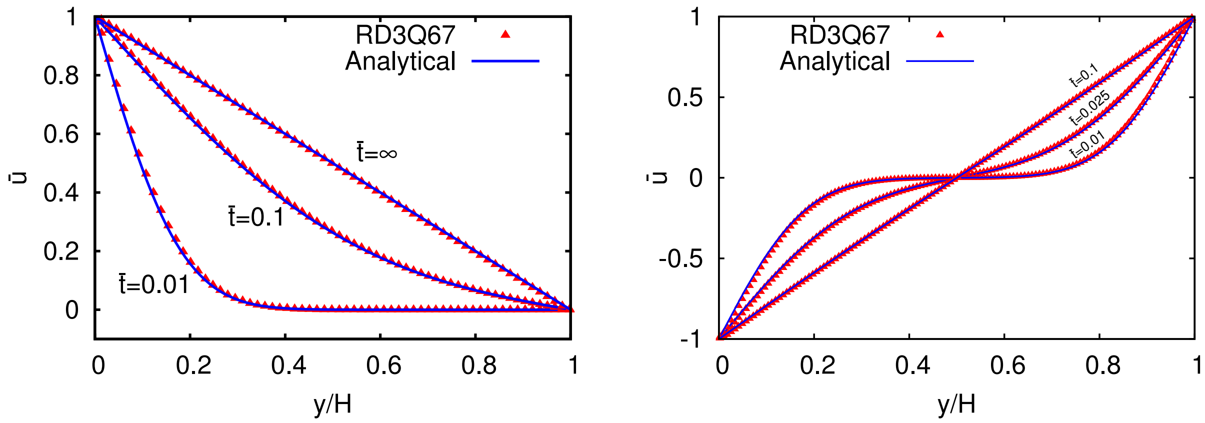

(a) Case (A) (b) Case (B)

Figure 7.3: Non-dimensionalized mean planar velocity profiles obtained from $RD3Q67$ at various diffusion times compared against the analytical solution.

Reynolds number $\mathrm{Re} = U_{\mathrm{wall}}H/\nu = 512$. The mean planar velocity at various times is compared against the analytical solution given by Eq.(7.12) in Figure 7.3 and is found to be in good agreement.

7.4 Heat conduction: Steady state

In this section, we consider the steady state for the heat transfer in one and two dimensions. The first two subsections simulate a fluid at rest with only one wall heated, while the third subsection studies the effect of the viscous heat dissipation due to a moving heated wall.

7.4.1 One-dimensional heat conduction

We consider the steady state for the heat transfer in fluid confined to a one-dimensional domain of height H. The top wall at $y = H$ is subjected to a constant elevated temperature θ_{top} and the bottom wall at $y = 0$ is maintained at θ_0. The steady state temperature profile is $\theta = \theta_0 + (\theta_{\mathrm{top}} - \theta_0)y/H$. The simulations were performed on a grid of size $8 \times 32 \times 8$ and Knudsen number $\mathrm{Kn} = 10^{-3}$. The relaxation time τ is related to Kn via $\mathrm{Kn} = \tau c_s/H$, where the sound speed $c_s = \sqrt{(5/3)\theta}$. The temperature profiles for various values of the temperature jump are given in Figure 7.4. It is seen that the model is accurate and stable for temperatures elevations as high as 50% of θ_0. Further, from the Figure 7.5(a) plots the L^2 norm for various grid sizes and reveals second order convergence.

As pointed in Eq.(7.9), the corrected thermal conductivity is expected to reduce the error. Figure 7.5(b) contrasts the L^2-norm obtained using the thermal conductivity correction to that obtained without using the correction. It is evident that for lower values of θ_{top} the L^2-norm remains almost the same while for higher values it decreases upon using the thermal conductivity correction.

7.4.2 Two-dimensional cavity heated at the top

We consider another simple heat transfer problem in a two-dimensional box of length L and width W subjected to an elevated temperatures at the top wall as represented in Figure 7.6. The simulations were performed on a grid of size $256 \times 128 \times 8$ with $\Delta\theta = 0.10\,\theta_0$ at $\mathrm{Kn} = 10^{-3}$. The rapid heating at the top wall will initiate thermoacoustic convection in the early stages of

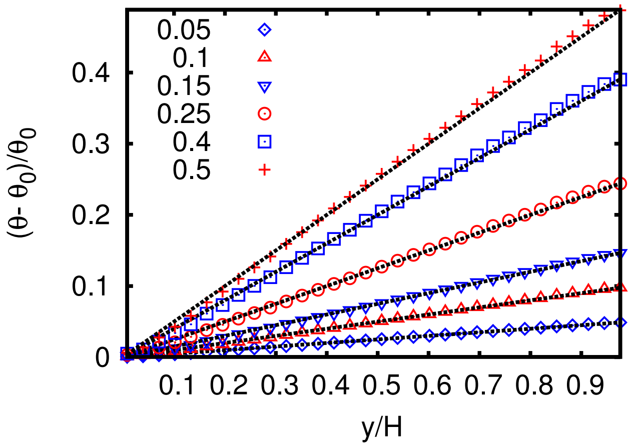

Figure 7.4: Temperature plots without including the thermal conductivity correction for different magnitudes of the top wall temperature.

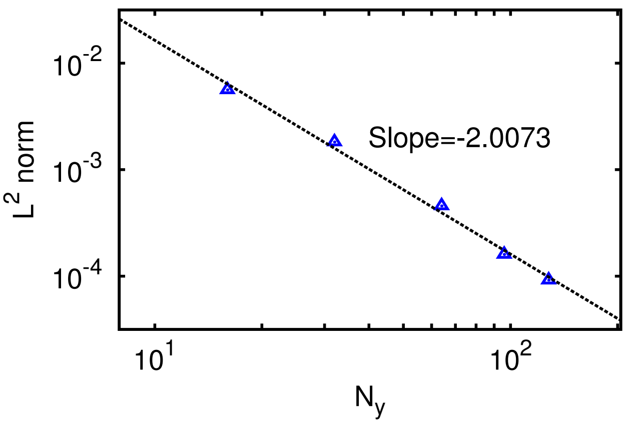

(a) L^2 norm at $\theta_{\text{top}} = 1.2\theta_0$ and different grid resolutions reveals second order convergence.

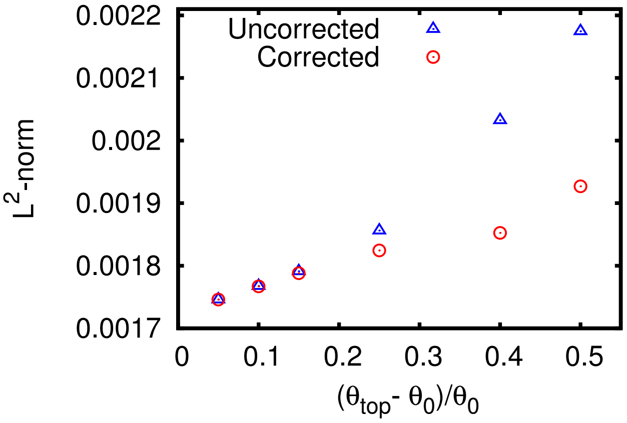

(b) Comparison for corrected and uncorrected thermal conductivity at various magnitudes of the top wall temperature. Here, resolution is kept fixed at $N = 32$.

Figure 7.5: L^2-norms of temperature

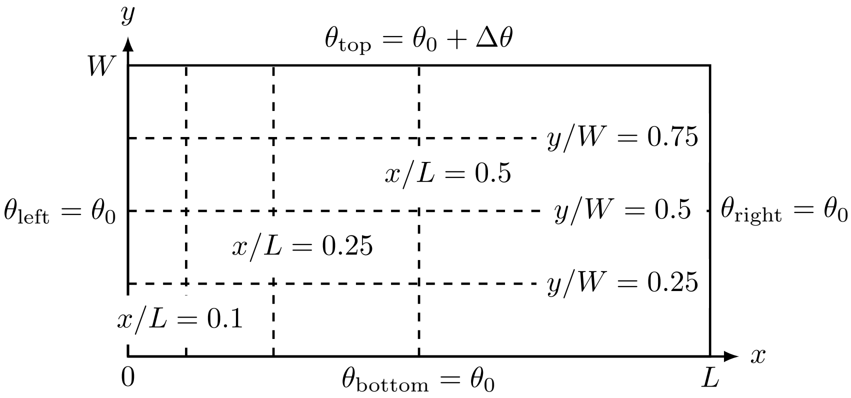
y
W
$\theta_{\text{top}} = \theta_0 + \Delta\theta$
$y/W = 0.75$
$x/L = 0.5$
$\theta_{\text{left}} = \theta_0$
$y/W = 0.5$
$\theta_{\text{right}} = \theta_0$
$x/L = 0.25$
$y/W = 0.25$
$x/L = 0.1$
x
0
$\theta_{\text{bottom}} = \theta_0$
L

Figure 7.6: Sketch representing the geometry of the two-dimensional box and the imposed wall temperatures.

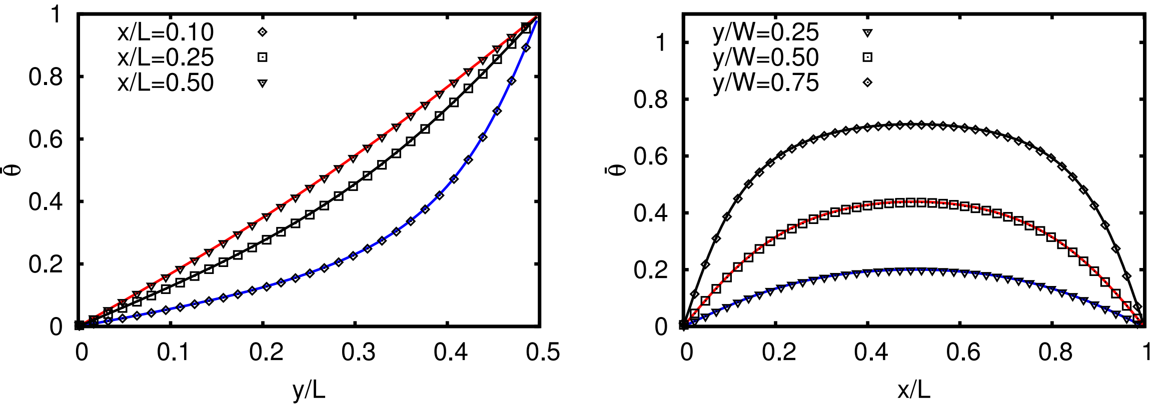

(a) Temperature plots along constant x-lines

(b) Temperature plots along constant y-lines

Figure 7.7: Steady-state conduction in a two-dimensional plate. The solid lines are the analytical solution of the conduction equation while the symbols are from simulations.

the simulation, which will be discussed in later sections. We study the system at steady state where the only mode of heat transfer is pure conduction.

The analytical expression for the normalized temperature $\bar{\theta}(x, y, t = \infty)$ is found as the steady state solution of conduction equation (see Appendix B.2 for details)

$$\bar{\theta}(x, y, t = \infty) = \frac{2}{\pi} \sum_{k=1}^{\infty} \frac{1 - \cos(k\pi)}{k} \sin(k\pi x) \frac{\sinh(k\pi y)}{\sinh(k\pi W/L)}. \tag{7.13}$$

The mean planar temperature profiles at $x = 0.1, 0.25, 0.5$ and $y = 0.25, 0.5, 0.75$ are represented in Figures 7.7a,7.7b respectively and are found to match well with the analytical solution.

7.4.3 Viscous heat dissipation

In this section, we consider the steady-state of flow induced by wall at $y = H$ moving with a constant horizontal velocity U_{wall} and maintained at a constant elevated temperature θ_{hot}. The lower wall at $y = 0$ is kept stationary at a constant temperature $\theta_{\text{cold}}(< \theta_{\text{hot}})$. This setup is well suited to validate the effect of viscous heat dissipation. Each layer of fluid drags the layer adjacent to it due to friction which results in the mechanical energy being converted to

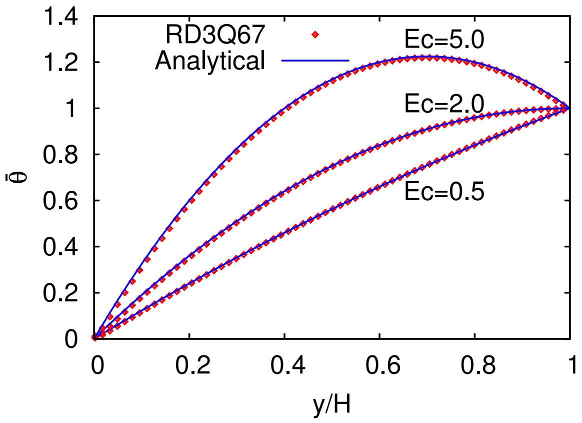

Figure 7.8: Mean planar temperature profiles obtained from $RD3Q67$ at steady state compared against the analytical solution.

thermal heating, and therefore, the heat produced affects the temperature profile in the bulk. The analytical solution for the temperature profile is (Bird *et al.*, 2015)

$$\frac{\theta - \theta_{\text{cold}}}{\theta_{\text{hot}} - \theta_{\text{cold}}} = \frac{y}{H} + \frac{\text{Ec}}{2}\frac{y}{H}\left(1 - \frac{y}{H}\right), \tag{7.14}$$

where the $\text{Ec} = U_{\text{wall}}^2/(c_p \Delta\theta)$ is the Eckert number that represents the ratio of viscous dissipation to heat conduction with c_p as the specific heat at constant pressure and $\Delta\theta = \theta_{\text{hot}} - \theta_{\text{cold}}$ is the temperature difference between the two walls.

Simulations were performed for $\text{Ec} = 0.5, 2.0, 5.0$ on a grid size of $24 \times 128 \times 24$ with $U_{\text{wall}} = 0.02$ and $\Delta\theta$ calculated according to respective Eckert numbers. The walls were maintained at temperatures $\theta_0 + 0.5\Delta\theta$ and $\theta_0 - 0.5\Delta\theta$ with periodic boundary condition in the other two directions. The normalized mean planar temperature profile at steady state is compared against the analytical solution given by Eq.(7.14) in Figure 7.8 and is found to be in agreement. This suggests that the thermal transport phenomenon is modeled correctly.

7.5 Compressible thermohydrodynamics

A variety of problems of practical interest have velocity and temperature dynamics coupled together. This coupling makes it nontrivial for any fluid solver to represent the physics accurately. The aim of this section is to benchmark the proposed model for thermal and compressible flows. The setups chosen are the Sod shock tube – a widely used test for the accuracy of compressible solvers, the thermoacoustic convection – which has the presence of various time and length scales, and the Rayleigh-Bénard convection- a standard test case for thermal flows (Frapolli *et al.*, 2014).

7.5.1 Sod shock tube

We study the time evolution of a one-dimensional front in Sod's shock tube. This is considered to be a standard test case to check the accuracy and stability of compressible flow solvers. The setup consists of an initially quiescent fluid in the two regions L and R. The two regions located in $x = -0.5$ to 0.0 and $x = 0.0$ to 0.5 respectively are separated by an interface at $x = 0$ across

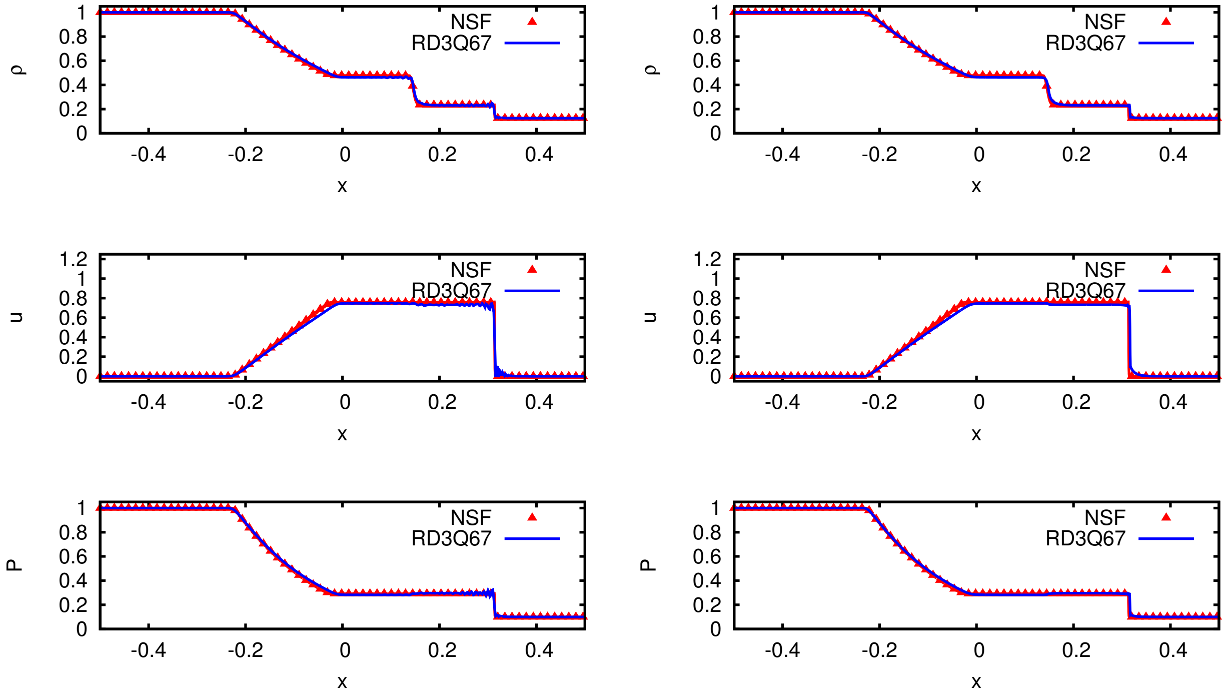

Figure 7.9: The figure shows the variation of density (ρ), velocity($\boldsymbol{u}$), and pressure (P) along the tube for the Sod's shock test. The figure contrasts $RD3Q67$ simulation results from run A (left) and B (right) with NSF equations at $t^* = 0.2$.

which the density and pressure have a jump. The initial condition is given by

$$\begin{pmatrix} \rho_L \\ u_L \\ p_L \end{pmatrix} = \begin{pmatrix} 1 \\ 0 \\ 1 \end{pmatrix}, \qquad \begin{pmatrix} \rho_R \\ u_R \\ p_R \end{pmatrix} = \begin{pmatrix} 0.125 \\ 0 \\ 0.1 \end{pmatrix}. \tag{7.15}$$

The presence of a sharp discontinuity in the initial condition at the center of the domain generates a moving compressive shock front in the low density region and rarefaction front in the high density region. These two fronts leave behind a central contact region of uniform pressure and velocity (Laney, 1998).

As a test case we consider the reference viscosity $\mu = 10^{-5}$. The simulations were performed on a coarse grid A of size $500 \times 8 \times 8$, and a refined grid B of size $2000 \times 8 \times 8$. The periodic boundary conditions were implemented in $y, z-$normal directions and standard bounce back in x-normal direction. The time scale is chosen based on the length of the domain and speed of sound in the right section of the domain. The simulations were run till the nondimensional time $t^* = 0.2$, which is much earlier than the time required for either of the fronts to hit the wall. The nondimensional time is defined as $t^* = tc_{sR}/L_{\text{ref}}$ where c_{sR} is the speed of sound in the right section of the domain.

Figure 7.9 contrasts the density, pressure and velocity obtained from the present model with those from the direct integration of Navier-Stokes-Fourier equations. Simulations on the coarse grid show oscillations in the region of discontinuity. The contact region shows a minute jump in the pressure and there exists a small discrepancy in velocity at the tail of the expansion front. It is evident that the speed of the shock is accurately captured by the model.

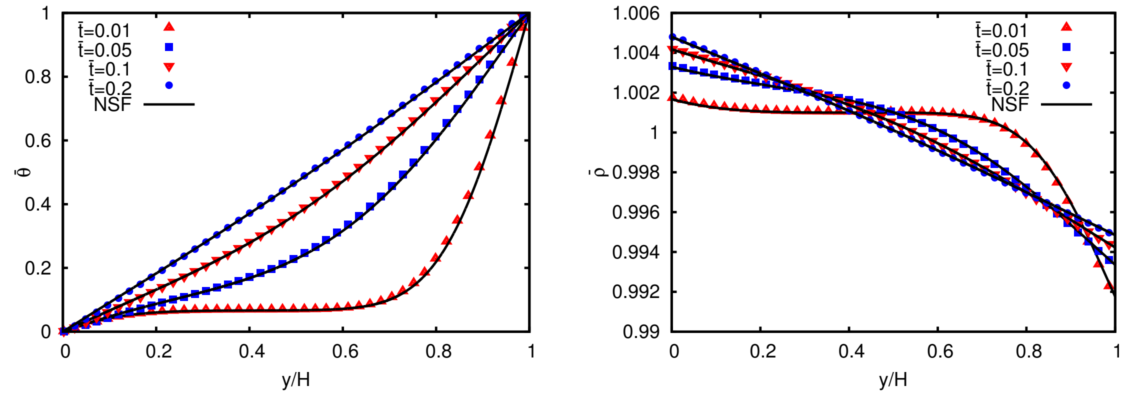

(a) Normalized temperature $\bar{\theta} = (\theta - \theta_{\text{cold}})/(\theta_{\text{hot}} - \theta_{\text{cold}})$ (b) Density $\bar{\rho} = \rho/\rho_0$

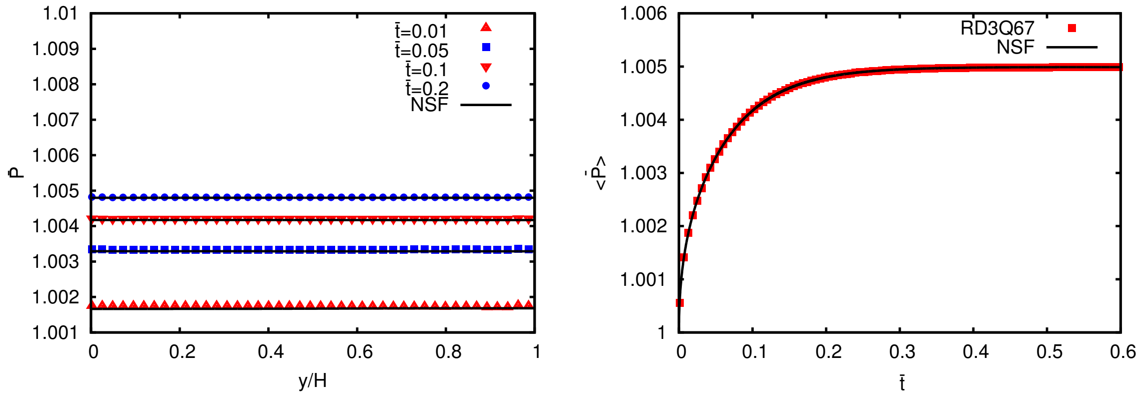

(c) Pressure $\bar{P} = \rho\theta/(\rho_0\theta_{\text{cold}})$ (d) $\langle \bar{P} \rangle$ is the volume averaged pressure

Figure 7.10: Temperature, density and pressure profiles for thermoacoustic convection at various times. Here $\bar{t} = t\nu/H^2$. The symbols are obtained from simulation while the lines are from the solution to the NSF equations.

7.5.2 Thermoacoustic convection

Thermoacoustic convection refers to the convective currents set up in a compressible fluid due to rapid heating of one of the walls (Larkin, 1967; Parang & Salah-Eddine, 1984; Huang & Bau, 1997). It manifests in the form of a pressure wave initiated at the heated wall that is reflected back and forth in the domain until it gets dissipated by viscosity. The thermally induced motion is known to enhance the heat transfer relative to pure conduction by addition of a convective mode (Larkin, 1967). As the steady state is attained the convective mode gradually dissipates and conduction becomes the dominant mode of heat transfer (Spradley & Churchill, 1975). The numerical modeling of thermoacoustic phenomenon is considered a challenging problem due to the presence of multiple time and length scales.

The simulation is performed in a box of height H with walls at the top and the bottom and periodic in the other two directions. The grid size is $8 \times 128 \times 8$ with $\theta_{\text{hot}} = 1.01\theta_0$, $\theta_{\text{cold}} = \theta_0$, and $u_{\text{top}} = u_{\text{bottom}} = 0$. The viscosity is calculated from the Knudsen number $\text{Kn} = 10^{-4}$. To benchmark the results, the compressible Navier-Stokes-Fourier (NSF) were solved using the scheme of Larkin (1967) subjected to the boundary conditions

$$\begin{aligned} u(y=0,t) &= u(y=H,t) = 0, \\ \theta(y=H,t) &= \theta_{\text{hot}}, \\ \theta(y=0,t) &= \theta_{\text{cold}}, \end{aligned} \tag{7.16}$$

and initial condition $\rho(y, t = 0) = \rho_0, u(y, t = 0) = 0$ and $\theta(y, t = 0) = \theta_{\text{cold}}$. Figure 7.10 compares the temperature, density, and pressure profile obtained from the $RD3Q67$ simulations with solution to NSF equations and they are found to be in agreement. This suggests that the current model is well suited for studying the various compressible flows.

7.5.3 Rayleigh-Bénard convection

Rayleigh-Bénard convection is considered to be an important benchmark for the thermal models (Shan, 1997). The setup consists of a horizontal layer of viscous fluid confined between two thermally well conducting parallel plates kept at a distance L. An adverse temperature gradient is maintained by keeping the bottom plate at an excess temperature θ_{bottom}, while the top plate is at a lower temperature θ_{top}. The flow is driven by the temperature induced unstable density gradients in the presence of external force field (usually gravitational field). The fluid in contact with the heated bottom plate becomes less dense due to which it experiences a buoyant force and ascends. On coming in contact with the cold top plate, it becomes more dense and starts to descend. This continuous motion of the fluid leads to formation of adjacent convective cells between the plates, within which the fluid moves in closed paths (Landau & Lifshitz, 2013).

The dynamics is characterized by the non-dimensional Rayleigh number (Ra), that represents the strength of buoyancy driven inertial force to the viscous force and is defined as

$$\text{Ra} = \frac{g_y \hat{\beta} \Delta\theta L^3}{\nu \alpha_T}, \tag{7.17}$$

where g_y is the gravity in the negative y-direction, $\hat{\beta} = -1/\rho(\partial\rho/\partial T)_P$ is the thermal expansion coefficient, $\Delta\theta$ is the temperature difference between the two walls, ν is the kinematic viscosity and α_T is the thermal diffusivity. Below a certain critical Rayleigh number ($\text{Ra}_\text{c} \approx 1708$) where the heat transfer is purely conductive in nature, a steady solution exists that has zero velocity in the entire domain and has a linear temperature profile

$$\theta = \theta_{\text{bottom}} - \Delta\theta \frac{y}{L}. \tag{7.18}$$

However, when Ra is increased above the critical value, this solution becomes unstable to small disturbances and the convection currents are set up. As Ra is increased further, the flow becomes turbulent in nature.

To model Rayleigh-Bénard convection in the LBM framework, one needs to incorporate the buoyancy and gravitational effects. This is done in the collision step via a forcing term F_i. The update of populations is

$$f_i(\mathbf{x} + \mathbf{c}_i\Delta t, t + \Delta t) = f_i(\mathbf{x}, t) + \alpha\beta[f_i^{\text{eq}}(\rho, \hat{\mathbf{u}}, \hat{\theta}) - f_i(\mathbf{x}, t)] + \left(1 - \frac{\alpha\beta}{2}\right)\Delta t F_i, \tag{7.19}$$

where

$$\hat{\boldsymbol{u}} = \frac{1}{\rho}\langle f, \boldsymbol{c}\rangle + \frac{\Delta t}{2}\boldsymbol{g},\ \hat{\theta} = \frac{\langle f, \boldsymbol{c}^2\rangle - \rho\hat{\boldsymbol{u}}^2}{3\rho}, \tag{7.20}$$

and $\boldsymbol{g} = \{0, -g_y(\rho - \rho_\infty)/\rho, 0\}$, ρ_∞ is the reference density, and $\alpha = 2$ is the single relaxation time standard LBM. For high Ra, α needs to be computed from the entropic formulation of LBM in order to suppress the disruptive numerical instabilities (Atif *et al.*, 2017). The force term is

$$F_i = \frac{f_i^{\text{eq}}(\rho, \hat{\boldsymbol{u}}, \hat{\theta})(\boldsymbol{c}_i - \hat{\boldsymbol{u}}) \cdot \boldsymbol{g}}{\hat{\theta}}. \tag{7.21}$$

It should be pointed that the alternate ways to evaluate the hydrodynamic moments involve

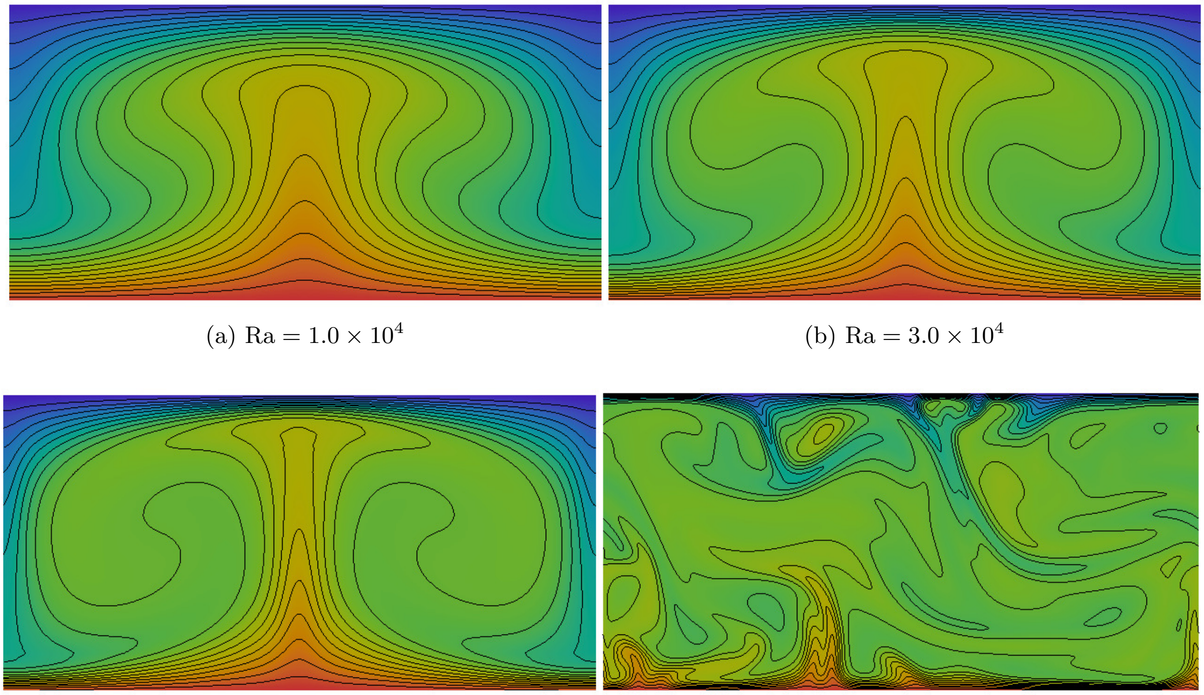

(a) Ra $= 1.0 \times 10^4$ (b) Ra $= 3.0 \times 10^4$

(c) Ra $= 1.5 \times 10^5$ (d) Ra $= 1.0 \times 10^7$

Figure 7.11: Temperature field for the Rayleigh-Bénard convection. The lines represent iso-temperature contours of temperature normalized from 0 to 1 in steps of 0.05.

averaging the moments before and after collision (Mazloomi *et al.*, 2015) or shifting them (Sbragaglia *et al.*, 2009) are subject of further research.

2-dimensional simulations

The 2-dimensional simulations were carried on a grid size of $256 \times 128 \times 8$ with $\theta_{\text{bottom}} = 1.05\theta_0$ and $\theta_{\text{top}} = 0.95\theta_0$. Temperature boundary conditions at the top and the bottom walls were imposed and periodic boundary conditions were applied in the other two directions. Any initial perturbation provided to the system triggers the instability. Following He *et al.* (1998*a*), the setup was initialized with a sinusoidal perturbation of the temperature field and left to evolve till two diffusion times. The Nusselt number (Nu) and the temperature contours at the steady state are independent of the initial perturbation provided to the system. Figure 7.11 depicts the iso-temperature contours for 2D Rayleigh-Bénard convection at various Ra. For quantitative analysis, we calculate the Nusselt number which is the measure of heat transfer in the system and represents the ratio of net heat transfer to the conductive heat transfer

$$\mathrm{Nu} = 1 + \frac{\left\langle u_y \tilde{\theta} \right\rangle}{\alpha_T \Delta\theta / H}, \tag{7.22}$$

where α_T is the thermal diffusivity, and $\langle\cdot\rangle$ represents average over the entire domain of flow. Here, $\tilde{\theta} = \hat{\theta} - (\theta_{\text{bottom}} - \Delta\theta y/L)$ is the deviation from the temperature distribution in the static state (Schumacher, 2009; Clever & Busse, 1974). In Figure 7.12, the Nusselt number obtained from current simulations are shown to have a good agreement with Clever & Busse (1974) and the empirical power law $\mathrm{Nu} = 1.56\,(\mathrm{Ra}/\mathrm{Ra}_{\text{cr}})^{0.296}$ (Shan, 1997). It should be reminded that this correlation itself is valid till Ra $\sim \mathcal{O}(10^5)$, above which the Nusselt-Rayleigh scaling changes (Toppaladoddi *et al.*, 2017).

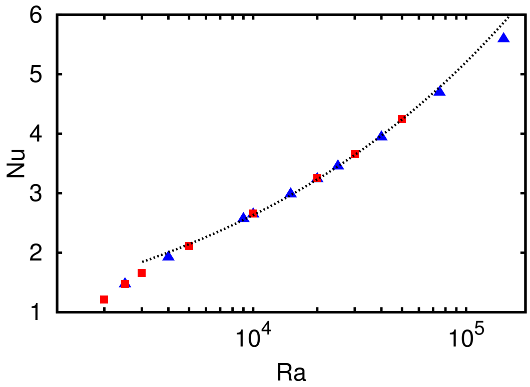

Figure 7.12: Nu vs Ra, triangles are from current simulation, squares are from Ref.(Clever & Busse, 1974), line is empirical power law $\mathrm{Nu} = 1.56(\mathrm{Ra}/\mathrm{Ra_c})^{0.296}$.

3-dimensional simulations

The 3-dimensional simulations were performed at $\mathrm{Ra} = 2.5 \times 10^6$ on grids of size $320 \times 160 \times 320$ and $480 \times 240 \times 480$, and at $\mathrm{Ra} = 1.0 \times 10^8$ on Grid C of size $640 \times 640 \times 640$. Temperature boundary conditions at the top and the bottom walls were imposed with $\theta_{\mathrm{bottom}} = 1.05\theta_0$ and $\theta_{\mathrm{top}} = 0.95\theta_0$, and periodic boundary conditions were applied in the other two directions. For $\mathrm{Ra} = 2.5 \times 10^6$, Figure 7.13 compares the nondimensional mean planar profiles of temperature and velocities with Kunnen *et al.* (2009) and Lavezzo *et al.* (2011). It is seen that the mean planar temperature shows a good match for both the grid resolutions, whereas the temperature fluctuations show a good match only for the grid with higher resolution. The velocity fluctuations match only qualitatively, but it is evident that as the grid resolution is increased the profiles show lesser deviation from Kunnen *et al.* (2009). Similarly, it can be seen from Figure 7.14 that for $\mathrm{Ra} = 1.0 \times 10^8$ the mean planar temperature shows a good match with that of Vashishtha *et al.* (2018), but the temperature fluctuations suggest that higher grid resolution is required for LBM to quantitatively match the fluctuations. The Nusselt number obtained for $\mathrm{Ra} = 2.5 \times 10^6$ is 11.45, while that of $\mathrm{Ra} = 1.0 \times 10^8$ is 29.38. Figure 7.15 visualizes the temperature profile for the two cases.

In Figure 7.16, a grid convergence study performed at $\mathrm{Ra} = 10^4$ shows second order convergence of the scheme. To test the accuracy of the model at large temperature deviations, a Rayleigh-Bénard simulation performed at $\mathrm{Ra} = 10^4$ on a grid size of $256 \times 128 \times 8$ with top wall temperature $0.5\theta_0$ and bottom wall temperature $1.5\theta_0$ gave a Nusselt number 2.6797. The Nusselt number for wall temperatures $(1 \pm 0.05)\theta_0$ was 2.6426, while the empirical power law suggests the Nusselt number to be 2.6321. Hence, the 50% temperature run gave an error of 1.8% whereas the 5% temperature deviation gave an error of only 0.4%. This suggests that the accuracy of the model is not compromised at large temperature deviations.

7.6 Outlook

In this chapter we have demonstrated that the $RD3Q67$ model exhibits accurate thermohydrodynamic behaviour with a high degree of accuracy and is therefore capable of simulating compressible and thermal hydrodynamics. Several test cases were simulated it was found to be nonlinearly stable for a wide range of parameters. The test cases confirm that the model correctly captures viscous heating, shocks, heat conduction and compressible hydrodynamics. The test case of thermoacoustic convection shows excellent agreement with the NSF equations

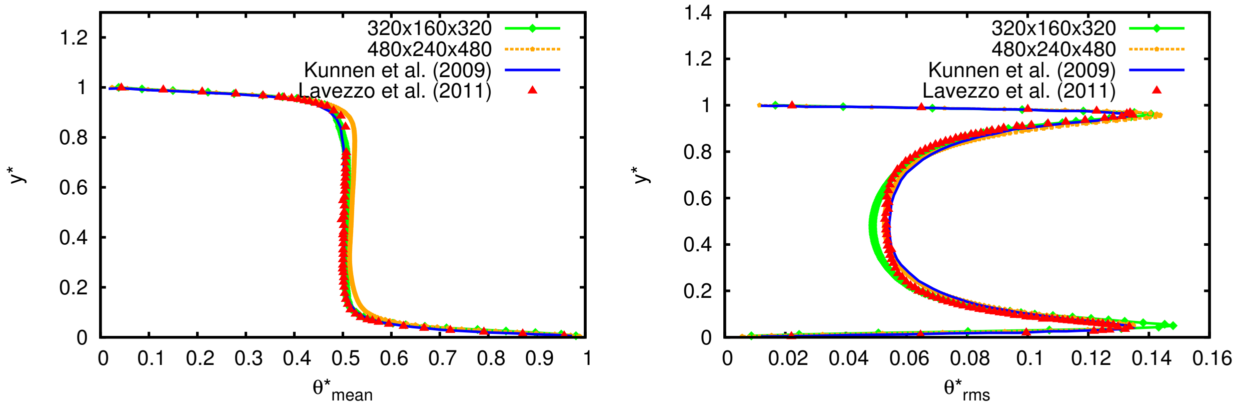

(a) Planar average of nondimensional temperature

(b) Planar average of fluctuations in nondimensional temperature

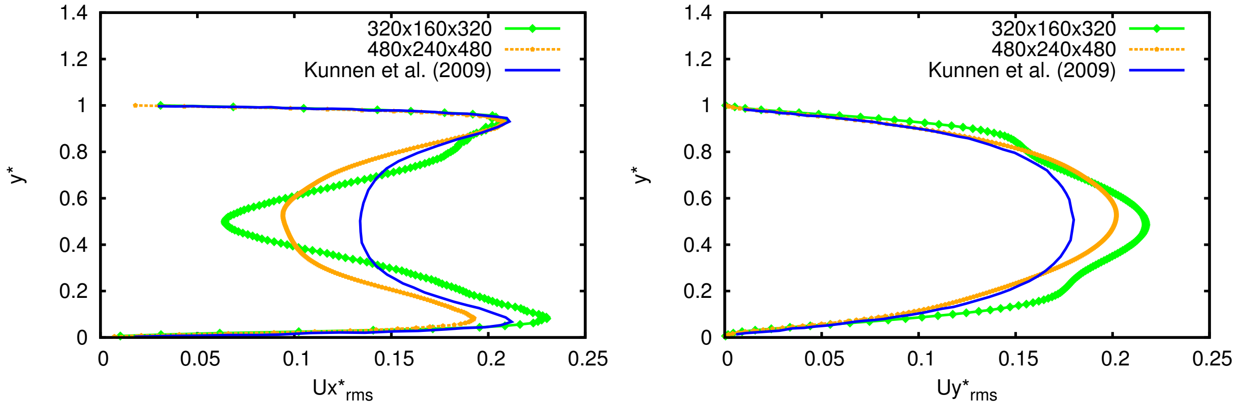

(c) Planar average of fluctuations in nondimensional horizontal velocity

(d) Planar average of fluctuations in nondimensional vertical velocity

Figure 7.13: Mean planar profiles for $\mathrm{Ra} = 2.5 \times 10^6$ averaged over ∼10 eddy turnover times.

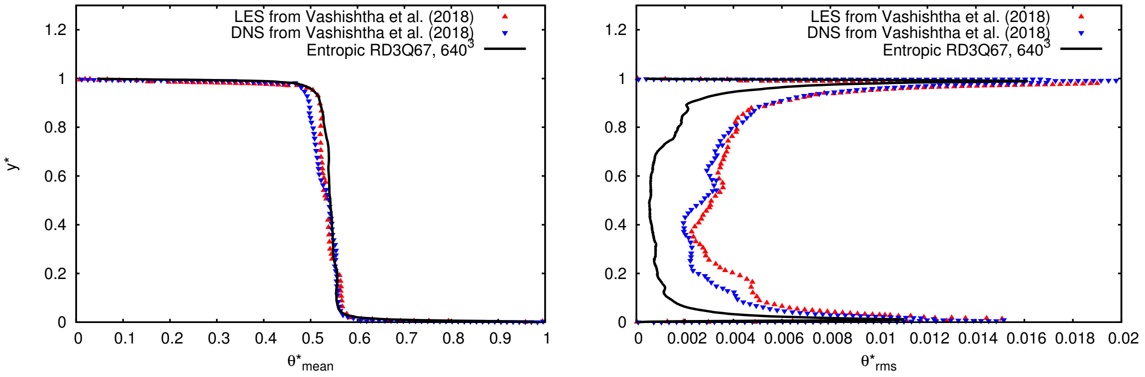

(a) Planar average of nondimensional temperature

(b) Planar average of fluctuations in nondimensional temperature

Figure 7.14: Mean planar profiles for $\mathrm{Ra} = 1.0 \times 10^8$ averaged over ∼10 eddy turnover times.

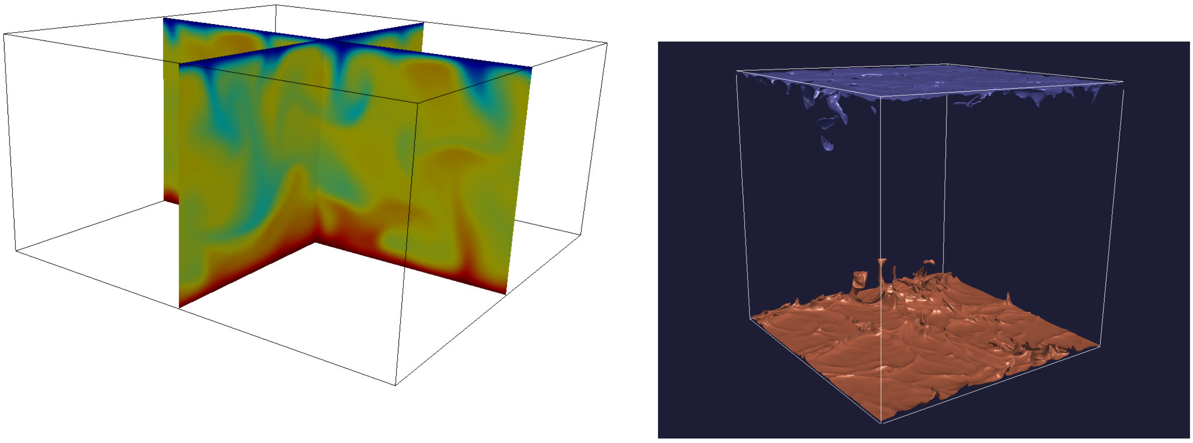

(a) Temperature at the vertical center planes for Ra = 2.5×10^6

(b) Iso-temperature contours near the walls for Ra = 10^8

Figure 7.15: Visualizations of the temperature profile.

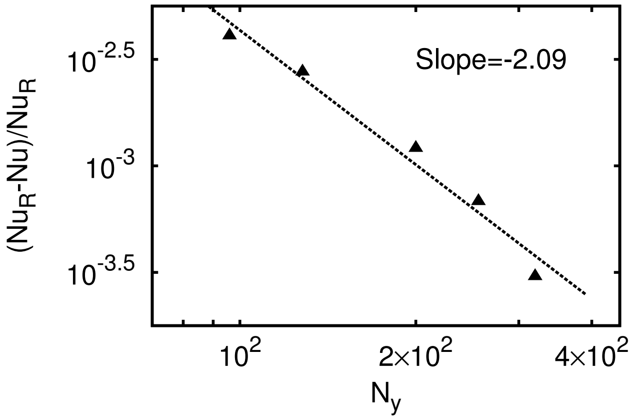

Figure 7.16: Grid convergence study for Ra = 10^4 reveals second-order convergence. The converged $\mathrm{Nu_R}$ is 2.6311 with 360 points in the vertical direction. The line is the fitted curve.

at the diffusive time scales. Some preliminary studies have shown that it also reproduces correct behaviour at acoustic time scales, which is a subject for further research. As the model is nonlinearly stable it opens up the possibility to study turbulent thermal flows such as the turbulent Rayleigh-Bénard convection. Recently, a Nusselt-Rayleigh scaling of $\mathrm{Nu} - 1 \propto \mathrm{Ra}^{0.483}$ was demonstrated (Toppaladoddi *et al.*, 2017) by considering rough walls. The ultimate test for the stability and accuracy of the model is its capability to capture this scaling which occurs when $\mathrm{Ra} \to 10^{13}$ (Zhu *et al.*, 2018).

In Section 7.4, we considered only the steady state of the two-dimensional cavity heated at the top. From Section 7.5.2, it is known that rapid heating/cooling of one of the walls of a cavity containing a compressible fluid will initiate convective currents that lead to enhancement of the net heat transfer over conduction. An avenue for further research is to quantify this enhancement for various Prandtl numbers, aspect ratios of the cavity, and time varying wall temperatures. The limitation on the Prandtl number is due to the BGK collision model and can be addressed by using quasi-equilibrium models (Ansumali *et al.*, 2007*a*; Thantanapally *et al.*, 2013*b*).

Chapter 8

Lattice Boltzmann model for nonideal fluids

The standard lattice Boltzmann method leads to an ideal gas equation of state. Several variations to simulate nonideal fluids have been proposed (Gunstensen *et al.*, 1991; Shan & Chen, 1993; Swift *et al.*, 1995; He *et al.*, 1998*b*; Ansumali, 2011). Most of the mentioned approaches model the microscopic physics and the interfacial dynamics at the mesoscopic level at an affordable computational expense. The LBM is considered advantageous for multiphase flows as it maintains a stable interface (typically a few grid points wide) and does not require explicit interface tracking. Shan & Chen (1993) considered the microscopic interactions between the nearest neighbours to model the collision operator for which the surface tension could be maintained automatically (Chen & Doolen, 1998). The interaction potential controlled the form of the equation of state of the fluid and gave rise to phase separation, however, the surface tension could not be freely adjusted (He & Doolen, 2002). Among the various multiphase models, of particular interest is the free-energy model (Swift *et al.*, 1995) as it allows for surface tension to be independent of the viscosity in addition to being thermodynamically consistent. Recently, the entropic lattice Boltzmann model was extended for multiphase flows to control the spurious currents at the liquid-vapour interface thereby opening the possibility to simulate large density ratios (Mazloomi *et al.*, 2015).

At the macroscopic scale, the multiphase LBMs can be considered diffuse interface models. These models smoothen the discontinuity at the interface over a thin but numerically resolvable layer (Jacqmin, 1999; Qiao *et al.*, 2018). The fluid properties transition over this layer smoothly as opposed to singular interfaces which have a sharp discontinuity. The surface tension is transformed into a volumetric forcing (Lee & Fischer, 2006) and is spread over the diffused interfacial region. An undesirable feature of the diffuse interface in LBM manifests in the form of the spurious currents that develop in the vicinity of the interface (Lee & Fischer, 2006; He & Doolen, 2002). In the case of a two-dimensional droplet immersed in a quiescent medium, the spurious currents form a pattern of eight eddies around the droplet (see Figure 8.1). Several attempts have been made to identify their origin and to alleviate these currents (Lee & Fischer, 2006; Shan, 2006). The departure of the LBM simulations from the theoretical phase densities and the magnitude of the spurious current depends upon the liquid-vapour density ratio, the equation of state, and the surface tension. Often they have been attributed to the violation of Gibbs-Duhem equality due to the discrete derivative operator (Wagner, 2006). It was mentioned by Wagner (2006) that an open problem in this field is the identification of a discrete derivative operator that preserves the Gibbs-Duhem equality at the interface.

In this chapter, we propose an alternate way of treating the discrete derivative such that the violation of Gibbs-Duhem relation at the interface is reduced. We show that this way of discretization leads to accurate liquid vapour phase densities and reduces the spurious currents. This chapter is organized as follows: we first review a few well known equations of state for nonideal fluids in Section 8.1. In Section 8.2, we discuss the van der Waals theory of a single component two-phase fluid followed by the equations of hydrodynamics. In Section 8.3, we discuss the methodology to incorporate nonideal effects in the kinetic theory and lattice Boltzmann model. It is followed by a brief review of evaluating second and fourth-order derivatives on a lattice and the justification of the choice of stencil employed to evaluate derivatives in Section 8.4. In Section 8.5, we propose a thermodynamically consistent discrete derivative operator that

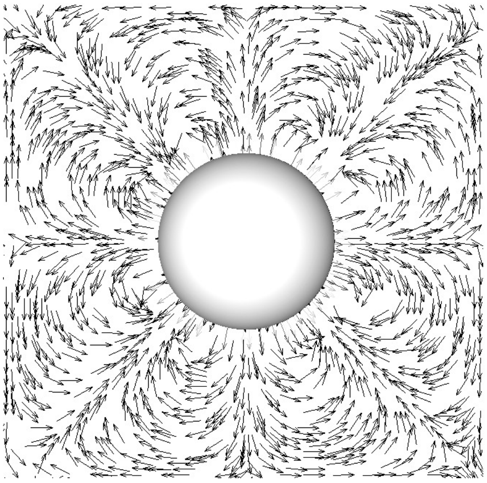

Figure 8.1: Spurious currents around a two-dimensional droplet organize in a pattern of eight eddies.

reduces the spurious currents and demonstrate its accuracy by comparing with theoretical phase densities. In Section 8.6, to prove the stability of the model we compare the phase densities obtained from a deeply-quenched liquid-vapour system with their corresponding theoretical values. In Section 8.7 we validate that the Laplace's law is obeyed and use it to calculate the surface tension and also study the deformation of a droplet in a simple shear flow. Finally, in Section 8.8, we extend the entropic formulation of LBM to two-phase flows and simulate collisions between two droplets.

8.1 Equations of state

An equation of state (EoS) correlating the phase densities, the temperature, and the pressure of a fluid in equilibrium state via the functional form

$$f(p, \rho, \theta) = 0. \tag{8.1}$$

The simplest EoS is the ideal gas equation of state for which $p = \rho k_B T/m$. A number of other EoS for real fluids are found in the literature, such as the van der Waals, Carnahan-Starling, Peng-Robinson, Redlich-Kwong, Redlich-Kwong-Suave, Patel-Teja, etc [for details see Smith *et al.* (1996)]. In this section, we list a few EoS widely employed in the lattice Boltzmann models along with their critical parameters.

1. **Van der Waals (vdW) EoS**: This is the simplest two parameter cubic equation of state and is given by

   $$p = \frac{\rho\theta}{1-\rho b} - a\rho^2, \tag{8.2}$$

   where a, b are positive parameters related to the molecular attraction and exclusion volume respectively. The first term captures the effect of non-vanishing sized particles while the second term represents the intermolecular attraction. The parameters are

   $$a = \frac{27 b\theta_c}{8}, \qquad b = \frac{1}{3\rho_c}, \tag{8.3}$$

are found by solving Eq.(8.2) and the system of equations

$$\left.\frac{\partial p}{\partial \rho}\right|_{\theta=\theta_c} = 0, \qquad \left.\frac{\partial^2 p}{\partial \rho^2}\right|_{\theta=\theta_c} = 0, \tag{8.4}$$

at the critical point. The critical compressibility factor $Z_c = p_c/(\rho_c \theta_c)$ predicted by this EoS is 0.375 whereas for a real fluid it is typically less than 0.3.

2. **Carnahan-Starling (CS) EoS**: This is an improvement of the vdW EoS where the fluid particles are approximated as hard spheres with intermolecular attractive forces. It is given by (Carnahan & Starling, 1969)

$$p = \rho\theta \frac{1+\eta+\eta^2-\eta^3}{(1-\eta)^3} - a\rho^2, \tag{8.5}$$

where $\eta = \rho b/4$, and

$$a = \frac{b\theta_c}{0.377332}, \qquad b = \frac{0.521772}{\rho_c}.$$

The critical compressibility factor $Z_c = p_c/(\rho_c \theta_c)$ predicted by this EoS is 0.359.

3. **Peng-Robinson (PR) type EoS**: This EoS has been widely recognized for predicting the accurate liquid density (Qiao *et al.*, 2018). The original Peng-Robinson EoS had van der Waals like repulsive part which we replace with Carnahan-Starling like repulsive part. It also had an acentric factor in attractive part that is ignored here. Therefore,

$$p = \rho\theta \frac{1+\eta+\eta^2-\eta^3}{(1-\eta)^3} - \frac{a\rho^2}{1+2\rho b-\rho^2 b^2}, \tag{8.6}$$

where a, b are van der Waal like critical parameters and $\eta = \rho b/4$. The critical parameters are

$$a = 1.851427622\frac{\theta_c}{\rho_c}, \quad b = \frac{0.353748714}{\rho_c}. \tag{8.7}$$

The critical compressibility factor $Z_c = p_c/(\rho_c \theta_c)$ predicted by this EoS is 0.276.

8.2 Thermodynamics of a single component two-phase fluid

In this section, we consider an isothermal system of a nonideal fluid. Van der Waals modified the free-energy density by incorporating terms that are large only when the density gradients are significant (van der Waals, 1979; Rowlinson & Widom, 1982). Therefore, the underlying free-energy functional $\Psi(x)$ is of the form

$$\Psi(\boldsymbol{x}) = \int [\mathcal{F}(\rho(\boldsymbol{x})) + \mathcal{I}(\nabla\rho(\boldsymbol{x}), \nabla^2\rho(\boldsymbol{x}), ...)] d\boldsymbol{x}, \tag{8.8}$$

where ρ is the density, $\mathcal{F}$ is the bulk free-energy, and $\mathcal{I}$ is the interfacial free-energy. The interfacial free-energy $\mathcal{I}(\nabla\rho(x), \nabla^2\rho(x), ...)$ is approximated to the lowest order as (Rowlinson & Widom, 1982; Wagner, 2006)

$$\mathcal{I}(\nabla\rho(x), \nabla^2\rho(x), ...) = \frac{\kappa(\rho)}{2}|\nabla\rho(x)|^2. \tag{8.9}$$

For simplicity, $\kappa(\rho)$, related to the surface tension, is taken constant. With this definition, the excess free-energy is the surface tension σ

$$\sigma = \int_{-\infty}^{\infty} \frac{\kappa}{2} |\nabla \rho(x)|^2 dx. \tag{8.10}$$

The above model of free-energy is the simplest model that gives two stable phases provided $\mathcal{F}$ has two minima and was first formulated by van der Waals (van der Waals, 1979).

The macroscopic mass and momentum conservation equations are given by (Lee & Lin, 2005; Suryanarayanan *et al.*, 2013)

$$\partial_t \rho + \partial_\alpha (\rho u_\alpha) = 0, \tag{8.11}$$

$$\partial_t (\rho u_\alpha) + \partial_\beta \left[p \delta_{\alpha\beta} + \rho u_\alpha u_\beta + \sigma_{\alpha\beta} + \sigma^{(\kappa)}_{\alpha\beta} \right] = 0, \tag{8.12}$$

where $\sigma_{\alpha\beta}$ is the viscous stress tensor

$$\sigma_{\alpha\beta} = -\rho\nu \left(\partial_\beta u_\alpha + \partial_\alpha u_\beta \right) + \frac{2}{3} \rho\nu \partial_\gamma u_\gamma \delta_{\alpha\beta}, \tag{8.13}$$

where ν is the kinematic viscosity, and $\sigma^{(\kappa)}_{\alpha\beta}$ takes the form

$$\sigma^{(\kappa)}_{\alpha\beta} = \kappa \left[\left(-\frac{1}{2} \partial_\gamma \rho \, \partial_\gamma \rho - \rho \partial^2 \rho \right) \delta_{\alpha\beta} + \{ \partial_\alpha \rho \, \partial_\beta \rho \} \right]. \tag{8.14}$$

and accounts for the interfacial stresses. The term within the curly braces in the above expression is known as the van der Waals stress (Rowlinson & Widom, 1982).

The nonlocal pressure tensor (also known as Korteweg's stress tensor) derived from the above description is consistent with the definition of the free-energy functional and is written as (Korteweg, 1901; Evans, 1979; Swift *et al.*, 1996)

$$P_{\alpha\beta} = \left[p - \frac{\kappa}{2} \partial_\gamma \rho \, \partial_\gamma \rho - \kappa \rho \, \partial^2 \rho \right] \delta_{\alpha\beta} + \kappa \partial_\alpha \rho \, \partial_\beta \rho, \tag{8.15}$$

where $\delta_{\alpha\beta}$ is the Kronecker delta and

$$p = \rho \mu_0 - \mathcal{F}, \tag{8.16}$$

is the equation of state describing the nonideal fluid, with $\mu_0 = \partial \mathcal{F} / \partial \rho$ as the bulk chemical potential. The net chemical potential μ can also be derived by Euler-Lagrange variational minimization of Eq.(8.8) (Rowlinson & Widom, 1982)

$$\mu = \frac{\delta \Psi}{\delta \rho} = \mu_0 - \kappa \partial^2 \rho, \tag{8.17}$$

and is related to the pressure tensor via the Gibbs-Duhem equality

$$\partial_\beta P_{\alpha\beta} = \rho \partial_\alpha \mu. \tag{8.18}$$

For a continuous system, the Gibbs-Duhem equality is trivially satisfied. However, it gets violated for a discrete system due to the definition of the discrete derivative which leads to thermodynamic inconsistency.

8.3 Incorporating nonideal effects in lattice Boltzmann

As stated earlier, the standard lattice Boltzmann leads to an ideal gas equation of state, i.e., the particles are devoid of any intermolecular attraction and occupy negligible volume. To incorporate the deviation from the ideal gas the intermolecular attraction, the repulsion between the particles due to their non-vanishing size, and the interface dynamics needs to be modeled. Swift *et al.* (1996) first suggested the implementation of Korteweg's stress in the lattice Boltzmann to model the nonideal contribution and the interface dynamics in a thermodynamically consistent manner. In LBM framework, the attractive and repulsive parts are added as a force term. In order to do so, one begins with the Boltzmann BGK equation for an isothermal nonideal gas (He *et al.*, 1998*b*)

$$\frac{\partial f_i}{\partial t} + c_{i\alpha}\frac{\partial f_i}{\partial x_\alpha} = \frac{f_i^{\mathrm{eq}}(\rho, \boldsymbol{u}, \theta_0) - f_i}{\tau} + F_i, \tag{8.19}$$

where the forcing term F_i is given by

$$F_i = \frac{g_\alpha^{\mathrm{nid}}(c_{i\alpha} - u_\alpha)}{\theta_0} f_i^{\mathrm{eq}}(\rho, \boldsymbol{u}, \theta_0). \tag{8.20}$$

The nonideal contributions are captured in g_α^{nid},

$$g_\alpha^{\mathrm{nid}} = -\frac{1}{\rho}\partial_\beta P_{\alpha\beta}^{\mathrm{nid}}, \quad P_{\alpha\beta}^{\mathrm{nid}} = P_{\alpha\beta} - \rho\theta_0\delta_{\alpha\beta}. \tag{8.21}$$

The above form of g_α^{nid}, known as the pressure formulation, is sufficient to incorporate the nonideal interactions and the Korteweg's stress tensor in the lattice Boltzmann model (Lee & Lin, 2005; Lee & Fischer, 2006; Mazloomi *et al.*, 2015). Alternatively, by exploiting the Gibbs-Duhem relation one can write the chemical potential formulation as (Lee & Fischer, 2006; Suryanarayanan *et al.*, 2013)

$$g_\alpha^{\mathrm{nid}} = -\partial_\alpha \mu^{\mathrm{nid}}, \tag{8.22}$$

where $\mu^{\mathrm{nid}} = \mu_0^{\mathrm{nid}} - \kappa\partial^2\rho$.

The Eq.(8.19) is integrated along the characteristics using the trapezoid rule to obtain the discrete (in space and time) evolution of populations as

$$\tilde{f}_i(\boldsymbol{x} + \boldsymbol{c}_i\Delta t, t + \Delta t) = \tilde{f}_i(\boldsymbol{x}, t) + \alpha\beta[f_i^{\mathrm{eq}}(\rho, \boldsymbol{u}, \theta_0) - \tilde{f}_i(\boldsymbol{x}, t)] + \left(1 - \frac{\alpha\beta}{2}\right)\Delta t F_i, \tag{8.23}$$

where $\tilde{f}_i$ is a transformation of the populations f_i defined as

$$\tilde{f}_i = f_i - \frac{\Delta t}{2\tau}[f_i^{\mathrm{eq}}(\rho, \boldsymbol{u}, \theta_0) - f_i] - \frac{\Delta t}{2}F_i, \tag{8.24}$$

$\beta = \Delta t/(2\tau + \Delta t)$ and $\alpha = 2$ for the standard LBM. For the entropic LBM the parameter α needs to be computed such that the dynamics is in compliance with the $\mathcal{H}$ theorem. The macroscopic variables are calculated as

$$\rho = \sum_i \tilde{f}_i, \qquad u_\alpha = \frac{1}{\rho}\sum_i \tilde{f}_i c_{i\alpha} + \frac{\Delta t}{2} g_\alpha^{\mathrm{nid}}. \tag{8.25}$$

It is worth noticing that the Eq.(8.23) does not conserve momentum. The change in momentum at each site during a time step is obtained by multiplying Eq.(8.23) with $c_{i\alpha}$ and summing over all directions as

$$\rho u_\alpha(t + \Delta t) - \rho u_\alpha(t) = \Delta t \rho g_\alpha^{\mathrm{nid}}. \tag{8.26}$$

In fact, this change in momentum is due to the nonideal nature of the fluid and leads to two stable phases separated by an interface. However, the global momentum of the system should be exactly conserved provided no net momentum exchange occurs at the boundary (Shan & Chen, 1993). This is an important feature of the discrete dynamics, satisfied by the pressure formulation [Eq.(8.21)] but not by the chemical potential formulation [Eq.(8.22)]. It is known that the chemical potential formulation is more accurate than the pressure formulation and leads to smaller spurious currents (Lee & Fischer, 2006; Suryanarayanan *et al.*, 2013). However, the thermodynamic consistency requires that the global momentum should stay preserved. This will be elaborated in the forthcoming sections, where we propose an alternate formulation that is similar to the chemical potential formulation but preserves global momentum.

8.4 Evaluating derivatives on a lattice

In this section, we briefly review the way to evaluate the discrete gradients and Laplacian in an isotropic manner. The discrete derivative is defined as

$$\nabla_\alpha \psi = \frac{1}{\hat{\theta}_0 \Delta t} \sum_i \hat{w}_i c_{i\alpha} \psi(\boldsymbol{x} + \boldsymbol{c}_i \Delta t). \tag{8.27}$$

Here, $\hat{w}_i$ are the weights of the lattice with discrete velocities $c_{i\alpha}$ and ψ is the function whose derivate needs to be calculated. The above definition can be understood as follows: we consider the Taylor expansion of $\mathcal{Q}_\alpha = \sum_i \hat{w}_i c_{i\alpha} \psi(\boldsymbol{x} + \boldsymbol{c}_i \Delta t)/(\hat{\theta}_0 \Delta t)$ (Thampi *et al.*, 2013*a*; Ramadugu *et al.*, 2013),

$$\begin{aligned}\mathcal{Q}_\alpha \equiv \frac{1}{\hat{\theta}_0 \Delta t} \sum_i \hat{w}_i c_{i\alpha} \psi(\boldsymbol{x} + \boldsymbol{c}_i \Delta t) = \frac{1}{\hat{\theta}_0 \Delta t} \Bigg[& \psi(\boldsymbol{x}) \sum_i \hat{w}_i c_{i\alpha} + \Delta t \frac{\partial \psi}{\partial x_\beta} \sum_i \hat{w}_i c_{i\alpha} c_{i\beta} \\ & + \frac{\Delta t^2}{2} \frac{\partial^2 \psi}{\partial x_\beta \partial x_\gamma} \sum_i \hat{w}_i c_{i\alpha} c_{i\beta} c_{i\gamma} + \frac{\Delta t^3}{6} \frac{\partial^3 \psi}{\partial x_\beta \partial x_\gamma \partial x_\kappa} \sum_i \hat{w}_i c_{i\alpha} c_{i\beta} c_{i\gamma} c_{i\kappa} \\ & + \frac{\Delta t^4}{24} \frac{\partial^4 \psi}{\partial x_\beta \partial x_\gamma \partial x_\kappa \partial x_\eta} \sum_i \hat{w}_i c_{i\alpha} c_{i\beta} c_{i\gamma} c_{i\kappa} c_{i\eta} \\ & + \frac{\Delta t^5}{120} \frac{\partial^5 \psi}{\partial x_\beta \partial x_\gamma \partial x_\kappa \partial x_\eta \partial x_\nu} \sum_i \hat{w}_i c_{i\alpha} c_{i\beta} c_{i\gamma} c_{i\kappa} c_{i\eta} c_{i\nu} + \mathcal{O}(\Delta t^6) \Bigg].\end{aligned} \tag{8.28}$$

The odd-order moments of weight are zero due to symmetry of the underlying lattice and further simplification of $\mathcal{Q}_\alpha$ leads to

$$\mathcal{Q}_\alpha \equiv \frac{1}{\hat{\theta}_0 \Delta t} \sum_i \hat{w}_i c_{i\alpha} \psi(\boldsymbol{x} + \boldsymbol{c}_i \Delta t) = \frac{\partial \psi}{\partial x_\alpha} + \frac{\Delta t^2 \hat{\theta}_0}{2} \frac{\partial}{\partial x_\alpha} \partial^2 \psi + \frac{3 \Delta t^4 \hat{\theta}_0^2}{8} \frac{\partial}{\partial x_\alpha} \partial^4 \psi + \mathcal{O}(\Delta t^6), \tag{8.29}$$

assuming the lattice is sufficiently isotropic. The emergence of the derivatives of ψ is seen on the right hand side of the above equation.

The second-order gradient is hence

$$\nabla_\alpha^{(2)} \psi = \frac{1}{\hat{\theta}_0 \Delta t} \sum_i \hat{w}_i c_{i\alpha} \psi(\boldsymbol{x} + \boldsymbol{c}_i \Delta t). \tag{8.30}$$

The fourth-order gradient is written as

$$\nabla_\alpha^{(4)} \psi = \frac{1}{\hat{\theta}_0 \Delta t} \sum_i \hat{w}_i c_{i\alpha} \psi(\boldsymbol{x} + \boldsymbol{c}_i \Delta t) - \frac{\hat{\theta}_0}{2} (\Delta t)^2 \nabla_\alpha (\nabla^2 \psi). \tag{8.31}$$

The Laplacian can also be evaluated as

$$\nabla^2\psi = \frac{2}{\Delta t^2\hat{\theta}_0}\left[\sum_i \hat{w}_i\psi(\boldsymbol{x}+\boldsymbol{c}_i\Delta t) - \psi(\boldsymbol{x})\right]. \tag{8.32}$$

Here, it remains to justify the choice of stencil for calculating derivatives. From Eq.(8.29) it is evident that the discretization errors are proportional to $\hat{\theta}_0 = \sum \hat{w}_i c_{ix}^2$ of the chosen stencil. For the crystallographic grid, the 15 velocity stencil comprising of the discrete velocities

$$c_i = \{(\pm1,0,0),(0,\pm1,0),(0,0,\pm1),(\pm0.5,\pm0.5,\pm0.5)\}, \tag{8.33}$$

is found to have the least $\hat{\theta}_0 = 1/6$ with $\hat{w}_0 = 14/36, \hat{w}_{\mathrm{SC}} = 1/36$ and $\hat{w}_{\mathrm{BCC}} = 2/36$, therefore is the ideal choice for computing derivatives.

8.5 Discrete derivative operator

As discussed earlier, for a continuous system the Gibbs-Duhem relation is trivially satisfied. However, for a discrete system it gets violated, i.e.,

$$\tilde{\partial}_\alpha P_{\alpha\beta} \neq \rho\tilde{\partial}_\beta\mu, \tag{8.34}$$

where $\tilde{\partial}_\alpha$ represents the discrete derivative operator (Wagner, 2006). This is the reason why the two formulations, namely the pressure and the chemical potential show different accuracy, stability, and spurious currents.

The chemical potential formulation is more accurate and has smaller spurious currents as compared to the pressure formulation (Lee & Fischer, 2006). However, one of its drawback is that the global momentum is not conserved. This is further explained in what follows: In the pressure formulation in one dimension, the second-order discrete derivative $\tilde{\partial}_\alpha^{(2)}$ at the n^{th} grid point is written as

$$\tilde{\partial}_\alpha^{(2)} P_{\alpha\beta} = \frac{1}{2\Delta x_\alpha}\left[P_{\alpha\beta}(n+1) - P_{\alpha\beta}(n-1)\right]. \tag{8.35}$$

With appropriate boundary conditions (say periodic), one can sum over the entire domain to show that

$$\sum_{n=1}^{N}\left[P_{\alpha\beta}(n+1) - P_{\alpha\beta}(n-1)\right] = 0. \tag{8.36}$$

The local change of momentum from Eq.(8.26) is $\Delta t\rho g_\alpha^{\mathrm{nid}}$. The global momentum conservation upon using Eqs.(8.21),(8.35),(8.36) follows as

$$\sum_{n=1}^{N}\Delta t\rho g_\alpha^{\mathrm{nid}} = -\sum_{n=1}^{N}\Delta t\tilde{\partial}_\alpha^{(2)} P_{\alpha\beta}^{\mathrm{nid}} = -\frac{\Delta t}{2\Delta x_\alpha}\sum_{n=1}^{N}\left[P_{\alpha\beta}^{\mathrm{nid}}(n+1) - P_{\alpha\beta}^{\mathrm{nid}}(n-1)\right] = 0. \tag{8.37}$$

However, for the chemical potential formulation the net global momentum is

$$\sum_{n=1}^{N}\Delta t\rho g_\alpha^{\mathrm{nid}} = -\frac{\Delta t}{2\Delta x_\alpha}\sum_{n=1}^{N}\rho(n)\left[\mu^{\mathrm{nid}}(n+1) - \mu^{\mathrm{nid}}(n-1)\right], \tag{8.38}$$

which is non-zero.

Fundamentally, this lack of momentum conservation is emerging due to the violation of the Leibniz rule. For this analysis we ignore the interfacial terms which will be added separately.

The bulk nonideal pressure using the thermodynamic relations is written as

$$p^{\mathrm{nid}} = \mu_0^{\mathrm{nid}}\rho - \mathcal{F}^{\mathrm{nid}}. \tag{8.39}$$

Taking the discrete derivative of the above equation one obtains

$$\tilde{\partial}_\alpha p^{\mathrm{nid}} = \left\{\mu_0^{\mathrm{nid}}\tilde{\partial}_\alpha\rho\right\} + \rho\tilde{\partial}_\alpha\mu^{\mathrm{nid}} - \tilde{\partial}_\alpha\mathcal{F}^{\mathrm{nid}}, \tag{8.40}$$

where the left hand side is the pressure formulation which conserves the global momentum. The term in curly braces on the right hand side is the chemical potential formulation which does not conserve the global momentum because the other two terms (although they cancel in the continuous case) are ignored in the discrete chemical potential formulation. It is interesting to note that if one defines the discrete derivative as

$$\tilde{\partial}_\alpha(AB) = A\tilde{\partial}_\alpha B + B\tilde{\partial}_\alpha A, \tag{8.41}$$

A, B being arbitrary functions, the Leibniz rule as well as the global momentum conservation holds.

Therefore, the global momentum conserving new formulation using Eq.(8.40) is written as

$$\rho g_\alpha^{\mathrm{nid}} = -\left[\rho\tilde{\partial}_\alpha^{(2)}\mu_0^{\mathrm{nid}} + \mu_0^{\mathrm{nid}}\tilde{\partial}_\alpha^{(2)}\rho - \tilde{\partial}_\alpha^{(2)}\mathcal{F}^{\mathrm{nid}} + \kappa\tilde{\partial}_\beta^{(2)}I_{\alpha\beta}\right], \tag{8.42}$$

where the interfacial stresses $I_{\alpha\beta}$ are given by

$$I_{\alpha\beta} = \left[-\frac{1}{2}\partial_\gamma\rho\,\partial_\gamma\rho - \rho\,\partial^2\rho\right]\delta_{\alpha\beta} + \partial_\alpha\rho\,\partial_\beta\rho. \tag{8.43}$$

Ideally, one would prefer to work with the fourth-order discrete derivatives [Eq.(8.31)] but they lead to violation of the global momentum conservation. One can, however, use the fourth order discrete derivative for $\tilde{\partial}_\alpha\mathcal{F}^{\mathrm{nid}}$, for which we use a convex combination of the second and fourth order discrete derivative. This brings us to the final form of g_α^{nid}

$$\rho g_\alpha^{\mathrm{nid}} = -\left[\rho\tilde{\partial}_\alpha^{(2)}\mu_0^{\mathrm{nid}} + \mu_0^{\mathrm{nid}}\tilde{\partial}_\alpha^{(2)}\rho - \eta\tilde{\partial}_\alpha^{(2)}\mathcal{F}^{\mathrm{nid}} - (1-\eta)\tilde{\partial}_\alpha^{(4)}\mathcal{F}^{\mathrm{nid}} + \kappa\tilde{\partial}_\beta^{(2)}I_{\alpha\beta}\right]. \tag{8.44}$$

The above route to calculating the discrete derivative is thermodynamically consistent, preserves the global momentum, and has a parameter $\eta \in [0,1]$ that will be selected such that errors are minimized.

For a one-dimensional system, a backward error analysis of Eq.(8.44) reveals that

$$\begin{aligned} -\rho g_x^{\mathrm{nid}} &= \rho\partial_x\mu_0^{\mathrm{nid}} + \mu_0^{\mathrm{nid}}\partial_x\rho - \partial_x\mathcal{F}^{\mathrm{nid}} + \kappa\partial_x^{(2)}I_{xx} + \Delta E, \\ &= \rho\partial_x\mu^{\mathrm{nid}} + \Delta E, \\ &= \partial_x P^{\mathrm{nid}} + \Delta E, \end{aligned} \tag{8.45}$$

where ΔE is the error term. The net surface tension in the discrete system is a combination of the interfacial terms and the numerical errors due to the discretization. For this analysis we set $\kappa = 0$, therefore, only the numerical errors contribute to the surface tension. Hence, we obtain the error term as

$$\Delta E = \frac{\Delta t^2\theta_0}{2}\left[\rho\partial_\alpha^3\mu_0 + \mu_0\partial_\alpha^3\rho - \eta\partial_\alpha^3\mathcal{F}\right] + \frac{3\Delta t^4\theta_0^2}{8}\left[\rho\partial_\alpha^5\mu_0 + \mu_0\partial_\alpha^5\rho - \partial_\alpha^5\mathcal{F}\right]. \tag{8.46}$$

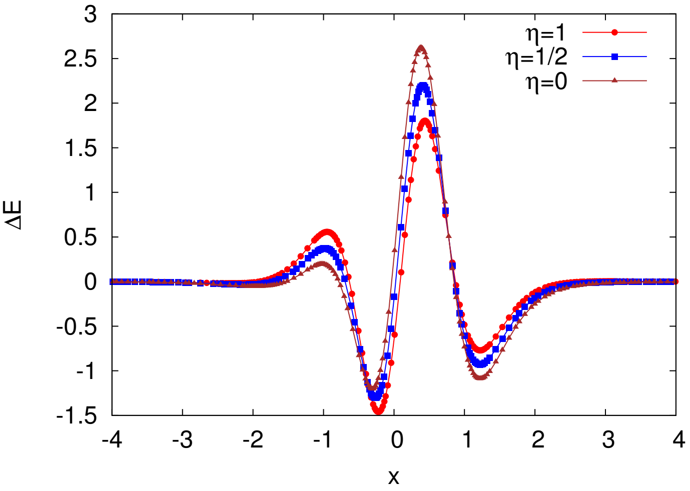

Figure 8.2: Nondimensional error for the proposed discretization scheme for various η. It is seen that $\eta = 1/2$ is the best choice as it shows the least fluctuation.

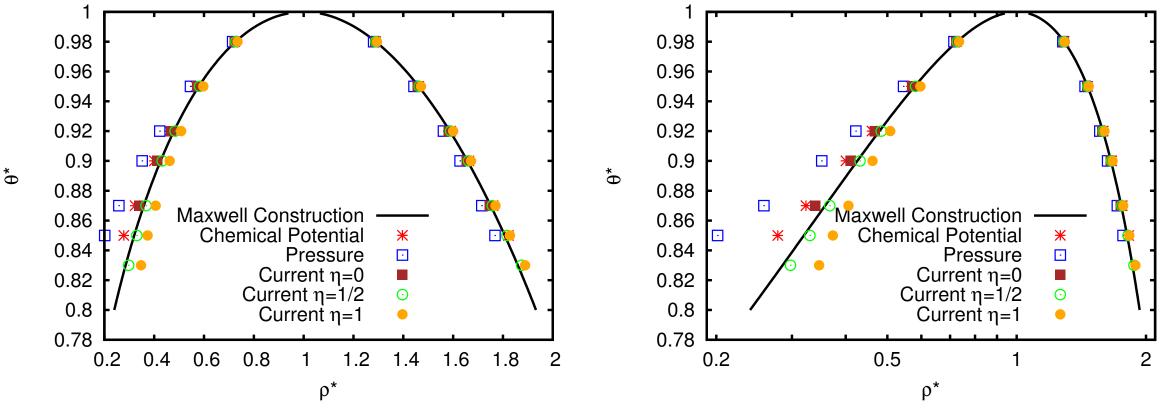

Figure 8.3: Liquid vapour densities of the van der Waals fluid for various formulations at different reduced temperature $\theta^* = \theta/\theta_c$. The same plot is represented on the linear scale (left) and the logarithmic scale (right) to emphasize the error in density of the gas phase.

Assuming a density profile (Lee & Fischer, 2006)

$$\rho(x) = \frac{\rho_{\text{Liq}} + \rho_{\text{Gas}}}{2} + \frac{\rho_{\text{Liq}} - \rho_{\text{Gas}}}{2} \tanh(x), \tag{8.47}$$

the nondimensional error is calculated and shown in Figure 8.2 for the van der Waals EoS at $\theta/\theta_c = 0.85$ for $\eta = 0, 1/2, 1$. It is evident that both $\eta = 1$ and $\eta = 0$ show larger fluctuations while $\eta = 1/2$ shows the least fluctuation. The parameter η can be further fine tuned to improve the accuracy, but for this work we restrict ourselves to $\eta = 1/2$.

To demonstrate the accuracy of the present model, we simulate a one dimensional interface of a van der Waals fluid on a grid of size $192 \times 4 \times 4$ using the $RD3Q41$ model (Namburi, 2017). Figure 8.3 shows the densities from the pressure formulation, chemical potential formulation, and the current scheme for three η values. It is evident that the current scheme predicts the values of phase density that matches with the theoretical Maxwell's construction values. From Figure 8.4 and Table 8.1, it can be seen the maximum magnitude of the spurious current is also reduced upon using the current formulation. Here, it should be pointed out that although $\eta = 0$ gives smaller spurious currents than $\eta = 1/2$, it succumbs to numerical instabilities at a higher $\theta/\theta_c = 0.87$.

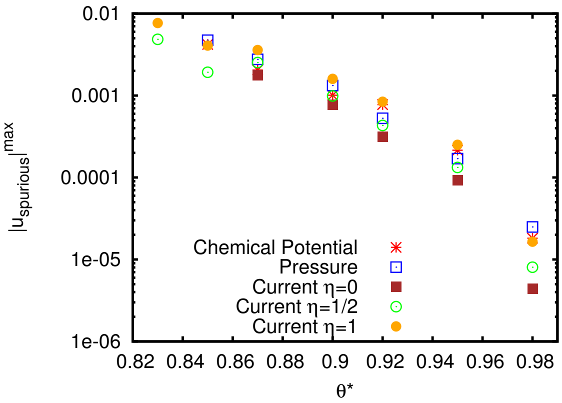

Figure 8.4: Spurious currents of the van der Waals fluid for various formulations at different reduced temperature $\theta^* = \theta/\theta_c$.

g_α^{nid}	Peng-Robinson [Eq.(8.6)]	Carnahan-Starling [Eq.(8.5)]
Pressure	6.376×10^{-3}	4.317×10^{-3}
Chemical potential	5.139×10^{-3}	4.281×10^{-3}
Current, $\eta = 1.0$	4.765×10^{-3}	5.565×10^{-3}
Current, $\eta = 0.5$	2.790×10^{-3}	3.706×10^{-3}

Table 8.1: Discretization scheme and the maximum magnitude of spurious current for various EoS on a grid of size 80 × 80 × 4 for various EoS at $\theta/\theta_c = 0.9$ using the model $RD3Q41$.

8.6 Quenching of a liquid-gas system

Quenching of a liquid-gas system exhibits phase separation and has been widely accepted as a test for thermodynamic consistency and stability of a multiphase lattice Boltzmann model (Wagner & Pooley, 2007). For $\theta < \theta_c$ the system shows phase separations where in the initial stages tiny bubbles of the liquid phase surrounded by the ambient gaseous phase are formed. As time progresses, the bubbles merge to form a stable structure, typically, a lamellar film, a cylindrical micelle, or a spherical droplet [see Figure 8.6]. Figure 8.5 shows the liquid and gas density obtained from $RD3Q41$ model compared against the theoretical values obtained from Maxwell's equal area construction, whereas Tables 8.2 and 8.3 list the values. It is seen that the model accurately recovers liquid-gas bulk densities hence is confirmed to be thermodynamically consistent.

8.7 Laplace law and Taylor's deformation test

In this section, we validate the proposed model for Laplace's law and Taylor's droplet deformation using the Peng-Robinsion type EoS [Eq.(8.6)]. According to Laplace's law, the inside of a stationary droplet has an excess pressure proportional to the surface tension

$$P_{\mathrm{i}} - P_{\mathrm{o}} = \frac{\sigma}{R}, \tag{8.48}$$

where P_{i}, P_{o} are the pressures inside and outside the droplet respectively, σ is the surface tension, and R is the radius of the droplet. Figure 8.7 shows setup for the Laplace's test and the value of surface tension σ obtained for two different values of κ.

The dynamics of a fluid drop suspended in another fluid was studied by Taylor (1934). He found that the deformation of the droplet for a small Reynolds number (Re) was only a function

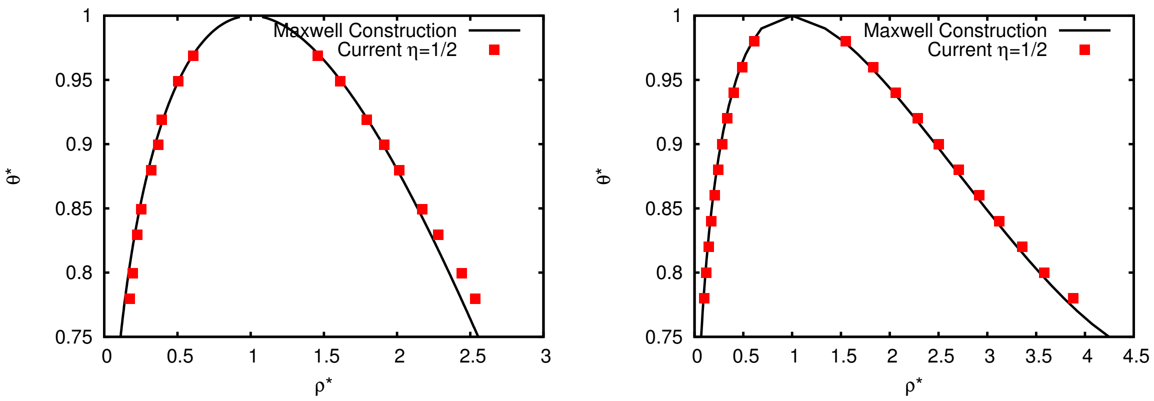

Figure 8.5: Equilibrium liquid and gas density $\rho/\rho_c = \rho^*$ obtained from $RD3Q41$ model for Carnahan Starling EoS (left) and Peng-Robinson type EoS compared against their respective Maxwell equal area construction at various $\theta/\theta_c = \theta^*$.

θ/θ_c	ρ_{liq} (Theory)	ρ_{liq} (Simulation)	ρ_{gas} (Theory)	ρ_{gas} (Simulation)
0.97	1.46	1.45	0.609	0.606
0.95	1.61	1.61	0.510	0.506
0.92	1.79	1.79	0.403	0.392
0.90	1.90	1.91	0.348	0.367
0.88	2.00	2.01	0.301	0.319
0.85	2.14	2.17	0.242	0.252
0.83	2.22	2.28	0.209	0.226
0.80	2.35	2.44	0.166	0.195
0.78	2.43	2.53	0.142	0.175

Table 8.2: Liquid and gas densities obtained from the proposed model compared with their corresponding Maxwell construction values for Carnahan-Starling EoS.

θ/θ_c	ρ_{liq} (Theory)	ρ_{liq} (Simulation)	ρ_{gas} (Theory)	ρ_{gas} (Simulation)
0.98	0.596020	0.614147	1.52725	1.54784
0.96	0.470612	0.491011	1.80422	1.83313
0.94	0.388844	0.399548	2.04273	2.06202
0.92	0.323261	0.336633	2.26023	2.28755
0.90	0.270872	0.284398	2.46917	2.49955
0.88	0.227217	0.241209	2.67433	2.70833
0.86	0.192037	0.204709	2.88048	2.91812
0.84	0.161138	0.171122	3.08956	3.12229
0.82	0.135434	0.144691	3.30622	3.35708
0.80	0.112238	0.118079	3.53471	3.58065
0.78	0.092664	0.098171	3.78422	3.88181

Table 8.3: Liquid and gas densities obtained from the proposed model compared with their corresponding Maxwell construction values for Peng-Robinson type EoS.

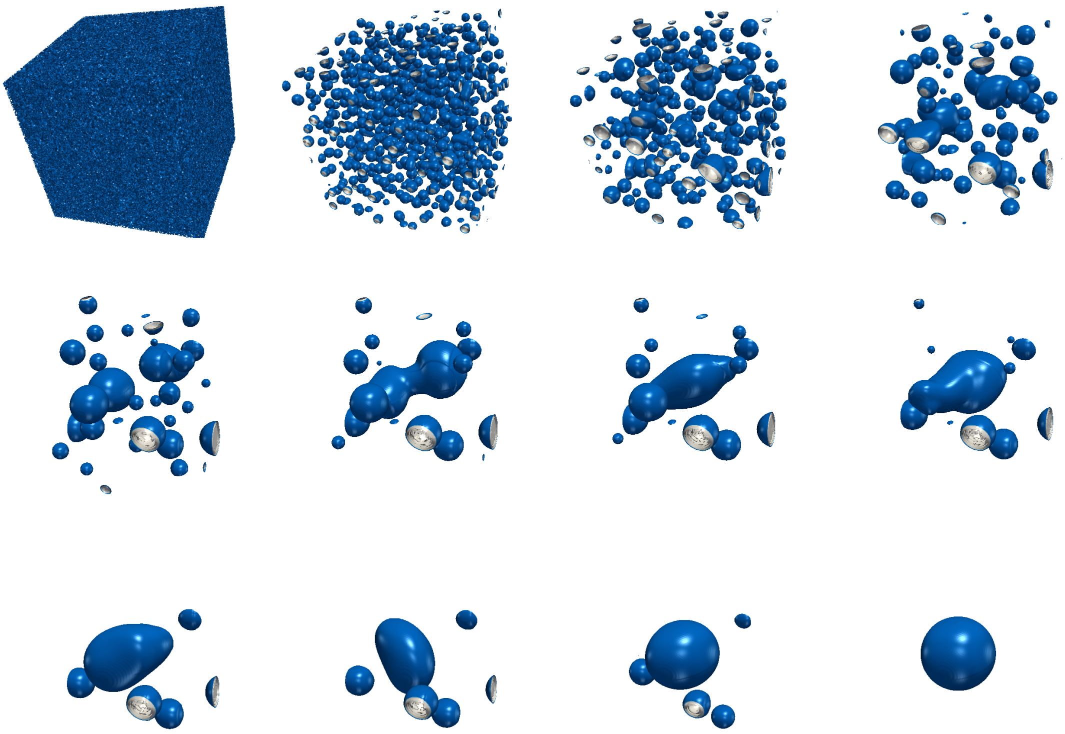

Figure 8.6: Deeply quenched liquid gas system forms a stable structure, typically a lamellar film, a cylindrical micelle, or a spherical droplet. Here, smaller droplets merge to form larger droplets.

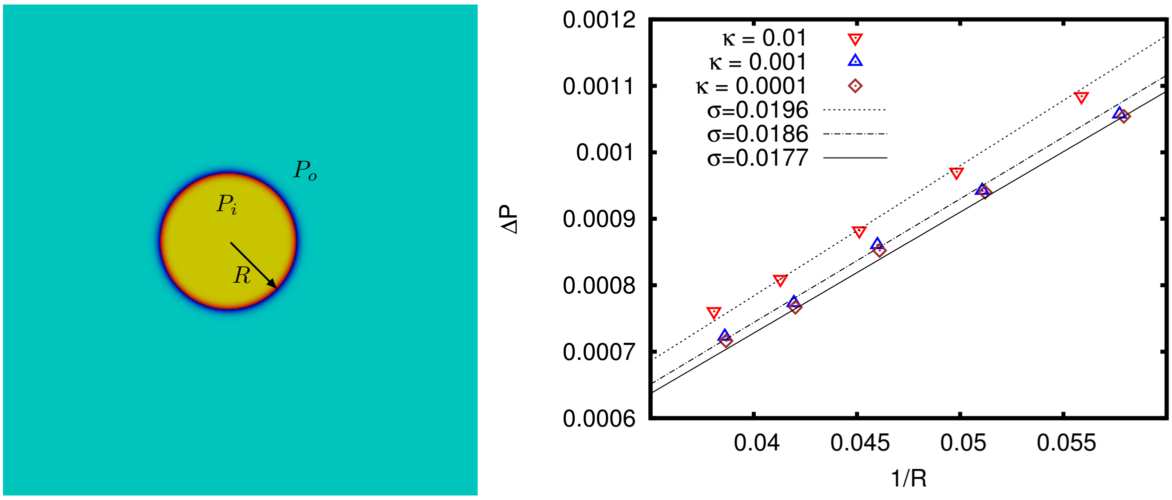

Figure 8.7: Laplace law: setup (left) and relation between pressure, surface tension, and radius (right).

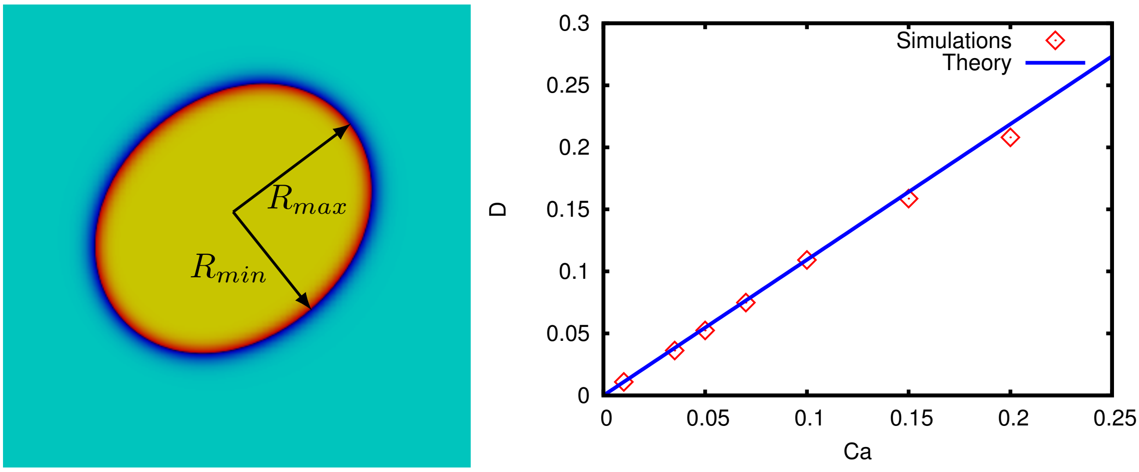

Figure 8.8: Taylors deformation test: A representation of the deformed droplet (left), and plot of D versus Ca (right).

of the nondimensional capillary number (Ca) and the viscosity ratio (λ) of the two fluids. In this setup, we consider a liquid droplet of density ρ_{Liq} and radius R_0 in equilibrium with its corresponding gas phase of density ρ_{Gas} confined between two parallel plates. The plates are a distance H apart and moving with a velocity u_w in opposite directions, due to which the droplet experiences a shear rate $\dot{\gamma} = 2u_w/H$. Assuming slow flow of a viscous fluid, Taylor (1934) derived the deformation D of the droplet from the spherical shape as

$$D = \frac{R_{\mathrm{max}} - R_{\mathrm{min}}}{R_{\mathrm{max}} + R_{\mathrm{min}}} = \frac{19\lambda + 19}{16\lambda + 16}\mathrm{Ca}, \tag{8.49}$$

where the capillary number Ca is

$$\mathrm{Ca} = R_0 \rho_{\mathrm{Gas}}\, \nu_{\mathrm{Gas}}\, \frac{\dot{\gamma}}{\sigma}. \tag{8.50}$$

It can be seen that Re of the fluid motion is small

$$\mathrm{Re} = \rho_{\mathrm{Gas}}\, \dot{\gamma} \frac{R_0^2}{\nu_{\mathrm{Gas}}} = \frac{R_0}{\nu_{\mathrm{Gas}}^2} \sigma \mathrm{Ca}. \tag{8.51}$$

The viscosity ratio λ is fixed to 1, and the surface tension is $\sigma = 0.0186$ corresponding to $\kappa = 0.001$. The droplet radius $R_0 = 24\Delta x$, while the height is $H = 96\Delta x$ and $\nu_{\mathrm{Gas}} = 0.147$ with $\Delta x = 1$. It can be seen that for small Ca ranging from 0.01 to 0.2, the Re is small as it ranges from ~ 0.2 to ~ 4. Figure 8.8 shows a schematic of the deformed droplet and the comparison of the deformation parameter D compared with Taylor's estimate. The simulations show a good match with the theory which suggests that the dynamics is modeled accurately.

8.8 Droplet Collision

We employ the proposed multiphase model and the Carnahan-Starling EoS (Carnahan & Starling, 1969) to simulate binary droplet collision as it offers interesting outcomes depending upon the control parameters (Mazloomi *et al.*, 2015). Three particular outcomes observed upon collision at various Reynolds number, Weber number and the impact parameter are coalescence, stretching separation, and reflexive separation (Inamuro *et al.*, 2004).

The setup consists of a rectangular box of $160\Delta x \times 200\Delta x \times 200\Delta x$ with two liquid phase droplets of diameter $D_0 = 45\Delta x$ and interface width $5\Delta x$ located in the ambient of gas phase

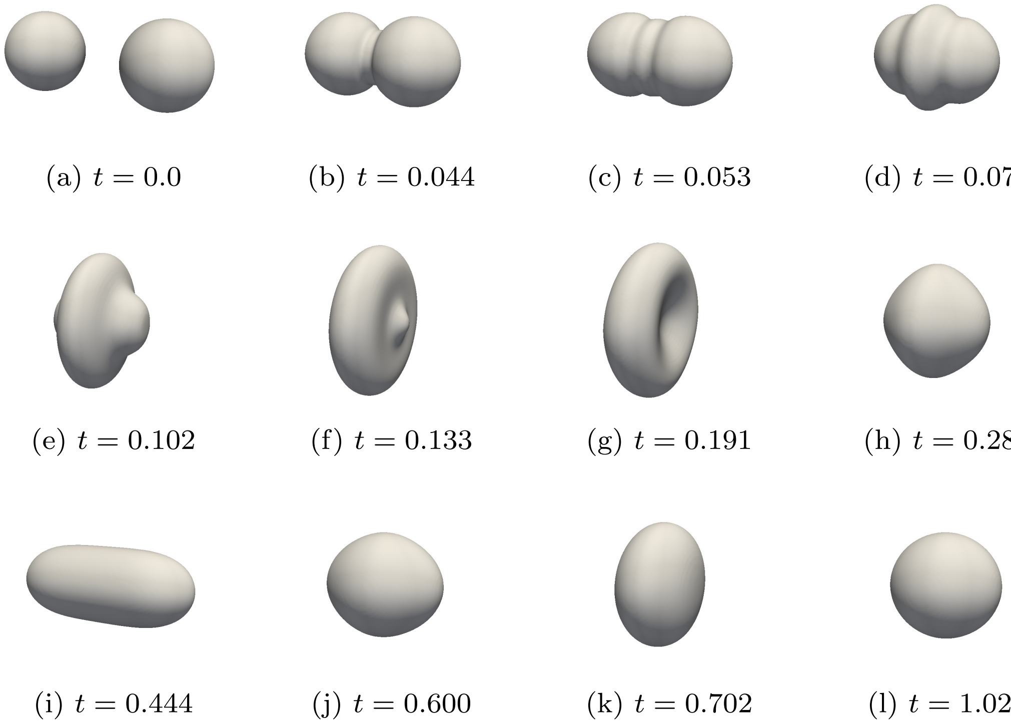

(a) $t = 0.0$ (b) $t = 0.044$ (c) $t = 0.053$ (d) $t = 0.071$

(e) $t = 0.102$ (f) $t = 0.133$ (g) $t = 0.191$ (h) $t = 0.289$

(i) $t = 0.444$ (j) $t = 0.600$ (k) $t = 0.702$ (l) $t = 1.027$

Figure 8.9: Head-on collision between two droplets at $\rho_{\text{liq}}/\rho_{\text{gas}} \approx 13$, Re $= 297.03$ and We$=$ 19.47.

with a distance of $30\Delta x$ between their centres. At $t = 0$, they are imparted a relative velocity $U_0 = 0.2\Delta x/\Delta t$ towards each other. The liquid phase having a density of $\rho_{\text{liq}}/\rho_c = 2.412$ is in equilibrium with the gas phase of density $\rho_{\text{gas}}/\rho_c = 0.185$ at $\theta/\theta_c = 0.8$. The chosen value of $\kappa = 0.001a\Delta x^2$ corresponds to a surface tension $\sigma = 0.223$. The kinematic viscosity of the liquid phase $\nu_{\text{liq}} = 0.0303$, hence, Reynolds number (Re) and the Weber number (We) are

$$\text{Re} = \frac{U_0 D_0}{\nu_{\text{liq}}} = 297.03, \quad \text{We} = \frac{\rho_{\text{liq}} U_0^2 D_0}{\sigma} = 19.47. \tag{8.52}$$

For calculating α required for the entropic formulation of LBM, we rewrite Eq.(8.23) as

$$\tilde{f}_i(\boldsymbol{x} + \boldsymbol{c}_i \Delta t, t + \Delta t) = \hat{f}_i(\boldsymbol{x}, t) + \alpha\beta[\hat{f}_i^{\text{eq}}(\rho, \boldsymbol{u}, \theta_0) - \hat{f}_i(\boldsymbol{x}, t)], \tag{8.53}$$

where the transformed populations $\hat{f}_i = \tilde{f}_i + \Delta t F_i$ and $\hat{f}_i^{\text{eq}} = f_i^{\text{eq}} + (\Delta t/2)F_i$. These transformations allow us to define $x_i = \hat{f}_i^{\text{eq}}/\hat{f}_i - 1$ and compute the path length α as detailed in Chapter 6. Figure 8.9 shows head-on collision between two droplets in thermodynamic equilibrium with the ambient. Similarly, Figure 8.10 shows collision between two droplets with their centers offset by a distance of $0.9D_0$.

8.9 Conclusions

In this chapter, we have proposed a thermodynamically consistent discretization of the forcing term for multiphase LBM which predicts accurate phase densities. The issue of spurious currents in multiphase LBMs was discussed and it was demonstrated that accurate discretization schemes reduce the magnitude of spurious currents. We have validated the proposed model for a number

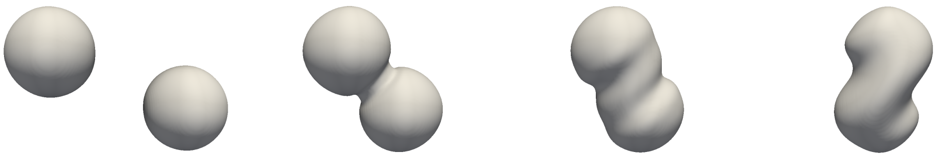

(a) $t = 0.0$ (b) $t = 0.027$ (c) $t = 0.036$ (d) $t = 0.049$

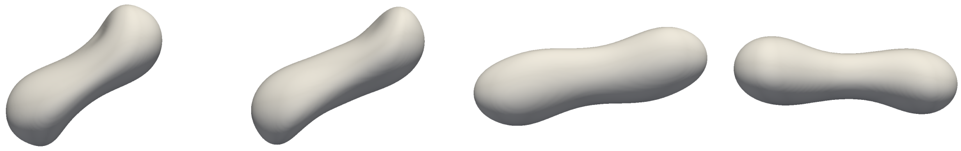

(e) $t = 0.076$ (f) $t = 0.089$ (g) $t = 0.120$ (h) $t = 0.164$

(i) $t = 0.222$ (j) $t = 0.276$ (k) $t = 0.311$ (l) $t = 0.556$

Figure 8.10: Offset collision between two droplets at $\rho_{\text{liq}}/\rho_{\text{gas}} \approx 13$, Re $= 297.03$ and We$= 19.47$.

of canonical test cases. The maximum density ratio at which the model remains stable for a closed form Peng-Robinson type EoS is ~ 50. However, as shown in Mazloomi *et al.* (2015), series form of equation of state could be employed to attain even higher density ratios.

Chapter 9
Outlook

The $\mathcal{H}$ theorem, an essential feature of the continuum kinetic theory, is explored in the context of the discrete space-time kinetic theory. The entropic lattice Boltzmann model (ELBM), developed about two decades ago, restores the $\mathcal{H}$ theorem to the discrete dynamics, thus rendering the simulations unconditionally numerically stable even on grossly under-resolved grids (Karlin *et al.*, 1999; Boghosian *et al.*, 2001). Despite significant progress, an analytical expression for the solution to the nonlinear equation in ELBM was lacking. In this thesis, we have developed a methodology to obtain such an analytical expression. There are three distinct advantages of this methodology: firstly, it provides an alternate kinetic route to modeling the subgrid phenomenon, secondly, it circumvents the need to iteratively solve the nonlinear equation thus reducing the computational cost associated with the ELBM, and lastly, it allows one to control dissipation depending on the scenario.

Further, a thermodynamically consistent higher-order $RD3Q67$ model has been validated for canonical test cases related to compressible thermohydrodynamics. By simulations of the Rayleigh-Bénard convection it has been shown that this model remains numerically stable for large Rayleigh numbers. This makes it a viable candidate to study scenarios involving natural convection and atmospheric flows. A discretization scheme has been proposed and validated for multiphase lattice Boltzmann model. This thermodynamically consistent scheme predicts accurate phase densities and results in reduced spurious currents. Furthermore, the discrete time $\mathcal{H}$ theorem is also proved for the generalized quasi-equilibrium collision model (Ansumali *et al.*, 2007*a*), to address flows with non-unitary Prandtl number.

As far as the modeling of subgrid phenomena is concerned, the widely employed large eddy simulation (LES) based approaches assume that the small scales are in equilibrium (Premnath *et al.*, 2009). They instantaneously dissipate all the energy transferred from the large scale, a mechanism modeled by eddy-viscosity, and are understood as a filtering on fluctuating turbulence (Malaspinas & Sagaut, 2012). The essentially entropic LBM discussed in this thesis is a kinetic route that circumvents the empirical modeling of subgrid phenomena, while adaptively filtering out fluctuations at a reduced computational expense. The entropic LBM seems to be an attractive alternate to the conventional way of simulating fluid flows. This is due to the fact that typically for engineering applications the direct numerical simulation turns out to be computationally unaffordable. On the other hand, the Reynolds averaged Navier-Stokes equations provide information only at the mean flow level, while the filter width in the large eddy simulation is problem dependent (Pope, 2000). It should be noted that the energy conserving $RD3Q67$ model studied in this thesis solves the compressible thermohydrodynamics. Hence, any simulation in addition to velocity fields will also give the correct density fluctuations, temperature field, and the acoustics.

In order to get an estimate of the computational requirement, we consider the simulation of flow past a bluff body of dimension $\sim 1m \times 1m \times 1m$ at a Reynolds number $\mathrm{Re} \sim 10^5 - 10^6$ and Mach number $\mathrm{Ma} \sim 0.05 - 0.1$, the required grid size to be simulated should be $\sim 10m \times 10m \times 10m$. The Kolmogorov scale η for such a flow is $\eta \sim L_{\mathrm{ref}}/\mathrm{Re}^{3/4} \approx 0.1mm$. The essentially entropic LBM which acts like an implicit adaptive subgrid model can be demanded to work at a resolution of $2mm$ (similar to the resolution required by LES). For such a system, the total number of grid points N is

$$N \sim \frac{10m \times 10m \times 10m}{2mm \times 2mm \times 2mm} = 10^{11}.$$

For estimation, let us consider the standard $D3Q27$ lattice, hence assuming single precision we have a RAM requirement of $27 \times 4\,\text{Bytes} \times 10^{11} \approx 10\text{TB}$. It is known that bottleneck for LBM simulations is the data movement, where 6 memory operations per point per iteration per discrete velocity is considered a lower estimate (Shet *et al.*, 2013). Therefore, the total amount of data movement requirement is

$$6\,\frac{\text{Operations}}{\text{discrete velocity} - \text{point}} \times 27\,\text{discrete velocity} \times 4\text{Bytes} \times 10^{11}\text{points} \approx 60\text{TB} \tag{9.1}$$

per iteration.

The clusters available in the market by the end of 2019 will be based on `Intel Cascade Lake` that offers 24 channels per node and a frequency of 2.9GHz, and `AMD EPYC Rome` that offers 16 channels per node and a frequency of 3.2GHz. Hence, a reasonable estimate of the data movement for a 200 node cluster is

$$16\,\text{channels per node} \times 3\text{GHz} \times 8\text{Bytes} \times 200\text{nodes} \approx 70\text{TB/sec}. \tag{9.2}$$

From Eqs.(9.1)-(9.2), approximately 1 sec per iteration is required. The total $\sim 10^5$ iterations are typically required for an engineering simulation. Therefore, the total time required for a typical simulation is

$$10^5\,\text{iterations} \times 1\,\text{sec/iterations} = 10^5\text{sec} \approx 1\text{ day}. \tag{9.3}$$

A number of petascale clusters of such configuration are being commissioned worldwide, including three exascale clusters (Cray, 2019). The rapid advancement of technology will ensure that in the next few years we will have enough computational resources to use the $RD3Q67$ model for realistic engineering simulations.

A natural derivative of the present work is to consider extending the $\mathcal{H}$ theorem to the various class of collision models. For example, if the methodology can be extended to the Boltzmann dynamics with a forcing model, an analytically tractable $\mathcal{H}$ theorem can be formulated for multiphase physics too. In Appendix C, we have proved the discrete time $\mathcal{H}$ theorem for the generalized quasi-equilibrium model. The $\mathcal{H}$ theorem for the quasi-equilibrium collision with a forcing model also requires further research. To this effect, the shifted equilibria (Sbragaglia *et al.*, 2009) can be used to introduce a forcing term into the quasi-equilibrium model, or the ellipsoidal BGK model. The ellipsoidal BGK model replaces the Maxwellian in the BGK model with an anisotropic Gaussian (Holway Jr, 1966) and satisfies the $\mathcal{H}$ theorem too (Andries *et al.*, 2000). It has Prandtl number as a free parameter with the restriction that it should be larger than 2/3, a range that encompasses a large number of fluids. Such models can be employed to study body force driven flows involving nonideal fluids at various Prandtl numbers.

There are multiple ways to incorporate the nonideal interactions into the lattice Boltzmann model (Shan & Chen, 1993; Wagner, 2006; Ansumali, 2011). These nonideal interactions lead to phase separation of the fluid into liquid and vapour phases. However, most works perform this phase transition in an isothermal setting. A few other works have a secondary distribution function to track the evolution of the temperature (Zhang & Chen, 2003; Gonnella *et al.*, 2010). The approach with shifted equilibrium, which gives the correct macroscopic thermohydrodynamic limit can be directly employed to simulate flows with phase transitions. This will open up the possibility to model convection in multiphase flows.

Clouds exert a direct influence on our day to day life. They are essential elements in metreology, weather forecasting, rainwater chemistry, agriculture, air traffic control, and the general circulation of the atmosphere, besides others (Yau & Rogers, 1996). The basic phenonmenon behind cloud formation is as follows: the water vapour evaporated from the earth's surface, primarily from the oceans, gets transported over long distances due to the atmospheric motions. It begins to ascend to higher altitudes because of encounter with a geographical barrier or the radiative heating of the atmosphere. At higher altitudes, as the temperature decreases the air tends to become saturated, thus leading to formation of visible clusters of tiny droplets condensed on small aerosol particles, which may remain in the liquid form or freeze to form ice crystals depending on the temperature. Collision and coalescence of smaller droplets lead to formation of larger drops that precipitate in the form of rain, snow, and hail (Khain & Pinsky, 2018). Thus, the formation, growth, and the precipitation of the atmospheric clouds involves amalgamation of many physical processes such as compressible turbulent flow, convection, radiative heat transfer, phase transition, nucleation and droplet interaction.

A fundamental understanding of the clouds is considered an important area of the atmospheric sciences. Clouds have a direct impact on the earth's energy budget, weather, and climate by blocking the sun's incoming radiation or by absorbing the thermal infrared radiation emitted by the earth's surface. Clouds cause rainfall, and are considered a key component in the hydrological cycle. Understanding clouds can lead to an accurate prediction of weather patterns, and can help prepare governments and farmers in advance to avoid loss of life and property. The study of cloud physics involves phenomena at two widely different scales: at the micrometer scale there is water vapour condensation to form liquid droplets or ice crystals, nucleation on aerosol particles, their growth and interaction, which is termed as "cloud microphysics", while at the the kilometer scale there are large scale air motions, wind, pressure patterns, and thermodynamic interactions, which is called "cloud dynamics" (Houze Jr, 2014). The phenomena at the two scales are coupled, for example, the latent heat released during the condensation of water vapour drives the circulation in the atmosphere, sometimes causing instabilities that lead to severe weather conditions (Kuo, 1965).

The lattice Boltzmann model, being a mesoscopic tool, is especially useful for systems where the macroscopic governing equations are not available but the microscopic physics is known (He & Doolen, 2002). The models proposed in this thesis can handle phase transition, two-phase flows, large Reynolds number flows and natural convection. Therefore, they can be used to develop a kinetic route to a physics based multiscale cloud model. The computational requirement for a cloud dynamics simulation for an area of $100km \times 100km \times 100km$ with a resolution of $2m \times 2m \times 2m$ is similar to flow past a bluff body as discussed above.

Appendix A

Evolution of the thermohydrodynamic moments

We begin with the Boltzmann BGK equation

$$\partial_t f + \partial_\beta \left(f c_\beta\right) = \Omega(f), \tag{A.1}$$

where $\Omega(f) = (f^{\mathrm{eq}} - f)/\tau$ is the collision kernel, with τ as the relaxation time. We define the peculiar velocity $\xi_\alpha = c_\alpha - u_\alpha$, and the integral

$$\int f\psi(\boldsymbol{\xi})d\boldsymbol{\xi} = \left\langle f, \psi(\boldsymbol{\xi})\right\rangle. \tag{A.2}$$

The various moments can be found as

$$\left\langle f, \left\{1, \xi_\alpha, \xi_\alpha\xi_\beta, \frac{1}{2}\xi^2, \xi_\alpha\xi_\beta\xi_\gamma, \frac{1}{2}\xi^2\xi_\alpha, \xi^2\xi_\alpha\xi_\beta, \xi^4\right\}\right\rangle = \left\{1, 0, p\delta_{\alpha\beta} + \sigma_{\alpha\beta}, \frac{3}{2}p, Q_{\alpha\beta\gamma}, q_\alpha, R_{\alpha\beta}, R\right\}. \tag{A.3}$$

The traceless part $\overline{A_{\alpha\beta}}$ of any second order tensor $A_{\alpha\beta}$ is defined as

$$\overline{A_{\alpha\beta}} = \frac{1}{2}\left(A_{\alpha\beta} + A_{\beta\alpha} - \frac{2}{3}A_{\gamma\gamma}\delta_{\beta\alpha}\right). \tag{A.4}$$

We also define

$$\overline{Q_{\alpha\beta\gamma}} = Q_{\alpha\beta\gamma} - \frac{2}{5}(q_\alpha\delta_{\beta\gamma} + q_\beta\delta_{\alpha\gamma} + q_\gamma\delta_{\alpha\beta}), \tag{A.5}$$

and

$$\overline{R_{\alpha\beta}} = R_{\alpha\beta} - \frac{1}{3}R\delta_{\alpha\beta}. \tag{A.6}$$

Multiplying the Eq.(A.1) with $\phi(\xi)$ one obtains

$$\partial_t \left(f\phi(\xi)\right) - f\partial_t\phi(\xi) + \partial_\beta\left(fc_\beta\phi(\xi)\right) - fc_\beta\partial_\beta\phi(\xi) = \Omega(f)\phi(\xi). \tag{A.7}$$

Applying the chain rule and integrating over the velocity space one obtains

$$\partial_t \left\langle f, \phi(\xi)\right\rangle - \left\langle f, (\partial_t\xi_\alpha)\partial_{\xi_\alpha}\phi(\xi)\right\rangle + \partial_\beta\left\langle f, (\xi_\beta + u_\beta)\phi(\xi)\right\rangle - \left\langle f, c_\beta(\partial_\beta\xi_\alpha)\partial_{\xi_\alpha}\phi(\xi)\right\rangle = \left\langle \Omega(f), \phi(\xi)\right\rangle. \tag{A.8}$$

Now substituting $\partial_t\xi_\alpha = \partial_t(c_\alpha - u_\alpha) = -\partial_t u_\alpha$ and $\partial_\beta\xi_\alpha = \partial_\beta(c_\alpha - u_\alpha) = -\partial_\beta u_\alpha$ we get

$$\begin{aligned}\partial_t \left\langle f, \phi(\xi)\right\rangle + (\partial_t u_\alpha)\left\langle f, \partial_{\xi_\alpha}\phi(\xi)\right\rangle + \partial_\beta\left\langle f, \xi_\beta\phi(\xi)\right\rangle + \partial_\beta\left[u_\beta\left\langle f, \phi(\xi)\right\rangle\right]\\ + (\partial_\beta u_\alpha)\left\langle f, c_\beta\partial_{\xi_\alpha}\phi(\xi)\right\rangle = \left\langle\Omega(f), \phi(\xi)\right\rangle.\end{aligned} \tag{A.9}$$

A.1 Evolution of density

Substituting $\phi(\xi) = 1$ in Eq.(A.9) we obtain the evolution of density (the continuity equation) as

$$\partial_t\rho + 0 + 0 + \partial_\alpha\left(\rho u_\alpha\right) + 0 = 0. \tag{A.10}$$

A.2 Evolution of velocity

Substituting $\phi(\xi) = \xi_\gamma$ in Eq.(A.9) we obtain the evolution of velocity as

$$0 + \partial_t u_\gamma + \frac{1}{\rho}\partial_\beta \left(p\delta_{\gamma\beta} + \sigma_{\gamma\beta}\right) + 0 + u_\beta \partial_\beta u_\gamma = 0. \tag{A.11}$$

A.3 Evolution of pressure, temperature, and the stress tensor

Substituting $\phi(\xi) = \xi_\gamma \xi_\kappa$ in Eq.(A.9) we obtain

$$\begin{aligned}\partial_t \left[p\delta_{\gamma\kappa} + \sigma_{\gamma\kappa}\right] + 0 + \partial_\beta Q_{\beta\gamma\kappa} + \partial_\beta \left[u_\beta \left(p\delta_{\gamma\kappa} + \sigma_{\gamma\kappa}\right)\right] + \left(\partial_\beta u_\alpha\right) \langle f, c_\beta (\xi_\kappa \delta_{\alpha\gamma} + \xi_\gamma \delta_{\alpha\kappa})\rangle \\ = \frac{1}{\tau}\left(\sigma^{\text{eq}}_{\gamma\kappa} - \sigma_{\gamma\kappa}\right).\end{aligned} \tag{A.12}$$

Substituting $c_\beta = \xi_\beta + u_\beta$ and integrating further we obtain

$$\begin{aligned}\partial_t \left[p\delta_{\gamma\kappa} + \sigma_{\gamma\kappa}\right] + \partial_\beta Q_{\beta\gamma\kappa} + \partial_\beta \left[u_\beta \left(p\delta_{\gamma\kappa} + \sigma_{\gamma\kappa}\right)\right] + (p\delta_{\beta\kappa} + \sigma_{\beta\kappa})\partial_\beta u_\gamma + (p\delta_{\beta\gamma} + \sigma_{\beta\gamma})\partial_\beta u_\kappa \\ = \frac{1}{\tau}\left(\sigma^{\text{eq}}_{\gamma\kappa} - \sigma_{\gamma\kappa}\right).\end{aligned} \tag{A.13}$$

Taking the trace (i.e., multiply with $\delta_{\gamma\kappa}$) of the above equation we obtain

$$3\partial_t p + 3u_\beta \partial_\beta p + 5p\partial_\beta u_\beta + 2\partial_\beta q_\beta + 2\sigma_{\beta\kappa}\partial_\beta u_\kappa = 0, \tag{A.14}$$

which gives the evolution of pressure as

$$\partial_t p + u_\beta \partial_\beta p + \frac{5}{3}p\partial_\beta u_\beta + \frac{2}{3}\sigma_{\beta\gamma}\partial_\beta u_\gamma + \frac{2}{3}\partial_\beta q_\beta = 0. \tag{A.15}$$

Substituting $p = \rho\theta$ in the evolution of pressure and rearranging the terms one obtains

$$\partial_t \theta + u_\beta \partial_\beta \theta + \frac{2}{3}\theta\partial_\beta u_\beta + \frac{2}{3\rho}\sigma_{\beta\gamma}\partial_\beta u_\gamma + \frac{2}{3\rho}\partial_\beta q_\beta + \theta\left[\partial_t \rho + \partial_\beta(\rho u_\beta)\right] = 0, \tag{A.16}$$

where the term in square braces is zero because of Eq.(A.10). Therefore, we obtain the evolution of temperature as

$$\partial_t \theta + u_\beta \partial_\beta \theta + \frac{2}{3}\theta\partial_\beta u_\beta + \frac{2}{3\rho}\sigma_{\beta\gamma}\partial_\beta u_\gamma + \frac{2}{3\rho}\partial_\beta q_\beta = 0. \tag{A.17}$$

Multiplying Eq.(A.15) with $\delta_{\gamma\kappa}$ and subtracting from Eq.(A.13) one obtains

$$\begin{aligned}&\partial_t \left[p\delta_{\gamma\kappa} + \sigma_{\gamma\kappa}\right] + \partial_\beta Q_{\beta\gamma\kappa} + \partial_\beta \left[u_\beta \left(p\delta_{\gamma\kappa} + \sigma_{\gamma\kappa}\right)\right] + (p\delta_{\beta\kappa} + \sigma_{\beta\kappa})\partial_\beta u_\gamma + (p\delta_{\beta\gamma} + \sigma_{\beta\gamma})\partial_\beta u_\kappa \\ &- \left[\partial_t p + u_\beta \partial_\beta p + \frac{5}{3}p\partial_\beta u_\beta + \frac{2}{3}\sigma_{\beta\gamma}\partial_\beta u_\gamma + \frac{2}{3}\partial_\beta q_\beta\right]\delta_{\gamma\kappa} = \frac{1}{\tau}\left(\sigma^{\text{eq}}_{\gamma\kappa} - \sigma_{\gamma\kappa}\right),\end{aligned} \tag{A.18}$$

which can be simplified as

$$\begin{aligned}\partial_t \sigma_{\gamma\kappa} + \partial_\beta \left[u_\beta \sigma_{\gamma\kappa}\right] + \partial_\beta Q_{\beta\gamma\kappa} - \frac{2}{3}\delta_{\gamma\kappa}\partial_\beta q_\beta + p\partial_\kappa u_\gamma + p\partial_\gamma u_\kappa - \frac{2}{3}p\delta_{\gamma\kappa}\partial_\beta u_\beta + \sigma_{\beta\kappa}\partial_\beta u_\gamma + \sigma_{\beta\gamma}\partial_\beta u_\kappa \\ - \frac{2}{3}\delta_{\gamma\kappa}\sigma_{\beta\gamma}\partial_\beta u_\gamma = \frac{1}{\tau}\left(\sigma^{\text{eq}}_{\gamma\kappa} - \sigma_{\gamma\kappa}\right).\end{aligned} \tag{A.19}$$

Rearranging the terms in the above equation we obtain the evolution of the stress tensor as

$$\partial_t \sigma_{\alpha\beta} + u_\gamma \partial_\gamma \sigma_{\alpha\beta} + \partial_\gamma \overline{Q_{\alpha\beta\gamma}} + \sigma_{\alpha\beta}\partial_\gamma u_\gamma + 2\overline{\sigma_{\gamma\beta}\partial_\gamma u_\alpha} + 2p\overline{\partial_\beta u_\alpha} + \frac{4}{5}\overline{\partial_\beta q_\alpha} = \frac{1}{\tau}\left(\sigma^{\mathrm{eq}}_{\alpha\beta} - \sigma_{\alpha\beta}\right). \tag{A.20}$$

A.4 Evolution of the heat flux

Substituting $\phi(\xi) = \xi^2 \xi_\alpha / 2$ in Eq.(A.9) we obtain

$$\begin{aligned} \partial_t q_\alpha + (\partial_t u_\beta)\left[\frac{5}{2}p\delta_{\alpha\beta} + \sigma_{\alpha\beta}\right] + \frac{1}{2}\partial_\beta R_{\alpha\beta} + \partial_\beta(q_\alpha u_\beta) + (\partial_\beta u_\alpha)\left\langle f, \frac{1}{2}\xi^2(\xi_\beta + u_\beta)\right\rangle \\ + (\partial_\beta u_\gamma)\left\langle f, \xi_\alpha \xi_\gamma(\xi_\beta + u_\beta)\right\rangle = \frac{1}{\tau}\left(q^{\mathrm{eq}}_\alpha - q_\alpha\right), \end{aligned} \tag{A.21}$$

which after substituting $\partial_t u_\beta$ from Eq.(A.11) is further simplified as

$$\begin{aligned} \partial_t q_\alpha - \left(u_\kappa \partial_\kappa u_\beta + \frac{1}{\rho}\partial_\beta p + \frac{1}{\rho}\partial_\kappa \sigma_{\beta\kappa}\right)\left[\frac{5}{2}p\delta_{\alpha\beta} + \sigma_{\alpha\beta}\right] + q_\beta \partial_\beta u_\alpha + \frac{1}{2}\partial_\beta R_{\alpha\beta} + \partial_\beta(q_\alpha u_\beta) + Q_{\alpha\beta\gamma}\partial_\beta u_\gamma \\ + \frac{3}{2}p u_\beta \partial_\beta u_\alpha + u_\beta(p\delta_{\alpha\gamma} + \sigma_{\alpha\gamma})(\partial_\beta u_\gamma) = \frac{1}{\tau}\left(q^{\mathrm{eq}}_\alpha - q_\alpha\right), \end{aligned} \tag{A.22}$$

where upon rearranging the terms we obtain the evolution for heat flux as

$$\begin{aligned} \partial_t q_\alpha + \frac{1}{2}\partial_\beta\left(\overline{R_{\alpha\beta}} + \frac{1}{3}R\,\delta_{\alpha\beta}\right) + \overline{Q_{\alpha\beta\gamma}}\partial_\gamma u_\beta + \partial_\beta\left(q_\alpha u_\beta\right) + \frac{7}{5}q_\beta \partial_\beta u_\alpha + \frac{2}{5}q_\alpha \partial_\beta u_\beta + \frac{2}{5}q_\beta \partial_\alpha u_\beta \\ - \frac{5}{2}\frac{p}{\rho}\partial_\alpha p - \frac{\sigma_{\alpha\beta}}{\rho}\partial_\beta p - \frac{5}{2}\frac{p}{\rho}\partial_\theta \sigma_{\alpha\theta} - \frac{\sigma_{\alpha\beta}}{\rho}\partial_\theta \sigma_{\beta\theta} = \frac{1}{\tau}\left(q^{\mathrm{eq}}_\alpha - q_\alpha\right). \end{aligned} \tag{A.23}$$

A.5 Constraints on the weights of DVM

It has been demonstrated that the moments of the discrete equilibrium f^{eq}_i should mimic the corresponding moments of the Maxwell Boltzmann distribution f^{MB} in order to obtain the correct equations of compressible thermohydrodynamics. The moments of the zero velocity Maxwell-Boltzmann distribution $\tilde{f}^{\mathrm{MB}} = f^{\mathrm{MB}}(\rho = 1, \boldsymbol{u} = 0, \theta)$ can be calculated from Gaussian integrals

$$\int_0^\infty dx\, x^{2n} \exp\left(-a x^2\right) = \frac{\sqrt{\pi} a^{2n+1}}{2^{n+1}}(2n-1)\cdot(2n-3)\cdot(2n-5)\cdots 3\cdot 1, \tag{A.24}$$

as

$$\int d\boldsymbol{c}\tilde{f}^{\mathrm{MB}}\left\{1, \boldsymbol{c}^2, \boldsymbol{c}^4, \boldsymbol{c}^6, \boldsymbol{c}^8, \boldsymbol{c}^{10}\right\} = \left\{1, 3\theta, 15\theta^2, 105\theta^3, 945\theta^4, 10395\theta^5\right\}. \tag{A.25}$$

The discrete equilibrium $\tilde{f}^{\mathrm{eq}}_i\left(\rho = 1, \boldsymbol{u} = 0, \theta_0\right)$ at zero velocity and reference temperature θ_0 is

$$\tilde{f}^{\mathrm{eq}}_i\left(\rho = 1, \boldsymbol{u} = 0, \theta_0\right) = w_i. \tag{A.26}$$

Hence, the moments of weights should mimic moments of the Maxwell-Boltzmann distribution, i.e.,

$$\left\langle w, \left\{1, \boldsymbol{c}^2, \boldsymbol{c}^4, \boldsymbol{c}^6, \boldsymbol{c}^8, \boldsymbol{c}^{10}\right\}\right\rangle = \left\{1, 3\theta_0, 15\theta_0^2, 105\theta_0^3, 945\theta_0^4, 10395\theta_0^5\right\}. \tag{A.27}$$

Appendix B
Analytical solutions

B.1 Analytical Solution for transient Couette/conduction

We evaluate some integrals for later use,

$$\int_0^1 \sin^2 n\pi y\, dy = \frac{1}{2}, \quad \int_0^1 y \sin n\pi y\, dy = -\frac{\cos n\pi}{n\pi}, \quad \int_0^1 \sin n\pi y\, dy = \frac{1-\cos n\pi}{n\pi}.$$

The equation we require to solve is

$$\frac{\partial \bar{\phi}}{\partial \bar{t}} = \frac{\partial^2 \bar{\phi}}{\partial \bar{y}^2},$$

with boundary and initial conditions as

$$\bar{\phi}(y,0) = 0.5 \quad \text{all ȳ},$$

$$\bar{\phi}(0,\bar{t}) = 0, \quad \bar{t} > 0,$$
$$\bar{\phi}(1,\bar{t}) = 1, \quad \bar{t} > 0.$$

Here $^-$ represents non-dimensional quantities and ϕ is velocity or temperature. The steady state solution is $\bar{\phi} = \bar{y}$. The deviation of actual field from the steady state can be written as

$$\hat{\phi} = \bar{\phi} - \bar{y}.$$

The governing equation, boundary condition and initial condition in terms of the deviation become

$$\frac{\partial \hat{\phi}}{\partial \bar{t}} = \frac{\partial^2 \hat{\phi}}{\partial \bar{y}^2},$$

with

$$\hat{\phi}(y,0) = 0.5 - \bar{y} \quad \text{all ȳ},$$
$$\hat{\phi}(0,\bar{t}) = 0, \quad \bar{t} > 0,$$
$$\hat{\phi}(1,\bar{t}) = 0, \quad \bar{t} > 0.$$

Using the separation of variables, the solution that vanishes for $t \to \infty$ is

$$\hat{\phi} = (c_1 \sin(n\pi\bar{y}) + c_2 \cos(n\pi\bar{y})) \exp(-\lambda\bar{t}),$$

where λ is the eigenvalue and c_1, c_2 are constants that remain to be determined. Now, $c_2 = 0$ follows form the boundary condition at $\bar{y} = 0$. The boundary condition at $\bar{y} = 1$ yields eigenvalues

$$\lambda = n^2\pi^2 \qquad \text{for} \qquad n = 1, 2, 3...$$

The general solution that satisfies the governing equation and boundary condition can then be written as

$$\hat{\phi} = \sum_{n=1}^{\infty} A_n \exp(-n^2\pi^2\bar{t}) \sin n\pi\bar{y}.$$

The coefficients A_n that satisfy the initial condition are now evaluated.

$$0.5 - \bar{y} = \sum_{n=1}^{\infty} A_n \sin n\pi\bar{y}.$$

It follows

$$A_n = \frac{\int_0^1 (0.5 - \bar{y}) \sin n\pi y \, dy}{\int_0^1 \sin^2 n\pi y \, dy} = \frac{1 + \cos n\pi}{n\pi}.$$

Therefore,

$$\boxed{\bar{\phi} = \bar{y} + \sum_{n=1}^{\infty} \frac{1 + \cos n\pi}{n\pi} \exp(-n^2\pi^2\bar{t}) \sin n\pi\bar{y}.}$$

B.2 Analytical Solution for 2D Transient Conduction

The governing equation is

$$\frac{\partial\bar{\phi}}{\partial\bar{t}} = \frac{\partial^2\bar{\phi}}{\partial\bar{x}^2} + \frac{\partial^2\bar{\phi}}{\partial\bar{y}^2},$$

with boundary and initial conditions as

$$\bar{\phi}(\bar{x}, \bar{y}, 0) = 0 \quad \text{all ȳ},$$

$$\bar{\phi}(0, \bar{y}, \bar{t}) = 0, \quad \bar{t} > 0,$$
$$\bar{\phi}(1, \bar{y}, \bar{t}) = 0, \quad \bar{t} > 0,$$
$$\bar{\phi}(\bar{x}, 0, \bar{t}) = 0, \quad \bar{t} > 0,$$
$$\bar{\phi}(\bar{x}, W/L, \bar{t}) = 1, \quad \bar{t} > 0.$$

We first find the steady state solution, for which we substitute $\hat{\phi}(x, y) = X(x) \cdot Y(y)$, hence

$$-\frac{1}{X}\frac{d^2X}{dx^2} = \frac{1}{Y}\frac{d^2Y}{dy^2} = \lambda^2.$$

The general solution is found as

$$X = c_1 \cos(\lambda x) + c_2 \sin(\lambda x),$$

$$Y = c_3 \exp(-\lambda y) + c_4 \exp(\lambda y).$$

Using the boundary condition $\bar{\phi}(0, y) = 0, \bar{\phi}(x, 0) = 0$, one obtains $c_1 = 0$ and $(c_3 + c_4) c_2 \sin(\lambda x) = 0$. Hence $c_3 = -c_4$ and

$$\bar{\phi}(x, y) = c_2 \sin(\lambda x) \cdot c_4(\exp(\lambda y) - \exp(-\lambda y)).$$

From the boundary condition at $(1, y)$ we obtain $\lambda = n\pi$ and therefore

$$\bar{\phi}(x, y) = \sum_{n=1}^{\infty} C_n \sin(n\pi x) \sinh(n\pi y).$$

Now, exploiting the boundary condition $\bar{\phi}(x, W/L) = 1$, one obtains

$$\bar{\phi}(x, W/L) = 1 = \sum_{n=1}^{\infty} C_n \sin(n\pi x) \sinh(n\pi W/L).$$

Multiply with $\sin(m\pi x)$,

$$C_n = \frac{1}{\sinh(n\pi W/L)} \frac{\int_0^1 \sin(m\pi x)dx}{\int_0^1 \sin^2(m\pi x)dx} = \frac{2(1-\cos(m\pi))}{m\pi}.$$

The steady state solution is found as

$$\boxed{\bar{\phi}_\infty = \frac{2}{\pi}\sum_{k=1}^{\infty} \frac{1-\cos(k\pi)}{k} \sin(k\pi x) \frac{\sinh(k\pi y)}{\sinh(k\pi W/L)}.}$$

The deviation from transients is $\hat{\phi} = \bar{\phi} - \bar{\phi}_\infty$. In terms of deviation, the governing equation and initial and boundary conditions become

$$\frac{\partial\hat{\phi}}{\partial\bar{t}} = \frac{\partial^2\hat{\phi}}{\partial\bar{x}^2} + \frac{\partial^2\hat{\phi}}{\partial\bar{y}^2},$$

with boundary and initial conditions as

$$\begin{aligned} \hat{\phi}(\bar{x},\bar{y},0) &= -\bar{\phi}_\infty \quad \text{all ȳ}, \\ \hat{\phi}(0,\bar{y},\bar{t}) &= 0, \quad \bar{t} > 0, \\ \hat{\phi}(1,\bar{y},\bar{t}) &= 0, \quad \bar{t} > 0, \\ \hat{\phi}(\bar{x},0,\bar{t}) &= 0, \quad \bar{t} > 0, \\ \hat{\phi}(\bar{x},W/L,\bar{t}) &= 0, \quad \bar{t} > 0. \end{aligned}$$

Using $\hat{\phi} = T(t)\cdot X(x)\cdot Y(y)$ and separation of variables, we have three equations as

$$\begin{aligned} \frac{\partial^2 X}{\partial x^2} + \lambda^2 X &= 0, \qquad X(0)=0, X(1)=0 \\ \frac{\partial^2 Y}{\partial y^2} + \kappa^2 Y &= 0, \qquad Y(0)=0, Y(W/L)=0 \\ \frac{\partial T}{\partial t} + (\lambda^2+\kappa^2)T &= 0. \end{aligned}$$

Therefore, $\lambda = m\pi$ and $\kappa = n\pi L/W$

$$\hat{\phi}_n = \exp(-(m^2 + n^2L^2/W^2)\pi^2 t)\cdot c_1\sin(m\pi x)\cdot c_3\sin(n\pi L/Wy)$$

Hence,

$$\hat{\phi} = \sum_{m=1}^{\infty}\sum_{n=1}^{\infty} A_{mn}\exp[-(m^2+n^2L^2/W^2)\pi^2 t]\cdot\sin(m\pi x)\cdot\sin(n\pi L/Wy)$$

Now, we need to find A_{mn} such that initial condition is satisfied. At $t = 0$,

$$-\bar{\phi}_\infty = \sum_{m=1}^{\infty}\sum_{n=1}^{\infty} A_{mn}\sin(m\pi x)\ \sin(n\pi L/Wy).$$

Multiply with $\sin(p\pi x)\sin(q\pi L/Wy)$ and integrate over $x = 0..1; y = 0..W/L$. The surviving terms are $m = p, n = q$. Hence

$$\int_0^{W/L} \int_0^1 -\bar{\phi}_\infty \sin(m\pi x) \sin(n\pi L/W y) dx\, dy = A_{mn} \int_0^{W/L} \int_0^1 \sin^2(m\pi x)\ \sin^2(n\pi L/W y) dx\, dy.$$

Using

$$\bar{\phi}_\infty = \frac{2}{\pi} \sum_{k=1}^{\infty} \frac{1-\cos(k\pi)}{k} \sin\left(k\pi x\right) \frac{\sinh(k\pi y)}{\sinh(k\pi W/L)}$$

one obtains

$$A_{mn} = -\frac{8}{\pi} \frac{L}{W} \sum_{k=1}^{\infty} \frac{1-\cos(k\pi)}{k \sinh(k\pi W/L)} \int_0^{W/L} \int_0^1 \sin(m\pi x) \sin(n\pi L/W y) \sin(k\pi x) \sinh(k\pi y) dx\, dy,$$

so $m = k$ and,

$$A_{mn} = -\frac{4}{\pi} \frac{L}{W} \frac{1-\cos(m\pi)}{m \sinh(m\pi W/L)} \int_0^{W/L} \sin(n\pi L/W y) \sinh(m\pi y) dy$$

or,

$$A_{mn} = -\frac{4}{\pi} \frac{L}{W} \frac{1-\cos(m\pi)}{m \sinh(m\pi W/L)} \left[\frac{m\pi \sin(n\pi L/W y) \cosh(m\pi y) - n\pi L/W \cos(n\pi L/W y) \sinh(m\pi y)}{(m^2 + n^2 L^2/W^2)\pi^2} \right]_0^{W/L}$$

or,

$$A_{mn} = \frac{4}{\pi^2} \frac{L}{W} \frac{1-\cos(m\pi)}{m \sinh(m\pi W/L)} \frac{nL/W \cos(n\pi) \sinh(m\pi W/L)}{m^2 + n^2 L^2/W^2}$$

or,

$$A_{mn} = \frac{4}{\pi^2} \frac{L^2}{W^2} \frac{1-\cos(m\pi)}{m} \frac{n \cos(n\pi)}{m^2 + n^2 L^2/W^2}$$

Appendix C

C.1 Discrete time $\mathcal{H}$ theorem for the generalized quasi-equilibrium model

The discrete evolution of populations using the generalized quasi-equilibrium collision kernel [see Section 4.3.1] for Prandtl number Pr < 1 is

$$f_i(t+\Delta t) = f_i(t) + \alpha\beta[\hat{f}_i - g_i(t)], \tag{C.1}$$

where $\alpha = 2$ is the standard path length and

$$\hat{f}_i = \left(1 - \frac{\tau}{\tau_1}\right) f_i^*(\rho, u, \theta, q_\alpha^{(f)}) + \frac{\tau}{\tau_1} f_i^{\text{eq}}(\rho, u, \theta). \tag{C.2}$$

For the case of Pr < 1, the heat flux $q_\alpha^{(f^*)} \equiv \left\langle f^*, c^2 c_\alpha \right\rangle$ is conserved by the quasi-equilibrium state, i.e., $q_\alpha^{(f^*)} = q_\alpha^{(f)}$, where

$$q_\alpha^{(f)} = \frac{\left\langle f, c^2 c_\alpha \right\rangle + \frac{\Delta t}{2\tau_1} \left\langle f^{\text{eq}}, c^2 c_\alpha \right\rangle}{1 + \frac{\Delta t}{2\tau_1}}. \tag{C.3}$$

It can be seen that $\hat{f}_i$ is a convex combination of f_i^* and f_i. Therefore,

$$\mathcal{H}[f^{\text{eq}}] < \mathcal{H}[\hat{f}] < \mathcal{H}[f^*] < \mathcal{H}[f], \tag{C.4}$$

as the equilibrium state has the least entropy, and the quasi-equilibrium state (f^*) is at lower entropy level than the pre-collisional state f. The equilibrium state f_i^{eq} and the quasi-equilibrium state f_i^* are found as minimizer of the $\mathcal{H}$ functional under appropriate constraints as

$$f_i^{\text{eq}} = w_i \exp(\mu + \zeta_\alpha c_{i\alpha} + \gamma c_i^2), \tag{C.5}$$
$$f_i^* = w_i \exp(\mu + \zeta_\alpha c_{i\alpha} + \gamma c_i^2 + \phi_\alpha c_i^2 c_{i\alpha}). \tag{C.6}$$

For the entropic formulation the path length needs to be evaluated such that $\mathcal{H}(t+\Delta t) < \mathcal{H}(t)$. Hence,

$$\Delta\mathcal{H} \equiv \mathcal{H}[f + \alpha\beta(\hat{f} - f)] - \mathcal{H}[f] \leq 0. \tag{C.7}$$

Consider Boltzmann's $\mathcal{H}$-functional $\mathcal{H}[f] = \langle f, \log(f/w) - 1 \rangle$. Substituting this form of $\mathcal{H}[f]$ and w from Eq.(C.5) in Eq. (C.7) we see that

$$\begin{aligned}\Delta\mathcal{H} &= \langle f, (1+\alpha\beta x)\log(1+\alpha\beta x) \rangle - \alpha\beta \left\langle \hat{f} - f, \log\frac{w}{f} \right\rangle \\ &= \langle f, (1+\alpha\beta x)\log(1+\alpha\beta x) \rangle - \alpha\beta\frac{\tau}{\tau_1} \left\langle f^{\text{eq}} - f, \log\frac{f^{\text{eq}}}{f} \right\rangle - \alpha\beta\left(1 - \frac{\tau}{\tau_1}\right) \left\langle f^* - f, \log\frac{f^{\text{eq}}}{f} \right\rangle\end{aligned} \tag{C.8}$$

where $x = \hat{f}/f - 1$. Multiplying and dividing the last term with $\exp(\phi_\alpha c^2 c_\alpha)$ one obtains

$$\begin{aligned}
\Delta\mathcal{H} &= \langle f, (1+\alpha\beta x)\log(1+\alpha\beta x)\rangle - \alpha\beta\frac{\tau}{\tau_1}\langle f, y\log(1+y)\rangle \\
&\quad - \alpha\beta\left(1-\frac{\tau}{\tau_1}\right)\left\langle f^* - f, \log\frac{f^{\mathrm{eq}}\exp(\phi_\alpha c^2 c_\alpha)}{f\exp(\phi_\alpha c^2 c_\alpha)}\right\rangle \\
&= \langle f, (1+\alpha\beta x)\log(1+\alpha\beta x)\rangle - \alpha\beta\frac{\tau}{\tau_1}\langle f, y\log(1+y)\rangle - \alpha\beta\left(1-\frac{\tau}{\tau_1}\right)\langle f, z\log(1+z)\rangle \\
&\quad + \alpha\beta\left(1-\frac{\tau}{\tau_1}\right)\left\langle f^* - f, \phi_\alpha c^2 c_\alpha\right\rangle \\
&= \langle f, (1+\alpha\beta x)\log(1+\alpha\beta x)\rangle - \alpha\beta\frac{\tau}{\tau_1}\langle f, y\log(1+y)\rangle - \alpha\beta\left(1-\frac{\tau}{\tau_1}\right)\langle f, z\log(1+z)\rangle \\
&\quad + \alpha\beta\left(1-\frac{\tau}{\tau_1}\right)\phi_\alpha\left[q_\alpha^{(f^*)} - \left\langle f, c^2 c_\alpha\right\rangle\right]
\end{aligned} \tag{C.9}$$

where $y = f^{\mathrm{eq}}/g - 1, z = f^*/g - 1$. Substituting $\left\langle f, c^2 c_\alpha\right\rangle$ from Eq.(C.3) one obtains

$$\begin{aligned}
\Delta\mathcal{H} &= \langle f, (1+\alpha\beta x)\log(1+\alpha\beta x)\rangle - \alpha\beta\frac{\tau}{\tau_1}\langle f, y\log(1+y)\rangle - \alpha\beta\left(1-\frac{\tau}{\tau_1}\right)\langle f, z\log(1+z)\rangle \\
&\quad + \alpha\beta\left(1-\frac{\tau}{\tau_1}\right)\frac{\phi_\alpha\Delta t}{2\tau_1}\left[\left\langle f^{\mathrm{eq}}, c^2 c_\alpha\right\rangle - q_\alpha^{(f)}\right].
\end{aligned} \tag{C.10}$$

Following the same idea as Section 6.3, the lower order solution for the path length is evaluated as the root of the quadratic equation $H_1(\alpha) = 0$,

$$\begin{aligned}
H_1(\alpha) = -\alpha^2\left\langle g, \frac{x^3}{2}\right\rangle_{\Omega^-} + \alpha\left\langle g, \frac{x^2}{2}\right\rangle - \frac{\tau}{\tau_1}\left\langle g, \frac{2y^2}{2+y}\right\rangle - \left(1-\frac{\tau}{\tau_1}\right)\left\langle g, \frac{2z^2}{2+z}\right\rangle \\
+ \left(1-\frac{\tau}{\tau_1}\right)\frac{\phi_\alpha\Delta t}{2\tau_1}\left[\left\langle f^{\mathrm{eq}}, c^2 c_\alpha\right\rangle - q_\alpha^{(f)}\right] = 0.
\end{aligned} \tag{C.11}$$

The above quadratic is similar to Eq.(6.48) with the addition of one term to the constant part. It should be noted than in the case of small departure from equilibrium $f_i \to f_i^{\mathrm{eq}}$, we have:

- From Eq.(C.3), $q_\alpha^{(f)} \to \left\langle f^{\mathrm{eq}}, c^2 c_\alpha\right\rangle$, therefore, the last term in the Eq.(C.11) vanishes.
- From Eq.(C.4), $f_i^* \to f_i^{\mathrm{eq}}$ and thus $\hat{f}_i \to f_i^{\mathrm{eq}}$. Therefore, $x_i \to 0, y_i \to 0, z_i \to 0$. Hence, Eq.(C.11) becomes like Eq.(6.48) and $\alpha \to 2$ limit is recovered.

The numerical implementation of the above formulation of discrete time $\mathcal{H}$ theorem for the generalized quasi-equilibrium model will be part of future studies.

References

Abe, T. 1997 Derivation of the lattice Boltzmann method by means of the discrete ordinate method for the Boltzmann equation. *J. Comput. Phys.* **131** (1), 241–246.

Abramowitz, M. & Stegun, I. A. 1965 *Handbook of Mathematical Functions: With Formulas, Graphs, and Mathematical Tables*, , vol. 55. Courier Corporation.

Adhikari, R., Stratford, K., Cates, M. E. & Wagner, A. J. 2005 Fluctuating lattice Boltzmann. *Europhys. Lett.* **71** (3), 473.

Aidun, C. K. & Clausen, J. R. 2010 Lattice-Boltzmann method for complex flows. *Annu. Rev. Fluid Mech.* **42**, 439–472.

Alexander, F. J., Chen, S. & Sterling, J. D. 1993 Lattice Boltzmann thermohydrodynamics. *Phys. Rev. E* **47**, R2249–R2252.

Andries, P., Le Tallec, P., Perlat, J. P. & Perthame, B. 2000 The Gaussian-BGK model of Boltzmann equation with small Prandtl number. *Euro. J. Mech. B* **19** (6), 813–830.

Ansumali, S. 2011 Mean-field model beyond Boltzmann-enskog picture for dense gases. *Commun. Comput. Phys.* **9**, 056703.

Ansumali, S., Arcidiacono, S., Chikatamarla, S., Prasianakis, N., Gorban, A. & Karlin, I. 2007*a* Quasi-equilibrium lattice Boltzmann method. *Eur. Phys. J. B* **56** (2), 135–139.

Ansumali, S., Karlin, I., C.E., F. & Boulouchos, K. 2006 Entropic lattice Boltzmann method for microflows. *Physica A* **359**, 289 – 305.

Ansumali, S. & Karlin, I. V. 2000 Stabilization of the lattice Boltzmann method by the H theorem: A numerical test. *Phys. Rev. E* **62** (6), 7999.

Ansumali, S. & Karlin, I. V. 2002*a* Entropy function approach to the lattice Boltzmann method. *J. Stat. Phys.* **107** (1-2), 291–308.

Ansumali, S. & Karlin, I. V. 2002*b* Kinetic boundary conditions in the lattice Boltzmann method. *Phys. Rev. E* **66** (2), 026311.

Ansumali, S. & Karlin, I. V. 2002*c* Single relaxation time model for entropic lattice Boltzmann methods. *Phys. Rev. E* **65** (5), 056312.

ANSUMALI, S. & KARLIN, I. V. 2005 Consistent lattice Boltzmann method. *Phys. Rev. Lett.* **95** (26), 260605.

ANSUMALI, S., KARLIN, I. V., ARCIDIACONO, S., ABBAS, A. & PRASIANAKIS, N. I. 2007*b* Hydrodynamics beyond navier-stokes: Exact solution to the lattice Boltzmann hierarchy. *Phys. Rev. Lett.* **98** (12), 124502.

ANSUMALI, S., KARLIN, I. V. & ÖTTINGER, H. C. 2003 Minimal entropic kinetic models for hydrodynamics. *Europhys. Lett.* **63** (6), 798.

ARCIDIACONO, S., MANTZARAS, J., ANSUMALI, S., KARLIN, I. V., FROUZAKIS, C. & BOULOUCHOS, K. B. 2006 Simulation of binary mixtures with the lattice Boltzman method. *Phys. Rev. E* **74**, 056707.

ASINARI, P. & KARLIN, I. V. 2010 Quasiequilibrium lattice Boltzmann models with tunable bulk viscosity for enhancing stability. *Physical Review E* **81** (1), 016702.

ATIF, M., KOLLURU, P. K., THANTANAPALLY, C. & ANSUMALI, S. 2017 Essentially entropic lattice Boltzmann model. *Phys. Rev. Lett.* **119**, 240602.

ATIF, M., NAMBURI, M. & ANSUMALI, S. 2018 Higher-order lattice Boltzmann model for thermohydrodynamics. *Phys. Rev. E* **98**, 053311.

BARTOLONI, A., BATTISTA, C., CABASINO, S., PAOLUCCI, P., PECH, J., SARNO, R., TODESCO, G., TORELLI, M., TROSS, W., VICINI, P. *et al.* 1993 LBE simulations of Rayleigh-Bénard convection on the APE100 parallel processor. *Int. J. Mod. Phys. C* **4** (05), 993–1006.

BATCHELOR, G. K. 2000 *An introduction to fluid dynamics*. Cambridge university press.

BENZI, R., BERNASCHI, M., SBRAGAGLIA, M. & SUCCI, S. 2013 Rheological properties of soft-glassy flows from hydro-kinetic simulations. *Europhys. Lett.* **104** (4), 48006.

BENZI, R., SUCCI, S. & VERGASSOLA, M. 1992 The lattice Boltzmann equation: theory and applications. *Phys. Rep.* **222** (3), 145–197.

BESSENYEI, M. 2008 Hermite–Hadamard-type inequalities for generalized convex functions. *J. Inequal. Pure Appl. Math* **9** (3), 51.

BHATNAGAR, P. L., GROSS, E. P. & KROOK, M. 1954 A model for collision processes in gases. i. small amplitude processes in charged and neutral one-component systems. *Phys. Rev.* **94** (3), 511.

BIRD, R. B., STEWART, W. E., LIGHTFOOT, E. N. & KLINGENBERG, D. J. 2015 *Introductory Transport Phenomena*, , vol. 1. Wiley New York.

BOGHOSIAN, B. M. & COVENEY, P. V. 1998 Inverse Chapman–Enskog derivation of the thermohydrodynamic lattice-BGK model for the ideal gas. *Int. J. Mod. Phys. C* **9** (08), 1231–1245.

Boghosian, B. M., Love, P. J., Coveney, P. V., Karlin, I. V., Succi, S. & Yepez, J. 2003 Galilean-invariant lattice-Boltzmann models with H theorem. *Phys. Rev. E* **68** (2), 025103.

Boghosian, B. M., Yepez, J., Coveney, P. V. & Wagner, A. J. 2001 Entropic lattice Boltzmann methods. *Proc. R. Soc. London, Ser. A* **457** (2007), 717–766.

Broadwell, J. E. 1964 Shock structure in a simple discrete velocity gas. *Phys. Fluids* **7** (8), 1243–1247.

Brownlee, R. A., Gorban, A. N. & Levesley, J. 2007 Stability and stabilization of the lattice Boltzmann method. *Phys. Rev. E* **75** (3), 036711.

Burg, J. 1967 Maximum entropy spectral analysis. In *Proceedings 37th Annual Meeting of the Society of Exploration Geophysicists*. Oklahoma City, OK.

Callen, H. B. 1998 Thermodynamics and an introduction to thermostatistics.

Carnahan, N. F. & Starling, K. E. 1969 Equation of state for nonattracting rigid spheres. *J. Chem. Phys.* **51** (2), 635–636.

Cercignani, C. 1988 *The Boltzmann Equation and Its Applications*. Springer, New York, NY.

Cercignani, C. 1997 Temperature, entropy, and kinetic theory. *Journal of statistical physics* **87** (5-6), 1097–1109.

Chapman, S. & Cowling, T. G. 1970 *The Mathematical Theory of Non-uniform Gases*. Cambridge University Press, Cambridge.

Chen, F., Xu, A., Zhang, G., Li, Y. & Succi, S. 2010 Multiple-relaxation-time lattice Boltzmann approach to compressible flows with flexible specific-heat ratio and Prandtl number. *Europhys. Lett.* **90** (5), 54003.

Chen, H., Chen, S. & Matthaeus, W. H. 1992 Recovery of the navier-stokes equations using a lattice-gas Boltzmann method. *Phys. Rev. A* **45** (8), R5339.

Chen, H., Orszag, S. A., Staroselsky, I. & Succi, S. 2004 Expanded analogy between Boltzmann kinetic theory of fluids and turbulence. *J. Fluid Mech.* **519**, 301–314.

Chen, H. & Teixeira, C. 2000 H-theorem and origins of instability in thermal lattice Boltzmann models. *Comp. Phys. Commun.* **129** (1), 21–31.

Chen, S. & Doolen, G. D. 1998 Lattice Boltzmann method for fluid flows. *Annu. Rev. Fluid Mech.* **30** (1), 329–364.

Chikatamarla, S. & Karlin, I. 2013*a* Entropic lattice Boltzmann method for turbulent flow simulations: Boundary conditions. *Physica A: Statistical Mechanics and its Applications* **392** (9), 1925–1930.

Chikatamarla, S. & Karlin, I. 2013*b* Entropic lattice Boltzmann method for turbulent flow simulations: Boundary conditions. *Physica A* **392** (9), 1925 – 1930.

Chikatamarla, S. S., Ansumali, S. & Karlin, I. V. 2006 Entropic lattice Boltzmann models for hydrodynamics in three dimensions. *Phys. Rev. Lett.* **97** (1), 010201.

Chikatamarla, S. S., Frouzakis, C. E., Karlin, I. V., Tomboulides, A. G. & Boulouchos, K. B. 2010 Lattice Boltzmann method for direct numerical simulation of turbulent flows. *J. Fluid Mech.* **656**, 298308.

Chikatamarla, S. S. & Karlin, I. V. 2006 Entropy and Galilean invariance of lattice Boltzmann theories. *Phys. Rev. Lett.* **97** (19), 190601.

Chikatamarla, S. S. & Karlin, I. V. 2009 Lattices for the lattice Boltzmann method. *Phys. Rev. E* **79** (4), 046701.

Clever, R. M. & Busse, F. H. 1974 Transition to time-dependent convection. *J. Fluid Mech.* **65** (4), 625645.

Coreixas, C., Chopard, B. & Latt, J. 2019 Comprehensive comparison of collision models in the lattice Boltzmann framework: Theoretical investigations. *Phys. Rev. E (in press)* .

Coreixas, C., Wissocq, G., Puigt, G., Boussuge, J.-F. & Sagaut, P. 2017 Recursive regularization step for high-order lattice boltzmann methods. *Phys. Rev. E* **96**, 033306.

Cray 2019 Cray announces third exascale supercomputer win. `https://www.cray.com/blog/cray-announces-third-exascale-supercomputer-win/`, [Online; accessed 23-August-2019].

Ambruş, V. E. & Sofonea, V. 2012 High-order thermal lattice Boltzmann models derived by means of Gauss quadrature in the spherical coordinate system. *Phys. Rev. E* **86**, 016708.

Deardorff, J. W. 1970 A numerical study of three-dimensional turbulent channel flow at large Reynolds numbers. *J. Fluid Mech.* **41** (2), 453–480.

d'Humières, D. 2002 Multiple–relaxation–time lattice Boltzmann models in three dimensions. *Philos. Trans. Royal Soc. A* **360** (1792), 437–451.

Dixon, S. L. & Hall, C. 2013 *Fluid mechanics and thermodynamics of turbomachinery*. Butterworth-Heinemann.

Dorschner, B., Bösch, F., Chikatamarla, S. S., Boulouchos, K. & Karlin, I. V. 2016*a* Entropic multi-relaxation time lattice Boltzmann model for complex flows. *J. Fluid Mech.* **801**, 623–651.

Dorschner, B., Frapolli, N., Chikatamarla, S. S. & Karlin, I. V. 2016*b* Grid refinement for entropic lattice Boltzmann models. *Phys. Rev. E* **94**, 053311.

Entezari, A., Dyer, R. & Mller, T. 2009 From sphere packing to the theory of optimal lattice sampling. In *Mathematical Foundations of Scientific Visualization, Computer Graphics, and Massive Data Exploration*, pp. 227–255. Springer.

Evans, R. 1979 The nature of the liquid-vapour interface and other topics in the statistical mechanics of non-uniform, classical fluids. *Adv. Phys.* **28** (2), 143–200.

Filippova, O. & Hänel, D. 1998 Grid refinement for lattice-BGK models. *J. Comput. Phys.* **147** (1), 219–228.

Franjić, I. & Pečarić, J. 2011 Schur-convexity and the Simpson formula. *Applied mathematics letters* **24** (9), 1565–1568.

Franjic, I. & Pecaric, J. 2012 Hermite-Hadamard type inequalities for higher order convex functions and various quadrature rules. *Acta Mathematica Vietnamica* **37** (1), 109–120.

Frapolli, N., Chikatamarla, S. & Karlin, I. 2018 Entropic lattice Boltzmann simulation of thermal convective turbulence. *Comp. Fluids* **175**, 2 – 19.

Frapolli, N., Chikatamarla, S. S. & Karlin, I. V. 2014 Multispeed entropic lattice Boltzmann model for thermal flows. *Phys. Rev. E* **90**, 043306.

Frapolli, N., Chikatamarla, S. S. & Karlin, I. V. 2015 Entropic lattice Boltzmann model for compressible flows. *Phys. Rev. E* **92** (6), 061301.

Frapolli, N., Chikatamarla, S. S. & Karlin, I. V. 2016*a* Entropic lattice Boltzmann model for gas dynamics: Theory, boundary conditions, and implementation. *Phys. Rev. E* **93** (6), 063302.

Frapolli, N., Chikatamarla, S. S. & Karlin, I. V. 2016*b* Lattice kinetic theory in a comoving Galilean reference frame. *Phys. Rev. Lett.* **117** (1), 010604.

Frisch, U., Hasslacher, B. & Pomeau, Y. 1986 Lattice-gas automata for the navier-stokes equation. *Phys. Rev. Lett.* **56** (14), 1505.

Gatignol, R. 1977 Kinetic theory boundary conditions for discrete velocity gases. *The Physics of Fluids* **20** (12), 2022–2030.

Geier, M., Pasquali, A. & Schnherr, M. 2017 Parametrization of the cumulant lattice Boltzmann method for fourth order accurate diffusion part ii: Application to flow around a sphere at drag crisis. *J. Comput. Phys.* **348**, 889 – 898.

Ghia, U., Ghia, K. & Shin, C. 1982 High-re solutions for incompressible flow using the navier-stokes equations and a multigrid method. *J. Comput. Phys.* **48** (1), 387 – 411.

Gonnella, G., Lamura, A., Piscitelli, A. & Tiribocchi, A. 2010 Phase separation of binary fluids with dynamic temperature. *Phys. Rev. E* **82**, 046302.

Gorban, A. N. & Karlin, I. V. 1994 General approach to constructing models of the Boltzmann equation. *Physica A* **206** (3-4), 401–420.

Gorban, A. N., Karlin, I. V., Zmievskii, V. B. & Nonnenmacher, T. 1996 Relaxational trajectories: global approximations. *Physica A* **231** (4), 648–672.

Gorban, A. N. & Packwood, D. 2012 Allowed and forbidden regimes of entropy balance in lattice Boltzmann collisions. *Phys. Rev. E* **86** (2), 025701.

Grad, H. 1949 On the kinetic theory of rarefied gases. *Commun. Pure Applied Math.* **2** (4), 331–407.

Gregory, N. & O'reilly, C. 1973 *Low-Speed aerodynamic characteristics of NACA 0012 aerofoil section, including the effects of upper-surface roughness simulating hoar frost*. HM Stationery Office London.

Guichard, F. & Couvreux, F. 2017 A short review of numerical cloud-resolving models. *Tellus A* **69** (1), 1373578.

Gunstensen, A. K., Rothman, D. H., Zaleski, S. & Zanetti, G. 1991 Lattice Boltzmann model of immiscible fluids. *Phys. Rev. A* **43**, 4320–4327.

Guo, Z., Shi, B. & Zheng, C. 2002 A coupled lattice BGK model for the Boussinesq equations. *Int. J. Numer. Methods Fluids* **39** (4), 325–342.

He, X., Chen, S. & Doolen, G. D. 1998*a* A novel thermal model for the lattice Boltzmann method in incompressible limit. *J. Comput. Phys.* **146** (1), 282 – 300.

He, X. & Doolen, G. D. 2002 Thermodynamic foundations of kinetic theory and lattice Boltzmann models for multiphase flows. *J. Stat. Phys.* **107** (1-2), 309–328.

He, X. & Luo, L. S. 1997*a* A priori derivation of the lattice Boltzmann equation. *Phys. Rev. E* **55** (6), R6333.

He, X. & Luo, L. S. 1997*b* Theory of the lattice Boltzmann method: From the Boltzmann equation to the lattice Boltzmann equation. *Phys. Rev. E* **56** (6), 6811.

He, X., Shan, X. & Doolen, G. D. 1998*b* Discrete Boltzmann equation model for nonideal gases. *Phys. Rev. E* **57**, R13–R16.

Higuera, F. J., Succi, S. & Benzi, R. 1989 Lattice gas dynamics with enhanced collisions. *Europhys. Lett.* **9** (4), 345.

Holway Jr, L. H. 1966 New statistical models for kinetic theory: methods of construction. *Phys. Fluids* **9** (9), 1658–1673.

Hörmander, L. 1971 Fourier integral operators. i. *Acta Math.* **127**, 79–183.

Hosseini, S. M., Vinuesa, R., Schlatter, P., Hanifi, A. & Henningson, D. S. 2016 Direct numerical simulation of the flow around a wing section at moderate reynolds number. *International Journal of Heat and Fluid Flow* **61**, 117–128.

Houze Jr, R. A. 2014 *Cloud dynamics*, , vol. 104. Academic press.

Huang, Y. & Bau, H. H. 1997 Thermoacoustic waves in a confined medium. *Int. J. Heat Mass Transfer* **40** (2), 407 – 419.

Inamuro, T., Tajima, S. & Ogino, F. 2004 Lattice Boltzmann simulation of droplet collision dynamics. *Int. J. Heat Mass Transfer* **47**, 4649.

Jacqmin, D. 1999 Calculation of two-phase navierstokes flows using phase-field modeling. *J. Comput. Phys.* **155** (1), 96 – 127.

Karlin, I., Bösch, F. & Chikatamarla, S. 2014 Gibbs' principle for the lattice-kinetic theory of fluid dynamics. *Physical Review E* **90** (3), 031302.

Karlin, I., Bösch, F., Chikatamarla, S. & Succi, S. 2015 Entropy-assisted computing of low-dissipative systems. *Entropy* **17** (12), 8099–8110.

Karlin, I. V., Ferrante, A. & Öttinger, H. C. 1999 Perfect entropy functions of the lattice Boltzmann method. *Europhys. Lett.* **47** (2), 182.

Karlin, I. V., Gorban, A. N., Succi, S. & Boffi, V. 1998 Maximum entropy principle for lattice kinetic equations. *Phys. Rev. Lett.* **81** (1), 6.

Khain, A., Ovtchinnikov, M., Pinsky, M., Pokrovsky, A. & Krugliak, H. 2000 Notes on the state-of-the-art numerical modeling of cloud microphysics. *Atmospheric Res.* **55** (3-4), 159–224.

Khain, A. P. & Pinsky, M. 2018 *Physical Processes in Clouds and Cloud Modeling*. Cambridge University Press.

Khattri, S. 2009 New close form approximations of ln(1 + x). *Teach. Math.* **12** (1), 7–14.

Korteweg, D. J. 1901 Sur la forme que prennet. *Arch. Neerl. Sci. Exactes Nat. Ser. II* **6**, 1–24.

Kozma, L. 2018 Useful inequalities. *http : //www.lkozma.net/inequalities_cheat_sheet/ineq.pdf* .

Krithivasan, S., Wahal, S. & Ansumali, S. 2014 Diffused bounce-back condition and refill algorithm for the lattice Boltzmann method. *Phys. Rev. E* **89**, 033313.

Kunnen, R., Geurts, B. J. & Clercx, H. 2009 Turbulence statistics and energy budget in rotating Rayleigh-Bénard convection. *Eur. J. Mech. B Fluids* **28** (4), 578–589.

Kuo, H.-L. 1965 On formation and intensification of tropical cyclones through latent heat release by cumulus convection. *J. Atmos. Sci.* **22** (1), 40–63.

Ladd, A. J. C. 1993 Short-time motion of colloidal particles: Numerical simulation via a fluctuating lattice-Boltzmann equation. *Phys. Rev. Lett.* **70** (9), 1339.

Ladd, A. J. C. 1994 Numerical simulations of particulate suspensions via a discretized Boltzmann equation. part 1. theoretical foundation. *J. Fluid Mech.* **271**, 285–309.

Lallemand, P. & Luo, L. S. 2000 Theory of the lattice Boltzmann method: Dispersion, dissipation, isotropy, Galilean invariance, and stability. *Phys. Rev. E* **61** (6), 6546.

LANDAU, L. D. & LIFSHITZ, E. M. 2013 *Course of theoretical physics: Fluid mechanics*. Elsevier.

LANEY, C. B. 1998 *Computational Gasdynamics*. Cambridge University Press.

LARKIN, B. 1967 Heat flow to a confined fluid in zero gravity. In *Thermophysics of Spacecraft and Planetary Bodies*, pp. 819–832. Elsevier.

LARSSON, J. & WANG, Q. 2014 The prospect of using large eddy and detached eddy simulations in engineering design, and the research required to get there. *Philos. Trans. Royal Soc. A* **372** (2022), 20130329.

LAVEZZO, V., CLERCX, H. & TOSCHI, F. 2011 Rayleigh-Bénard convection via lattice Boltzmann method: code validation and grid resolution effects. In *J. Phys.: Conf. Ser.*, , vol. 333, p. 012011. IOP Publishing.

LEAL, L. G. 2007 *Advanced Transport Phenomena: Fluid Mechanics and Convective Transport Processes*, , vol. 7. Cambridge University Press.

LEBOWITZ, J. L., FRISCH, H. L. & HELFAND, E. 1960 Nonequilibrium distribution functions in a fluid. *Phys. Fluids* **3** (3), 325–338.

LEE, T. & FISCHER, P. F. 2006 Eliminating parasitic currents in the lattice Boltzmann equation method for nonideal gases. *Phys. Rev. E* **74**, 046709.

LEE, T. & LIN, C.-L. 2005 A stable discretization of the lattice Boltzmann equation for simulation of incompressible two-phase flows at high density ratio. *Journal of Computational Physics* **206** (1), 16 – 47.

LEVERMORE, C. D. 1996 Moment closure hierarchies for kinetic theories. *J. Stat. Phys.* **83** (5-6), 1021–1065.

LIBOFF, R. L. 2003 *Kinetic theory: classical, quantum, and relativistic descriptions*. Springer Science & Business Media.

LOVE, E. 1980 Some logarithm inequalities. *The Math. Gazette* **64** (427), 5557.

LUO, L.-S. & GIRIMAJI, S. S. 2002 Lattice Boltzmann model for binary mixtures. *Physical Review E* **66** (3), 035301.

LUO, L.-S. & GIRIMAJI, S. S. 2003 Theory of the lattice Boltzmann method: two-fluid model for binary mixtures. *Physical Review E* **67** (3), 036302.

MALASPINAS, O., DEVILLE, M. & CHOPARD, B. 2008 Towards a physical interpretation of the entropic lattice Boltzmann method. *Phys. Rev. E* **78**, 066705.

MALASPINAS, O. & SAGAUT, P. 2012 Consistent subgrid scale modelling for lattice boltzmann methods. *J. Fluid Mech.* **700**, 514–542.

MAXWELL, J. C. 1860 Illustrations of the dynamical theory of gases. *Phil. Mag. ("Scientific Papers Vol. I")* **19** (31), 377–409.

Mazloomi, A., Chikatamarla, S. S. & Karlin, I. V. 2015 Entropic lattice boltzmann method for multiphase flows. *Phys. Rev. Lett.* **114** (17), 174502.

Mazloomi M., A., Chikatamarla, S. S. & Karlin, I. V. 2015 Entropic lattice Boltzmann method for multiphase flows: Fluid-solid interfaces. *Phys. Rev. E* **92**, 023308.

McNamara, G. R., Garcia, A. L. & Alder, B. J. 1997 A hydrodynamically correct thermal lattice Boltzmann model. *J. Stat. Phys.* **87** (5-6), 1111–1121.

McNamara, G. R. & Zanetti, G. 1988 Use of the Boltzmann equation to simulate lattice-gas automata. *Phys. Rev. Lett.* **61** (20), 2332.

Meadows, D. 2008 *Thinking in Systems: A Primer*. Chelsea Green Publishing.

Mendoza, M., Boghosian, B. M., Herrmann, H. J. & Succi, S. 2010 Fast lattice Boltzmann solver for relativistic hydrodynamics. *Phys. Rev. Lett.* **105** (1), 014502.

Meneveau, C. 2011 Lagrangian dynamics and models of the velocity gradient tensor in turbulent flows. *Annu. Rev. Fluid Mech.* **43**, 219–245.

Meng, J. & Zhang, Y. 2014 Diffuse reflection boundary condition for high-order lattice Boltzmann models with streamingcollision mechanism. *J. Comput. Phys.* **258**, 601 – 612.

Minion, M. L. & Brown, D. L. 1997 Performance of under-resolved two-dimensional incompressible flow simulations, ii. *J. Comput. Phys.* **138** (2), 734–765.

Mohamad, A. A. & Kuzmin, A. 2012 The soret effect with the d1q2 and d2q4 lattice Boltzmann model. *Int. J. Nonlinear Sci. Numer. Simul.* **13** (3-4), 289–293.

Monaco, R. & Preziosi, L. 1991 *Fluid Dynamic Applications of the Discrete Boltzmann Equation*, , vol. 3. World Scientific.

Namburi, M. 2017 Crystallographic lattice Boltzmann method. PhD thesis, Jawaharlal Nehru Centre for Advanced Scientific Research.

Namburi, M., Krithivasan, S. & Ansumali, S. 2016 Crystallographic lattice Boltzmann method. *Sci. Rep.* **6**, 27172.

Niculescu, C. & Persson, L.-E. 2007 *Convex Functions and Their Applications: A Contemporary Approach*. Society for Industrial and Applied Mathematics.

Oliemans, R. V. A. 2012 *Computational fluid dynamics for the petrochemical process industry*. Springer Science & Business Media.

Parang, M. & Salah-Eddine, A. 1984 Thermoacoustic convection heat-transfer phenomenon. *AIAA J.* **22** (7), 1020–1022.

Peng, Y., Shu, C. & Chew, Y. 2003 Simplified thermal lattice Boltzmann model for incompressible thermal flows. *Phys. Rev. E* **68** (2), 026701.

Pope, S. B. 2000 *Turbulent flows*. Cambridge univ. press.

Premnath, K. N., Pattison, M. J. & Banerjee, S. 2009 Dynamic subgrid scale modeling of turbulent flows using lattice-Boltzmann method. *Physica A* **388** (13), 2640–2658.

Press, W. H., Teukolsky, S. A., Vetterling, W. T. & Flannery, B. P. 1992 Numerical recipes in C++. *The art of scientific computing* **2**, 1002.

Qian, Y. H., d'Humières, D. & Lallemand, P. 1992 Lattice BGK models for navier-stokes equation. *Europhys. Lett.* **17** (6), 479.

Qian, Y. H. & Zhou, Y. 1998 Complete Galilean-invariant lattice BGK models for the navier-stokes equation. *Europhys. Lett.* **42** (4), 359.

Qiao, Z., Yang, X. & Zhang, Y. 2018 Mass conservative lattice Boltzmann scheme for a three-dimensional diffuse interface model with peng-robinson equation of state. *Phys. Rev. E* **98**, 023306.

Ramadugu, R., Thampi, S. P., Adhikari, R., Succi, S. & Ansumali, S. 2013 Lattice differential operators for computational physics. *Europhys. Lett.* **101** (5), 50006.

Reichl, L. E. 1999 A modern course in statistical physics.

Rowlinson, J. & Widom, B. 1982 Molecular theory of capillarity.

Sbragaglia, M., Benzi, R., Biferale, L., Chen, H., Shan, X. & Succi, S. 2009 Lattice Boltzmann method with self-consistent thermo-hydrodynamic equilibria. *J. Fluid Mech.* **628**, 299309.

Sbragaglia, M. & Sugiyama, K. 2010 Volumetric formulation for a class of kinetic models with energy conservation. *Phys. Rev. E* **82**, 046709.

Schumacher, J. 2009 Lagrangian studies in convective turbulence. *Phys. Rev. E* **79**, 056301.

Shakhov, E. M. 1968 Generalization of the Krook kinetic relaxation equation. *Fluid Dyn.* **3** (5), 95–96.

Shan, X. 1997 Simulation of Rayleigh-Bénard convection using a lattice Boltzmann method. *Phys. Rev. E* **55**, 2780–2788.

Shan, X. 2006 Analysis and reduction of the spurious current in a class of multiphase lattice Boltzmann models. *Phys. Rev. E* **73**, 047701.

Shan, X. 2010 General solution of lattices for Cartesian lattice Bhatanagar-Gross-Krook model. *Phys. Rev. E* **81**, 036702.

Shan, X. & Chen, H. 1993 Lattice Boltzmann model for simulating flows with multiple phases and components. *Phys. Rev. E* **47**, 1815–1819.

Shan, X. & He, X. 1998*a* Discretization of the velocity space in the solution of the Boltzmann equation. *Phys. Rev. Lett.* **80**, 65–68.

SHAN, X. & HE, X. 1998*b* Discretization of the velocity space in the solution of the Boltzmann equation. *Phys. Rev. Lett.* **80** (1), 65–68.

SHAN, X., YUAN, X.-F. & CHEN, H. 2006 Kinetic theory representation of hydrodynamics: a way beyond the Navier–Stokes equation. *Journal of Fluid Mechanics* **550**, 413–441.

SHET, A. G., SORATHIYA, S. H., KRITHIVASAN, S., DESHPANDE, A. M., KAUL, B., SHERLEKAR, S. D. & ANSUMALI, S. 2013 Data structure and movement for lattice-based simulations. *Phys. Rev. E* **88**, 013314.

SINGH, S., SUBRAMANIAN, G. & ANSUMALI, S. 2013 Lattice Fokker Planck for dilute polymer dynamics. *Phys. Rev. E* **88** (1), 013301.

SINGH, S. K. & ANSUMALI, S. 2015 Fokker-Planck model of hydrodynamics. *Phys. Rev. E* **91**, 033303.

SINGH, S. K., THANTANAPALLY, C. & ANSUMALI, S. 2016 Gaseous microflow modeling using the Fokker-Planck equation. *Phys. Rev. E* **94**, 063307.

SLOTNICK, J., KHODADOUST, A., ALONSO, J., DARMOFAL, D., GROPP, W., LURIE, E. & MAVRIPLIS, D. 2014 *CFD vision 2030 study: a path to revolutionary computational aerosciences*. NASA CR-2014-218178.

SMAGORINSKY, J., MANABE, S. & HOLLOWAY, J. L. 1965 Numerical results from a nine-level general circulation model of the atmosphere. *Mon. Weather Rev* **93** (12), 727–768.

SMITH, J. M., VAN NESS, H. & ABBOTT, M. 1996 Introduction to chemical engineering thermodynamics.

SOE, M., VAHALA, G., PAVLO, P., VAHALA, L. & CHEN, H. 1998 Thermal lattice Boltzmann simulations of variable Prandtl number turbulent flows. *Physical Review E* **57** (4), 4227.

SOFO, A. 2016 Integrals of logarithmic and hypergeometric functions. *Commun. Math.* **24** (1), 7 – 22.

SOFONEA, V. 2006 Lattice Boltzmann approach to thermal transpiration. *Phys. Rev. E* **74**, 056705.

SPRADLEY, L. W. & CHURCHILL, S. W. 1975 Pressure- and buoyancy-driven thermal convection in a rectangular enclosure. *J. Fluid Mech.* **70** (4), 705720.

SUCCI, S. 2001 *The Lattice Boltzmann Equation: for Fluid Dynamics and Beyond*. Oxford University Press, Oxford.

SUCCI, S., FILIPPOVA, O., CHEN, H. & ORSZAG, S. 2002*a* Towards a renormalized lattice Boltzmann equation for fluid turbulence. *J. Stat. Phys.* **107** (1-2), 261–278.

SUCCI, S., KARLIN, I. V. & CHEN, H. 2002*b* Colloquium: Role of the H theorem in lattice Boltzmann hydrodynamic simulations. *Rev. Mod. Phys.* **74** (4), 1203.

Suryanarayanan, S., Singh, S. & Ansumali, S. 2013 Extended BGK Boltzmann for dense gases. *Commun. Comput. Phys.* **13** (3), 629648.

Swift, M. R., Orlandini, E., Osborn, W. R. & Yeomans, J. M. 1996 Lattice Boltzmann simulations of liquid-gas and binary fluid systems. *Phys. Rev. E* **54**, 5041–5052.

Swift, M. R., Osborn, W. R. & Yeomans, J. M. 1995 Lattice Boltzmann simulation of nonideal fluids. *Phys. Rev. Lett.* **75**, 830–833.

Taylor, G. I. 1934 The viscosity of a fluid containing small drops of another fluid. *Proc. Royal Soc. A* pp. 501–523.

Thampi, S. P., Ansumali, S., Adhikari, R. & Succi, S. 2013*a* Isotropic discrete laplacian operators from lattice hydrodynamics. *J. Comput. Phys.* **234**, 1–7.

Thampi, S. P., Golestanian, R. & Yeomans, J. M. 2013*b* Velocity correlations in an active nematic. *Phys. Rev. Lett.* **111** (11), 118101.

Thantanapally, C., Patil, D. V., Succi, S. & Ansumali, S. 2013*a* Universal mechanism for saturation of vorticity growth in fully developed fluid turbulence. *J. Fluid Mech.* **728**, R4.

Thantanapally, C., Singh, S., Patil, D. V., Succi, S. & Ansumali, S. 2013*b* Quasiequilibrium lattice Boltzmann models with tunable Prandtl number for incompressible hydrodynamics. *Int. J. Mod. Phys. C* **24** (12), 1340004.

Thompson, G., Rasmussen, R. M. & Manning, K. 2004 Explicit forecasts of winter precipitation using an improved bulk microphysics scheme. part i: Description and sensitivity analysis. *Mon. Weather Rev.* **132** (2), 519–542.

Toppaladoddi, S., Succi, S. & Wettlaufer, J. S. 2017 Roughness as a route to the ultimate regime of thermal convection. *Phys. Rev. Lett.* **118**, 074503.

Topse, F. 2007 *Some Bounds for the Logarithmic Function*. Nova Science.

Tosi, F., Ubertini, S., Succi, S. & Karlin, I. V. 2006 Optimization strategies for the entropic lattice Boltzmann method. *J. Sci. Comput.* **30** (3), 369.

Tsallis, C. 1988 Possible generalization of Boltzmann-Gibbs statistics. *J. Stat. Phys.* **52** (1-2), 479–487.

Vahala, G., Pavlo, P., Vahala, L. & Martys, N. S. 1998 Thermal lattice-Boltzmann models (tlbm) for compressible flows. *Int. J. Mod. Phys. C* **9** (08), 1247–1261.

Vashishtha, S., Verma, M. K. & Samuel, R. 2018 Large-eddy simulations of turbulent thermal convection using renormalized viscosity and thermal diffusivity. *Phys. Rev. E* **98** (4), 043109.

van der Waals, J. D. 1979 The thermodynamic theory of capillarity under the hypothesis of a continuous variation of density. *Journal of Statistical Physics* **20** (2), 200–244.

WAGNER, A. J. 1998 An H-theorem for the lattice Boltzmann approach to hydrodynamics. *Europhys. Lett.* **44** (2), 144.

WAGNER, A. J. 2006 Thermodynamic consistency of liquid-gas lattice Boltzmann simulations. *Phys. Rev. E* **74**, 056703.

WAGNER, A. J. & POOLEY, C. M. 2007 Interface width and bulk stability: Requirements for the simulation of deeply quenched liquid-gas systems. *Phys. Rev. E* **76**, 045702.

WEHRL, A. 1978 General properties of entropy. *Rev. Mod. Phys.* **50**, 221–260.

YAU, M. K. & ROGERS, R. 1996 *A short course in cloud physics*. Elsevier.

YUAN, P. & SCHAEFER, L. 2006 Equations of state in a lattice Boltzmann model. *Phys. Fluids* **18** (4), 042101.

YUDISTIAWAN, W. P., KWAK, S. K., PATIL, D. V. & ANSUMALI, S. 2010 Higher-order Galilean-invariant lattice Boltzmann model for microflows: Single-component gas. *Phys. Rev. E* **82** (4), 046701.

ZEE, A. 2010 *Quantum field theory in a nutshell*, , vol. 7. Princeton university press.

ZHANG, R. & CHEN, H. 2003 Lattice Boltzmann method for simulations of liquid-vapor thermal flows. *Phys. Rev. E* **67**, 066711.

ZHU, X., MATHAI, V., STEVENS, R. J. A. M., VERZICCO, R. & LOHSE, D. 2018 Transition to the ultimate regime in two-dimensional Rayleigh-Bénard convection. *Phys. Rev. Lett.* **120**, 144502.

Curriculum vitae

Personal:

- Name: Mohammad Atif
- Sex: Male
- Nationality: Indian
- Date of birth: 02 May 1993

Education:

- **Ph.D.** (2015-2019)
    - Title: Thermodynamics of the entropic lattice Boltzmann model
    - Advisor: Prof. Santosh Ansumali
    - Engineering Mechanics Unit
    - Jawaharlal Nehru Centre for Advanced Scientific Research, Bangalore (India)
- **Bachelor of Engineering (Honours)** (2011-2015)
    - Thesis advisor: Prof. Amol Marathe
    - Department of Mechanical Engineering
    - Birla Institute of Technology and Science, Pilani (India)

List of publications:

- **M. Atif**, P. K. Kolluru, and S. Ansumali. Discrete kinetic modeling of thermohydrodynamics (*Under preparation*).
- **M. Atif**, P. K. Kolluru, C. Thantanapally, and S. Ansumali. Essentially entropic lattice Boltzmann model: Theory and simulations (*Submitted*).
- P. K. Kolluru, **M. Atif**, M. Namburi, and S. Ansumali. Lattice Boltzmann model for weakly compressible flows (*Submitted*).
- **M. Atif**, M. Namburi, and S. Ansumali. Higher-order lattice Boltzmann model for thermohydrodynamics, *Phys. Rev. E* **98**, 053311 (2018).
- **M. Atif**, P. K. Kolluru, C. Thantanapally, and S. Ansumali. Essentially entropic lattice Boltzmann model, *Phys. Rev. Lett* **119**, 240602 (2017).